Molecular mapping of the rabbit atrioventricular node

Ian David Greener

Submitted in accordance with the requirements for the degree of Doctor of Philosophy

The University of Leeds

Institute of Membrane and Systems Biology

May 2006

The candidate confirms that the work submitted is his own and that appropriate credit has been given where reference has been made to work of others

Abstract

The atrioventricular node (AVN) of the heart is responsible for the important conduction delay between atrial systole and ventricular systole. The anatomical architecture and functional properties of the AVN are complex. Ionic currents have been characterised in the AVN at both the whole tissue level and single cell level. However, little is known about the molecular basis of these ionic currents. There were two aims of this research: 1) to generate an accurate three-dimensional reconstruction of the rabbit AVN conduction axis and 2) to use *real time* PCR and *in situ* hybridisation to measure levels of mRNA for specific ion channels and membrane proteins in the rabbit AVN and surrounding atrial and ventricular tissue. Neurofilament-M (NF-M) immunolabelling revealed a tract of cells extending from the posterior nodal extension through the compact node to the common bundle. The PNE appeared to correspond to the slow pathway. Loosely packed atrial muscle comprised the anterior region of the AVN conduction axis closest to the enclosed part of the AVN and most likely represents the fast pathway. Lower nodal cells extended from the common bundle to the lower extremities of the compact node and PNE. Significant differences in the mRNA levels between the PNE and atrial muscle for the pacemaker channel HCN4, I_{Na} channels $Na_v1.1$ and $Na_v1.5$, the $I_{Ca,L}$ channel $Ca_v1.3$, the I_{to} channel β-subunit KChIP2 and Cx43 were found. HCN1, $Na_v1.1$, $Ca_v1.3$ and NF-M mRNA were significantly higher in the PNE, compact node and common bundle compared to the atrium and ventricle. $K_{ir}2.1$ mRNA was significantly higher in the ventricular muscle compared to the PNE and atrial muscle. Atrial natriuretic peptide (ANP) mRNA, was significantly higher in the atrial muscle compared to other tissues. For mRNAs for the I_{to} channels, $K_v4.2$ and $K_v4.3$, the delayed rectifier K^+ channels, $K_v1.5$, ERG, K_vLQT1 and minK, the inward rectifier K^+ channels, $K_{ir}2.2$, $K_{ir}6.2$ and β-subunit SUR2A, and the Ca^{2+} handling proteins, RYR2, RYR3, NCX1 and SERCA2a, there were no significant differences between tissues. *In situ* hybridisation staining revealed further complexity of the AVN conduction axis tissue. A region of loosely packed atrial tissue immediately adjacent to the nodal tissue was KChIP2 negative and $Na_v1.5$ negative, and the lower nodal cells were both $Ca_v1.2$ and $Ca_v1.3$ positive. This study has described a complex architecture of the AVN and added further complexity by providing a detailed account of ion channel expression throughout this tissue.

Table of contents

Figures

Chapter 1

Chapter 2

Chapter 3

Chapter 4

Chapter 5

Chapter 6

Chapter 7

Chapter 8

Chapter 9

Chapter 10

Abbreviations

4-AP	4-aminopyridine
A	Adenine
ACh	Acetylcholine
Amp^r	Ampicillin resistance
ANOVA	Analysis of variance
ANP	Atrial natriuretic peptide
AM	Atrial muscle
AP	Atrial appendage
AVN	Atrioventricular node
bp	Base pairs
BCIP	5-bromo-4-chloro-3-indolyl phosphate
C	Cytosine
cAMP	Cyclic adenosine monophosphate
CHO	Chinese hamster ovary
cDNA	Complementary deoxyribonucleic acid
CHAPS	3-[(3-Cholamidopropyl)dimethyl amino]-1-propanesulfonate
C_t	Cycle threshold
CT	Crista terminalis
Cx	Connexins
DIG	Digoxigenin
DNA	Deoxyribonucleic acid
dNTP	Deoxynucleoside triphosphate
EDTA	Ethylendiaminetetraacetic acid
Endo	Endocardial
Epi	Epicardial
ER	Endoplasmic reticulum
ERG	Ether-a-go-go-related gene
G	Guanine
GAPDH	Glyceraldehyde 3 phosphate dehydrogenase
HCN	Hyperpolarization-activated, cyclic nucleotide gated channel

$I_{Ca,L}$	L-type Ca^{2+} current
$I_{Ca,T}$	T-type Ca^{2+} current
I_f	Funny current
$I_{K,1}$	Inward rectifying K^+ current
$I_{K,r}$	Rapidly activated delayed rectifier K^+ current
$I_{K,s}$	Slowly activated delayed rectifier K^+ current
$I_{K,ur}$	Ultra-rapidly activated delayed rectifier K^+ current
I_{Na}	Na^+ current
$I_{Na\text{-}Ca}$	Na^+ - Ca^{2+} exchange current
IPTG	Isopropyl-β-D-thiogalactopyranoside
ISH	*In situ* hybridisation
I_{st}	Sustained inward current
I_{to}	Transient outward current
KChAP	K^+ channel associated protein
IVC	Inferior vena cava
LA	Left atrium
LSARB	Left branch of the sinoatrial node ring bundle
LV	Left ventricle
M	Mitochondria
MCS	Multiple cloning site
MIRP1	MinK-related peptide
mRNA	Messenger ribonucleic acid
NBT	Nitroblue tetrazolium
NCX	Na^+-Ca^{2+} exchanger
NF-M	Medium neurofilament
OCT	Optimal cutting compound
PBS	Phosphate buffered saline
PCR	Polymerase chain reaction
PFA	Paraformaldehyde
PV	Pulmonary veins
PVA	Polyvinyl alcohol
QPCR	Quantitative polymerase chain reaction
RNase	Ribonucleic acid
rRNA	Ribosomal ribonucleic acid

RT	Reverse transcription
RV	Right ventricle
RYR	Ryanodine receptor
SAN	Sinoatrial node
SANc	Sinoatrial node centre
SANp	Sinoatrial node periphery
S.E.M	Standard error of the mean
SERCA2a	Sarco-endoplasmic reticulum calcium ATPase isoform 2a
SR	Sarcoplasmic reticulum
SSC	Sodium saline citrate
SUR2A	Sulfonylurea receptor 2A
SVC	Superior vena cava
T	Thymine
TBE	Tris boric EDTA
TE	Tris EDTA
TEA	Triethanolamine
T_m	Melting temperature
TTX	Tetrodotoxin
VDCC	Voltage-dependent calcium channels
X-gal	5-bromo-4-chloro-3-indolyl-β-D-galactopyranoside

Acknowledgements

I would like to take this opportunity to thank my supervisors Professor Mark Boyett and Dr. Rudi Billeter for not only giving me the opportunity to undertake this PhD but also for helping to make the experience successful and enjoyable. Mark's professional attitude and guidance has helped me greatly. In addition, I hope I can adopt some of Rudi's enthusiasm for science, in-depth thinking and ingenious approaches in future research projects.

My fellow work colleagues, James, Halina, and Gillian have offered continual advice throughout and have been most enjoyable to work with and I hope to continue this in the future. Jue has been a pleasure to work with during the three-dimensional reconstruction.

Thanks to Jamel, Dallas, Mark, Crocket and Pickles who have made a weekly game of 5-a-side possible, lunchtimes and coffee breaks entertaining and most importantly, accompanied me on many a drunken night-out.

The time I have spent with my current housemates, Nick, Ben, Phil and the more recent Czech addition, Petr (from whom a little Czech has been learnt) has been amusing, especially with their constant humour.

Finally, I am greatly indebted to my family for their support over the years, which has enabled me to be in this position and for which I am very grateful.

Chapter 1

General introduction

1.1 Atrioventricular node (AVN)

1.1.1 The cardiac conduction system

The sinoatrial node (SAN) is the primary pacemaker in the heart; the SAN centre is the leading pacemaker site capable of generating spontaneous action potentials. These impulses propagate to the periphery of the SAN to excite the working atrial muscle. Electrical excitation continues throughout the atria and eventually reaches the AVN where there is a delay in impulse propagation sufficient to allow atrial systole to occur and fill the ventricles during ventricular diastole. The impulse proceeds through the bundle of His/common bundle to the bundle branches and Purkinje fibres permitting excitation of the ventricles and ventricular systole to occur.

1.1.2 Role of the atrioventricular node in cardiac function

The atrioventricular node (AVN) is well known as the structure which is responsible for the conduction delay in the cardiac cycle thereby allowing ventricular filling to occur prior to ventricular systole (Dagget et al., 1970). In addition, the AVN can prevent ventricular tachycardia during fast rates of atrial excitation, for example, during atrial fibrillation (Dreifus et al., 1971) and also act as a subsidiary pacemaker if the sinoatrial node (SAN) fails. The AVN is located at the base of the right atrial septum immediately adjacent to the tricuspid valve annulus and the ostium of the coronary sinus (Anderson and Ho, 1998).

1.1.3 Anatomical and histological classification

The classification of the AVN is one of major debate with conflicting anatomical and functional definitions (Anderson et al., 1974; Billette et al., 1976). In terms of anatomical

landmarks, the triangle of Koch, describes the collective AVN area. The triangle is demarcated superiorly by the Tendon of Todaro, which extends from the union of the Eustachian and Thebesian valves to enter the aortic root. The ventricular aspect is the hinge of the septal cusp of the tricuspid valve. Finally, the coronary sinus and inferior part of the right atrium comprise the base of the triangle (Fig. 1.1).

1.1.4 Nomenclature used to describe AVN structures

The discrepancies which have arisen over the years to describe the AVN structures both functionally and histologically are due to the fact that the heart is situated differently in the human compared to animals. Ultimately, the correct description of the AVN should be based on human orientation, since, this structure is clinically very important and therefore to aid clinicians in their treatment of AVN pathologies such as catheter ablation, experimental findings from animals should be described with the human nomenclature in mind. In animals, the AVN is described with the membranous septum being anterior and the coronary sinus being posterior; with the tendon of Todaro and tricuspid valve annulus being left and right lateral, respectively. In humans, however, the membranous septum is located superiorly and the coronary sinus inferiorly; the tendon of Todaro anteriorly and the tricuspid valve annulus posteriorly, these descriptions are based on the fact that in humans the apex of the triangle of Koch points up and not to the front. A common AVN nomenclature based on human descriptions has been requested by a panel of experts in this field (Cosio et al., 1999), however, in this thesis when describing the findings of landmark papers in AVN research which have been carried out on animals I have used the nomenclature given in that text due to the obvious problems of rewording the text to agree with human nomenclature. Histological decriptions of subcellular groups within serial sections of the AVN have also been described by different means. The compact node is the "half-oval" shaped group of cells originally described by Tawara (1906) as the "knot" or "knoten" group of cells, however, this structure has been further separated into circumferential transitional cells, mid-nodal cells and lower nodal cells (Anderson, 1972; Fig. 1.4).

1.1.5 Histological descriptions

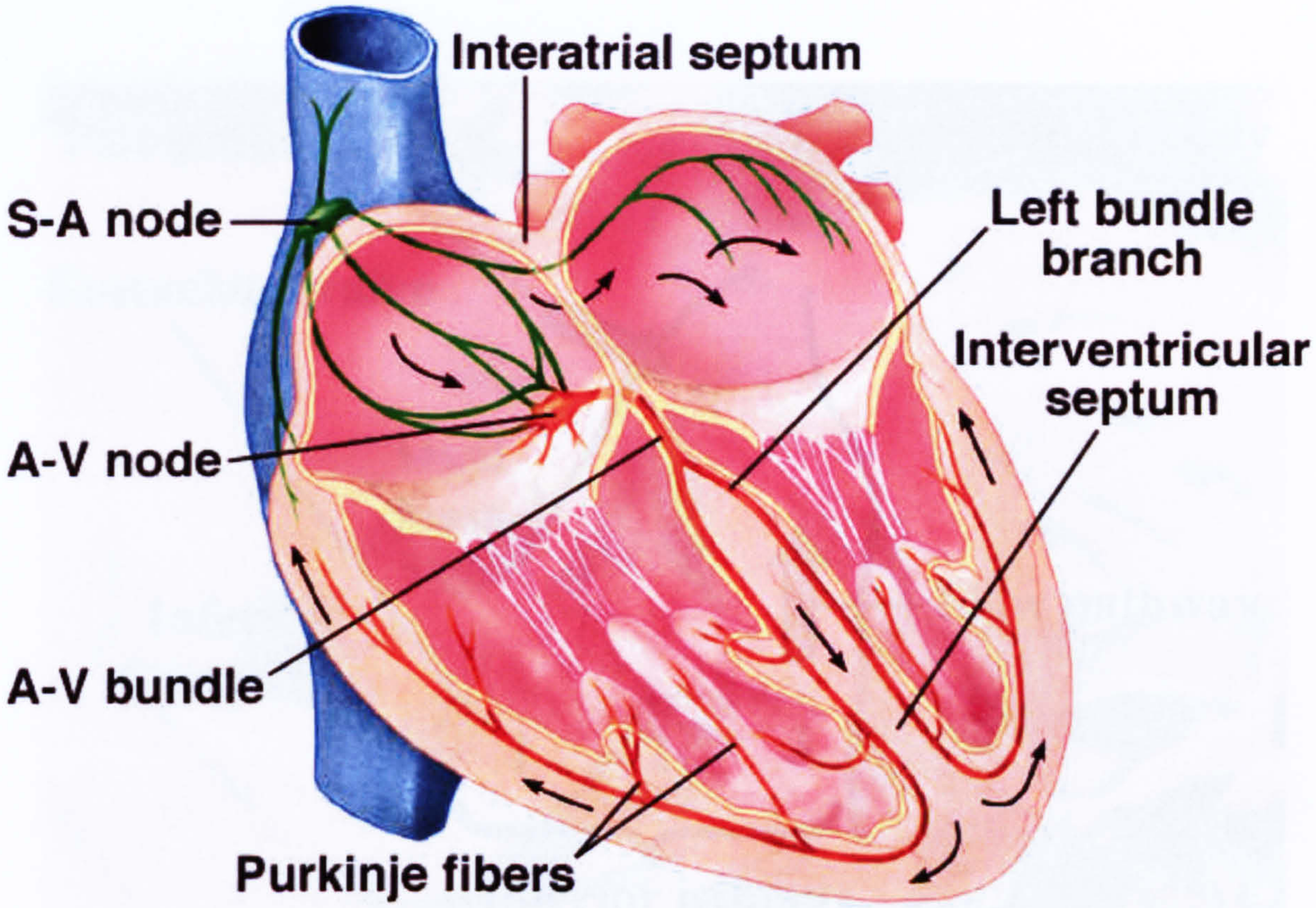

Figure 1.1 Schematic diagram of the mammalian heart showing the major components of the conduction system. A depolarising action potential originates from the the SA node in the upper right atrium. The action potential propagates throughout the right and left atria to reach the AVN, where a delay occurs to allow ventricular filling before ventricular systole. Eventually the impulse is propagated to the His bundle and then down the bundle branches to the Purkinje fibres with ultimate excitation of the ventricular muscle From McGraw-Hill, 2006.

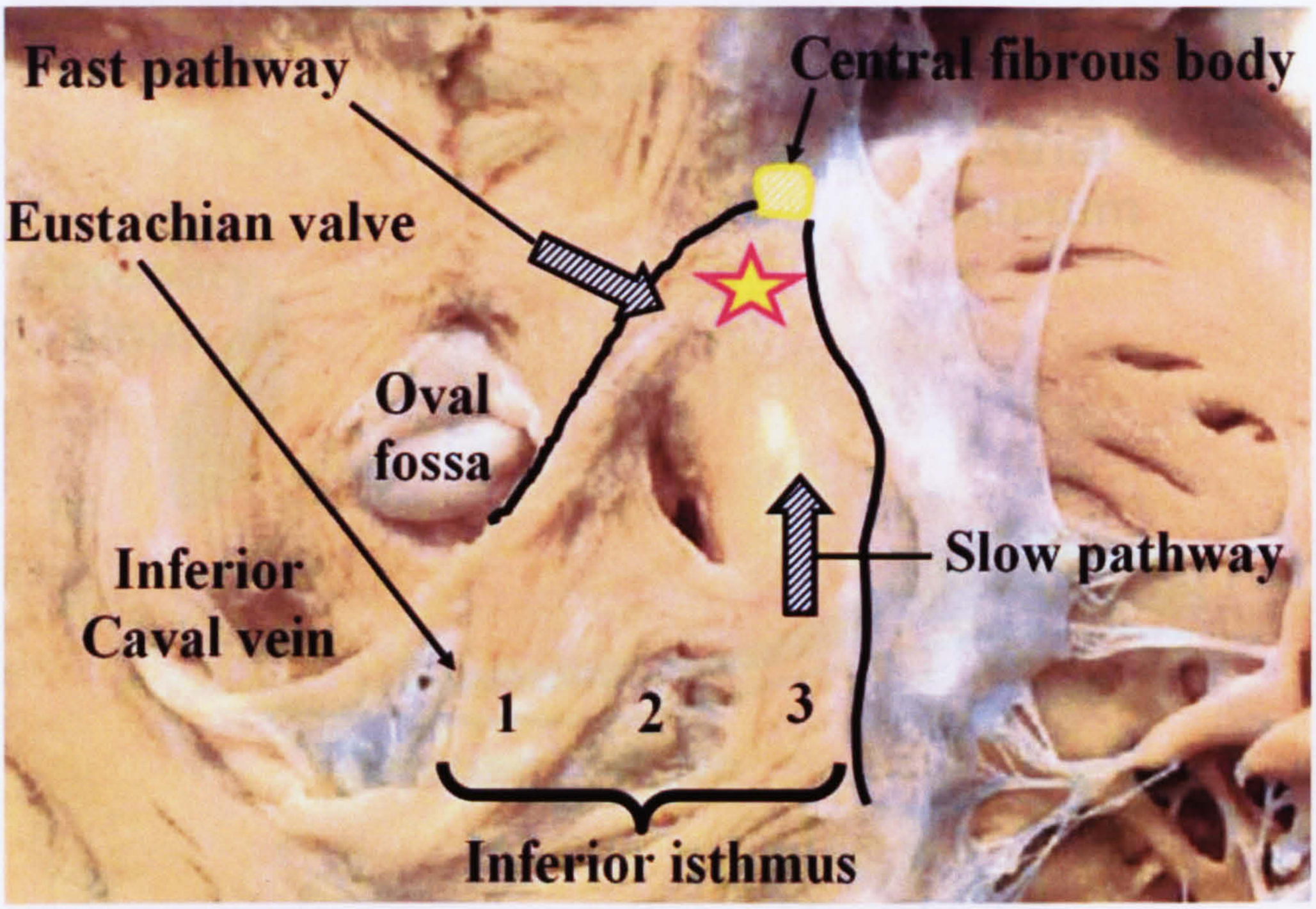

Figure 1.2 Anatomical landmarks surrounding the AVN region. Arising from the area of the inferior vena cava is the Eustachian valve which extends to form the tendon of Todaro passing posteroanteriorly to embed itself within the central fibrous body. Located on the lateral side of the tendon of Todaro are the Oval fossa and coronary sinus. Most inferiorly is the inferior isthmus which comprises the inferior approaches to the AVN such as the septal isthmus; morphological structures which lead into this area have been implicated in the genesis of atrioventricular nodal reentrant tachycardia, in particular, the slow pathway. More anteriorly an impulse can arrive at the AVN via a fast pathway. Making up the final (right-side) border of the AVN is the tricuspid valve annulus mainly formed from the fusing of the septal cusp of the tricuspid valve to the right ventricular wall. The star indicates the approximate location of the compact node. From Anderson and Ho (2006).

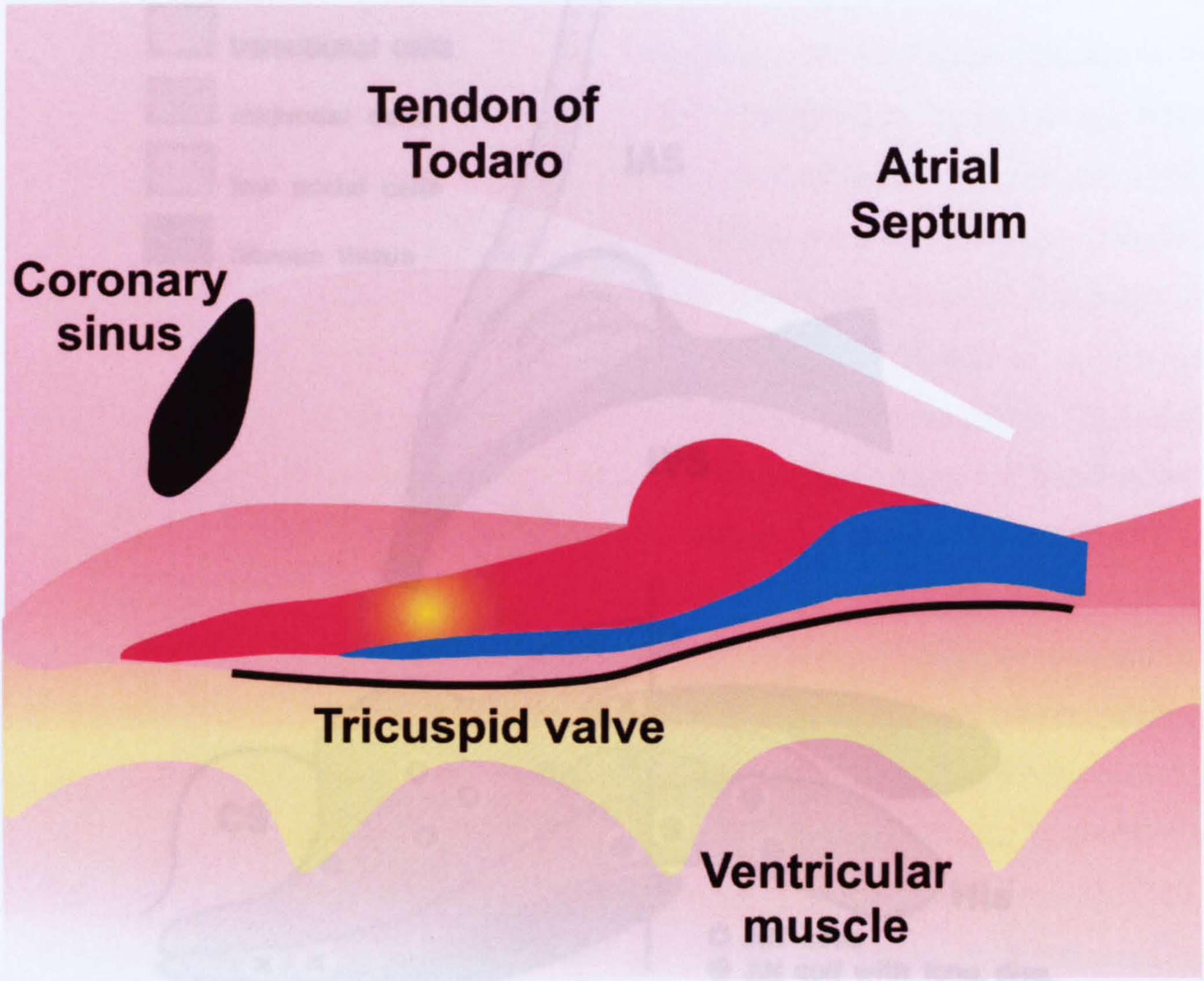

Figure 1.3 Schematic diagram of the AVN showing landmarks and structures. Red area: tract of NF-M positive cells extending from the common bundle (right most), through the compact node (circular structure) to the posterior/inferior nodal extension. The orange area represents the area where AVN pacemaking originates. Blue area: region of lower nodal cells.

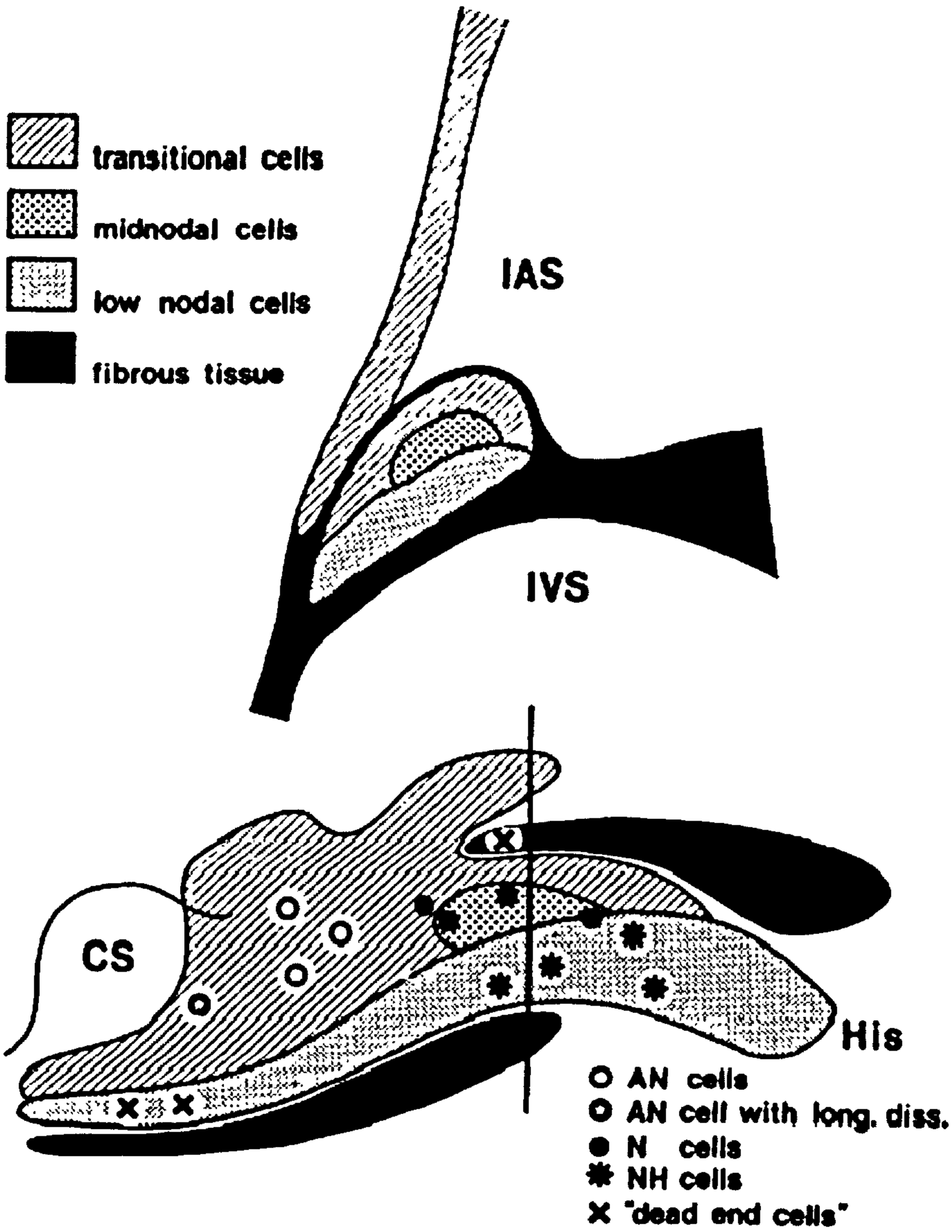

Figure 1.4 Schematic diagram showing the complex architecture of the AVN. Upper panel shows a section perpendicular to the tricuspid valve annulus through the superior part of the node at the level shown by the black line in the lower panel. Lower panel shows regions where action potentials from the various cell types (AN, N and NH) are present in the rabbit AVN. From Meijler and Janse, (1988).

Histological descriptions vary between species. Historically, the rabbit has been the animal of choice for investigating cardiac function since its electrophysiology most closely resembles that of human. His, (1893) was the first to suggest the presence of an atrioventricular bundle that conducted impulses through the atrioventricular junction to the ventricles. However, it was not until the turn of the 20th century when Sunao Tawara, whilst working in the laboratory of Ludwig Aschoff, first decsribed the AVN (Tawara, 1906). Aschoff (1910) and Mockenberg (1910) set out anatomical rules for defining conduction tract structures. They suggested that conduction tract structures should be histologically discrete from the working myocardium, serially traceable from section to section and insulated from adjacent working myocardium by a sheath of fibrous tissue. The nodal structures of the heart, however, only meet two of these criteria: they are histologically discrete and can be traced serially from section to section, but are not encapsulated by a fibrous sheath throughout. The most anterior/superior part of the AVN junction is the bundle of His/common bundle (BoH/CB) and its branches, both of which are encased in a fibrous capsule; this contacts more posteriorly/inferiorly the "true" or compact node (a dense "knot" of cells; Tawara, 1906). In the human, the compact node occurs where the cells emerge from the insulating tissues of the central fibrous body. The cells sit collectively as a half oval of branching fascicles (bundles) of densely packed small cells set in a fibrous matrix. In addition, the compact node in rabbit is surrounded by "circumferential transitional cells", which are more prominent when the node is enclosed in the central fibrous body, forming a "collar" around the compact node (Anderson, 1972). More posteriorly/inferiorly, the circumferential transitional cells form a connection with the atrial myocardium.

Any cell type beyond the compact node can then be subclassified into particular histologically distinct areas that are collectively referred to as the "AV junction". In rabbits, a large proportion of the AV conduction axis is encased within the fibrous tissues of the AV junction. However, these cells, unlike man and dog, show marked histological heterogeneity (Anderson, 1972). For example, in the rabbit, the segment closest to the atrial tissue shows a layered arrangement, with a tract of cells extending back into the atrial musculature. These cells are known as lower nodal cells (LNCs) and are a small bundle of

histologically distinct cells, which form a continuity from the penetrating bundle passing parallel to tricuspid valve annulus to contact the atrial myocardium inferiorly (Fig. 1.3).

Beyond the tract of densely packed cells are loosely arranged, transitional cells, which, as the name suggests, have a histological appearance in-between that of typical atrial and nodal cells. The area in which these cells lie is often referred to as the Atrial/Atrio-nodal (A/AN) region (Meijer and Janse, 1988). Toward the base of the triangle of Koch, at the level of the coronary sinus and inferior septal isthmus, a layer of transitional cells form the full thickness of the atrial wall (Anderson, 1972).

In rabbit there is a lack of atrial myocardial overlay cells. This is because the segments of elongated transitional cells, interspersed between fibrous tissue, form the full thickness of the atrial wall.

In humans the AVN architecture is slightly different whereby the compact node continues to penetrate the AV junction posteriorly, however, it bifurcates in two different directions, one travelling anterosuperiorly and one posteroinferiorly, with the former extension being much shorter than the latter (Inoue and Becker, 1998).

The well-formed inferior extension of the node represents the ring of histologically specialised cells from which the node itself is derived. In the developing heart this ring encircles the vestibule of the tricuspid valve (see below – development of heart).

1.1.6 Structural abnormalities - Mahaim fibres

On occasions, in the newborn, small bundles of nodal cells can penetrate the central fibrous body (in addition to the normal compact node and common bundle). If these persist into adulthood and actually form connections with the crest of the ventricular septum, they are referred to as paraspecific or "Mahaim" fibres first described by Mahaim and Winston (Anderson et al., 1996). In these cases, premature atrial stimuli which normally produce a prolongation of the P-R interval fail to do so i.e. the P-R interval remains short because the AVN is bypassed (Brechenmacher et al., 1976).

1.1.7 Blood Supply

The AVN is supplied with oxygenated blood from the posterior septal artery, a branch of the right coronary artery. In the human, this passes between the inferior nodal extensions and penetrates the AV junction at the level of the compact node (Anderson and Ho, 1972).

1.1.8 Functional classification of the AVN

Functional classification of the AVN is historically based on electrophysiological studies of the AVN and is different from traditional histological classification. Functionally, the AVN encompasses the whole area within the triangle of Koch, because this area is accountable for the electrophysiological behaviour attributed to the AVN.

1.1.8.1 Dual pathway physiology

1.1.8.1.1 Anterograde conduction

Moe (1956) and Mendez and Moe (1966), using electrophysiological techniques, described a dual-conduction system in the AVN of rabbit hearts. Mendez and Moe (1966) postulated that the presence of two distinct pathways could explain AVN reentrant tachycardia (AVNRT), a common pathophysiological condition of the heart. Janse (1969) further characterised the dual-pathways in the rabbit by determining the direction from which the pathways entered the enclosed part of the node. One pathway travels superiorly/anteriorly along the interatrial septum and the second, travels along the crista terminalis to pass posteriorly/inferiorly, at the level of the inferior septal isthmus, just below the coronary sinus (Fig. 1.2, arrows). These findings were later found to be similar in dog (Spach et al., 1971; Spach et al., 1979). Furthermore, the anterior input to the AVN curves in a posterior direction to join the posterior input. The activation sequence of the compact node is harder to interpret since some superficial cells can be activated up to 40 ms earlier than deeper cells and the speed of propagation is slow; it takes 60 ms for the action potential to cover a

distance of approximately 1mm (Janse et al., 1978). Activation in the last part of the conduction axis (common bundle) is rapid and synchronous.

The dual pathways can be used to explain the discontinuous AVN conduction curve which is a characteristic feature of AVN conduction (Fig. 1.5; Moe et al., 1956). To obtain a conduction curve, the atria are regularly stimulated at a basic cycle length (S1) and then a premature stimulus (S2) is applied. The conduction curve is a plot of the atrial-His conduction time for the premature beat (A2H2) as a function of the preceding atrial prematurity (A1A2). The earlier the premature beat, the longer the conduction time (Fig. 1.4). In human, there is a profound "jump" in the conduction curve (Fig. 1.5) at a given prematurity (Yamashiro et al., 1998). In the rabbit, the curve is smoother (Tchou et al., 1997). Conduction at longer A1A2 intervals reflects conduction along the anterior pathway. Conduction at shorter A1A2 intervals reflects conduction along the posterior pathway. The point at which there is a jump in the conduction curve is the effective refractory period (ERP) of the anterior pathway.

Due to the difficulty in performing experimental procedures on humans it was long thought that only a single "upper-common pathway" existed i.e. dual pathways do not exist. The application of radiofrequency ablation for the successful elimination of the slow pathway in AVNRT suggested that an additional inferior input maybe crucial in the human AVN (Perry and Garson, 1993; Fig. 1.5). The dual pathways can also be referred to as "slow" and "fast" pathways. The slow- and fast-pathways correspond to the posterior and anterior pathways, respectively (Denes et al., 1975). This terminology was chosen in relation to conduction times obtained during premature stimulation. The inferior pathway is termed "slow" because of the slow conduction times at short A1A2 intervals, whereas, the anterior pathway is termed "fast" because of the faster conduction times at longer A1A2 intervals.

The names "fast" and "slow" can be misleading, however, since these names relate to premature stimulation. Indeed, Mendez and Moe (1966), during basic stimulation, found very similar activation times along both anterior and posterior pathways and, in fact, postulated that the normal basic beat is propagated along the posterior pathway to excite the compact node and eventually common bundle, whereas, the anterior pathway only serves during reentry to conduct the impulse in a retrograde manner. Although dual pathway

physiology best explains AVN function, slow-pathway conduction is not solely limited to the posterior nodal extension, especially during arrhythmias (Ross et al., 1985). Indeed, patients treated for AVNRT using catheter ablation in which the region of the inferior septal isthmus is ablated still show discontinuous AVN conduction curves, suggestive of an intact slow-pathway (Ruder et al., 1991). It is thought that a molecular substrate for AVNRT may exist. Indeed, Medkour et al. (1998) proposed that in rabbits the posterior nodal extension was the molecular substrate underlying the slow-pathway. If dual pathways are responsible for AVNRT, it is possible that a unique expressional pattern of connexins, ion channels or exchangers confer these pathways more vulnerable to conduction in a slow manner. Pathophysiological studies have also provided us with clues as to how the AVN functions normally, Scherlag et al., (1995) concluded: "that the persistence of AV conduction, albeit modified, after SP and FP ablation, suggests the existence of multiple AV nodal inputs, whereas retrograde conduction (see section 1.9.1) relies on a dual exit from the AV node to the atria". Stein and Lerman (1994) using patients with AVNRT undergoing slow pathway ablation showed: 1) Both inputs are necessary for normal conduction 2) anterior atrial input had a longer refractory period and that Wenckebach cycle length were increased 3) Both inputs summate to stimulate the central node.

1.1.9 Arrhythmias associated with the AVN

The AVN is the major site responsible for two major arrythmias, paroxysmal supraventricular tachycardia and atrioventricular nodal reentrant tachycardia (AVNRT). In addition to the slow- and fast-pathways, it is generally believed that the perinodal tissue (transitional tissue) is necessary for circuit formation and successful AVN reentry (Mendez and Moe, 1966; Iinuma et al., 1983). There are three types of reentry: slow-fast, fast-slow and slow-slow. Slow-fast reentry is the most common. In this case, an impulse travels along the slow pathway anterogradely and enters the compact node and then proceeds retrogradely along the fast pathway to re-excite the atrial tissue which, in turn, forms a continuous connection for the impulse to re-emerge at the area of inferior septal isthmus, to complete the circuit (Yamabe et al., 1999). In the case of fast-slow reentry, an impulse travels anterogradely along the fast pathway and enters the AVN at the compact node; it then proceeds retrogradely along the slow-pathway to excite the atria around the inferior

septal isthmus. Since the atrium forms a continuous connection this excites the whole atria around the triangle of Koch allowing an impulse to re-enter at the fast pathway, thus forming the circuit (Goldberger et al., 1992). Slow-slow reentry is rare in the human. An impulse travels anterogradely along the slow-pathway and then travels retrogradely along its original path (Silka et al., 1994). Nikloski and Efimov (2001), using potentiometric dyes and fluorescent imaging elegantly showed the dual-pathway AVN conduction system during reentry (Fig. 1.6). Clinical treatment of AVNRT is by the way of catheter ablation of the slow pathway, since a portion of this area can be destroyed without impairing normal AVN function (Jackman et al., 1992).

1.1.9.1 Wenckebach cycles

In 1899, the cardiologist, Karel Frederik Wenckebach, first described this cardiac phenomena. It is a form of incomplete atrioventricular heart block in which there is a progressive lengthening of the AH conduction time and the P-R increasing until there is not a ventricular response. This is followed by a conducted beat with a short AH conduction time and P-R interval, and then the cycle repeats itself.

1.1.9.2 Atrioventricular block

Atrioventricular conduction can be delayed, intermittently blocked, or completely blocked and this is classified as first, second, or third degree block, respectively.

1.1.9.2.1 First degree block

In first degree block, there is a delay in conduction of the atrial impulse to the ventricles, usually at the level of the AVN. This results in prolongation of the PR interval to >0.2 s. A QRS complex follows each P wave, and the PR interval remains constant.

1.1.9.2.2 Second-degree block

There are three types of second degree block. Mobitz type I block (Wenckebach phenomenon) is usually at the level of the AVN, producing intermittent failure of

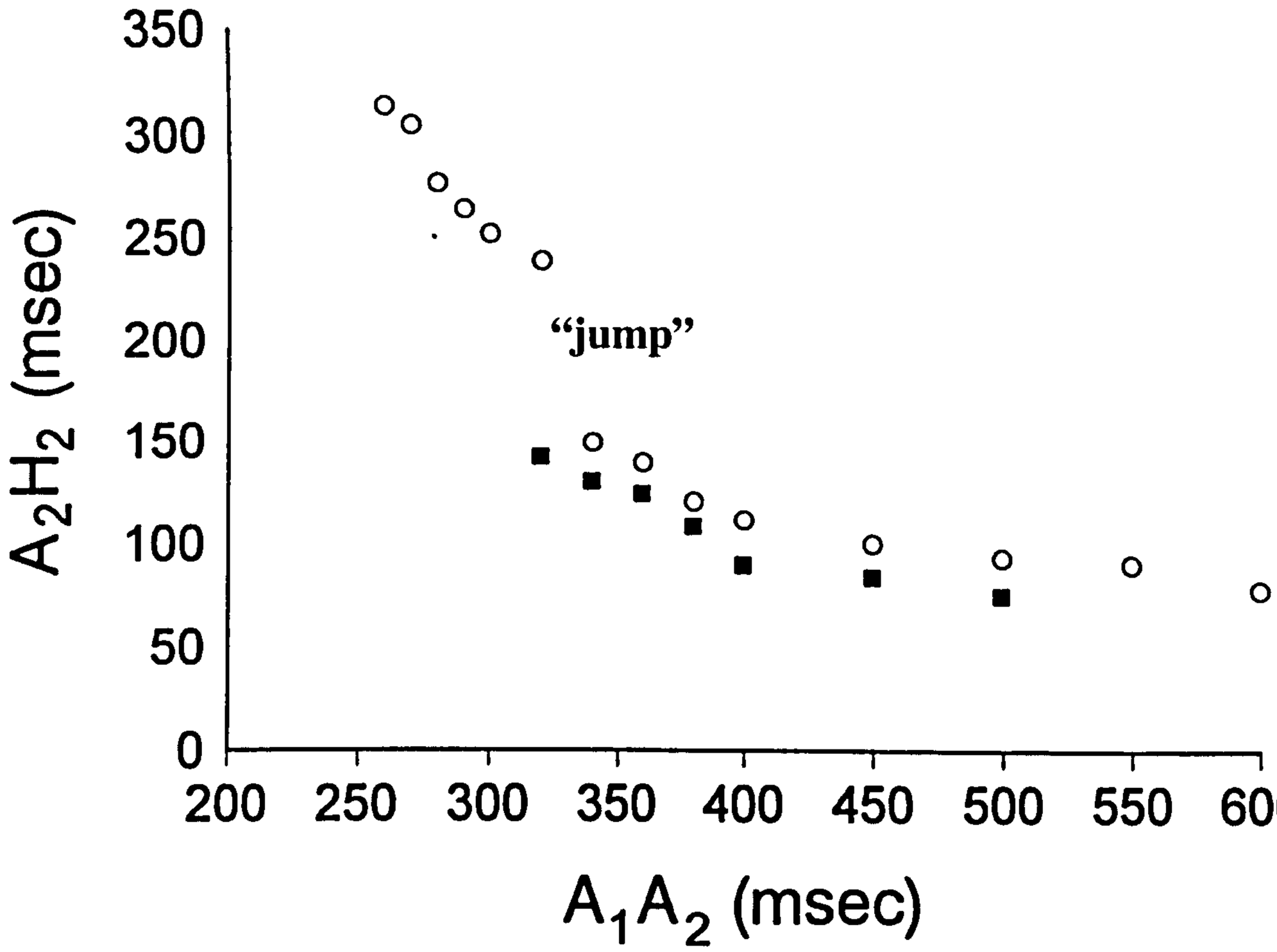

Figure 1.5 Discontinuous AVN conduction curve. A2H2 interval is plotted against the prematurity of atrial impulses (A1A2) in a human patient with dual AVN pathways. Successful conduction was achieved at all coupling intervals. However, note the "jump" in the conduction curve (A1A2 ~330-320 ms). Open circles represent conduction before slow pathway ablation. Filled squares represent conduction after slow pathway ablation. Note, after slow pathway ablation, the failure to conduct at shorter A1A2 intervals. From Sheahan et al., (1996).

transmission of the atrial impulse to the ventricles. As discussed above, initial PR interval is normal but progressively lengthens with each successive beat until eventually atrioventricular transmission is blocked completely and the P wave is not followed by a QRS complex. The PR interval then returns to normal, and the cycle repeats. Mobitz type II block is less common but is more likely to produce symptoms. There is an intermittent failure of conduction of P waves. The PR interval is constant, though it may be normal or prolonged. The block is often at the level of the bundle branches and is therefore associated with wide QRS complexes. 2:1 atrioventricular block is difficult to classify, but it is usually a Wenckebach variant. High degree atrioventricular block, which occurs when a QRS complex is seen only after every three, four, or more P waves, may progress to complete third degree atrioventricular block.

1.1.9.2.3 Third-degree or complete block (AV Block)

In third degree block, there is complete failure of conduction between the atria and ventricles, with complete independence of atrial and ventricular contractions. The P waves bear no relation to the QRS complexes and usually proceed at a faster rate. A pacemaker in the bundle of His produces a narrow QRS complex, whereas more distal pacemakers tend to produce broader complexes. These subsidiary pacemakers trigger ventricular contractions. Occasionally no escape rhythm occurs and asystolic arrest ensues. The rate and QRS morphology of an escape rhythm vary depending on the site of the pacemaker. Complete heart block is most often caused in adults by heart disease or as a side effect of drug toxicity. Heart block also can be present at or even before birth. This is called congenital heart block.

1.1.10 Dead-end pathways

There are cells that have been shown to be activated but not to participate in the transmission of the impulse through the AVN. Anderson et al. (1974) described a layer of atrial overlay cells which terminated at the beginning of the septal cusp of the tricuspid valve. The tract of lower nodal cells which extend posteriorly from the compact node and can be considered part of the posterior nodal extension has been described as a dead-end pathway (Van Capelle et al., 1972). Van Capelle et al. (1974) described the existence of an

action potential in the anterior portion (presumably lower nodal cells) of the AVN even in the presence of AV block during Wenckebach phenomena. This suggests that the impulse in the lower nodal cells is insufficient to activate the much larger anterior portion of the node. Dead-end pathways are thought to draw local circuit current during normal conduction and therefore facilitate the slowing of impulse propagation (Weidmann, 1974).

1.1.11 Histological evidence for the existence of dual pathways

Anderson et al. (1997) have produced detailed accounts of AVN architecture and structures potentially involved in AVN function during normal and disease states (Sanchez-Quintana et al., 1997; Anderson and Ho, 1998; Ho and Anderson, 1998). Combined anatomical and electrophysiological studies have provided evidence about the orientation of cells comprising major AVN anatomical areas (Hocini et al., 1998; Anderson et al., 1974). Inoue and Becker (1998) provided the first morphological evidence for the existence of a slow pathway in humans, an inferior extension of the compact node. This was also confirmed in rabbits (Medkour et al., 1998). Anatomically, identification of the fast pathway, however, has proved more elusive. It is widely thought that this pathway is not morphologically distinct, and that one of the many anterior atrionodal inputs could provide the substrate for reentry. Lin et al. (2001) using rabbit AVN preparations ablated the region believed to be the fast-pathway and showed the posterior nodal extension to sustain conduction at all cycle lengths. Furthermore, additional lesions to the posterior nodal extension caused third-degree AV block illustrating the role played by the posterior nodal extension in slow-pathway conduction and concealment.

1.1.12 Concealed pathways

To add to the electrophysiological complexity of the AVN, a phenomena known as concealed conduction has been described. With concealed conduction, an impulse travelling from the atria penetrates the AVN but fails to traverse it completely (Langendorf, 1948; Langendorf and Pick, 1956). Although concealed conduction fails to excite the AVN, it has subsequent effects on following impulses and is thought to have profound effects on AVN impulse propagation during atrial fibrillation (Meijler et al., 1996).

1.1.13 Properties of slow conducting cardiac tissue

The AVN is specialised for slow conduction. The conduction velocity of the action potential is affected by many factors. Here I will consider four factors relevant to the AVN: 1) Fibre orientation has long been considered an important determinant of the speed of conduction: conduction is generally faster in the longitudinal direction as opposed to the transverse direction (Spach et al., 1971, 1981, 1982). 2) Shaw and Rudy (1997) using mathematical models to simulate the cardiac action potential have demonstrated that a lack of Na^+ channels leads to reduced membrane excitability, which effectively slows conduction. For example, in ventricular cells during ischemia, the external K^+ concentration rises. This depolarises the membrane potential to about -60 mV, which inactivates the majority of the Na^+ channels, leading to a decrease in the upstroke velocity of the action potential. The action potential upstroke is now generated mainly by L-type Ca^{2+} channels (Shaw and Rudy, 1997). As a result, the conduction velocity of the action potential is reduced from ~ 500 cm/s to as low as 17 cm/s (before the onset of conduction block (Kagiyama et al., 1982). 3) Intercellular coupling of cells is the result of gap junctions formed by connexins, between cells. Gap junctional conductance determines the speed of conduction velocity. 4) Decreased coupling in cells leads to an increase in safety factor, because the leakage of current is reduced – which allows for very slow conduction velocities, below 1cm/s (Shaw and Rudy, 1997). When SF is combined with the degree of electrical coupling, conduction can proceed as low as 0.26 cm/s (Rohr et al., 1998). A long persistent current is necessary for safe conduction when there is poor cell-cell coupling, since it provides a depolarising current over the entire period of the coupling delay. These conditions are likely to be necessary for impulse propagation through the slow-pathway.

1.1.14 Microelectrode recordings

Numerous studies exist which make use of microelectrode techniques to investigate action potential recordings throughout the entire triangle of Koch region (e.g. Matsuda et al., 1958; Hoffman et al., 1958; Anderson et al., 1974). These studies showed various action potential configurations in different regions of the tissue (Fig. 1.7). Action potentials

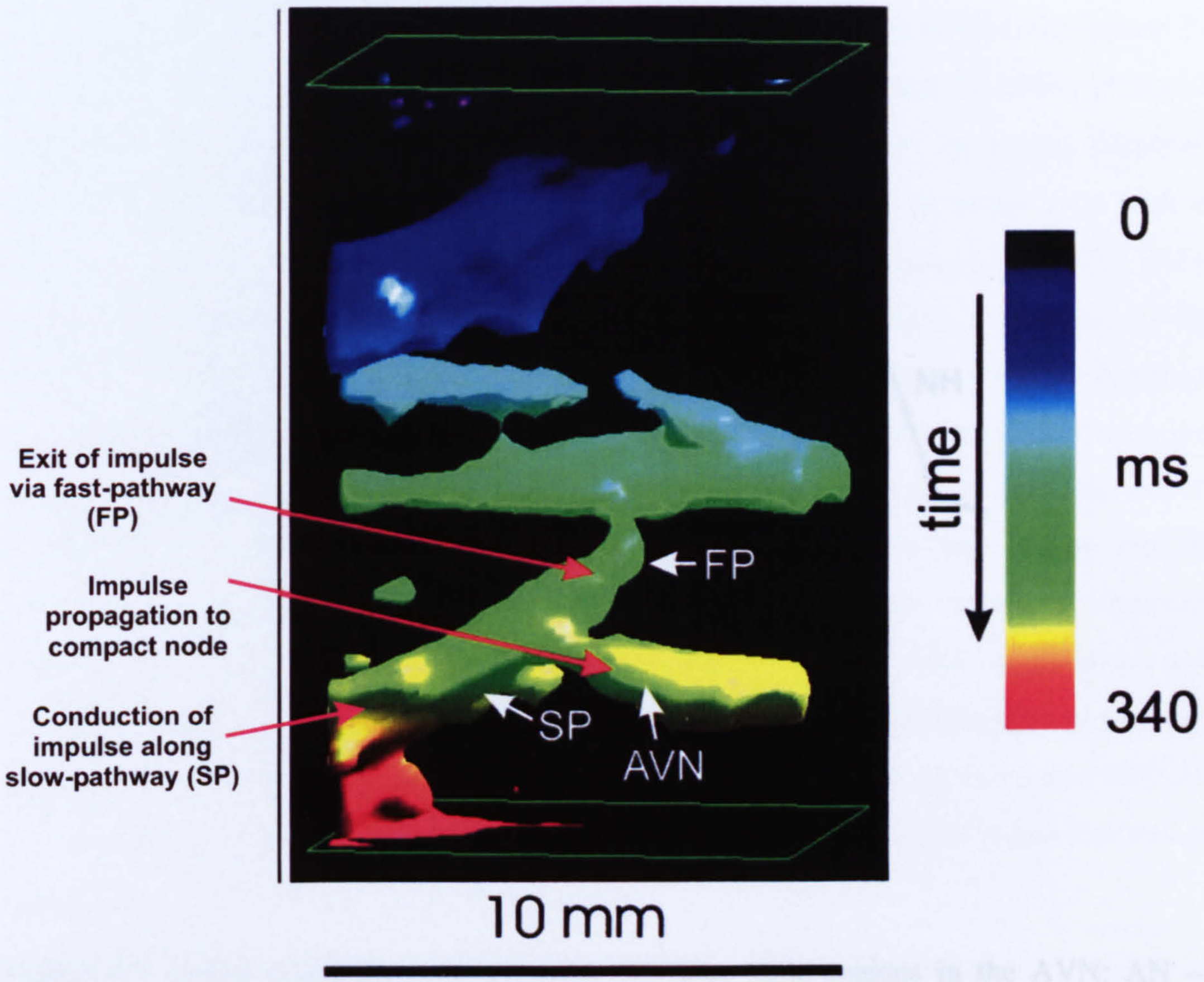

Figure 1.6 Fluorescent visualisation of the dual pathways in the rabbit AVN during slow-fast reentry. Using the voltage-sensitive dye, di-4-ANNEPS, it is possible to visualise the route of impulse propagation during reentrant tachycardia in isolated rabbit AVN preparations. During slow-fast reentry, an impulse conducts along the slow pathway anterogradely to excite the compact node. The impulse is then able to exit the node by passing retrogradely along the fast-pathway to re-excite the adjoining atrial septal tissue and form a reentrant circuit From Nikolski et al., (2003).

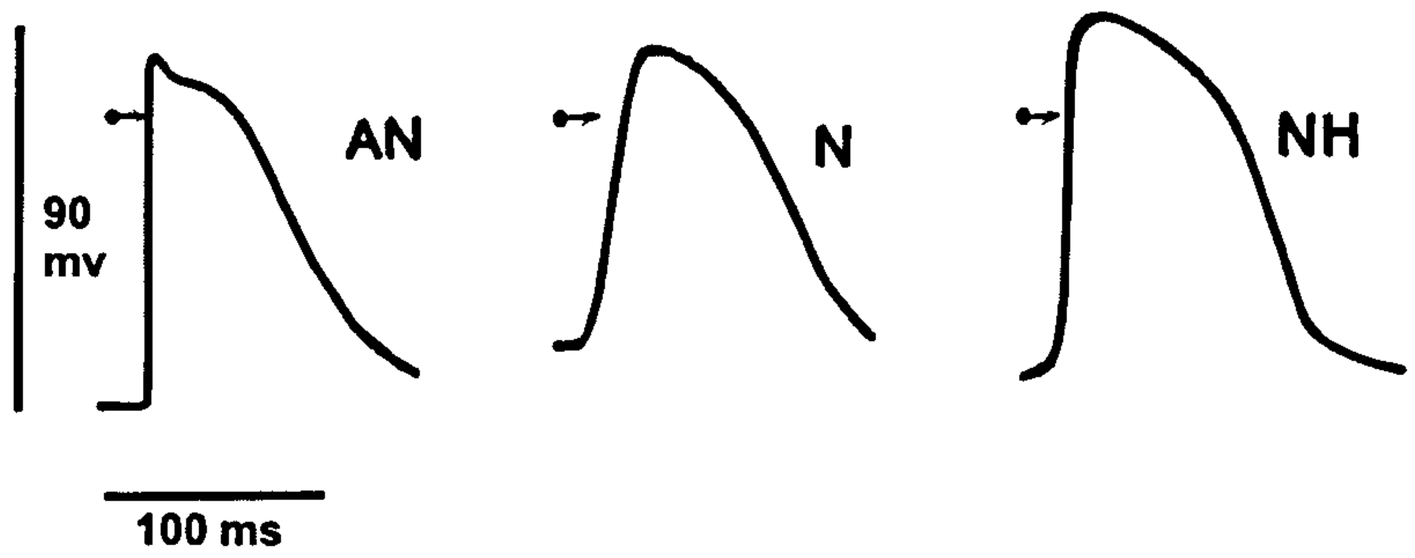

Figure 1.7 Action potentials recorded from the three main regions in the AVN: AN – atrionodal, N - nodal and NH - nodal-His. Clearly, N cells have the slowest rate of rise during phase 0 and a more depolarised maximum diastolic potential. A small notch is evident in the AN cells. NH cells have a large plateau phase and show similarities in action potential morphology to ventricular cells. From Billette, 1987.

recorded from the posterior nodal extension area have slow upstrokes and a low diastolic membrane potential (-60 mV) typical of nodal action potentials (Billette, 1987; McGuire et al., 1996). In contrast, the major characteristics of the atrial myocyte action potential are a relatively negative resting membrane potential of ~ 80 mV and a rapid upstroke (phase 0) of > 100 V/s. Three distinct cell types are present in the AVN based on action potential morphology and functional characteristics: 1) AN cells, display an action potential intermediate between that of "true" atrial cells and those of typical nodal cells with a relatively negative resting membrane potential (~ -72 mV), fast upstroke (~ 102 V/s) and a distinct notch (phase 1). 2) N cells are "true" nodal cells and have a high maximum diastolic potential of, with a pacemaker potential (~ -64 mV) and a very slow upstroke velocity (~ 18 V/s). 3) NH cells have a resting potential of ~ -64 mV and a slow upstroke velocity of 17 V/s (Billette, 1987). N and NH cells are distinguished by their action potential duration which at 80% repolarisation is ~ 80 ms for N cells and ~ 92 ms for NH cells. Uncovering ion channel distribution throughout specific cellular subgroups comprising the triangle of Koch, with regards to a cells action potential morphology, will provide us with a better understanding of the physiology and possibly the pathophysiology of the AVN. However, a major drawback of microelectrode recordings using multicellular AVN preparations is the major interference generated from adjacent cells which can lead to misleading results regarding the electrical properties of a single cell.

1.1.15 Single cell recordings

Single AVN cells from rabbit and guinea-pig have been isolated which retain normal morphology, and their action potentials and ionic currents characterised (Hancox and Levi, 1993; Hancox and Levi, 1994a; Hancox and Levi, 1994b; Hancox et al., 1997; Munk et al., 1996; Mitcheson and Hancox, 1999a; Mitcheson and Hancox, 1999b; Convery and Hancox, 2000). These studies describe two distinct cell types: 1) Rod cells, which possess action potentials like the AN cells and have the unique ability to be stimulated before repolarisation is complete (Munk et al., 1996). These cells have I_f which is activated at more negative potentials than that of their counterpart (ovoid/spindle) cells, however, at x25 fold less I_f density. All cells have a rapid inward Na^+ current (I_{Na}) and L-type Ca^{2+}

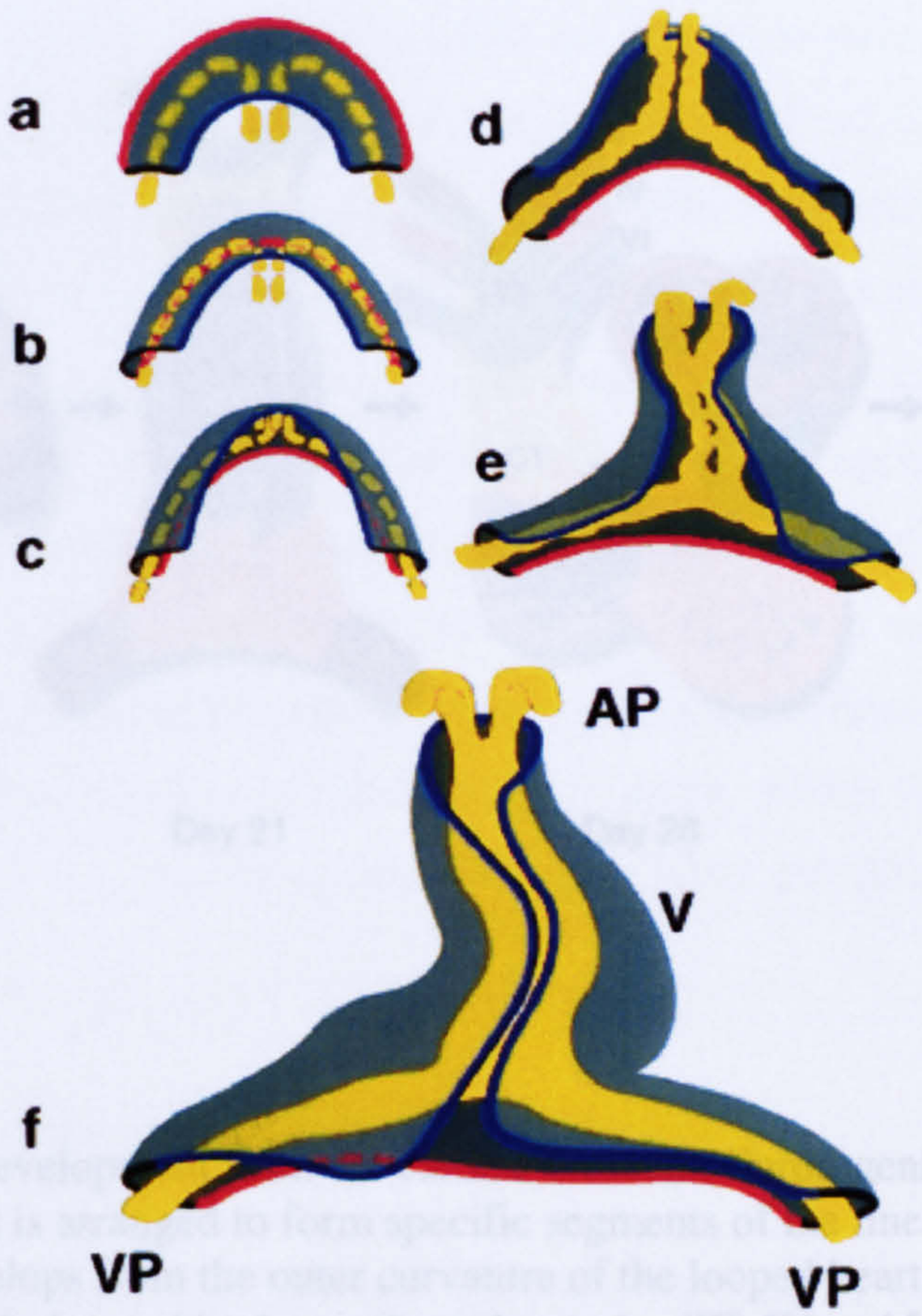

Figure 1.8 Formation of the cardiac tube. The stages a-f show the devlopment of the cardiac tube from the flat cardiogenic crescent. It can be seen that the myocardial crescent (grey) grows around the fusing endocardial vesicles (yellow) to form the cardiac tube. AP: anterior pole. VP: venous pole. V: future ventricle. From Moorman et al., (1998).

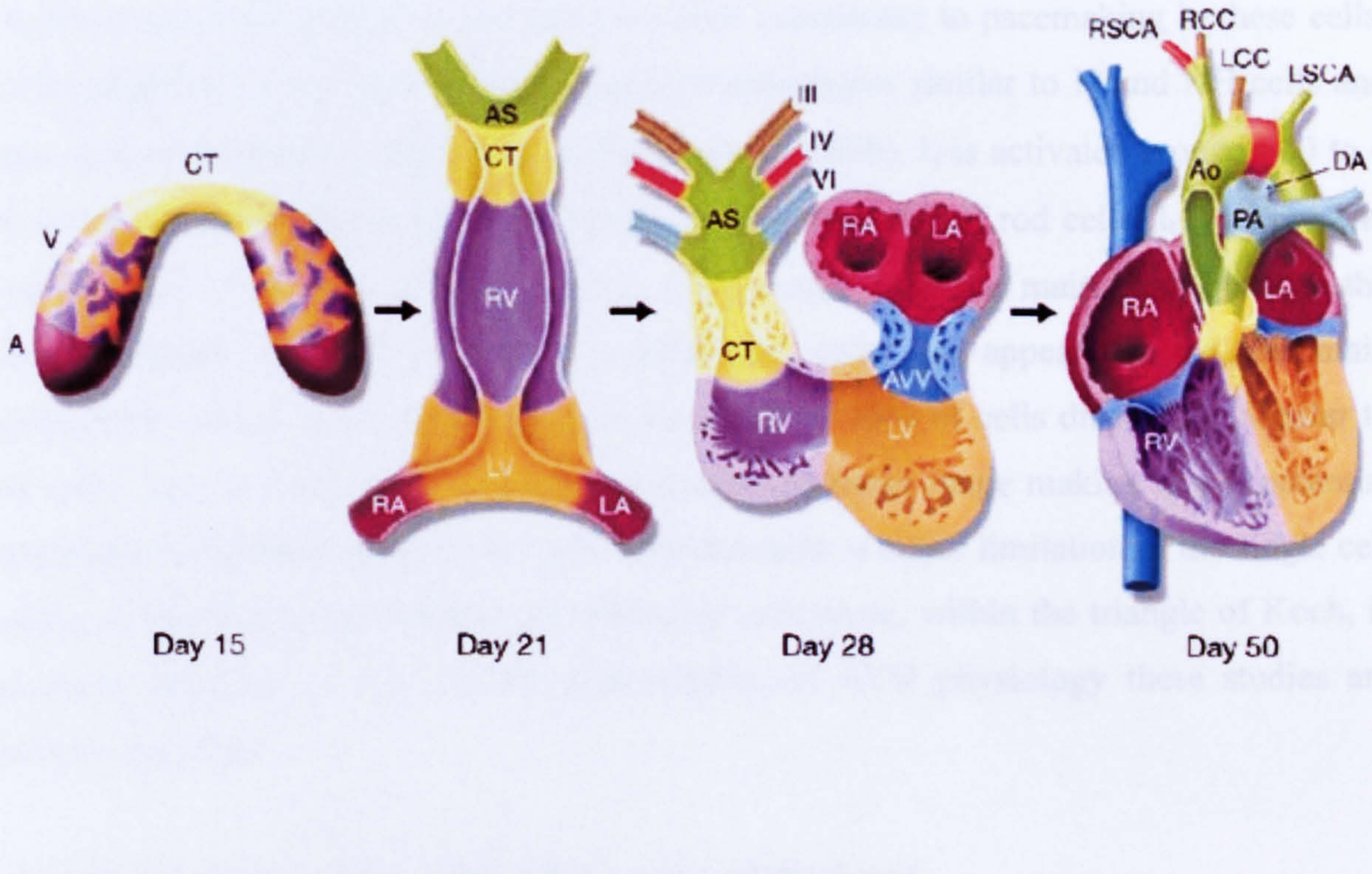

Figure 1.9 Cardiac development from the cardiac crescent. Cardiogenic precursors form a crescent (day 15) that is arranged to form specific segments of the linear heart tube. Each cardiac chamber develops from the outer curvature of the looped heart tube. Neural crest cells are predominantly located in the aortic arch arteries (III, IV and VI) and the aortic sac (AS). Mesenchymal cells form the cardiac valves from the conotruncal (CT) and atrioventricular valve (AVV) segments. A, atrium; Ao, aorta; DA, ductus arteriosus; LA, left atrium; LCC, left common carotid; LSCA, left subclavian artery; LV, left ventricle; PA, pulmonary artery; RA, right atrium; RCC, right common carotid; RSCA, right subclavian artery; RV, right ventricle; V, ventricle. From Srivastava and Olson, (2000).

current ($I_{Ca,L}$) which contribute to the action potential upstroke. Repolarisation is achieved by the presence of a transient outward current (I_{to}) and the delayed rectifier current, I_{Kr}. In addition I_{Kr} is thought to contribute to pacemaker depolarisation. I_{NCX} is present over the pacemaker potential range making this a possible contributor to pacemaking in these cells. 2) Ovoid/spindle cells, have action potential morphologies similar to N and NH cells and show post-repolarisation refractoriness (Munk et al., 1996). I_f is activated around –60 to –90 mV however, is x25 fold greater current density than that of rod cells. $I_{Ca,L}$ is present, however only ~ 30% of cells display I_{Na}, suggesting $I_{Ca,L}$ is the main contributor to the action potential upstroke in some ovoid/spindle cells. I_{Kr} appears to be the main repolarising current in ovoid/spindle cells since only ~ 50% of cells display I_{to}. Similar to rod cells, I_{NCX} is measurable over the pacemaker potential range making this a potential contributor to pacemaking in these cells. Unfortunately, a major limitation of the single cell studies is that the precise location of where the cells arose, within the triangle of Koch, is uncertain, therefore to our overall understanding of AVN physiology these studies are limited somewhat.

1.1.16 Development of the conduction system of the heart

Historically, the avian heart has been the species most studied to understand the early development of conduction system in the heart (Lamers et al., 1991).

The primordial heart begins to form in the cardiogenic plate at the cranial end of the embryo. Angiogenic cell clusters, which lie in the plate, fuse to form the heart tube (Patten and Kramer, 1933; Fig. 1.8). The primary heart tube is a peristaltic pump that moves blood in one direction due to a unidirectional wave of contractions along the tube (Patten, 1949). This slow-conducting heart tube then develops fast-conducting regions flanking either side of it; these eventually become the atria and ventricles (Fig. 1.9).

This configuration guarantees that the ventricles never contract before the atria have finished contracting. The SAN and AVN will eventually arise from the inflow tract (IFT) and atrioventricular canal (AVC) of the slow-conducting myocardium. The first signs of pacemaking in the avian heart come from the IFT (Hirota et al., 1979) and is initially found

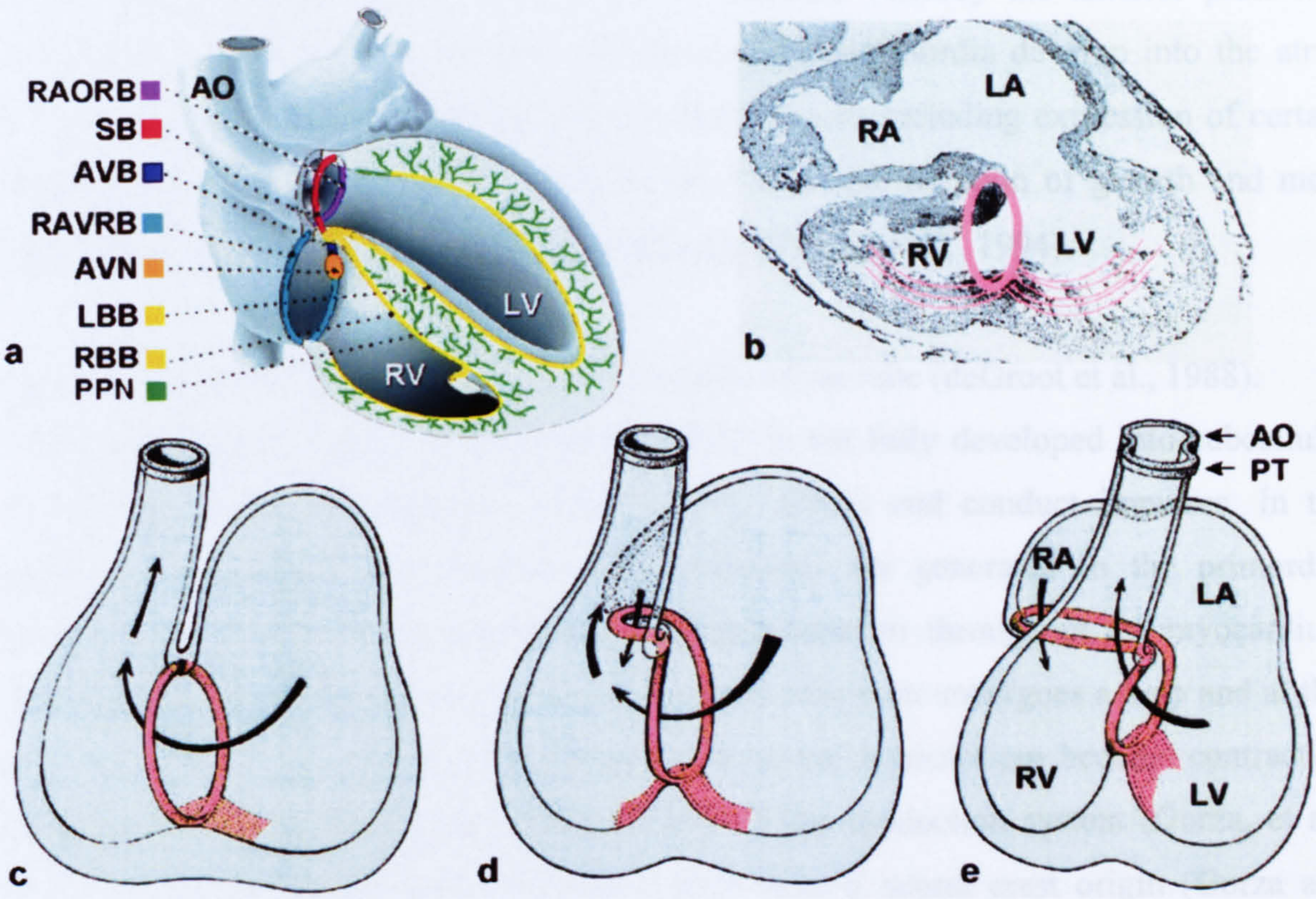

Figure 1.10 Development of the ventricular conduction system. a: schematic diagram showing all regions of the ventricular conduction system which are all retained in the adult chicken heart (in the adult mammalian heart only some components remain). b: section through a 5 week old human heart immunolabeled for GIN2. c.d and e: development of ventricular conduction system in human 5 (c), 6 (d) and 7 (e) week old embryos immunolabeled for GIN2. RAORB, retroaortic root branch; SB, septal branch; AVB, atrioventricular bundle; RAVRB, right atrioventricular ring bundle; AVN, atrioventricular node; LBB, left bundle branch; RBB, right bundle branch; PPN, purkinje network. From Moorman et al., (1998).

on the left-side (Sakai et al., 1983). The IFT eventually becomes incorporated into the right atrium. The heart takes on an anteroposterior position whereby the anterior primordia differentiate to become the ventricles and the posterior primordia develop into the atria. Retinoic acid plays an important part in this development including expression of certain genes (induction of alpha-MHC; Yutzey et al., 1994) and direction of growth and most importantly the development of an atrial phenotype (Yutzey et al., 1994).

The SAN is found towards the posterior extremities of the tube (deGroot et al., 1988).
In the early stages of heart development the CCS is not fully developed into subcellular regions. However, the embryonic heart can still initiate and conduct impulses. In the embryonic chick heart spontaneous action potentials are generated in the primordial sinoatrial region and are propagated from posterior-anterior throughout the myocardium where cells are coupled via gap-junctions. The heart tube then undergoes a loop and at this point does A-V delay become apparent and cells of the myocardium become contractile. The presence of typical neural proteins in cells of the conduction system (Gorza, et al., 1994) has led to the suggestion that these cells have a neural crest origin (Gorza and Schiaffino, 1988). Moorman et al. (1997) state "Regarding the origin of the SAN, it is more probable that it originates from existing myocardium, because its function has been shown from the first heartbeat onward". Vassal-Adams (1982) points out that the atria and ventricles develop from the primary myocardium between which a delay can be detected on the ECG; there is no additional recruitment of neural crest cells for this function to occur.

Keith and Flack in (1907) were the first to describe the ventricular conduction system (Keith and Flack, 1907; Fig. 1.10) and stated that it formed from the "remains of the primitive cardiac tube" and this has become known as the "escape" hypothesis (Moorman and Christoffels, 2003). An alternative hypothesis also exists which is termed the "recruitment" hypothesis, whereby the cells of the conduction system differentiate locally from myocytes that have already differentiated into working myocardium (Gourdie et al., 1995). Much of the work investigating the origin of the cells comprising the cardiac conduction system have involved work at the molecular level, such as, the role of gene expression in the differentiation of myocardial cells into working myocardium and conduction system tissue.

1.1.17 Molecular basis for cardiac cell specialisation

In mammals there is the formation of an early linear heart tube very soon after the formation of the cardiac chambers occurs (Moorman et al., 1998). The chick embryo has undergone detail analysis for cardiac chamber formation since the heart in this species develops more slowly. The developing heart, at the stage of the embryonic tube, each myocardial cell has the ability to be a pacemaking cell (Moorman et al., 1998). Each cell possesses inherent rhythmical activity and is poorly coupled to its neighbours due to a lack of Cx45 gap junctions (Delorme et al., 1997). The action potentials recorded from this region have slow upstrokes similar to pacemaker action potentials, due to the predominance of Ca^{2+} currents (Galper and Caterall, 1978). This myocardium is referred to as "primary myocardium". Once the cardiac chambers have formed this is referred to as "secondary myocardium" (Moorman and Lamers, 1994). Secondary myocardium can be distinguished from the primary myocardium by an abundance of the gap junctional proteins Cx40 and Cx43, and also atrial natriuretic factor (NppA). Action potentials with fast upstrokes, due to the presence of Na^{+} channels, can be recorded from these regions (Galper and Caterall, 1978).

AVN delay can be recorded before the identification of a morphologically distinct AVN (Vassal-Adams, 1982). It is the function of the atrioventricular canal to delay impulses before the full development of a true AVN (Arguello et al., 1988). The AVN is the primary myocardium remaining between the atria and ventricles (de Jong et al., 1992). The morphologically distinct AVN in mouse does not appear until Carnegie stage 15 (~5 weeks human development; Viragh and Challice, 1977). The tissues of the SAN, AVN and bundle of His, retain their primary myocardium phenotype. The molecular mechanisms underlying this are being investigated. The T box (Tbx) family of transcription factors have particular importance in the development of the cardiac conduction system (Brand, 2003). Tbx2, Tbx3 and Tbx5 are the most important of these. Tbx5 for instance is necessary for the activation of the gene that encodes Cx40 and NppA (Hiroi et al., 2001; Habets et al., 2002). Basson et al. (1995) showed that mutations in the gene encoding this transcription factor cause serious cardiac conduction malformations. In contrast, Tbx2 and Tbx3 are repressors

of transcription and in association with another transcription factor, Nkx2-5, are able to repress expression of NppA and Cx40 genes, suggestive of a role for these transcription factors in preventing formation of secondary myocardium (Paxton et al., 2002; He et al., 1999). Interestingly, the expression patterns of Tbx2 and Tbx3 and also Cx40, Cx43 and Cx45 match very closely the anatomic descriptions of the AVN given by Keith and Flack in (1907) (Fig. 1.11). Mouse Tbx2 is a potent repressor of gene expression and weak activator of gene expression. Two repressor domains exist (one at the amino-terminal and one at the carboxy-terminal), and one amino-terminal activator domain exists (although this is largely dependent on the DNA promoter context; Paxton et al., 2002).

Other factors exist regarding the origin of cardiac myocytes. Hall et al. (2004) have postulated that the differentiation of myocytes is influenced by hemodynamic factors.

1.1.18 Development of the nodal phenotype

Nodal cells of the heart display a number of characteristics similar to those of early cardiac cells, most notably: small size; poorly organized actin and myosin filaments, and a poorly developed sarcoplasmic reticulum. There is a scarcity of connexins in SAN and AVN tissues (Van Kempen et al., 1991). The AVN of cow (Komuro et al., 1987), chicken (deGroot et al., 1987) and human (Kuro-o et al., 1986) shows co-expression of the contractile proteins, α- and β- myosin heavy chain, whereas only expression of β-myosin heavy chain was found in rats (deGroot et al., 1989). The cytoskeletal protein, desmin, has been shown to delineate the conduction system in cow (Ossthoek et al., 1993). Gorza and Vitadello (1989) and Vitadello et al. (1996) have elegantly shown neurofilament -L and –M delineates the rabbit conduction system.

1.2 From DNA to Protein

1.2.1 basic processing of proteins/ion channels

1.2.1.1 DNA structure

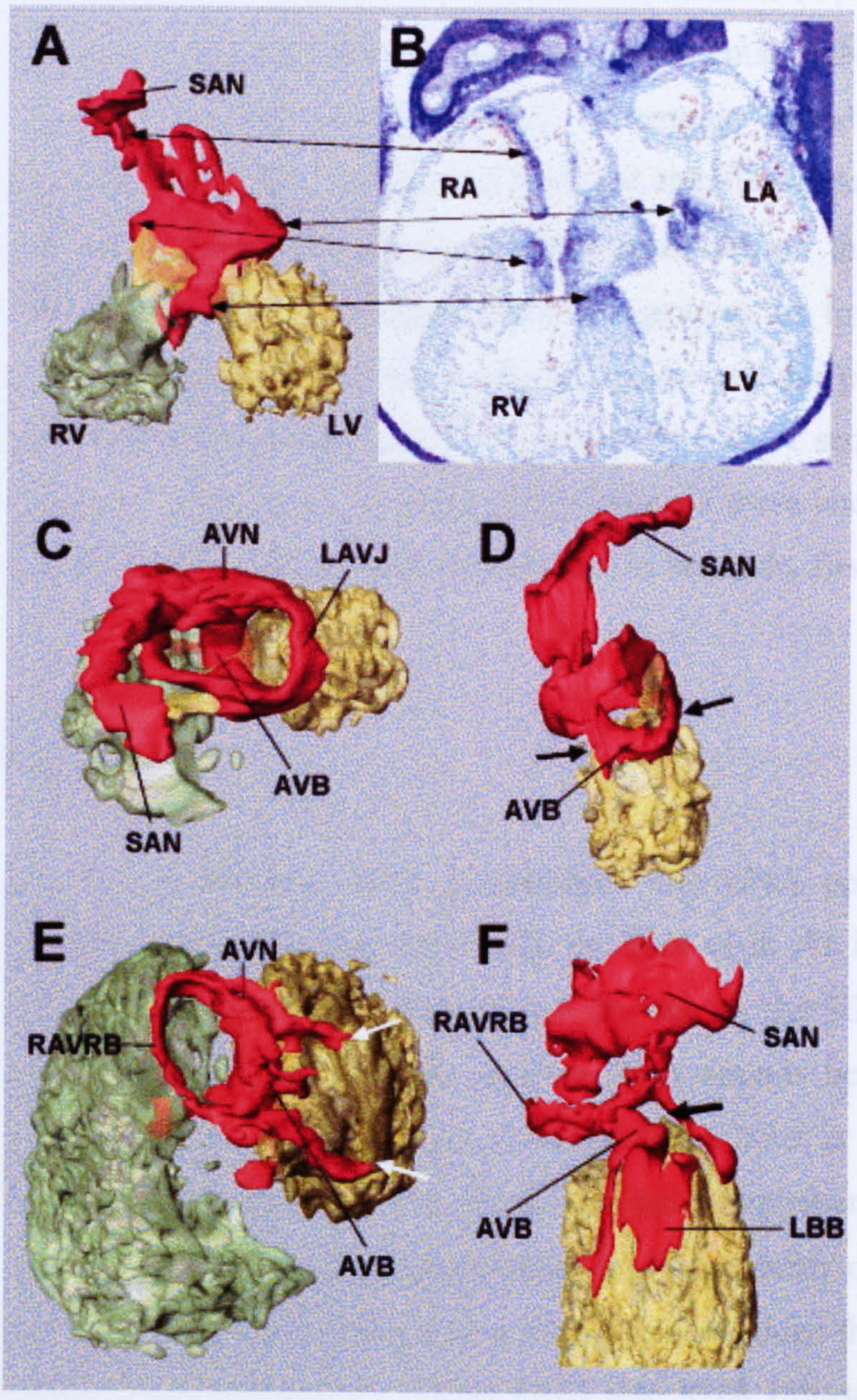

Figure 1.11 Three-dimensional reconstructions of the T-box transcription factor, Tbx3, expression in the embryonic heart. Serial sections through E12.5 mouse hearts were stained for TBX3 (B) and three-dimensionally reconstructed (A,C-F) Tbx3 clearly delineates the conduction system of the mouse heart. These data indicate that Tbx3 is an important molecule in the development of the conduction system morphology. From Hoogars et al., (2004).

Deoxyribose nucleic acid (DNA) sequence forms our genetic code. It is made up of various combinations of four nucleotides, adenine (A), thymine (T), cytosine (C) and guanine (G), to form genes. It is structured into a double-helix (two complementary DNA strands linked together in a 5′-3′ or non-template strand and 3′-5′ or template strand) with the bases (nucleotides) lining the inside of this structure in a favoured complementary, A-T and G-C, manner. In addition, DNA contains a sugar-phosphate backbone on the outside of the double-helix (Watson and Crick, 1953). Major and minor grooves are formed which play an important role in protein-DNA interactions which regulate cellular processes such as DNA replication, transcriptional control and DNA repair. The DNA sequences inherited from our parents ultimately decide the function of our heart as these encode the proteins comprising the cells of the heart. For a functional protein to be made, firstly a gene has to be switched on.

1.2.1.2 DNA replication

DNA is transcribed by the enzyme RNA polymerase. The RNA polymerase moves stepwise along the DNA, unwinding the DNA helix in front of it. As it progresses, the polymerase adds nucleotides (small "T" shapes) one by one to the RNA chain at the polymerisation site. The polymerase rewinds the two DNA strands behind this site to displace the newly formed RNA. A short region of DNA/RNA helix is therefore formed only transiently, and the RNA transcript is a single-stranded complementary copy of the template strand of DNA. The incoming nucleotides are in the form of ribonucleoside triphosphates (ATP, UTP, CTP and GTP), whose hydrolysis provides the energy for the polymerisation reaction. RNA polymerase copies DNA into RNA (transcription) and is a large subunit protein. It binds randomly to DNA but strongly to a specific promoter sequence. This promoter contains the start signal for transcription. RNA polymerase will stop when it reaches a termination or stop signal. It will only polymerise RNA in the 5′ to 3′ direction (DNA is read from 3′ to 5′). Since the promoter sequences are asymmetric, the promoter will bind the polymerase in only one orientation, thus determining which strand of the DNA will be transcribed. Therefore, the RNA is complementary to the template DNA strand and equivalent (except for the T's which have been replaced by U's) to the non-template strand

Four types of RNA are produced in a cell: mRNA (coding information), tRNA (adaptor between mRNA and amino acids), rRNA (part of ribosome; participates in protein synthesis), and some small non-coding RNAs (used in splicing, RNAi and other cellular processes).

1.2.1.3 mRNA translation

tRNA molecules are adaptors for the translation of RNA into protein. Each amino acid has at least one tRNA. tRNA is specific for codons (three nucleotides) in the RNA and brings correct amino acids to the matching codons. Protein production is catalysed on ribosomes. Ribosomes are structures that are similar (but not the same) in eukaryotes and prokaryotes. Ribosomes are large complexes of proteins and rRNAs. They consist of two subunits: a large subunit which catalyses peptide bond formation and a small subunit (e.g. 18S and 28S) which binds mRNA and tRNAs

Ribosomes move along the mRNA from the 5′ end to the 3′ end and the protein is subsequently produced from the NH_2-terminal to the COOH-terminal. Three codons, UAA, UGA and UAG are used as stop-codons to terminate translation.

1.2.1.4 Protein transport

When protein synthesis begins, the polypeptide chain starts with a "hydrophobic signal sequence" which initially inhibits protein synthesis. However, this allows association with the endoplasmic reticulum (ER), which, at the point of ribosome attachment is known as rough endoplasmic reticulum (RER). thereby facilitating entry of the polypeptide into the lumen of the RER. Once this signal sequence is detected then protein synthesis can resume at a normal rate. Eventually the signal sequence is cleaved by a signal peptidase leaving only the protein with its NH_2- and COOH-terminal (Neuhof et al., 1998). From the RER the proteins are transported to the Golgi complex by way of vesicles; these vesicles require ATP in order to transport to the Golgi complex. The Golgi complex traffic the proteins to

their final destination, which in terms of ion channels is the plasma membrane. ER to Golgi transport can be controlled by scaffold proteins such as PDZ (PSD95/DLG/ZO-1) domain-containing proteins and Homer proteins (Standley et al., 2000; Ma et al., 2001; Fig. 1.12). Interestingly, the region of the ion channel to be located outside the plasma membrane is already being arranged at the level of the RER: this portion of the protein will always be inside the vesicle. The inside of the vesicle then becomes continuous with the inside of the Golgi cisternae. Carbohydrate groups are attached and any subunits may be joined in these cisternae. The protein is then passed to the final region of the Golgi called the "trans face". There it is placed in vacuoles that bud from this region of the Golgi complex. These may be a certain size or density, characteristic of the cell itself. The vacuoles continue to condense the proteins and the final mature secretory granule is then moved to the membrane for secretion.

Release of a completed polypeptide chain from a ribosome is often not the last chemical step in the formation of a protein. Various covalent modifications often occur, either during or after assembly of the polypeptide chain. Most proteins undergo co- and /or post-translational modifications. Knowledge of these modifications is important, because they may alter the physical and chemical properties (folding, conformation distribution, stability, activity) and, consequently, function of the proteins. Moreover, the modification itself can act as an added functional group. Examples of the biological effects of protein modifications include phosphorylation for signal transduction, ubiquitination for proteolysis, attachment of fatty acids for membrane anchoring and association, glycosylation for protein half-life, targeting, cell:cell and cell:matrix interactions. Consequently, the analysis of proteins and their post-translational modifications is particularly important for the study of heart diseases such as heart failure and cardiac hypertrophy. There are many points at which the expression of an ion channel at the surface can be post-transcriptionally altered: mRNA processing; mRNA translation; protein processing; assembly of subunits; transport to cell membrane; assembly into channel complex; as functional channels in the cell membrane; and degradation of assembled proteins.

1.2.1.5 Factors regulating gene expression

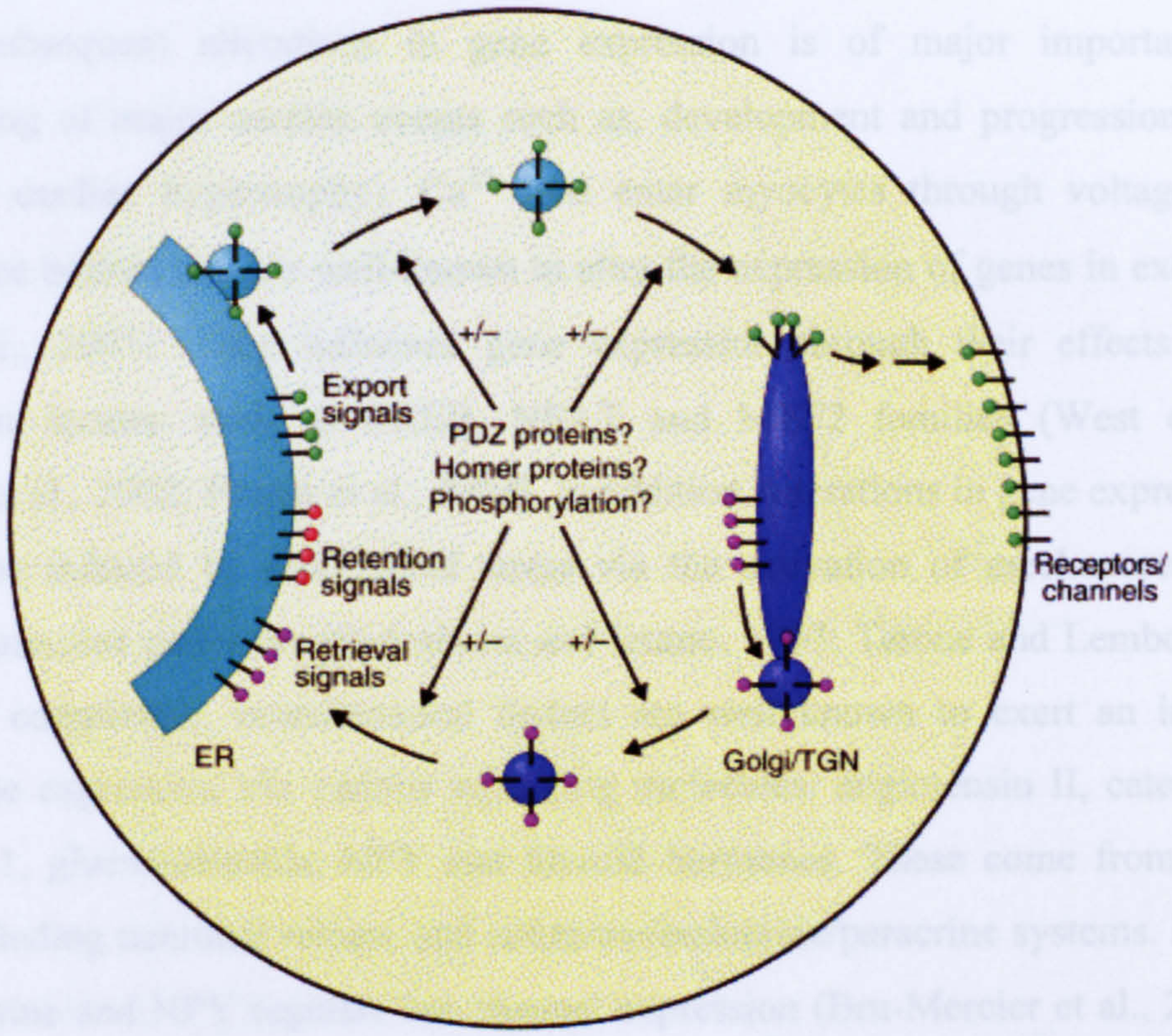

Figure 1.12 The surface densities of receptors and ion channels can be controlled by the rate of their ER to Golgi transport. ER export signals increase surface expression and ER retention/retrieval signals decrease it. PDZ domain-containing proteins and Homer proteins can potentially regulate the effectiveness of these trafficking signals. TGN, trans-Golgi network. From Ma and Jan, (2002)

There are numerous effectors of gene expression. The link between electrical activity of a cell and subsequent alterations in gene expression is of major importance in the understanding of major cardiac events such as, development and progression of disease states (e.g. cardiac hypertrophy). Ca^{2+} ions enter myocytes through voltage-gated ion channels (see below) and are well-known to alter the expression of genes in excitable cells (West et al., 2001). They influence gene expression through their effects on certain transcription factors, such as CREB, NFAT and MEF2 families (West et al., 200; McKinsey et al., 2002; Hogan et al., 2003). In addition, alterations in gene expression in the heart can be induced by mechanical stress via the activation of mechanoreceptors and autocrine/paracrine pathways (Sadoshima and Izumo, 1997; Tarone and Lembo, 2003). To add to the complexity, neurohumoral factors are well known to exert an influence on cardiac gene expression via various signalling molecules: angiotensin II, catecholamines, endothelin-1, glucocorticoids, NPY and thyroid hormones. These come from a range of sources including neuronal release and autocrine/endocrine/paracrine systems. In the heart, norepinephrine and NPY regulate ion channel expression (Bru-Mercier et al., 2003; Protas et al., 2003).

1.3 Role of ion channels and ion exchangers in electrical and contractile function

1.3.1 Cardiac action potential

As previously described, electrical activity in the heart originates in the centre of the SAN (Boyett et al., 2000) from which an action potential propagates throughout the heart resulting in contraction. The typical cardiac action potential can be divided in to different phases numbered 0-4.

1.3.2 Phase 4 (resting potential)

Phase 4 represents the resting phase of atrial and ventricular cells (upper panel, Fig. 1.13). The resting membrane potential of working myocardial cells is approximately –80 mV for

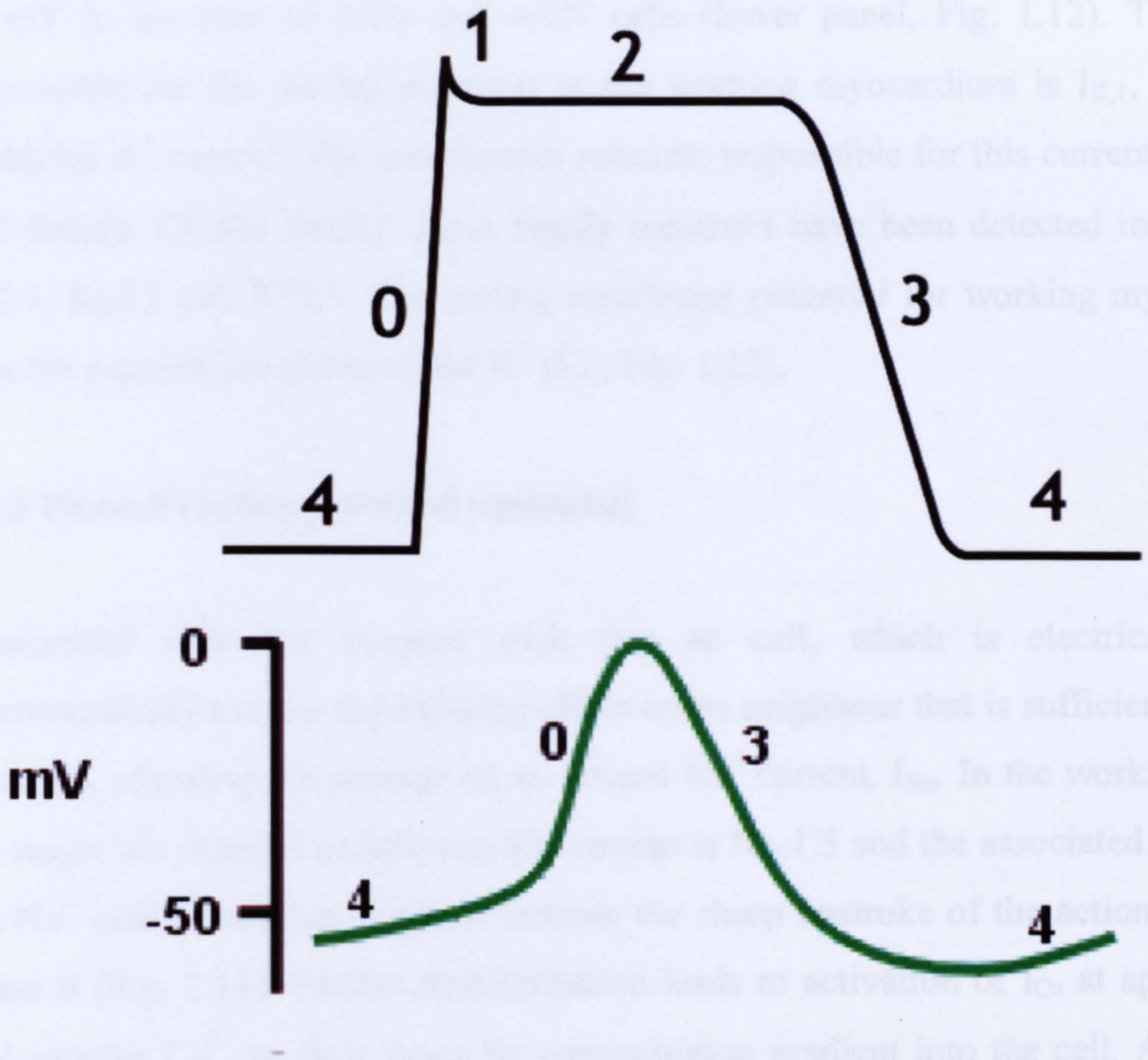

Figure 1.13 Cardiac action potentials. The upper action potential is typical of ventricular cells; phase 4 represents the resting potential which is ~ -80 mV; this is followed by a rapid upstroke, phase 0; early repolarisation produces a marked notch appearance in phase 1; this is proceeded by the plateau phase or phase 2; late repolarisation or phase 3 brings the membrane potential back to its resting state. In contrast, the lower action potential trace represents that seen in pacemaker cells of the SAN or AVN; phase 4 of the action potential is also known as the pacemaker potential (there is no resting membrane potential) and is largely due to the presence of I_f current carried by HCN channels; this is followed by slowly rising depolarization phase during phase 0; repolarisation or phase 3 then pursues to bring the cell to its maximum diastolic potential. From www.cvphysiology.com.

ventricular and atrial cells. Cells of the conduction system however, do not have a stable resting membrane potential and their maximum diastolic potential is approximately -40 to -50 mV in the case of SAN and AVN cells (lower panel, Fig. 1.12). The ionic current responsible for the resting potential in the working myocardium is $I_{K,1}$, a strong inward rectifying K^+ current. The ion channel subunits responsible for this current are members of $K_{ir}2$ family. Of this family, three family members have been detected in cardiac muscle: $K_{ir}2.1$, $K_{ir}2.2$ and $K_{ir}2.3$. The resting membrane potential for working myocardial cells is near the equilibrium potential for K^+ (E_K; Fig. 1.13).

1.3.3 Phase 0 (action potential upstroke)

Myocardial cells are coupled such that an cell, which is electrically active, can electrotonically exert a depolarizing effect on its neighbour that is sufficient to activate Na^+ channels, allowing the passage of an inward Na^+ current, I_{Na}. In the working myocardium, the major ion channel underlying this current is $Na_v1.5$ and the associated Na^+ influx along the Na^+ electrochemical gradient induces the sharp upstroke of the action potential during phase 0 (Fig. 1.13). Further depolarisation leads to activation of I_{Ca} at approximately –40 mV causing Ca^{2+} to flow down its concentration gradient into the cell. As the membrane becomes increasingly depolarised, the Na^+ channels inactivate rapidly and eventually the action potential peak is reached.

Phase 0 of SAN and AVN action potentials is markedly different from that of working myocardial cells (Fig. 1.13). There is an absence of a rapid upstroke due to the lack of the rapid inward Na^+ current carried by $Na_v1.5$ channels. The more positive maximum diastolic potential of SAN and AVN cells (~ -60 to –50 mV) render the majority of $Na_v1.5$ channels inactive and therefore are unable to pass current. The neuronal isoforms of sodium channels, in particular, $Na_v1.1$ are thought to play a role in the action potential upstroke due to their more positive voltage-dependence of inactivation. In addition, it is thought that the $I_{Ca,L}$ contributes substantially to the upstroke of SAN and AVN action potentials due to its positive voltage-dependence profile.

1.3.4 Phase 1 (early repolarisation)

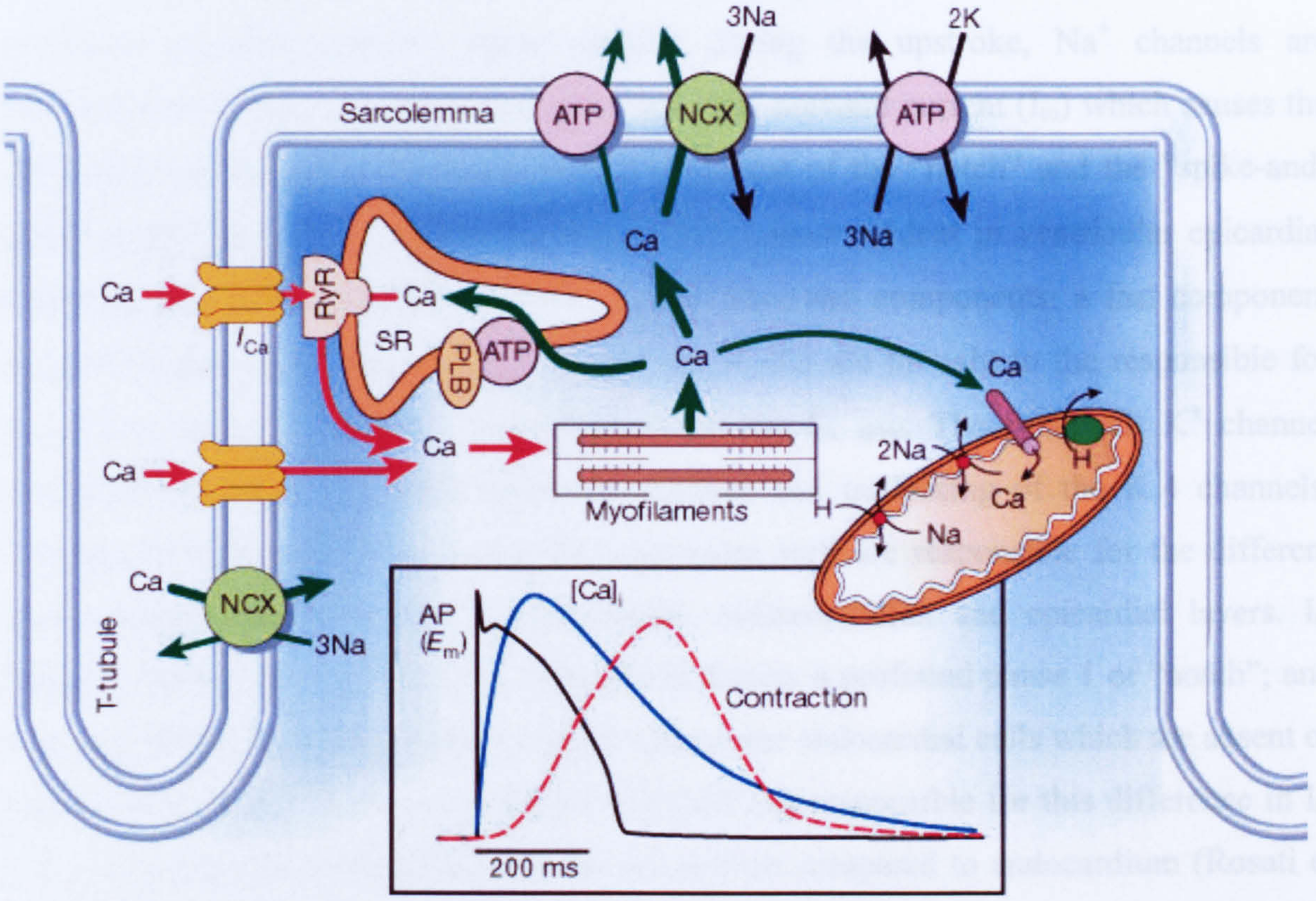

Figure 1.14 Schematic diagram to show the arrangement of subcellular structures involved in EC-coupling in the typical atrial or ventricular myocyte. Transverse-tubule (t-tubule) invaginations are essential for efficient transmission of action potential deep into the cell. Depolarization of the t-tubule allows Ca^{2+} to enter the cells via. L-type Ca^{2+} channels resulting in Ca^{2+} release from the SR Ca^{2+} stores. This Ca^{2+} activates myofilaments resulting in contraction and also Ca^{2+} regulatory proteins on the cell surface including NCX and Ca^{2+} ATPase which extrude Ca^{2+} from the cytosol. In addition, mitochondria also act as a store for internal Ca^{2+} ions. Inset shows the time course of an action potential, Ca^{2+} transient and contraction measured in a rabbit ventricular myocyte at 37 °C. NCX, Na^+/Ca^{2+} exchange; ATP, ATPase; PLB, phospholamban; SR, sarcoplasmic reticulum. From Bers et al., (2002).

Phase 1 is the initial repolarisation phase following the upstroke (Fig. 1.13). As the membrane potential becomes more positive during the upstroke, Na^+ channels are inactivated and there is an activation of the transient outward current (I_{to}) which causes the rapid early repolarisation phase and the development of the "notch" and the "spike-and-dome" morphology of the action potential. This is most evident in ventricular epicardial cells (Litovsky and Antzelevitch, 1988). I_{to} can have two components: a fast component ($I_{to,fast}$) and slow component ($I_{to,slow}$). Kv4.2 and Kv4.3 are thought to the responsible for $I_{to,fast}$ while Kv1.4 is thought to be responsible for $I_{to,\ slow}$. The β-subunit K^+ channel interacting protein 2 (KChIP2) alters the kinetics and trafficking of the K_v4 channels. Transmural differences in I_{to} across the ventricular wall are responsible for the different action potential morphologies in endocardial, midmyocardial and epicardial layers. I_{to} density is greatest in the epicardial cells which display a profound phase 1 or "notch"; and decrease gradually through midmyocardial cells to the endocardial cells which are absent of phase 1. In humans and dogs a gradient in KChIP2 is responsible for this difference in I_{to} with a x25 fold greater expression in the epicardium compared to endocardium (Rosati et al., 2001). In rats, however, the transmural gradient in I_{to} appears to be due to a gradient of $K_v4.2$ and $K_v4.3$ subunits (Dixon and McKinnon, 1994).

I_{to} in SAN cells shows fast and slow time courses of inactivation at intervals which suggest the presence of both $K_v1.4$ and K_v4 channels (Lei et al., 2001). In AVN cells the time course of inactivation is biexponential ~ 14 ms and ~ 112 ms at a holding potential of 0 mV, suggesting contribution from predominantly Kv4 channels (Mitcheson and Hancox, 1999). I_{to} in both the SAN and AVN cells plays an important role in action potential repolarisation.

In addition to the voltage-dependent components of I_{to}, a Ca^{2+}-dependent transient outward current carried by Cl^- ions, $I_{Cl(Ca)}$, is also present in the heart (Kawano et al., 1995). The underlying channel has no voltage-dependence but is activated by a rise in intracellular Ca^{2+} during the Ca^{2+} transient and has been extensively characterised in rabbit (Kawano et al., 1995), ferret (Campbell et al., 1993) and dog (Litovsky and Antzelevitch, 1988) myocytes.

1.3.5 Phase 2 (plateau)

The plateau phase accounts for the long duration of the cardiac action potential (Fig. 1.13). The major current underlying the plateau phase is the L-type Ca^{2+} current, $I_{Ca,L}$. The α-subunit, $Ca_v1.2$, is the major Ca^{2+} channel isoform in the atria and ventricles, although $Ca_v1.3$ been shown to be expressed in the SAN. A increase in the intracellular Ca^{2+} concentration during the Ca^{2+} transient induces extrusion of Ca^{2+} from the cell via the Na^+-Ca^{2+} exchanger in a $3Na^+$:$1Ca^{2+}$ fashion. The exchanger is electrogenic and it generates a net inward current during the plateau phase. In addition to the inward currents, outward K^+ currents are activated during the plateau phase. Three delayed rectifier K^+ currents have been described in cardiac tissue based on their activation properties: ultra-rapid ($I_{K,ur}$), rapid ($I_{K,r}$) and slow ($I_{K,s}$) delayed rectifier currents. The plateau phase is the result of a near balance of the various inward and outward currents.

1.3.6 Phase 3 (late repolarisation)

Eventually the $I_{Ca,L}$ inactivates and the outward K^+ currents predominate, thereby allowing the cell to repolarize (Fig. 1.13). The three delayed rectifier currents, $I_{K,ur}$, $I_{K,r}$, $I_{K,s}$ are also involved in the final stages of repolarization. The ion channel underlying $I_{K,ur}$, is $K_v1.5$, which displays rapid activation kinetics (Wang et al., 1993; Fedida et al., 1993). $I_{K,r}$ is mediated by the K^+ channel, human ether-a-go-go related gene, HERG. Interestingly, mutations in HERG, which alter the kinetics of the channel, have been shown clinically to be responsible for "long-QT syndrome", which is manifested as a prolongation of the QT-interval in the ECG of affected individuals. Furthermore, at the cellular level, an increase in action potential duration can be detected. This illustrates the role of $I_{K,r}$ in ventricular repolarization. The α-subunit, KvLQT1, and the β-subunit, minK are thought to underlie $I_{K,s}$. As the name suggests, mutations in KvLQT1, also cause a prolongation of the QT interval (Wang et al., 1999). The final stages of cardiac repolarization are achieved by the inward rectifier K^+ current, $I_{K,1}$, which, as well as being responsible for the resting membrane potential, activates at potentials near to the equilibrium potential for K^+ therefore returning the cell to its resting membrane potential.

1.3.7 Excitation-Contraction coupling

In the heart, "excitation-contraction (EC) coupling" describes the cellular process by which the spread of electrical activity leads to the generation of contractile force (Fig. 1.14). During the cardiac action potential Ca^{2+} enters the cell down its electrochemical gradient via L-type Ca^{2+} channels which are found predominantly in the transverse tubules (t-tubules) of cardiac myocytes (Kawai et al., 1999; Fig. 1.14). Ca^{2+} entry via $I_{Ca,L}$ triggers further release of Ca^{2+} from the sarcoplasmic reticulum (SR), in a process known as Ca^{2+} induced Ca^{2+} release (CICR) (Fabiato and Fabiato, 1978; Fig. 1.14). The Ca^{2+} release channels on the SR are known as ryanodine receptors because of their sensitivity to the plant alkaloid, ryanodine. They are co-localised with the Ca^{2+} channels in the t-tubules enabling a rapid Ca^{2+} release upon excitation (Franzini-Armstrong and Protasi, 1997). Ca^{2+} entry through L-type Ca^{2+} channels will result in a local subsarcolemmal increase in Ca^{2+} concentration which leads to the opening of ryanodine receptors; further release of Ca^{2+} from the SR will then lead to even more opening of ryanodine receptors, which is known as "positive-feedback". Cheng et al. (1993) first coined the phrase "Ca^{2+} sparks" to describe local release of Ca^{2+} as a result of spontaneous openings of single or a few ryanodine receptors on the SR. Ca^{2+} sparks can be induced via opening of L-type Ca^{2+} channels or spontaneously as a result of the ryanodine receptor open probability being non zero at rest (Niggli, 1999). The co-localisation of L-type Ca^{2+} channels with ryanodine receptors for efficient uniform CICR, leads to the formation of most Ca^{2+} sparks in the vicinity of t-tubules (Lopez-Lopez et al., 1995; Fig. 1.14) with numerous sparks comprising a typical Ca^{2+} transient.

Excitation-contraction coupling is thought to play a role in SAN and AVN pacemaking. However, the extent of this contribution to pacemaking in these regions is somewhat controversial. Ryanodine has been shown to reduce spontaneous activity in the rabbit SAN, in particular, with depression of the later part of diastolic depolarization (Hata et al., 1996). Similar findings by Rigg et al. (2000) in guinea-pig with 2 μM ryanodine have been shown. The effect of sarcoplasmic reticulum Ca^{2+} release on ionic currents in rabbit SAN has been shown by Li et al. (1997) where 10 μM ryanodine abolished inward I_{NCX} which is thought

to contribute to the pacemaker potential and could therefore explain the reduced spontaneous activity in these studies. In contrast, the findings of Bogdanov et al. (2001) show that 30 μM ryanodine abolishes spontaneous beating of rabbit SAN cells. However, Honjo et al. (2003) have shown, in intact preparations and single cells from SAN, that relatively high (30 μM) concentrations of ryanodine to reduce spontaneous firing by ~ 20% which is consistent with the notion that sarcoplasmic reticulum release of Ca^{2+} has a minor role to play in SAN pacemaking. The discrepancies between studies could be due to the type of cells (i.e. "large" or "small") used for the effects of ryanodine on spontaneous activity. There is limited data concerning sarcoplasmic reticulum Ca^{2+} AVN pacemaking. Hancox et al. (1994) have showed that the sarcoplasmic reticulum Ca^{2+} release is stimulated by L-type Ca^{2+} channels but failed to investigate the effect of ryanodine on spontaneous activity.

1.3.7.1 The sarcoplasmic reticulum (SR)

The cardiac SR is an intracellular membrane compartment which is responsible for the storage and release of Ca^{2+} during the cardiac cycle (Fig. 1.14). During an action potential, a wave of depolarization travels along the cell's surface membrane and descends into the t-tubules, ultimately activating L-type Ca^{2+} channels. L-type Ca^{2+} channels in the t-tubule membrane and ryanodine receptors on the surface of the sarcoplasmic reticulum are colocalised and there is a stoichiometry of 4 ryanodine receptors: 10 L-type Ca^{2+} channels (Bers et al., 1993; Fig. 1.14). The cardiac SR also contains the SR Ca^{2+}-ATPase (SERCA2a) protein (Stewart and MacLennan, 1974; Zarain-Herzberg, 1990), which pumps Ca^{2+} from the cytoplasm back into the SR with the use of ATP. SERCA2a activity is regulated by phospholamban which exerts an inhibitory influence on SERCA2a restricting its ability to pump Ca^{2+}. In addition, phospholamban is itself regulated as a result of phosphorylation by cAMP dependent protein-kinases (Fig. 1.14). In the phosphorylated state, phospholamban's effectiveness at inhibiting the SERCA2a pump is impaired thereby allowing Ca^{2+} ions to be pumped back into the SR (Ambudkar et al., 1984).

1.3.7.2 Contractile proteins

Myofilaments convert chemical energy (ATP) in to mechanical force in a Ca^{2+}-dependent manner. Myofilaments are composed of thick (myosin) and thin filaments. The thin filaments are made up of actin, tropomyosin and the troponin complex. Actin is a globular protein arranged in repeating subunits. Tropomyosin molecules are made up of two helical peptide chains, which lie in the groove between the actin molecules and add to the structural rigidity of the thin filament. Attached to the tropomyosin molecules at regular intervals are troponin complexes which are composed of troponin-T (TnT; which attaches to the tropomysoin), troponin-I (TnI; which blocks the myosin binding site on the actin) and troponin-C (TnC; which binds Ca^{2+} during excitation-contraction coupling). Ca^{2+} released by the SR increases the intracellular Ca^{2+} concentration from about 10^{-7} to 10^{-5} M. The free Ca^{2+} binds to troponin-C (Tn-C) and induces a conformational change in the regulatory complex such that troponin-I (Tn-I) exposes a site on the actin molecule that is able to bind to the myosin ATPase located on the myosin head (Wegner and Walsh, 1981). This binding results in ATP hydrolysis (due to the presence of myosin ATPase) that supplies energy for a conformational change to occur in the actin-myosin complex. The result of these changes is a movement ("ratcheting") between the myosin heads and the actin, such that the actin and myosin filaments slide past each other thereby shortening the sarcomere length. Ratcheting cycles occur as long as the cytosolic Ca^{2+} remains elevated.

Cytosolic Ca^{2+} levels must be reduced to resting levels (~10^{-7} M) to allow relaxation to occur. When cytoplasmic Ca^{2+} falls, Ca^{2+} is released from TnC and the troponin-tropomyosin complex reverts to its original configuration preventing an actin-myosin interaction. To restore resting levels, Ca^{2+} is primarily sequestered back into the SR via SERCA2a (Periasamy et al., 2001) and extruded from the cell via Na^{+}- Ca^{2+} exchange (NCX) and Ca^{2+}-ATP-ase (McDonald et al., 2000; Seckin et al., 2001).

1.3.7.3 Calcium extrusion

Reuter and Seitz (1968) were the first to describe a Na/Ca^{2+} exchanger (NCX) in guinea-pig heart muscle (Reuter and Seitz, 1968). It has since been shown to be the primary method of Ca^{2+} extrusion in myocytes (Blaustein and Lederer, 1999; Fig. 1.14). The stoichiometry of Na^{+}- Ca^{2+} exchange is in the ratio of $3Na^{+}$:$1Ca^{2+}$ (Reeves and Hale, 1984). In humans,

NCX is responsible for removing ~37 % of Ca^{2+} from the cytoplasm (although the importance of the NCX is species-dependent). The activity of the Na^{+}-Ca^{2+} exchanger is altered by intracellular concentrations of Na^{+} and Ca^{2+} and ion flow can be reversed leading to Ca^{2+} influx and Na^{+} efflux. The plasma membrane Ca^{2+}-ATPase (PMCA) is also a Ca^{2+} extrusion mechanism, but this makes up a very small percentage of the total Ca^{2+} extruded from the cell (Monteith and Roufogalis, 1995).

1.4 Aims and Objectives

The AVN is complex and electrically heterogeneous. It has multiple action potential morphologies (Billette, 1987) and various cell types (Hancox et al., 1993; Munk et al., 1996). An anatomically accurate 3D model of AVN would be a valuable educational tool for studying the complex morphology of the AVN. In addition, a 3D model of the AVN could be used to build up a virtual representation of the right atrium or even the whole heart since a 3D model of the SAN already exists (Dobrzynski et al., 2005). Furthermore, accurate anatomical 3D models can be used for building mathematical models to study electrophysiological phenomena and further our understanding of cardiac physiology/pathophysiology. 3D models of the rabbit AVN exist but are limited in their use since cellular subgroups can only be defined by certain histological criteria and fail to provide any indication of conduction properties of the AVN. NF-M has been elegantly shown by Gorza and Vitadello (1989) and Gorza et al. (1994) to delineate the conduction system of the rabbit. Cx43 is the major connexin in cardiac tissue and is a good marker for deducing conduction properties of cardiac tissue. Firstly, by combining histology, and immunohistochemical labeling of NF-M and Cx43 we aimed to build a 3D model which provided information regarding distinct cellular subgroups and their conduction properties together with a full reconstruction of nodal cells throughout the AVN conduction axis.

The electrical properties of cardiac tissue i.e. action potential morphologies are ultimately determined by the currents that pass through the cell and therefore by the expression of ion channels and ion exchangers. Functional work regarding electrical properties of the AVN has taken two approaches to date: 1) intact AVN preparations, which are limited to providing information about nodal conduction time and refractory periods (Mendez and

Moe, 1966) and to a certain extent action potential characteristics of certain regions (Billette, 1987) and, 2) single cell studies which give a good idea of the different action potentials and ionic currents in certain cell types (Hancox et al., 1997; Munk et al., 1996) but are limited in their application to the overall understanding of AVN function due to a lack of specific localization of the cell type to an area within the triangle of Koch. Our second aim therefore, was to provide an idea of electrical activity in specific regions of the rabbit AVN by accurately quantifying and localizing mRNA transcripts encoding the major cardiac ionic currents and exchangers in specific subcellular groups throughout the rabbit AVN conduction axis using *real time* PCR and *in situ* hybridization.

Chapter 2

Materials and Methods

I have used a number of approaches in this study in order to elucidate the molecular composition of the rabbit AVN. These included histology, immunhistochemistry, *real-time* polymerase chain reaction, riboprobe synthesis and *in situ* hybridisation. This chapter describes the methods, reagents and equipment used to carry out these techniques.

2.1 AVN tissue preparation

2.1.1 Obtaining animals for AVN preparations

Male New Zealand white rabbits (1.5-2.5 kg) and Sprague-Dawley rats were used in this research. The animals were obtained through the University of Leeds, Central Biomedical Services and University of Manchester, Biomedical Services Unit. All procedures were carried out under licence in accordance with the regulations of the United Kingdom Animals (Scientific Procedures) Act 1986. The rabbits were humanely killed by lethal injection with sodium iso-pentaborbitone (90mg/kg) into the marginal ear vein.

2.1.2 Gross dissection of structures within AVN

A step-by-step guide to the dissection of the rabbit AVN is shown in Fig. 2.1. Whole hearts were removed and superfused with oxygenated Tyrode's solution, the composition of which is shown in table 2.1, warmed to 37°C in a water bath. The hearts were then pinned to a dissection chamber. Surrounding fatty and connective tissue was removed. A large horizontal incision was made through the ventricles (Fig. 2.1A) to remove the apex thereby leaving only the base of the ventricles, atria and accompanying vessels (Fig. 2.1B). A vertical incision immediately toward the left side of the heart was made to remove the remaining left ventricle and left atrium (Fig. 2.1B). The aorta and

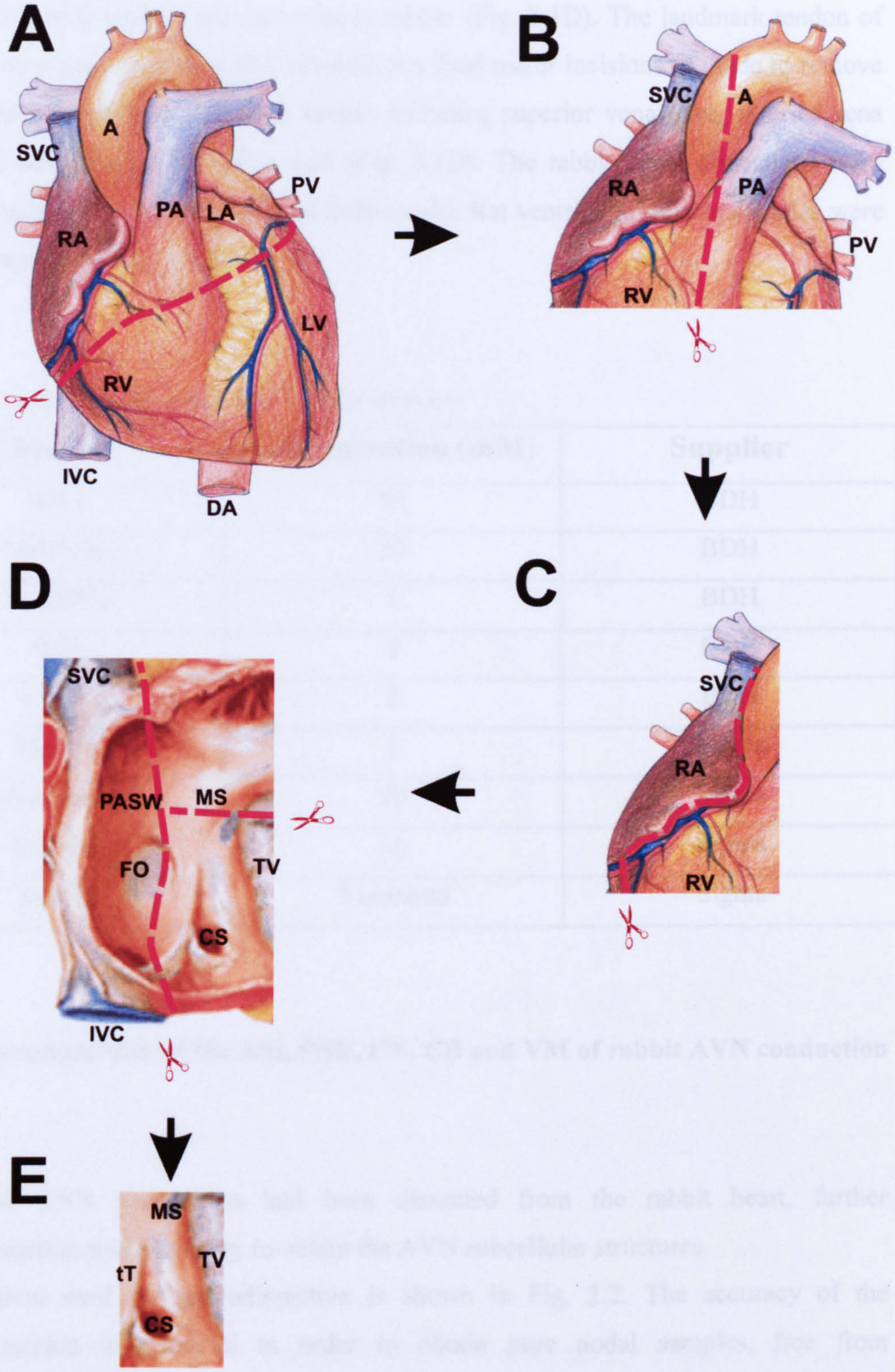

Figure 2.1 Schematic flow diagram illustrating the procedure for gross dissection of AVN preparations from rabbit hearts. Red dashed lines indicate where incisions were made with microdissection scissors. SVC, superior vena cava; A, atrium; PV, pulmonary vein; LA, left atrium; LV, left ventricle; DA, descending aorta; RV, right ventricle; IVC, inferior vena cava; RA, right atrium; PA, pulmonary artery; PASW, posterior atrial septal wall; MS, membranous septum; TV, tricupsid valve; CS, coronary sinus; FO, fossa ovalis; tT, tendon of Todaro.

pulmonary artery were removed. The inside of the right atrium was exposed by making a cut along the fold of the right atrial free wall (Fig. 2.1C) then pinning back the free-wall (endocardial surface up) onto silicon rubber (Fig. 2.1D). The landmark tendon of Todaro was clearly visible, which allowed two final major incisions to made to remove the remaining regions of the right atrium including superior vena cava, inferior vena cava and bulk of posterior atrial wall (Fig. 2.1D). The rabbit AVN dissections were carried out by myself and Dr. Halina Dobrzynski. Rat ventricular muscle samples were kind donations from Dr. Mark Fowler.

Table 2.1 Tyrode's solution composition for AVN dissection

Chemical	Concentration (mM)	Supplier
NaCl	93	BDH
$NaHCO_3$	20	BDH
Na_2HPO_4	1	BDH
KCl	5	BDH
$CaCl_2$	2	BDH
$MgSO_4$	1	Sigma
Sodium acetate	20	Sigma
Glucose	10	Sigma
Insulin	5 units/ml	Sigma

2.1.3 Microdissection of the AM, PNE, CN, CB and VM of rabbit AVN conduction axis

Once the AVN preparation had been dissected from the rabbit heart, further microdissection was necessary to obtain the AVN subcellular structures

The method used for microdissection is shown in Fig. 2.2. The accuracy of the microdissection was crucial in order to obtain pure nodal samples, free from contamination from surrounding regions, to enable accurate determination of gene expression patterns.

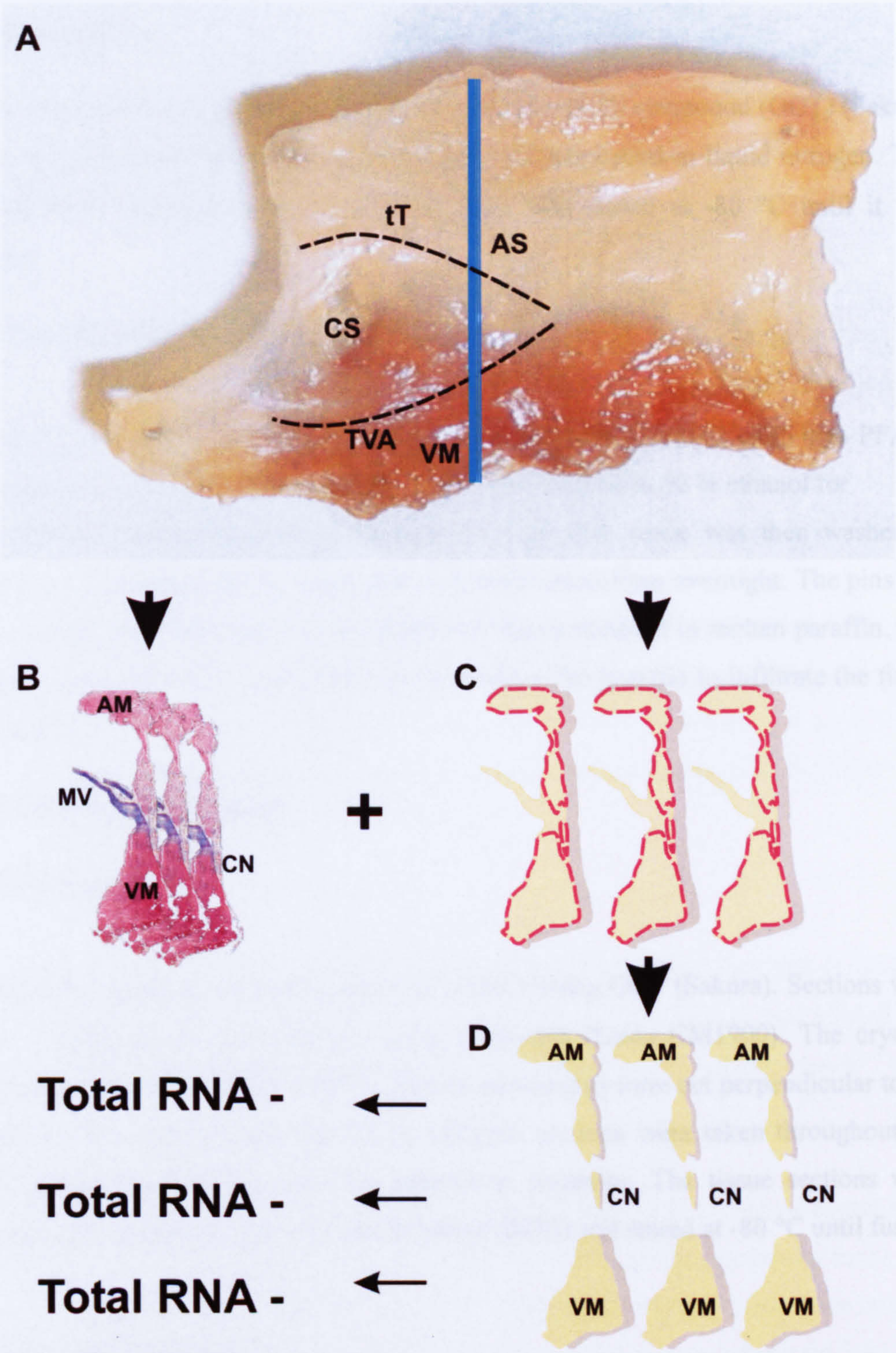

Figure 2.2 Schematic diagram illustrating microdissection procedure for isolating AVN regions. A, a typical AVN preparation is dissected from the rabbit heart as explained in figure 2.1; blue lines indicate plane in which sections were cut; AS, atrial septum; VM, ventricular muscle; TVA, tricuspid valve annulus; CS, coronary sinus; tT, tendon of Todaro. B, 10μm serial sections are taken and stained for Masson's trichrome to identify subcellular structures; AM, atrial muscle; CN, compact node; VM, ventricular muscle; MV, mitral valve. C, 3 x 60μm sections are taken adjacent to the Masson's trichrome stained sections and are subjected to freeze-drying overnight. D, Specific tissue regions are microdissected out of the freeze-dried tissue and total RNA is isolated.

2.2 Fixation and embedding of the AVN tissue

2.2.1 Frozen tissue

Whole AVN preparations were immersed in optimal cutting compound (OCT) (Sakura) before being dropped into a container of isopentane suspended in liquid nitrogen. This ensured rapid freezing of the tissue. The tissue was stored at -80 °C until it was required.

2.2.2 Paraffin embedded AVN tissue

The AVN preparation, while still pinned onto silicon rubber, was fixed in 4 % PFA in PBS overnight at 4 °C. After fixation, the tissue was washed in 90 % ethanol for 4 hr, followed by a 100 % ethanol wash for 3 hr. The tissue was then washed in chloroform for 30 min, before being placed in fresh chloroform overnight. The pins and silicon rubber were removed and the tissue was then embedded in molten paraffin. The paraffin embedded tissue was left for 24 hr to allow the paraffin to infiltrate the tissue and solidify.

2.3 Sectioning of AVN tissue

2.3.1 Cryo-sectioning

Frozen AVN preparations were secured on a chuck using OCT (Sakura). Sections were cut at a thickness of 10 or 60 µm using a cryostat (Leica CM1900). The cryostat temperature was set between ~ -20 °C. The tissue sections were cut perpendicular to the tricuspid valve annulus (see Fig. 2.2A). Multiple sections were taken throughout the AVN preparation, running from the anterior to posterior. The tissue sections were mounted onto superfrost plus microscope slides (BDH) and stored at -80 °C until further use.

2.3.2 Paraffin sectioning

The paraffin block was melted onto the chuck and trimmed with reference to the tissue inside. Serial 10 µm sections were cut in the same orientation using a rotary microtome (As500 Universal/Semithin, Anglia Scientific). Multiple sections were taken throughout

the AVN preparation, running from the anterior to posterior part of the tissue. As the sections were cut, short ribbons were formed and placed in a 10 °C water bath. The sections were collected from the water bath on superfrost plus microscope slides (BDH) and dried for a minimum of 24 hr at 37 °C.

2.4 Histology

Masson's trichrome 10 µm cyro-sections or 12 µm paraffin sections were cut perpendicular to the crista terminalis and subsequently mounted on Superfrost Plus glass slides (BDH). The sections were fixed in Bouin's fluid for 15 min, and washed three times in 70 % ethanol (each wash 10 min). Masson's trichrome staining was carried out on these fixed sections: staining in ceslestine blue (5 min), rinsing with deionised water, staining in Cole's alum haematoxylin (5 min), washing out with tap water (15 min), acid fuschin stain (10 min), rinsing with deionised water, phosphomolybdic acid (5 min), draining off and staining with methyl blue (90 sec), rinsing with deionised water and treatment with 1 % acetic acid (2 min). After staining, the tissue sections were dehydrated through graded ethanol washes (70 to 100 %), cleared in two xylene washes (each wash 5 min), and mounted glycerol jelly (BDH).

2.5 Immunohistochemsitry

Antibodies. Antibodies used were: (a) mouse monoclonal anti-neurofilament-M (160 kD; catalogue number MAB5254; Chemicon, Harrow, UK); (b) mouse monoclonal anti-Cx43 (catalogue number MAB3068; Chemicon) (c) Biotinylated anti-mouse (Chemicon).

Immunoenzyme labelling: Immunoenzyme experiments were carried out on paraffin-embedded intact AVN preparations. ~10 µm sections were cut (perpendicular to the coronary sinus) and subsequently mounted on Superfrost Plus glass slides. Prior to the immunoenzyme technique, tissue sections were dewaxed in xylene and treated with 100 % ethanol for 10 min. Tissue sections were then treated with H_2O_2 in methanol (0.6%) for 30 min. The tissue sections were then treated with an antigen unmasking solution (Vector; H-3300; Vector Labs) in a microwave for 10 min at boiling point. They were then treated with 0.2 % Triton-X 100 diluted in 0.01M PBS for 30 min, washed in PBS

three times (each wash 10 min) and blocked with normal horse serum (diluted in PBS according to the instructions in the Vectastain ABC kit, PK-6102, Vector Labs) for 60 min. The sections were then incubated with the anti-mouse neurofilament and anti-mouse Cx43 primary antibodies for 24 h at 4°C. Each primary antibody was diluted in 1 % BSA in PBS at a dilution of 1:100. After incubation in the primary antibodies, the sections were washed three times in PBS over 30 min, and incubated with biotinylated anti-mouse secondary antibody for ~2 h and washed again three times in PBS over 30 min. The sections were then incubated in ABC reagents for 60 min and this was again followed by three washes in PBS over 30 min. The biotinylated anti-mouse secondary antibody and ABC reagents were prepared according to the instructions in the Vectastain ABC kit (Vector Labs). The sections were developed in DAB solution for 5-10 min. The DAB solution was prepared according to the instructions in the Vector Peroxidase Substrate Kit (SK-4100; Vector Labs). Finally, the sections were washed in distilled H2O for 10 min, dehydrated in graded ethanols (50 to 100 %), cleared in xylene, and mounted in a permanent mounting medium (VectaMount; H-5000; Vector Labs). No labelling above background was obtained when the primary antibodies were omitted (data not shown). Immunoenzyme labelled sections were stored at room temperature for subsequent viewing with the Leica Materials Workstation.

2.6 3 Three-dimensional reconstruction

10 μm serial sections from paraffin-embedded AVN preparation were Masson's trichrome stained at 200 μm intervals. The stained sections were imported into Corel Draw 10 and distinct tissue regions were selected to produce digitised images at each level. The digitised images were then incorporated into MATLAB by Jue Li to produce the final 3-dimensional model.

2.7 *Real time* polymerase chain reaction (*real time* PCR)

The high sensitivity of *real time* PCR makes this method an ideal tool to study the expression of ion channels in cardiac tissue, where mRNA expression is considered to be low. In addition, *real time* PCR requires a relatively low input of RNA as opposed to

other techniques such as northern blotting and RNAse protection assays. Furthermore, this technique is extremely sensitive and specific. It is therefore possible to study the RNA extracted from tiny tissue samples, such as the AVN pieces used in this study. In addition, whole genome arrays were not able to be used due to the lack of gene sequence data available for rabbit.

This technique made use of technological advancements, in the way of precision optics and intercalating fluorescent dyes. The amplification of cDNA is measured in real-time as the reaction proceeds, by measuring the progress of amplification through each step. This enables us to follow later stages of an amplification precisely. Thus, allowing for very small differences in initial gene target to be measured.

Due to the sensitivity of the procedure, there are issues regarding variability. These come under two main groups: Biological and technical. Biological is defined as that such as differences in gene expression due to differences in genetic make-up, physiological states, gender, inter-individual variability etc. Technical variation can also be referred to as noise or "measurement-error" introduced into the experiment and this could be due to a number stages in RNA/cDNA preparation such as, RNA quality, reverse transcription (RT), PCR efficiency and cDNA priming. High variability can reduce the measurement of small differences between samples and also decreases the power of statistical tests.

2.7.1 Variability of the system:

It is essential to keep *real time* PCR conditions as constant as possible especially the quantity of RNA input for each sample into the RT and also the RT conditions. This includes: cycle conditions, reaction volume and primer design.

Housekeeping genes try to eliminate experimental variability during the reverse-transcription, amplification etc. because these genes should not vary in their expression.

2.7.2 RNA isolation from the AVN

Histological analysis of the atrioventricular conduction axis (Chapter 3) revealed a complex architecture. Together with functional data regarding the rabbit AVN, it is clear that three important tissue structures lie within the Triangle of Koch: the common bundle (CB; most anterior); the compact node (CN) and the posterior nodal extension (PNE; most posterior). The anatomical landmarks demarcating the triangle of Koch, notably the tendon of Todaro, central fibrous body (CFB), tricuspid valve annulus (TVA) and the inferior septal isthmus can be visualized easily within the right atrium. With fresh AVN tissue it is difficult to visualise the major components of the AVN conduction axis and therefore using conventional methods of RNA isolation on fresh tissue would make it impossible to accurately dissect the major components without contaminating the samples with surrounding tissue. The most feasible way we could identify and locate the conduction system structures for each preparation was either with a histological approach and/or using immunohistochemistry with a neurofilament-M (NF-M) antibody to delineate the nodal structures. Histology was cheaper, quicker and more convenient than immunhistochemistry. The methods available to use in conjunction with serial sections were: 1) frozen tissue which could be used with thick (60μm) sections which could then be microdissected in a cold room after Masson's trichrome staining of adjacent 10μm sections, however, the thick sections would be hard to manipulate when frozen and there would be a risk of the tissue thawing, 2) using fixed tissue, however, the RNA isolated from fixed tissue is highly degraded and therefore would be unsuitable for real-time PCR analysis, 3) Freeze-drying the tissue, which is less harsh a treatment than fixation and based on experience of using this tissue by Dr. Rudi Billeter (Billeter, 1980) whereby he was able to measure enzyme activity and show that substrates were not metabolised thus indicating a lack of enzyme activity which in terms of RNA integrity is favourable since RNases will be inactive (probably due to the removal of the hydration shell surrounding the enzyme) and therefore the RNA isolated should be relatively intact; even upon rehydration (addition of RLT; see section 2.) during the RNA isolation procedure the RLT reagent contains RNase inhibitors and therefore should prevent any RNA degradation. Therefore, by uniquely combining histological staining with freeze-drying of adjacent cryosections (Fig. 2) we were able to: 1) Determine the level along the AVN conduction axis which we were. 2) Identify the sub-cellular structures within the confines of the AVN conduction axis 3) Accurately dissect the major components of the rabbit AVN without contamination from surrounding tissues. 4) Obtain good quality RNA for real-time PCR analysis.

2.7.3 Freeze-drying

The fundamental principle in freeze-drying is sublimation, the shift from a solid directly into a gas. Water will sublime from a solid (ice) to a gas (vapour) when the molecules have enough energy to break free but the conditions aren't right for a liquid to form. There are two major factors that determine what phase (solid, liquid or gas) a substance will take: heat and atmospheric pressure. For a substance to take any particular phase, the temperature and pressure must be within a certain range. The freeze-dryer consists of a freeze-drying chamber in which the samples are placed, a cold-trap which is essentially a metal coil which is cooled to ~-80 C and attached is a vacuum pump which generates a negative pressure of $\sim 10^{-2}$ Bar. Under these conditions water is extracted from the tissue in its frozen state directly into the gaseous phase.

2.7.4 Optimisation of RNA Isolation from freeze-dried AVN tissue

Firstly, we needed to be able to extract RNA from freeze-dried tissue. A rabbit AVN preparation was cut like previously described (section 2.) with 10 µm sections subjected to Masson's trichrome staining followed by three adjacent 60 µm sections which were immediately frozen in liquid nitrogen and subsequently freeze-dried overnight.
RNA was extracted (See total RNA tissue extraction) and run on a 4% formaldehyde-agarose RNA gel (Fig. 2.3) to check for integrity. 18S and 28S bands are clearly visible in lanes 2 and 3, for atrial myocardium (AM) and ventricular myocardium (VM), respectively. No visible 18S and 28S bands are detectable for AVN (compact node) sample - lane 4. This is due to the amount of RNA contained in this particular sample being below the level of detection for an RNA gel (< 100 ng). These are good reasons to assume that the nodal sample was of similar integrity to the AM and VM samples i.e. good yield and integrity from AM and VM.

2.7.5 RNA Quantification

RNA from those samples were then quantified on the Lightycler (Roche) using RiboGreen Quanitification Kit (Molecular Probes). A standard curve of ribosomal RNA was run alongside the three tissue samples. Indeed, the AVN sample was significantly

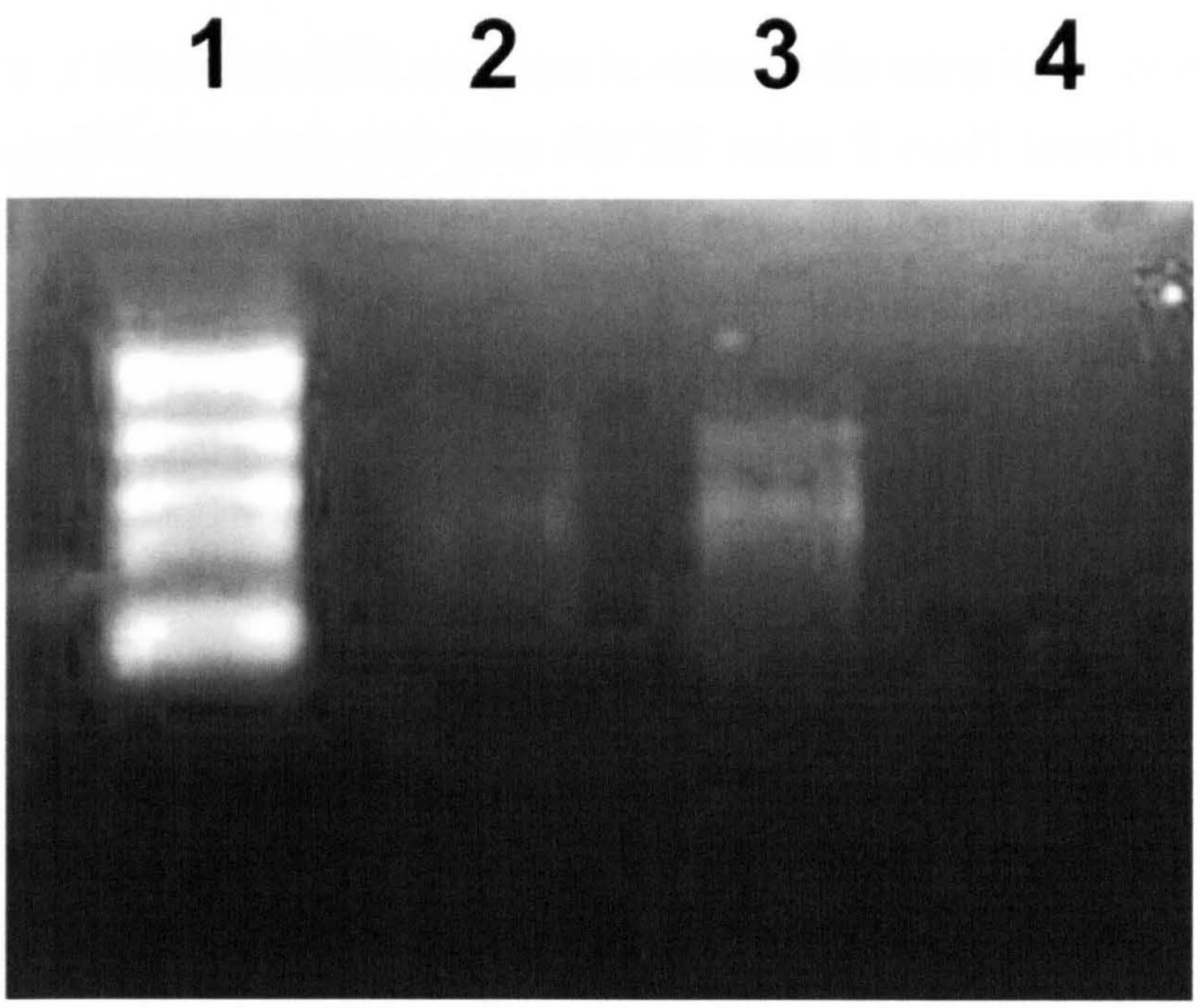

Figure 2.3 First attempt at RNA isolation from freeze-dried AVN, AM and VM tissue. Lane 1, RNA ladder; Lane 2, AM sample; Lane 3, VM sample; Lane 4, AVN sample. AM (lane 2) and VM (lane 3) samples are visible and there appears good 18S:28S ratio with little sign of degradation (forward smear). Lane 4 containing the AVN sample appears absent of 18S and 28S bands which is due to the relatively small yield from this sample due to significantly less tissue being used for RNA extraction.

lower (12.2 ng) compared to that of the AM (158 ng) and VM (387 ng) thus explaining why the AVN sample was not detected on the RNA gel.

2.7.6 Reverse Transcription

Although the AVN sample RNA could not be detected the integrity of the AM and VM samples appeared very good with good 18S:28S ratios. It could therefore be assumed that the AVN sample, albeit at a lower quantity, was good quality RNA. Therefore, this RNA was subsequently reverse-transcribed using SuperScript II first strand-synthesis (Invitrogen) according to the manufacturers instructions.

2.7.7 *Real Time* PCR

Finally, *real time* PCR was performed on the cDNA generated for each sample. The housekeeping gene 28S showed no significant difference between samples. Neurofilament-M (NF-M) was significantly higher in the AVN sample (Ct = 23) when compared to AM and VM (Ct = 30) samples, indicating accurate dissection. The L-type calcium channel ($Ca_v1.3$; alpha1D) was significantly higher in the AVN (Ct = 32) than VM (Ct = 36) and failed to be detected in the AM. The alpha subunit KvLQT1 underlying the slow component of the delayed rectifier channel was not significantly different in any sample (Ct = 30), as expected.

The next step was to accurately dissect AVN, AM and VM samples from seven rabbits in order to obtain statistically sound *real time* PCR data. The same procedures were followed as above. However, upon *real time* PCR analysis of all ion channel transcripts for which primers had been optimised the real-time results were extremely variable. More abundant transcripts and markers such as 28S, NF-M, ANP, HCN4, $Ca_v1.3$ (alpha1D), could be measured to a certain extent (in some samples transcripts failed to be detected). However, other ion channel transcripts which are known to be present could be measured in some samples and not others. In particular, $Ca_v1.2$ mRNA (alpha1C) which should be highly abundant in the AM failed to be detected, suggesting that this transcript had been degraded. On the other hand, it could be that certain ion channel transcripts are more susceptible to degradation when subjected to these extraction methods (Newbury, 2006).

2.7.8 Testing RNA-later and RNA-later ICE on freeze-dried tissue

We concluded that the RNA might be partially degraded during the freeze-dry process. Therefore, we set out to try and protect the RNA during the freeze-dying process using RNA later and RNA-later ICE which are RNA stabilising agents for fresh and frozen samples, respectively. We dissected three fresh pieces of rat ventricular myocardium and placed them in RNA-later. At the same time we submerged four pieces of frozen rat ventricular myocardium in RNA-later ICE. Control VM samples were also processed. All VM samples were subjected to freeze-drying overnight and total RNA was isolated the next day. The three RNA-later-treated VM samples varied in RNA quality, with one sample yielding very high amounts (Fig. 2.4; lane 6) and the other two (Fig. 2.4; lanes 5 & 7) low yields and poor 18S:28S ratio. RNA later-ICE- treated VM samples provided higher RNA yields and 18S:28S ratio (Fig. 2.4; lanes 8-11). In contrast, the RNA isolated from control (normal) VM samples was of poor quality and lower yield (Fig. 2.4; lanes 1-3).

In light of these findings, it was decided RNA later-ICE should be tested on the AVN. There were certain issues regarding penetrability of the RNA later-ICE into tissue. However, it was another area which proved to be a major problem. Once the AVN preparation had been subjected to RNA-later ICE its physical properties changed somewhat, in particular, the freezing point of the tissue had been lowered, most probably, due to the ethanol in the RNA later-ICE. The tissue became very "rubbery" in consistency, therefore, it was impossible to cut it on the cryostat after RNA later-ICE treatment. Due to the ingredients of the RNA later-ICE being proprietary information, it was difficult to understand exactly what properties the reagent had.

Assuming that RNases in the tissue had been inhibited by the RNA later-ICE, if we could remove the ethanol from the tissue without removing the RNase inhibitor we would be able to cut the tissue and preserve RNA integrity. Therefore, by soaking a piece of rat VM previously treated with RNA later-ICE in DEPC-treated PBS solution we aimed to remove the ethanol from the tissue, whilst maintaining RNA protection. However, after RNA extraction, the RNA was completely degraded (Fig. 2.5; lane 4).

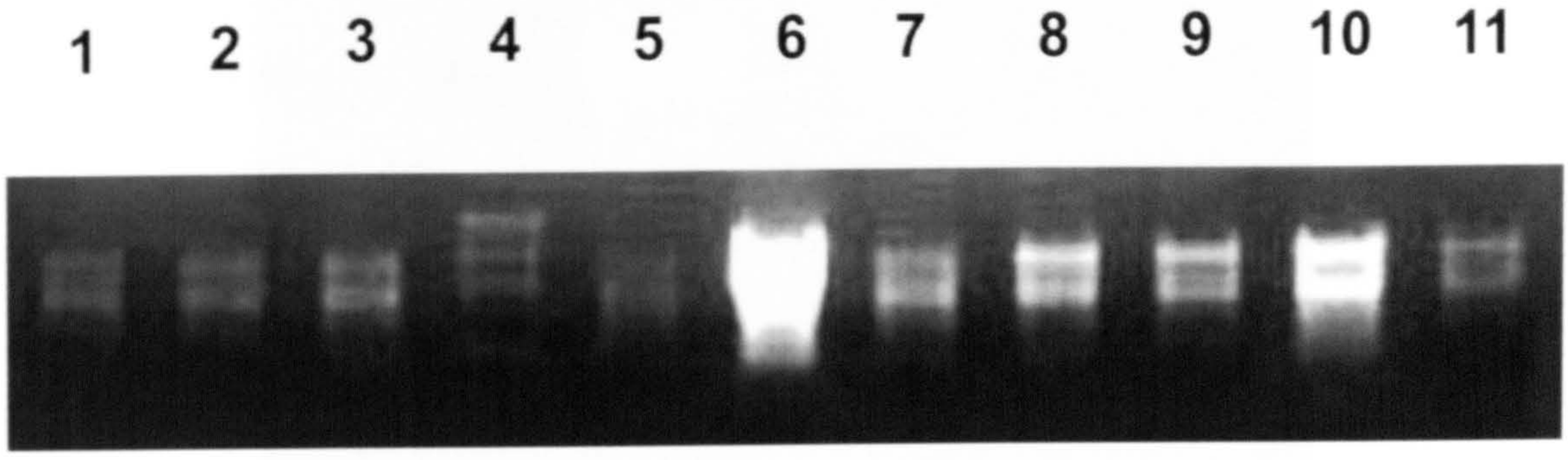

Figure 2.4 RNA isolated from freeze-dried ventricular tissue normal, RNA later treated, RNA later ICE pre-treated. Lanes 1, 2, 3 normal ventricular muscle; lane 4, RNA ladder; lanes 5, 6 and 7 RNA later treated; lanes 8, 9, 10, and 11, RNA later ICE pre-treated.

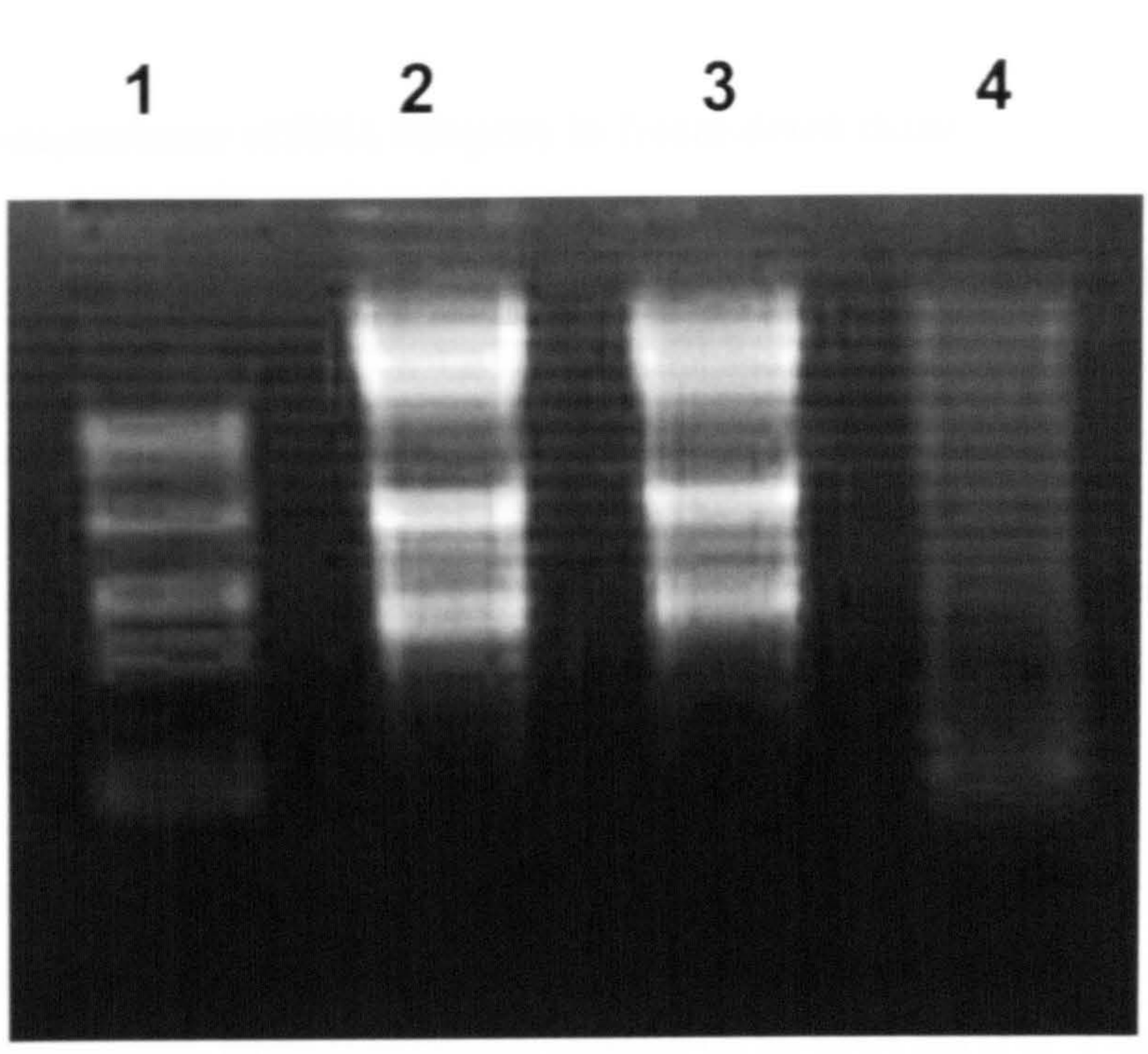

Figure 2.5 Ventricular muscle treated with RNA later-ICE and RNA later ICE with DEPC-PBS wash-out. Lane 1, RNA ladder; lanes 2 & 3, VM treated with RNA later-ICE; lane 4, VM treated with RNA later-ICE then washed out with DEPC-PBS solution. VM samples in lanes 2 & 3 are of very good quality with good integrity of 18S and 28S bands. However, after DEPC-PBS post-treatment the RNA is almost completely degraded with additional bands below 18S band in lane 4.

2.7.9 Time-dependence of RNA integrity in freeze-dried tissue

The initial freeze-drying procedure was carried out at the University of Nottingham, which meant cutting the tissue in Leeds then transporting the samples on dry ice in order to be freeze-dried overnight. Then the samples would be transported back to Leeds in a sealable bag containing SiO2 to keep the samples dry. We came up with the idea that the tissue, once exposed to the air may absorb moisture in the form of water vapour and that this was sufficient to provide a hydration shell for the RNases and thus activate them; over time this would lead to RNA degradation.

Control, RNA-later treated and RNA-later ICE-treated AVN tissue were subjected to freeze-drying overnight. These pieces of tissue were left on the bench for 5 days then the RNA was isolated. Upon running the samples on an RNA gel (Fig. 2.6), the control tissue was entirely degraded, the RNA-later-treated sample showed a typical smear of degraded RNA and the RNA later-ICE-treated sample showed partial degradation with 18S and 28S bands visible, but a poor 2:1 ratio.

RNA gels provide limited information with regards to the quality of RNA obtained and the sensitivity of detection. Therefore, to be certain of the quality of the RNA we were extracting we decided the RNA needed to undergo more stringent testing for potential degradation. This was achieved in the way of Agilent NanoLabChips (which are more sensitive and better standardised) run on the Agilent 2100 Bioanalyser. 1 µl samples of AM and VM from all seven rabbits were analysed to produce electropherogram plots of 18S:28S ratios. Upon inspection the plots were smooth and showed very little sign of degradation (additional noise bands in between 18S and 28S peaks; Fig. 2.7).

2.7.10 Interference of cryotube electrostatic charge

The nodal tissue samples are very small in size (less than 1 mm in diameter and 2 mm in length, making them difficult to handle. Electrostatic charges carried by the Cryotubes (Nunc. Denmark) causes the nodal tissue pieces to stick to the side of the tubes. The initial step in the RNA isolation procedure is the addition of a

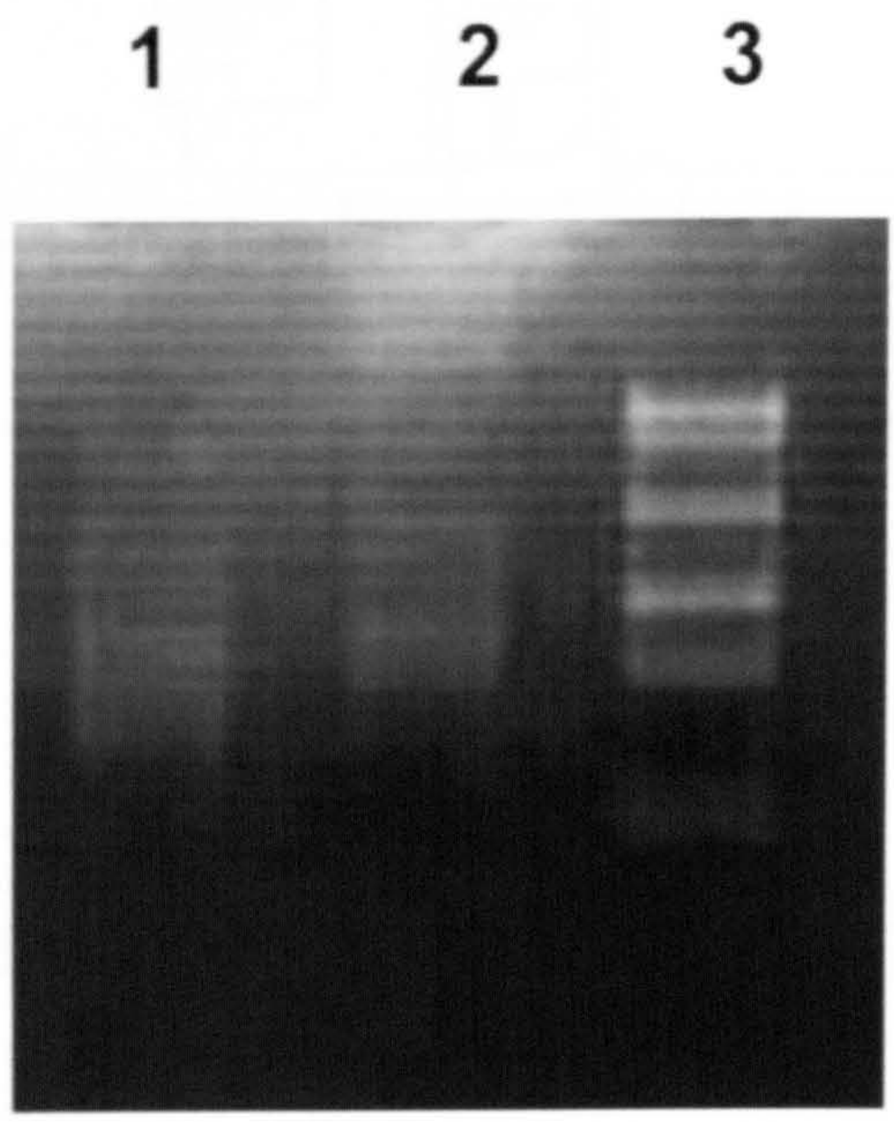

Figure 2.6 Freeze-dried ventricular tissue left on bench for 5 days. Lanes 1 and 2, ventricular muscle left on bench for 5 days; lane 3, RNA ladder. It can be clearly seen that the RNA is of poor quality with low yield and 18S and 28S bands of poor integrity.

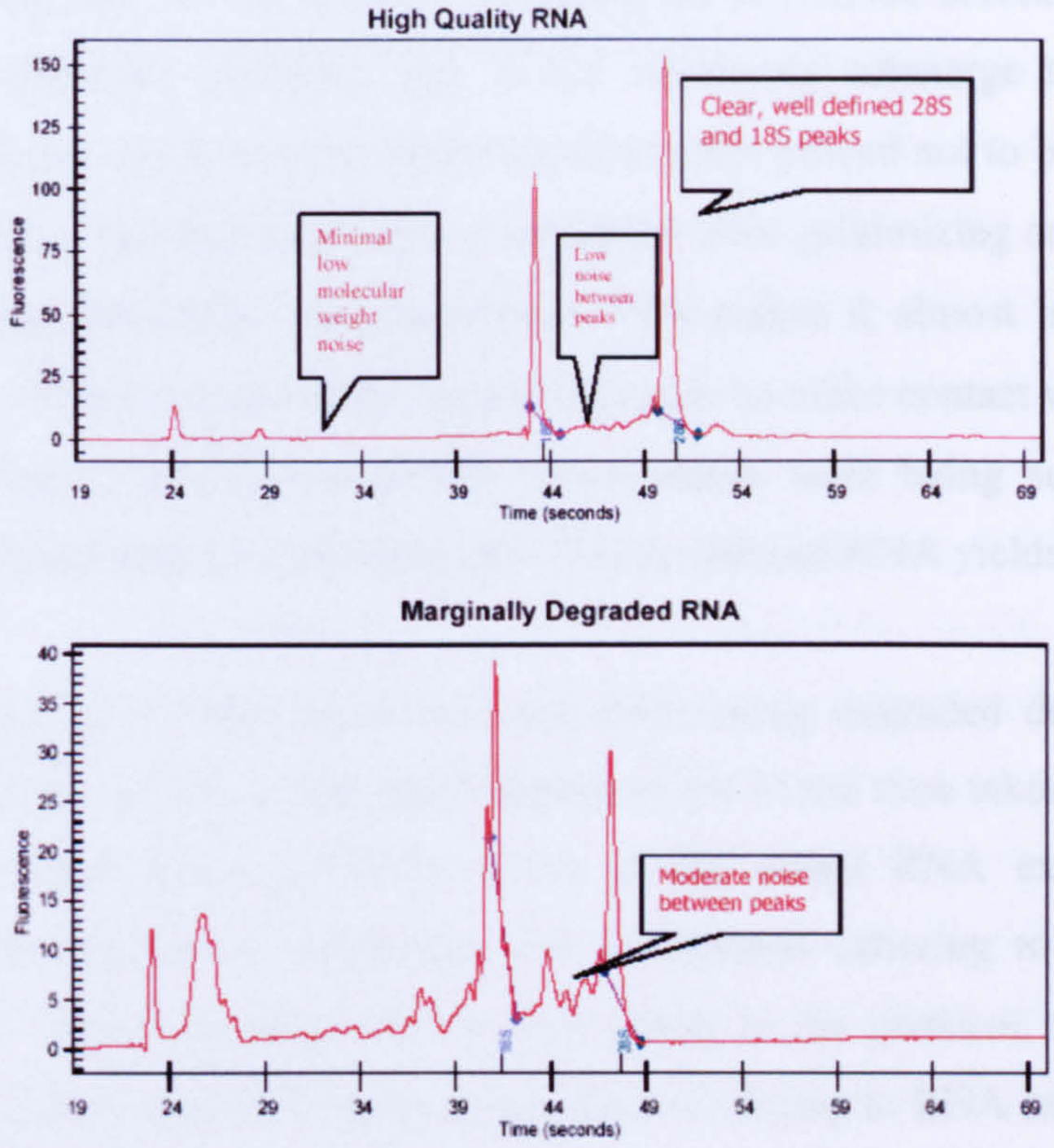

Figure 2.7 Examples of electropherogram plots obtained from the Agilent 2100 Bioanalyser. Upper 2 panels show examples of high quality RNA (upper) and marginally degraded RNA (middle). Lower panel, example of one of our VM samples; note, the lack of interference between peaks of the VM sample indicating the isolation of good quality RNA from freeze-dried tissue.

RLT/betamecaptoethanol solution. In order to transfer the tissue pieces from the side to the bottom of the tube, it was assumed by adding the RLT/BME solution directly above these pieces would be sufficient; this would effectively submerge the tissue in the RLT/BME solution. However, on closer inspection this proved not to be the case and in fact, on addition of the RLT/BME the tissue pieces were gelatinizing and sticking to the side of the tube, becoming semi-transparent. This makes it almost impossible to see them and also making it difficult for the homogenizer to make contact with. Therefore it was very unlikely that those particular tissue pieces were being submerged in the RLT/BME mixture which would ultimately lead to reduced RNA yields.

Our results had shown that rather than the RNA being degraded during the freeze-drying process, the quality of the RNA depended on: 1) the time taken from extraction of the freeze-dried pieces of AVN tissue to the actual RNA extraction and, 2) Minimising the amount of tissue loss due to material adhering to the side of the cryotube. Two critical procedures were then added to the protocol, namely: 1) rapid processing of tissue samples from the point of freeze-drying to RNA extraction, in order to reduce possible RNA degradation over time and, 2) Using a rotary oven during the RLT/Beta-mercaptoethanol/proteinase K step in order to bring into contact the mixture with any tissue samples adhered to the side of the tube.

2.7.11 Rotary Oven

The conventional approach to RLT/Beta-mercaptoethanol/proeinase K incubation is to use a water bath in which the cryotubes are placed vertically. However, there is the risk that pieces of tissue which are adhered to the side of the tube fail to exposed to the solution. The use of a rotary oven overcomes this. A rotary oven consists of an oven which is pre-heated to incubation temperature (55 C); within the oven is a cylindrical chamber which rotates and therefore can be used to attach the cryotubes containing the tissue samples and RLT/Beta-mercaptoethanol/proeinase K solution; this allows each part of the inside of the cryotube to be continually exposed to the RLT/Beta-mercaptoethanol/proeinase K solution which overcomes the problem of tissue pieces potentially sticking to the side of the tube and not being exposed to the RLT/Beta-mercaptoethanol/proeinase K solution.

2.7.12 Total RNA tissue extraction

Total RNA was extracted from rabbit AVN tissue samples (the dissection of which is described in section 2.1.2.1) using the Qiagen RNeasy Mini isolation kit with a modified manufacturer's protocol. Each AVN preparation was cut into three or four 10 µm sections followed by 3 x 60 µm sections using a cryostat (Leica CM1900, UK). This method of tissue allowed for the identification of subcellular nodal structures using Masson's trichrome staining (see below) of the 10 µm sections. The 3 x 60 µm sections were placed in a crytoube (nunc) filled with liquid nitrogen and placed in a liquid nitrogen filled dewar. Pierced caps were put onto the cryotubes before they were placed in a freeze-dryer overnight (Thermo MicroModulyo). The freeze-dried sections were then microdissected using a dissecting microscope and optical light source. Microdissected material for each tissue type was pooled into separate cryotubes. Beta-mercaptoethanol was added to RLT buffer (1:100). To each cryotube containing the microdissected samples, 333 µl of the RLT/beta-mercaptoethanol mixture was added together with 617 µl of RNase free H_2O and proteinase K (Qiagen) stock solution (50 µl). The mixture was vortexed and tubes were incubated in a rotary oven, at 55 °C, for 1-3 hr. This allowed a vast majority of proteins (including RNases) to be digested and allowed contact of the mixture with any material which may have adhered to the side of the tube (see below). The sample was then centrifuged at 13000 rpm for 5 min and the supernatant transferred to a 15 ml tube. Another 1 ml of RLT/mercaptoethanol was added to this and the tube vortexed. This increases the salt concentration to favour RNA over DNA precipitation upon the addition of alcohol. 1 ml of 100% ethanol was applied and the mixture vortexed again. The samples were spun in several batches of 730 µl through Qiagen columns, at 13000 rpm, the flow-through decanted. DNase stock was made up containing DNase and RDD. 700 µl of RW1 buffer was applied to the spin columns and spun through at 13000 rpm for 15 s, the flow-through decanted and the step repeated in order to ensure proteinase K is washed out and so prevent reduction of the DNase activity in the next step. 80 µl of RDD/DNase mix (2.7 Kunitz units/µl) was carefully added to the middle of the silica matrix of the column for ¾ to 1 hr. This allowed the digestion of genomic DNA. RW1 buffer was applied to the spin columns and spun through at 13000 rpm for 15 s, followed by addition of RPE buffer (500 µl) and a 15 s spin at 13000 rpm. A further spin for 2 min with RPE buffer (500 µl) was carried out and the sample re-eluted in 50 µl DEPC-treated Millipore H_2O. 0.5 µl

glycogen (Roche), 3 M sodium acetate (0.1 volumes) pH 5.4 was added, followed by 100 % ethanol (2.5 volumes). Glycogen was added to aid RNA precipitation and for visualisation of the RNA pellet. The mixture was precipitated overnight at -20°C and spun the next day at 13000 rpm at 4 °C for 30 min. The pellet was washed with 70 % ethanol and spun again at 13000 rpm for 5 min. The sample was then allowed to air dry for 30 min and re-eluted in 20 µl of RNase free H_2O.

2.7.13 RNA quality control and quantification

It has been well established that in order to achieve reliable *real time* PCR results, good quality RNA is required i.e. non-degraded RNA. If RNA is partially degraded, then the cDNA synthesised will not be completely representative of the extracted RNA and misleading results can be generated (Bustin, 2002). It is important that equal amounts of RNA from the different tissue samples are used as template for the reverse transcription reaction used to generate the cDNA.

Nano LabChips for the Agilent 2100 Bioanalyser were used whereby each Nano LabChip is pre-loaded with a gel-dye mix to fill the microchannels. 1 µl of each RNA sample is loaded into one of twelve wells in the Nano LabChips obtained together with a standard curve (RNA 600 ladder). The dye contained within the microchannels intercalates with the RNA and an electropherogram plot of the RNA is obtained thus allowing 18S:28S determination and also the quality of RNA to be interpreted by the amount of interfering noise peaks between 18S:28S peaks. This method provides a more accurate determination of RNA quality and quantity over RNA gels.

2.7.14 Formaldehyde gel electrophoresis

Formaldehyde gels were used to assess both the quality and quantity of the RNA extracted (Fig. 2.8). The preparation of the RNA gel (1 % agarose, 1x MOPS, 0.7% formaldehyde) involved dissolving 1% of low melting point NuSieve GTG agarose (BMA products) in 88% (v/v) of RNase free H_2O. This was allowed to cool to ~55 °C and MOPS buffer was added to a 1x concentration (Eppendoff). Finally, deionised 37 % formaldehyde was added to a final concentration of 0.7% and the gel solution poured

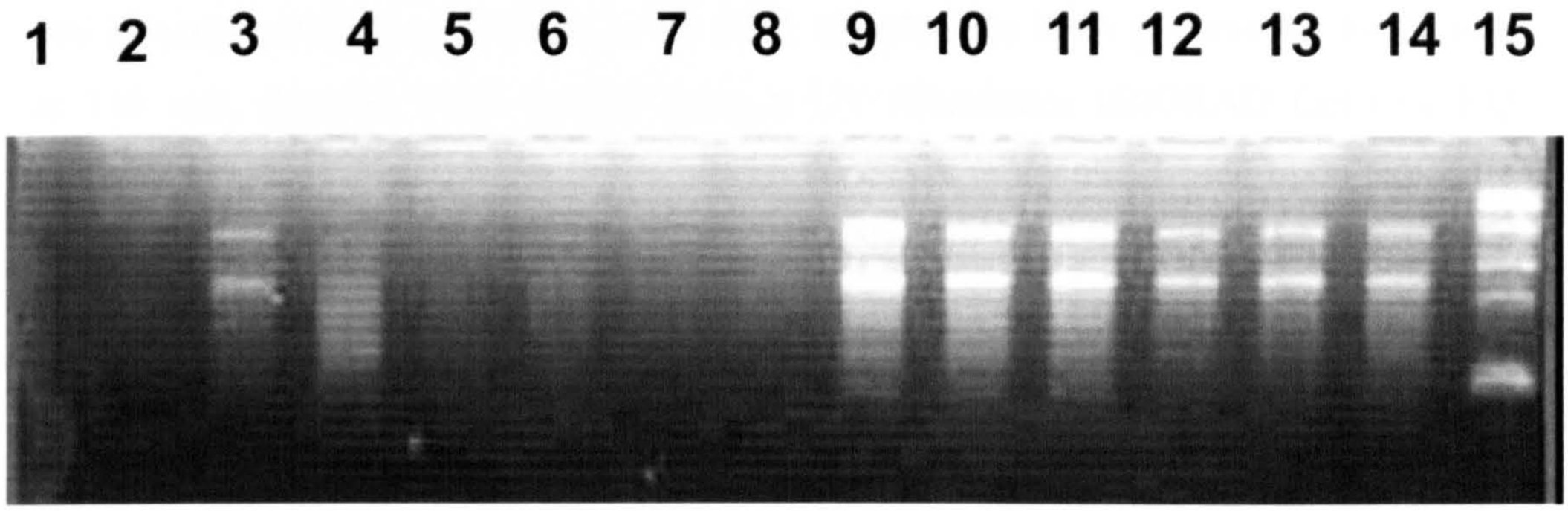

Figure 2.8 Freeze-dried atrial (AM1-8) and ventricular tissue (VM1-6) samples. Lanes 1-8, atrial tissue samples 1-8; lanes 9 - 14, ventricular samples 1-6; lane 15, RNA ladder. Note, only AM samples in lanes 3 & 4 are visible, the other AM samples are beyond the level of detection. All VM samples can be clearly visualised with good 18S:28S ratios.

into a pre-prepared plate and comb mould. The gel was allowed to set at 4 °C. It was then transferred to an electrophoresis tank containing running buffer (1x MOPS, 0.7 % formaldehyde). A mixture of 1x MOPS and 0.25 µg/µl EtBr was made up with 10x MOPS (40 µl), and ethidium bromide (10mg/ml; 10 µl). To the RNA sample (1 µl) the following was added: deionised formamide (10 µl), 37 % deionised formaldehyde, (3.3 µl), 1x MOPS and 0.25 µg/µl EtBr (2.5 µl) and RNase free H_2O (3.2 µl). The mixture was thoroughly vortexed and incubated at 55 °C for 15 min. The sample (20 µl) was mixed with loading buffer (43.5 % Glycerol, 2M EDTA, 0.02 % bromophenol blue), (2 µl) and loaded into the wells along side a 0.24 – 9.5 kb RNA ladder (Invitrogen) which had be prepared in the same way as the RNA sample. The RNA gel was ran for 20 min at 130 mA. Samples were viewed using a UV illuminator (BIORAD Gel Doc EQ system). Ethidium bromide intercalates with the RNA molecules which upon exposure to UV light emits fluorescence. The quality of RNA can be assessed by observing if the RNA bands present on the gel smear forwards. If so, this indicates that the RNA is partially degraded (Fig. 2.5, lane 4; Fig. 2.6, lane 1). If little smearing was present the RNA was considered to be of an acceptable quality. The quantity of RNA present in the sample could be estimated, as the amount of fluorescence emitted is proportional to the amount of RNA present. The amount of RNA present in the sample could be calculated by comparing the fluorescence emitted from the sample with the RNA ladder. This was done with Quantity One software.

2.7.15 RiboGreen RNA quantitation assay

In order to obtain accurate quantitation of RNA yields from small AVN samples the ribogreen assay (Molecular Probes) was used which provides fast and good estimates of RNA yields before generating cDNA. Standard curves were constructed by generating ribosomal RNA standards (0, 100, 500, 1000 and 2500 ng/ml) and measuring the fluorescence.

The LightCycler in fluorimeter mode (470 nm excitation, 530 nm emission) or the Flexstation (490 nm excitation, 515 nm cut-off and 540 emission; Molecular devices) were the instruments used to read fluorescent measurements of ribogreen. The standards were diluted in RNase free Tris EDTA (TE). Ribogreen was diluted 1:200 (High-range assay) or 1:2000 (low range assay) in TE and samples were loaded into glass capillaries (LightCycler) or 96-well plates (Flexstation), 10 µl 1:200 or 1:2000 ribogreen and 10 µl

standard (LightCycler), or, 25 µl 1:200 or 1:2000 ribogreen and 25 µl standard (Flexstation). Following 5 min incubation at room temperature fluorescence emissions were measured. Test samples of RNA were diluted appropriately in TE and prepared in the same way.

2.7.16 Reverse transcription (RT)

The RT step generates the first strand of cDNA from the extracted RNA which is used as the DNA input in the *real time* PCR reaction. It is therefore important that great care is taken with the RT step in order to achieve accurate quantification. The input for the RT for each sample was 200 ng of total RNA based on the ribogreen quantification since all samples had to be equivalent to the sample of the lowest yield (which was ~ 200 ng). The Superscript III First Stand cDNA Synthesis System (Invitrogen) was used with random hexamer primers, following the manufacturer's protocol. Random hexamer primers were chosen over Oligo-dT since there was a chance that the RNA we are using is 1) slightly degraded and therefore since the poly-A tail is highly likely to be cleaved then oligo-dT would fail to prime, and 2) some of the RNA molecules are likely to have a high secondary structure which is more likely to inhibit oligo-dT priming than random hexamer 3) we only need to generate small amplicons during *real time* PCR so only require short stretches of cDNA which random hexmaer priming would provide better chance of obtaining over oligo-dT priming. All RNA samples which were to be compared through *real time* PCR underwent RT at the same time using the same master mix. The cDNA samples were diluted 1 in 10 with molecular biology grade H_2O and stored at -80 °C.

This system was chosen because the Superscript III reverse transcriptase contains a point mutation which disables RNase H activity and is more active than other reverse transcriptases at higher temperatures which allows for the reverse transcription of mRNAs with high secondary structures. This prevents degradation of the RNA template during first strand cDNA synthesis, allows the RT to be carried out at higher temperatures and results in a greater yield of cDNA.

Random hexamers were used to prime the RT reaction even though it has been argued that these are less sensitive than the use of specific primers or oligo-dT priming (Lekanne Deprez et al., 2002). For this study, where the aim was to screen the cDNA for many different transcripts, specific priming would not be suitable. In the case of specific priming, a separate RT reaction would have had to be performed for each transcript which requires too much RNA. This would have required further dilution of the RNA and resulted in a low chance of success for the experiment. Oligo-dT priming was deemed not to be appropriate, as it requires the 3' polyA tail to be present. This is susceptible to degradation that would lead to under-representation of that mRNA in the cDNA. In addition, the reverse transcriptase can 'fall off' the RNA when it encounters strong secondary structures, so that if the mRNA is primed for RT at the 3' end of the mRNA then the RNA downstream of the secondary structure will not be transcribed. In addition, ribosomal RNA can not be used as a housekeeper gene with oligo-dT primed cDNA as it does not have a 3' polyA tail.

2.7.17 *Real Time* PCR

Real time PCR measures the fluorescence emitted during the reaction as an indicator of the DNA amplified during each PCR cycle (i.e. in real time). The fluorescence is generated by a reporter dye. The signal increases in direct proportion to the amount of DNA in the reaction. Recording the amount of fluorescence emitted at each cycle enables the monitoring of the PCR reaction during the late exponential phase where the first detectable increase in the amount of target template occurs. The greater the starting copy number of cDNA target, the sooner a significant increase in fluorescence occurs (Fig. 2.11).

In this study two different fluorescent reporter systems were used:

2.7.18 TaqMan Probes

A TaqMan Probe is a labelled oligonucleotide which is usually 20 to 25 bases in length and is specific for the DNA sequence between the two primer sites on the target DNA fragment (Fig. 2.9). The probe is labelled at the 5' end with a fluorescent group, while a quenching group is attached to the 3' end. The TaqMan probe is added to the PCR along

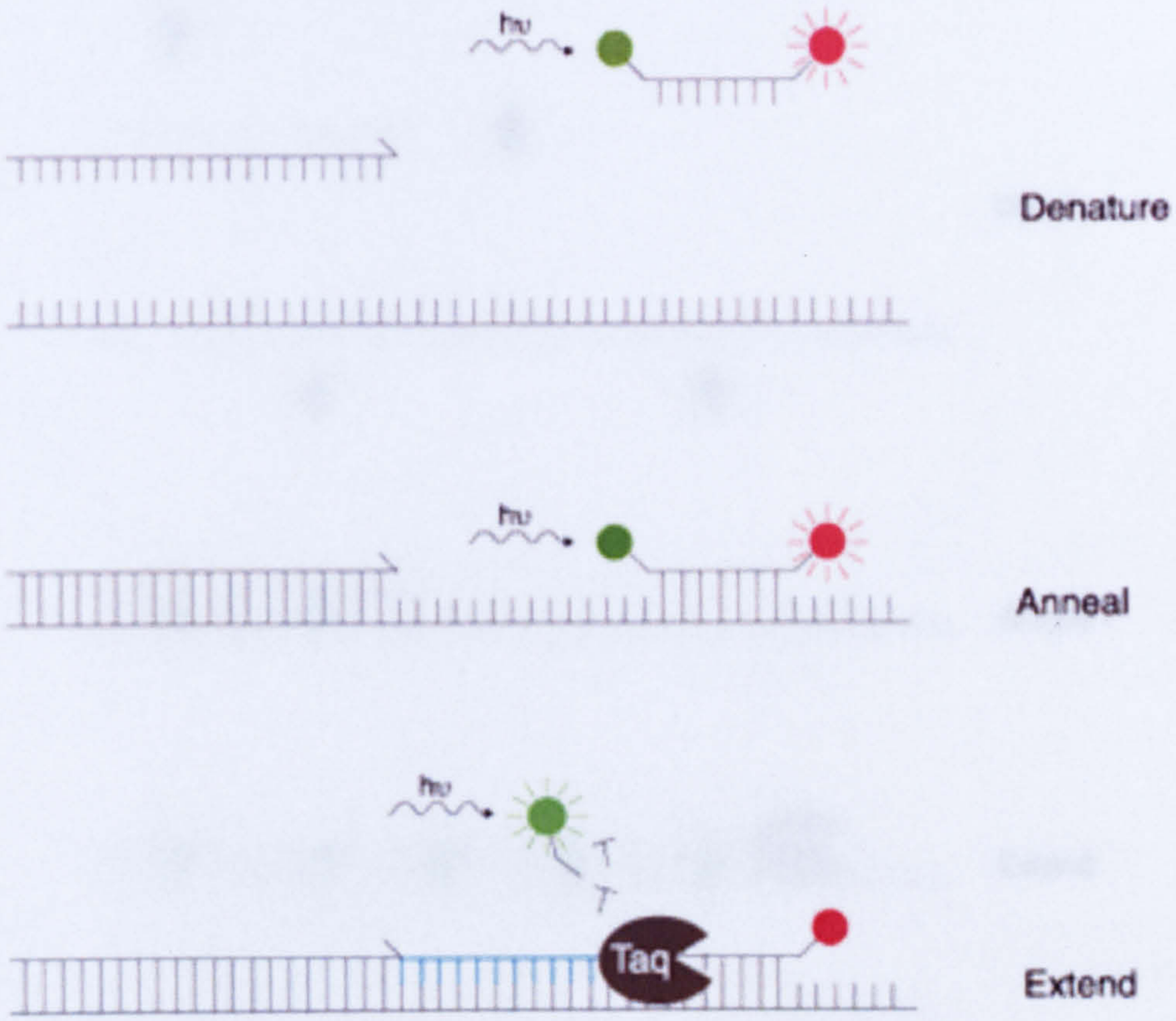

Figure 2.9 A probe specific to the amplicon sequence is designed with the reporter and quencher dye system. When the probe is intact (Denature) there is no fluorescence since the quencher lies close enough the reporter dye to quench its fluorescence. However, during extension (extend) the Taq polymerase cleaves the probe thus allowing the reporter dye to move away from the quencher and emit fluoresence.

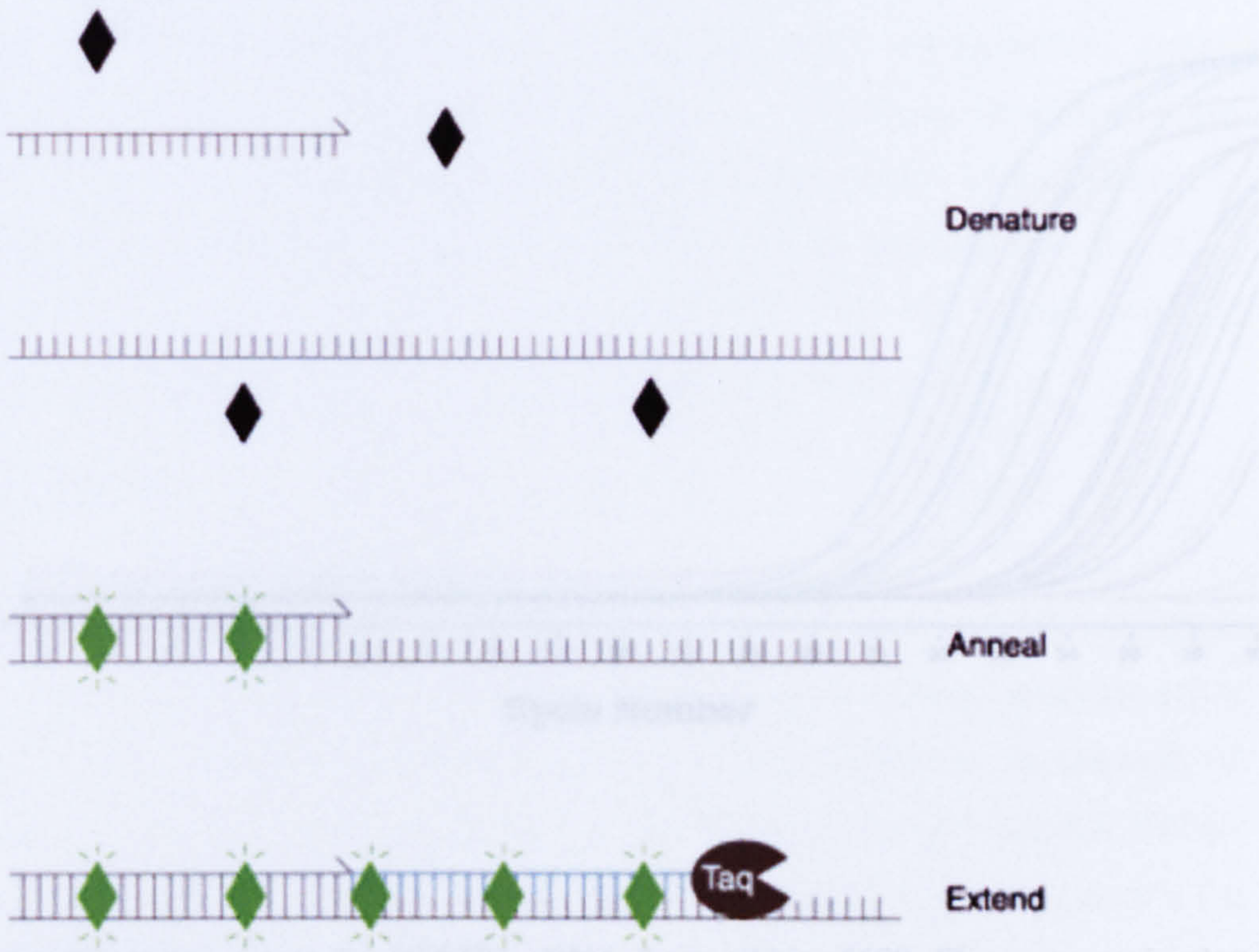

Figure 2.10 SYBR green PCR detection system. SYBR green molecules only fluoresce when bound to double-stranded DNA therefore during the denaturation phase no fluorescence is emitted. During annealing and extension more SYBR green molecules can bind and fluoresce, therefore fluorescence in a reaction is proportional to the amount of double-stranded DNA present. This allows us to measure DNA amplification in real-time.

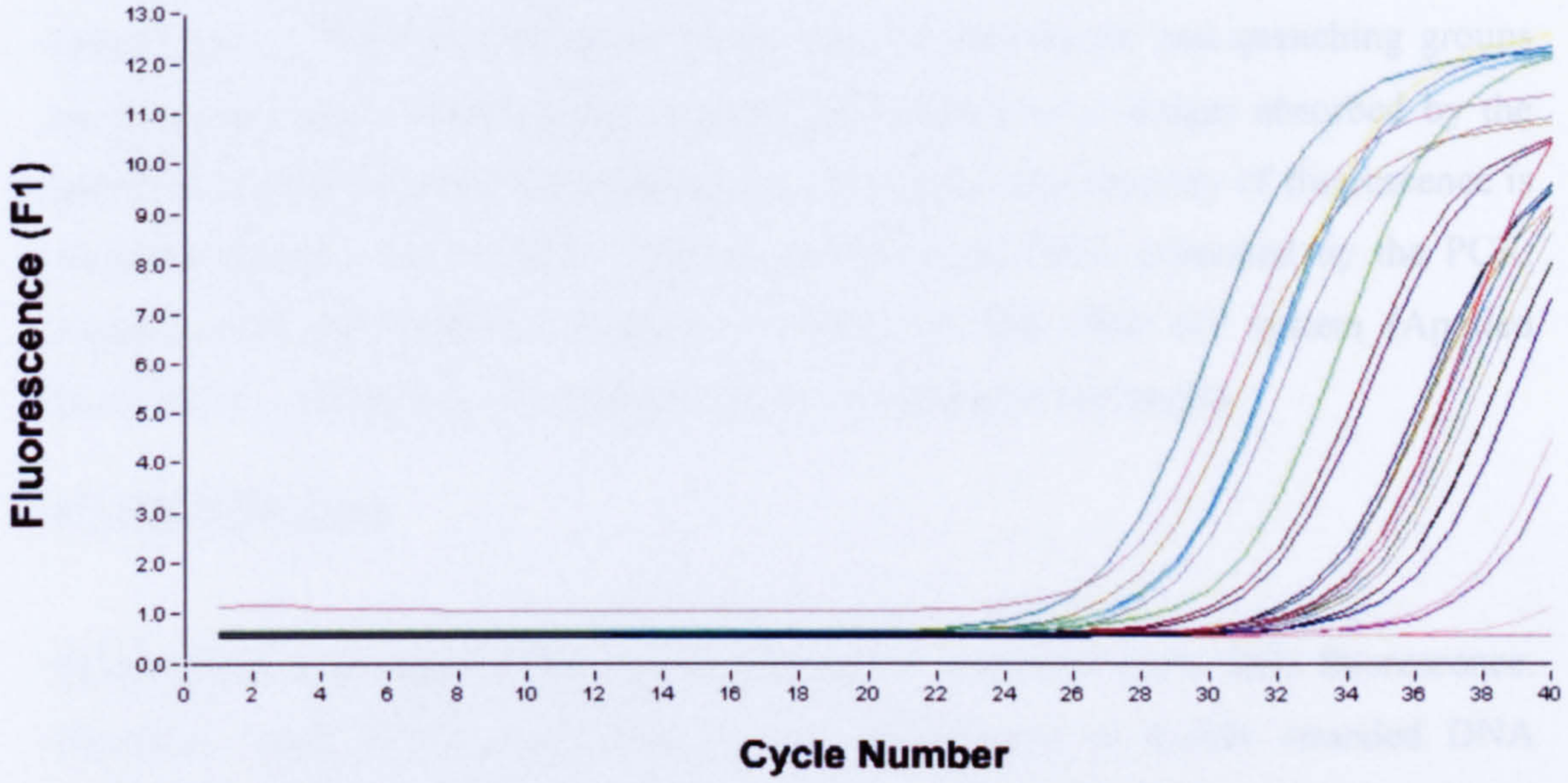

Figure 2.11 Amplification curves for KChIP2 cDNA from rabbits 5678. Fluorescence is plotted against cycle number. The greater the abundance of the transcript in a particular sample the lower the cycle number. Exponential phases of amplification are clearly visible.

with the primers required to amplify the specific DNA fragment. When both the fluorescent and quenching groups are present in close proximity to each other, as is the case on the intact probe, any fluorescence released by the fluorescent group is absorbed by the quenching group. As the PCR progresses, it generates more target DNA for the probe to hybridise to, which occurs right after the denaturing step of the PCR cycle. During the next extension phase, the 5' to 3' exonuclease activity of the DNA polymerase degrades the hybridised probe, thus the fluorescent and quenching groups are no longer held close together and the fluorescence is no longer absorbed by the quencher resulting in increased fluorescence emissions. The intensity of fluorescence is therefore directly proportional to the amount of target DNA generated by the PCR. TaqMan *real time* PCR was carried out using an ABI 7900 HT system (Applied Biosystems). See table 2.3 for primers and probe sequences for targets.

2.7.19 SYBR-green

SYBR-green is an agent which, when unbound in solution, emits little fluorescence. However, when SYBR-green binds to the minor grove of double stranded DNA (dsDNA), it emits a strong fluorescent signal (Fig. 2.10). Therefore, the intensity of fluorescence emitted is directly proportional to the amount of dsDNA present. SYBR-green *real time* PCR was performed with a LightCycler (Roche). See table 2.2 for a list of primer sequences and targets.

2.7.20 Primer and probe design

For accurate quantification, it is important that the PCR primers used amplify the desired DNA fragment both specifically and efficiently. To achieve this, the following steps were followed when designing PCR primers:

1. The target transcript nucleotide sequence was compared to the entire Genbank database using BLAST (Altshul and Lipman, 1990). This identified regions which were specific for the target of interest thus preventing non-specific amplification.
2. These stretches of unique sequence were also assessed for the ability to form RNA secondary structures using the mfold program (Zuker, 2003). This is important as it has been shown that an RNA with strong secondary structure in the fragment chosen for PCR is not efficiently reverse transcribed (Pallansch et

Table 2.2 LightCycler primers and PCR conditions

Target transcript	Accession number	Primer sequence 5'- 3'	Fragment length (bp)	Annealing Temp. (°C)	Primer conc. (µM)	$MgCl_2$ conc. (mM)
28S****	AF460236	GTTGTTGCCATGGTAATCCTGCTCAGTACG TCTGACTTAGAGGCGTTCAGTCATAATCCC	133	64	1 1	2
ANP*	M12046	GGAACCGAGAGGAAGGAAGA CCAGAATGCCAGACAGAAGAG	111	55	1 1	4
Ca_v 1.2*	X15539	GAGTCACCCTCCCACGAGAA GCAGTGTTGTTGGCATTGTTG	101	57	1 1	2
Ca_v 1.3*	DQ220009	AGGTAGAGCGGTCCGAGTCCTT CTCTGCTTGTCGCTGTCTTTGTT	162	60	1 0.5	4
Cx40	DQ242483	GAGGAAGTGAACGGCAGGA CAGGAAGATCCGTAGAGCAG	129	54	1 1	2
Cx43	AY382590	CGTTTACACCTGCAAAAGAGACC CCACCAGCATGAAGATAATGAAGA	98	57	2 2	2
Cx45	DQ242487	ATGTACCTGGGCTATGCCATTC GGTCCTCTTCATGGTCCTCTTCT	145	57	0.5 2	2
ERG*	U87513	GGCTATCCTGGGGAAGAATG GTCCCGGTGGATCTTGTG	121	55	0.5 0.5	4

HCN1*	AF168122	TCAGGTTTTATTGGGATTTAATAATGCT TGGTGTTGTTGTCTGTTCTGTAAAGA	101	52	0.5 0.5	2
HCN4*	AB022927	GCTGTCCTGTCGTCTTGTTTCTC CGGTTATTGTTGGTGGTGTATCTC	74	57	2 2	2
KChIP2 **	DQ218451	AACAACTGCAGGAGCAAATCAAG GGTGTCAAAGGCATTGAAGAGAA	182	57	2 2	2
Kir2.1*	AF021138	TCATCAACGTGGGTGAGAAG CCAAAACACACAGCCAAAAA	140	55	0.5 0.5	2
Kir2.2*	AJ29021138	TTCGTCAAGAAGAACGGACA AAGGCCAGCGAGAAGATAAG	137	55	0.5 0.5	2
Kir6.2 ****	AF006262	TTTCCTCCGCCTTCCTTTTCT ATCATGAGCCCTACGATGTTCTG	127	57	2 2	2
Kv1.4*	AF493544	TCCTCTTCATTGGGGTCATC AGCTGCGTCTGTTCCTCATT	286	55	1 1	2
Kv1.5*	AF056943	AGCTGCTTGTGCGTTTCTTTG AGGGTGATGAAGTAGGGGAAGATG	103	60	1 1	4
Kv4.2 *	AF508735	GTTCGCTGAGTGGTGTCTTG TTGTCTGCTCGTTGGTTTTG	94	55	0.5 0.5	2
Kv4.3	AF198445	CTTCTACCGCACCGGCAAGCT TCCTGGTTGTTCTCCGAGTCGTT	186	55	1 1	2

KvLQT1	AJ291316	AGGAGCTGATCACCACCCTGTA ATCTGCGTAGCTGCCGAACTC	124	58	1 2	2
minK	L41659	CTACATCCGCTCCCAGAAACT GCTGGTTTTCAAGGACGTAGC	139	59	2 0.5	2
$Na_v1.1$	DQ242485	GCAGGCCAATGTCCAGAA AGCCCAGCTGAAGGTATCAA	90	55	1 1	2
$Na_v1.5$	DQ242484	TTGTGGACCTGGGCAATG TCTTGAGGCCTGCAATGACT	87	56	1 1	2
NFM*	Z47378	GGTGAGCAGGAAGAAGGAGA ACTGGTGATTTTGGCACAGG	176	55	2 2	2
NCX1	AY33398	TCCATGCTAGAGACCATCCTGTT CTTGGTGTGTTCTCCCAAGATG	143	56	0.5 0.5	2
RYR2*	OCU50465	GTGTTGCCTCTCCACCTCTC CCTCACCTGTGGTGTCCTCT	80	55	2 2	2
SERC2A ***	X02814	TGAAAATGCAATTGAAGCCCT ACACTCTTTCTGTCCTGCCGA	75	56	1 1	2
SUR2A*	AF087468	CGTACTCCGAGAGGGAACTTTG ATCCTGACGGTTCATGAGTGTTT	88	57	2 2	2

Primers designed by: * = Dr. J. Tellez, ** = Dr. G. Graham, *** = Prof. G. Smith, **** = Dr. R. Billeter.

Table 2.3 Primers, TaqMan probes used with ABI 7900 HT

Target transcript	Accession number	Primer sequence 5'- 3'	TaqMan probe sequence 5'-3'	Fragment length (bp)	Primer conc. (nM)
RYR3	X68650	CACCAAAGCACAGAGGGACA AAGACGAGACGTCGCAGGAG	N/A	99	900
GAPDH	L23961	GATTCCACCCACGGCAAGT CGCTCCTGGAAGATGGTGAT	CCACGGCACGGTCAAGGCTGA	92	900 900

al., 1990). Such a fragment will at best be under-represented in the cDNA or in a worse case yield aberrant relative quantities. Therefore, sequences with generated secondary structures for which mfold calculated free energies less than -16 kcal/mol were not considered for primer design.

3. For primers used with the SYBR-green detection system on the LightCycler, primer design was undertaken with the aid of Primer 3 software. For the design of primers and probes used for the TaqMan quantification system on the ABI 7900 HT system Primer Express software was used. The following parameters were considered important:
    a. Size of PCR fragment: A fragment size of ~100 bp was considered optimal, larger PCR fragments may amplify at lower efficiencies and it may be difficult to differentiate between primer dimers and specific PCR products of shorter lengths using the melting curve.
    b. Primer size: The primer should be made up of 23 bases to optimise accuracy and specificity (Beasley et al., 1999).
    c. T_m of primer/probe: This is the temperature at which half of the primer/probe and target hybrids will dissociate. The optimum temperature has been determined as 62 °C for primers (Beasley et al., 1999) and 10°C greater than the primers T_m, for probes (Applied Biosystems, 1999).
    d. GC content of the primer/probe: G/C bonds are stronger than A/T bonds. The optimum GC content is considered to be ~50 %, which should enable a primer T_m of 62 °C to be achieved. Any greater GC content can lead to non-specific binding of the primer/probe.
    e. No GC clamp: The final two bases at the 3' end should not both be G or C, as this can more frequently lead to mispriming and primer dimers.
    f. Minimal 3' self complementarity: Both primers should not contain any sequence which is complementary to the final three base at the 3' end of each primer. This prevents the formation of primer dimers, which occur when the 3' ends of the primers bind to complementary sequences within the primer allowing DNA polymerase primer extension to occur. Primer dimer amplification competes with the specific PCR for regents and so can reduce the efficiency of the specific reaction and hence the accuracy of the *real time* PCR.

g. DNA secondary structure: DNA sequences around the target sequence of the primers were checked for secondary structures using the mfold program; these secondary structures can inhibit primer binding and therefore prevent efficient amplification of product.

The primers were synthesised by MWG Biotech and the probes were synthesised by Applied Biosystems. It should be noted that the performance of primers can vary depending on the source of synthesis. The primer sequences and PCR conditions used with the SYBR-green detection system on the LightCycler are listed in Table 2.3 and the sequences of primers and probes used with the TaqMan detection system on the ABI 7900 HT system are listed in Table 2.3.

2.7.21 Primer optimisation

The optimal PCR primer and Mg^{2+} concentrations were determined with rabbit whole heart cDNA diluted 1 in 50, which was prepared as described above to 2.3. Optimal conditions should amplify the specific product with the lowest threshold cycle (C_t) value without non-specific product amplification such as primer dimers. The specificity of the reaction was assessed using the melting curve and running the PCR products on a 2% agarose gel and sequencing of products in some cases.

2.7.22 Primer concentration

The concentration of the primers used for *real time* PCR is a key variable for successful quantification. If the primer concentration is too high it can result in primer-dimer formation. If the primer concentration is too low, the sensitivity of the PCR may be compromised. Therefore, for each transcript, the optimal primer concentration was determined by testing a range of primer concentrations. The primer concentrations tested with LightCycler were between 0.5 and 2 μM and for the ABI 7900 HT Sequence Detection system 50 and 900 nM. The resulting optimal primer concentrations are shown in Tables 2.2 and 2.3.

2.7.23 Mg^{2+} concentration

DNA polymerase is active at 2 mM Mg^{2+} (Lawyer et al., 1989). It is advantageous to optimise the Mg^{2+} concentration, as Mg^{2+} is a key ionic component of the PCR reaction mixture. It has two roles in PCR: firstly to promote DNA/DNA interactions and secondly to form the complexes with dNTPs that are the actual substrates for Taq Polymerase. When Mg^{2+} is too low, primers are less likely to anneal to the target DNA. When Mg^{2+} is too high, the base pairing can become too strong and can lead to non-specific primer binding. Therefore, between 2 and 6 mM Mg^{2+} concentrations were tested with each primer pair for the LightCycler. The resulting optimal concentrations are shown in Table 2.2. The master mix used with the ABI 7900 HT system already contained Mg^{2+}, therefore the Mg^{2+} concentration was not adjusted for these assays.

2.8 Specificity of PCR

2.8.1 Melting curves

In contrast to the Taqman probe, which is specific for a sequence, SYBR-green will bind to all double stranded DNA present. It is important for accurate quantification with SYBR-green that the PCR is only amplifying the specific PCR fragment. This can be determined by running a melting curve after the PCR reaction, where the DNA products are denatured. Different DNA species will denature different temperatures, due to varying characteristics such as fragment length and base composition. The temperature at which the DNA denatures can be determined as the mid-point of the sigmoid curve produced by the SYBR-green fluorescence with increasing temperature. Its second derivative is a peak in a Gaussian curve (Fig. 2.12).

2.8.2 DNA gel

The specificity of the PCR can also be checked by running the PCR products on an agarose gel alongside a DNA ladder to determine that only one DNA fragment has been generated and that it is of the correct size. This is especially useful when using TaqMan probes since a melting curve can not be performed with that system since the detector is also cleaved. However with SYBR-green, melting curves of two products can have similar profiles, so that running the PCR products on a gel gives a more accurate view of the products generated by the PCR.

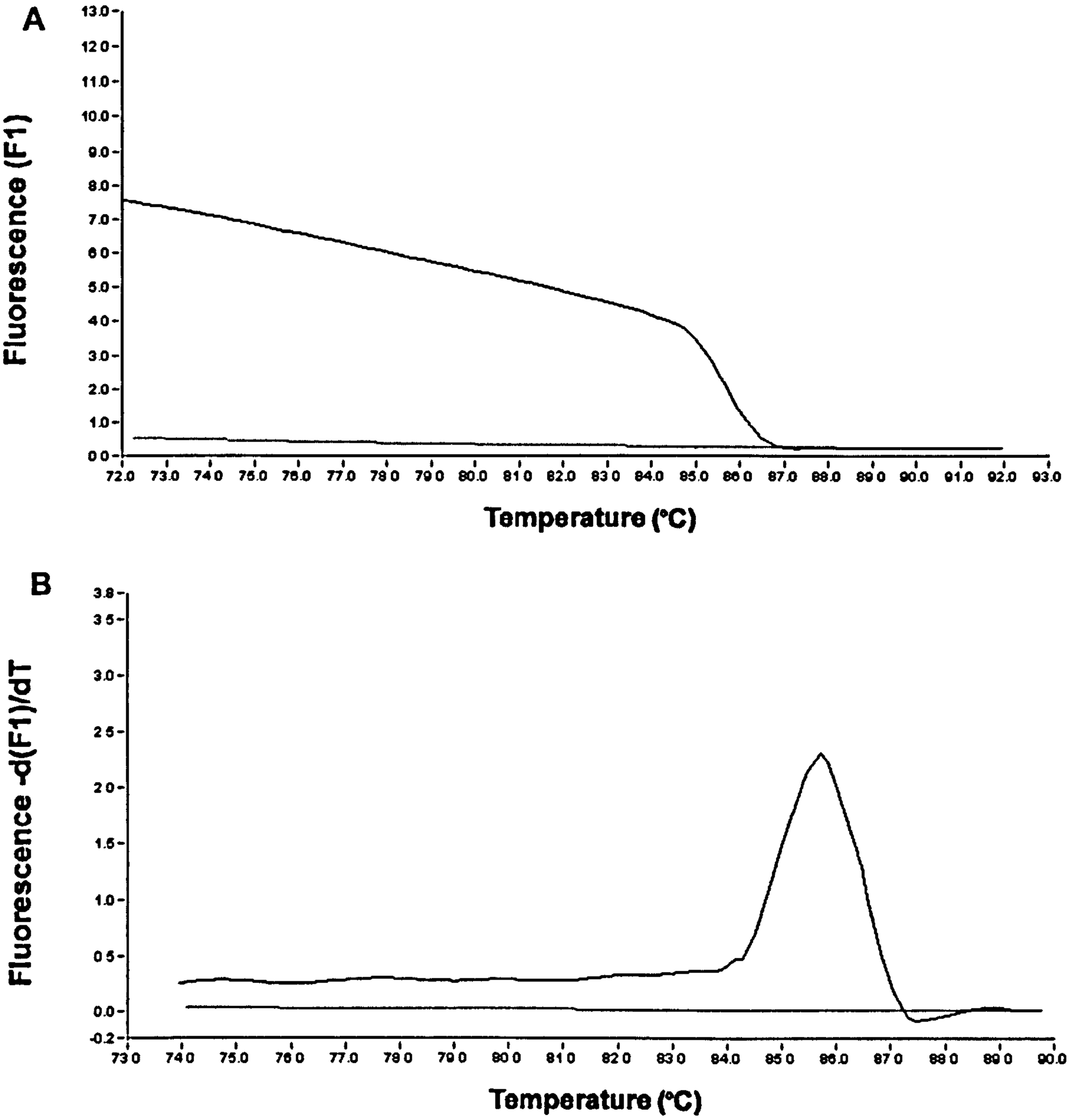

Figure 2.12 Melting curve (A) and peak (B) for KChIP2 cDNA from AM8 and water control. Fluorescence is plotted against temperature. A, As the temperature rises sample AM8 the bound SYBR Green molecules bound to the double-stranded DNA gradually fall off as the melting point of the cDNA is reached thereby producing a decline in fluorescence. Note, fluorescence is zero for water control as no double-stranded DNA is generated. B, the derivative of fluorescence over time is plotted against temperature. A peak can be seen when the melting point of the cDNA fragment is reached. Note, since no cDNA is present in the water control, no peak is seen.

The DNA gel is composed of 2 % agarose (BDH), 0.5x TBE (45 mM Tris base, 45 mM Boric acid, 1mM EDTA) and 0.7 µg/ml ethidium bromide. The DNA samples and 100 bp DNA ladder (New England BioLabs) were mixed with 3 µl of gel loading buffer (43.5 % Glycerol, 2M EDTA, 0.02 % bromophenol blue) to a final concentration of 33% Glycerol, 1.5m EDTA, 0.015% bromophenol blue, and loaded into individual wells in the gel. The gel was run in 0.5x TBE running buffer for 18 min at 200 V. The DNA bands were then scanned using a UV illuminator (BIORAD Gel Doc EQ system). When the amount of DNA present on the gel required quantifying, this was done by comparing the fluorescence of the DNA band of a known concentration (from the DNA ladder) with the DNA band of an unknown concentration using Quantity One software.
Real time PCR protocol

2.9 LightCycler

10 µl reactions were set up consisting of 1x SYBR-green I master mix (Roche), 1 µl of cDNA template, between 2 and 6 mM $MgCl_2$ and 0.5 and 2 µM of each primer. The following PCR protocol was set up: hot start, 10 min at 95 °C; 40 cycles of: denaturation (28S *real time* PCR was 23 cycles), 15 s at 95 °C; annealing, 5 s at optimal temperature determined during optimisation of primers; extension, 1 s per 25 bases of product size at 72 °C. At the end of the final cycle a melting curve was generated by heating to 95 °C. Fluorescence was measured at the end of each extension step and continuously throughout the melting curve. The reaction was carried out in glass capillaries (Roche), which have a large surface area to volume ratio that allows rapid heating or cooling between cycles.

2.10 ABI 7900HT

50 µl reactions were set up, consisting of 1x TaqMan Universal PCR master mix (Applied Biosystems), 1 µl of cDNA template, 50, 300 or 900 nM of each primer and 50 nM TaqMan Probe. The following PCR protocol was used: i) AmpErase uracil-N-glycosylase activation, 2 min at 50 °C. ii) hot start, 10 min at 95 °C. iii) 40 cycles of: denaturation, 15 s at 95 °C; annealing/extension, 1 min at 62 °C. The PCR was carried out in a MicroAmp optical 96-well reaction plate (Applied Biosystems) sealed with an optical adhesive cover (Applied Biosystems).

2.11 Relative quantification using a calibrator sample

To determine the relative number of target transcript cDNA molecules present in each sample cDNA, a calibrator sample which contains a mixture of cDNA which is representative of each tissue type, was run alongside the samples in the PCR reaction.

2.12 *Real time* PCR quantification

The following equation was used to calculate the relative abundance of cDNA in each sample for ABI 7900HT (since a reaction efficiency of 2 is achieved):

No. of input molecules for S_1 (target) x 2^{Ct} = No. of molecules generating fluorescence

Therefore, for a given fluorescence (X):

X = No. of input molecules for S_1 (target) x 2^{Ct1} = No. of input molecules for S_2 (control) x 2^{Ct2}

Rearrange equation so that:

$$X = \frac{\text{No. of input molecules for } S_1 \text{ (target)}}{\text{No. of input molecules for } S_2 \text{ (control)}} = \frac{2^{Ct1}}{2^{Ct2}} = 2^{Ct1-Ct2} \text{ or } 2^{\Delta Ct}$$

We use the actual calculated efficiency for the LightCycler, therefore:

$$X = E^{\Delta Ct}$$

The efficiency was determined from the fluorescence recorded at the end of each elongation step, using the following equation:

$$E = \sqrt{F_n/F_{n-2}}$$

Where F is fluorescence measured and n is cycle number.

To correct for variation of RNA input into the RT, the number of cDNA molecules quantified was normalised to the average of the number of molecules quantified for three housekeeper genes namely, GAPDH, 28S and Na/K pump.

2.13 Statistical analysis

Significant differences between the number of cDNA molecules of a specific transcript from a certain tissue were identified using One-way ANOVA. Statistical comparisons for individual variables were done by Student-Newman-Keuls method.

2.14 *In situ* hybridisation (ISH)

ISH is a method by which specific mRNA sequences can be detected within the cytoplasm of a cell, through hybridising the sequence of interest to a labelled complementary strand of a RNA probe. ISH is a very useful technique for investigating regional variations in the expression of a specific mRNA within tissues.

When the ISH technique was first developed, the only way to detect nucleotide probes was by labelling them with radioisotopes and detecting by autoradiography (Gall and Pardue, 1969; John et al., 1969). This method had several disadvantages: long development periods (several weeks); relatively short shelf life of the radiolabelled probe; safety issues when working with radioactive probes; and the scatter of the radioactive signal prevented high resolution localization of the probe. More recently, non-radioactive labelling and detection systems have been developed for ISH, such as digoxigenin labeled probes, which have the same sensitivity of radiolabelled probes (Komminoth, 1992) and overcome the above mentioned problems. For this study, digoxigenin labelled uridine was used to label the probes. An anti-digoxigenin antibody was then be used to detect it. Digoxigenin is a steroid isolated from the digitalis plant. As its blossoms and leaves are the only known source of digoxigenin, the chances of the anti-digoxigenin antibody, for which digoxigenin is a potent hapten, cross-reacting in animal tissue is very low (Farquharson et al., 1990).

Different types of nucleotide probes can be used with ISH, such as oligonucleotide probes, single stranded DNA probes and/or double stranded DNA probes. For this study, RNA probes (riboprobes) were used, since RNA-RNA hybrids are more stable at higher temperatures and allow more stringent hybridisation conditions and are cheaper than their DNA probe counterparts. In addition, RNA-RNA hybrids are also resistant to RNase degradation, which allows RNase to be used to destroy any unhybridised probe after hybridisation, thus reducing the potential for a background signal.

2.14.1 Riboprobe synthesis

Riboprobes were synthesed by *in vitro* transcription of the corresponding DNA fragment by the SP6 or T7 RNA polymerase. Therefore, to successfully synthese a riboprobe, a template DNA fragment of the desired sequence is required to be flanked by SP6 and T7 RNA polymerase promoter sites to initiate RNA transcription.

2.14.2 Template DNA synthesis

The DNA required for the synthesis of the riboprobe can be generated through PCR. The primer design for the PCR follows the same rules as described in section 2.7.20, except that the required PCR fragment length is preferably ~500 bp. cDNA synthesised in the same manner as described previously was used as an input into the PCR. Two PCR methods were used during the course of this study. Both approaches used the Whatman Biometra thermocycler.

2.14.3 Standard hot start PCR

The PCR was carried out in a 50 µl reaction volume consisting of the following: 1x Promega PCR buffer, $MgCl_2$ (2 mM), forward and reverse primers (0.5 µM), cDNA (2 µl), dNTPs (0.2 mM), Promega Taq polymerase (2.5 U). Taq polymerase was added while the reaction temperature was held at 80 °C for 3 min, which occurred after the initial 3 min 94 °C denaturation step in order to prevent primer dimer formation as the reaction mixture heated to 94 °C. The PCR then followed a set cycle programme for 20-40 cycles: denaturation, 30 s at 94 °C; annealing, 45 s at 5 °C below primer T_m; extension, 75 s at 72 °C.

2.14.4 AccuPrime PCR

The AccuPrime master mix contains an accessory protein which inhibits non-specific hybridisation of the PCR primer during every cycle of the PCR. This should increase the specificity and yield of the PCR. The PCR was carried out in a 25µl reaction volume consisting of the following: 1x Invitrogen AccuPrime Super Mix I, forward and reverse primers (0.5 µM), cDNA (1 µl). The reaction mixture underwent an initial denaturation step (2 min at 94 °C) and then followed a set cycle programme for 20-40

cycles: denaturation, 30 s at 94 °C; annealing, 45 s at 5 °C below primer T_m as stated in Table 2.3; extension, 75s s at 68 °C.

2.14.5 Addition of RNA polymerase promoter sites

Once the correct DNA fragment has been amplified by PCR, RNA polymerase promoter sites must be added to the ends of the DNA fragment to enable the transcription of DNA to synthese the riboprobe. I found it advantageous to clean the PCR amplified DNA fragment using the PCR purification MinElute kit (Qiagen) before it was manipulated further. The concentration of this purified DNA was determined.

2.14.6 Lign'scribe non-cloning promoter addition

Lign'scribe involves the ligation of a T7 promoter sequence to the ends of the DNA fragment, followed by PCR amplification of the ligated DNA fragments with the T7 promoter in specific orientations. In an attempt to increase ligation efficiency, both S1 nuclease and proteinase K treatments were originally tried before ligation to create blunt ends and remove the *Taq* polymerase from the ends of the DNA fragment. However, these pretreatments were determined to have no beneficial effects on the ligation therefore the manufacturer's (Ambion) protocol was followed. PCR amplification of the ligated fragments was often problematic, marred by the generation of DNA fragments of incorrect size and band smearing (Fig. 2.11). In some cases, this could be alleviated by extracting the specific DNA band from a DNA gel as described below, and reamplifying the DNA through PCR. The PCR conditions for the amplification of the lign'scribe ligated DNA fragments were the same as those described in section 2.14.3, a 55 °C annealing temperature was used.

2.14.7 pGEM-T Easy vector system

An alternative approach for adding RNA polymerase promoter sites to the DNA fragment was provided by the pGEM-T Easy vector system. This involved cloning the DNA fragment into the pGEM-T Easy plasmid where the multiple cloning site was flanked by the T7 and SP6 promoter sequences (Fig. 2.13).

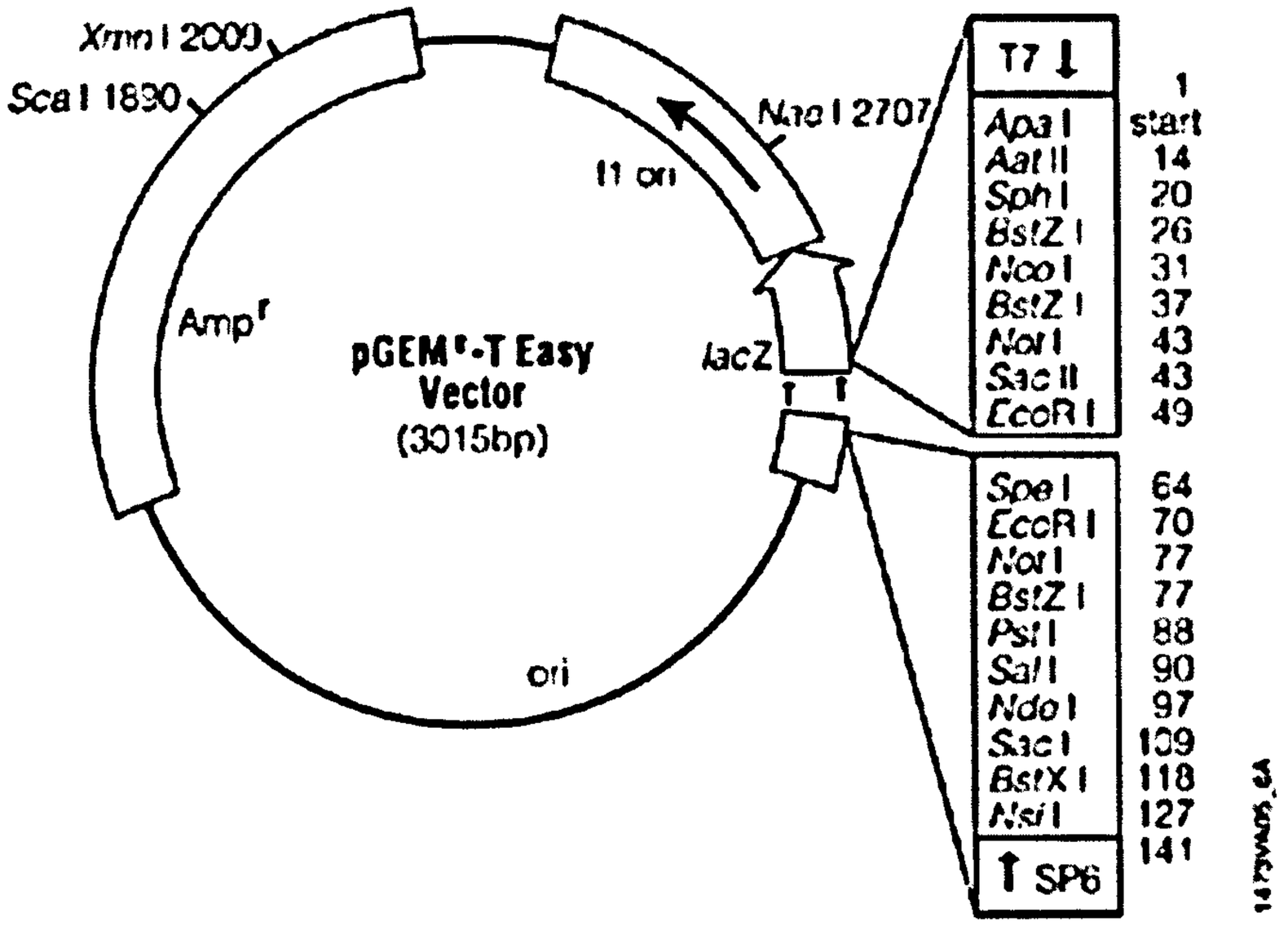

Figure 2.13 p-GEM T-easy vector used to generate riboprobes. Once the insert has been ligated into the vector it can be sub-cloned and thus amplified several fold in colonies. Furthermore, the target insert can be manipulated using the various restriction enzyme recognition motifs to cut the fragment, PCR amplified using M13 forward and reverse primer sites, or used to generate riboprobes using the T7 or SP6 RNA polymerase recognition sites.

2.14.8 Ligation

DNA fragments were ligated into pGEM-T Easy plasmids (Promega) according to the manufacturer's protocol. The plasmid had been cut by the manufacturer, adding a 3' terminal thymine to both ends producing complementary ends to the adenine overhangs normally present on the PCR DNA fragment.

2.14.9 Transformation of competent *E.coli* bacterial cells

10 ng of DNA, in a 2 µl volume, was mixed with 50 µl of JM109 competent cells (Promega), gently mixed and left on ice for 20 min. The mixture was then heat shocked for 45-50 s at exactly 42 °C (this allows permeabilisation of the cell membrane allowing uptake of the plasmid DNA). Following heat shock, the mixture was left on ice for 2 min, mixed with 950 µl of SOC medium (Flowgen) and incubated for 1.5 hr at 37 °C while shaking at 150 rpm. The transformed cells were then evenly spread out on LB plates (containing: ampicillin, 100 µg/ml; IPTG, 100 mM; X-gal, 50 mg/ml) and incubated overnight at 37 °C to allow the formation of individual bacterial colonies.

2.14.10 Selection and screening of colonies

The presence of amplicillin on the LB plates only allows cells that have been transformed with the intact pGEM-T Easy plasmid to survive, multiply and form colonies, as the pGEM-T Easy plasmid contains an ampicillinase gene which confers amplicillin resistance on the host bacteria. As a result, all colonies present on the plate should contain the plasmid.

To select a colony that contains plasmid with the PCR DNA fragment, blue-white screening is utilised. This involves the inactivation of the *lacZ* gene, on the pGEM-T Easy plasmid when the PCR DNA fragment is inserted into the gene sequence (Fig. 2.13). The *lacZ* promoter is activated by the IPTG present on the LB plates. In case of an uninterrupted *lacZ* gene this leads to the synthesis of an enzyme which uses X-gal as a substrate to synthese a blue product. Insertional inactivation of the *lacZ* gene

Table 2.4 Primers and PCR conditions used to generate DNA template for riboprobe synthesis

Target transcript	Species	Accession number	Primer sequence 5'- 3'	Fragment length (bp)	Annealing Temp. (°C)	No. of PCR cycles
ANP	Rabbit	M12046	CAAGCACTAAGTGAGCAG CGACTCGATGCAATGAGA	385	53	30
$Ca_v1.3$ Short 5'	Rabbit	-	CAGCAGAYCAAYACCACNCA GCRTTATTGAGATTGGCATTTG	179	56	35
$Ca_v1.3$ Short 3'	Rabbit	-	GACAARCAGAGGAGTGCNGAC TCNCTGTAGCCAGGACCAAA	260	62	35
$Ca_v1.3$ Long 1	Rabbit	-	AATTCGGTGTGTCATAACCATCA ATCGGCGATTTCGTATTTTGTC	1070	55	35
$Ca_v1.3$ Long 2	Rabbit	-	ATAGGAAAGCAACTTCCCACCTC AAAGTCCTGGAGCTCGTAGCC	1163	55	35
$Ca_v1.3$	Rat	NM017298	CAAATGCCAATCTCAATAACGC TCACTGTAGCCAGGACCAAA	1154	55	35
$Ca_v1.2$ (1)	Rabbit	X15539	CAATTTGCAGCAATGCCATA CGTTGGCATTCATGTTGG	355	59	25
$Ca_v1.2$ (2)	Rabbit	X15539	AGCTCAGCTCCAAGAGATGC AGATGCAGGGGCAGGACT	343	59	25
$Ca_v3.1$	Rabbit	-	ACTCTCTGCCCAATGACAGC TCCGGAGGGTCTATGGAGAT	814	60	35
ERG	Rabbit	U87513	CATGAACGCGGTGCTGAAG CTTGCGTTGCCGGTTGAAT	523	56	30
GAPDH	Rabbit	L23961	GGAGAAAGCTGCTAAGTATG GCTGTAGCCAAATTCGTT	217	53	20

HCN1	Rabbit	AF168122	ATCCCTGCTAATTGTTGAAGCAG GACTCGCAGCTAATGAAAGAAGG	451	46	40
HCN1 (nested)	Rabbit	AF168122	TTCAAAAGACCTGTTTAGCATTCA GACTCGCAGCTAATGAAAGAAGG	247	55	35
HCN4	Rabbit	AB022927	GCACGTCACCCTCACTCTG CGGTTATTGTTGGTGGTGTATC	263	55	35
HCN4 (nested)	Rabbit	AB022927	AAACTGCCGTCCAACCTGT CGGTTATTGTTGGTGGTGTATC	109	53	35
HCN4 (1)	Rat	AF247453	ACAGGACCTGAAGCTCATCTCA CTGAAGGAAGAAGGGAGCAAGAA	417	55	35
HCN4 (3)	Rat	AF247453	TGCTACTACTTCGGTGGCCATA CCACCTAGCGCCTTATGAAAGTGG	387	55	35
Kir2.1	Rabbit	D21057	GGCCCGAAACAGTTACACA CCCATTAACATTATGGAGAAAGAGA	629	55	35
M13	pGEM-T Easy plasmid	N/A	CCCAGTCACGACGTTGTAAAACG AGCGGATAACAATTTCACACAGG	267 + insert	58	35
NFM	Rabbit	Z47378	GAAGTCTCCAGTGAAGGCTACCA CAGCTTTCTTCTTTGGCACATCT	503	60	25
$Na_v1.5$	Rabbit	DQ242484	ACCATCTTYCGGTTCAGY GTAGATCTTYCCTGCRGACCT	867	60	35
Cx43	Rabbit	DQ242486	YYADATCTCCAGGTCATCAGG GYGARAAYGTCTGCTATGACAA	801	60	35

N= A,T,C or G; **R**= A or G; **Y**= C or T.

prevents the development of the blue colour, hence all white colonies should possess the plasmid with the PCR DNA fragment inserted.

PCR can be used to screen the white colonies to check if an insert is present and of the correct size and therefore is the correct insert. This is done using M13 primers that flank the T7 and SP6 promoter sequences on the plasmid (Fig. 2.13). A pipette with disposable tips was used to pick the colony from the plate and insert it directly into the PCR buffer. The PCR protocol used was the same as described in section 2. The high temperatures of the PCR along with the detergents present in the PCR buffer lyses the bacterial cells, exposing the DNA for PCR amplification. PCR conditions and primer sequences are shown in Table 2.4.

2.14.11 Preparation for insert transcription

The PCR fragment generated when the colonies were screened for the correct insert was used to generate the template for transcription. This was done by diluting the PCR product 1 in 100 with molecular biology grade H_2O and repeating the PCR, in order to generate pure PCR fragments with minimal presence of the whole plasmid. It is advantageous if the rest of the plasmid sequences are not present in the transcription reaction, since the whole sequence of the plasmid will be transcribed, generating longer than necessary riboprobes.

2.14.12 *In vitro* RNA transcription

Prior to transcription, the DNA templates were cleaned using the PCR purification MinElute kit (Qiagen), which removed contaminants which may inhibit the transcription. This process increased the concentration of the DNA, as only 10 µl of EB buffer were required for elution of the DNA from the column. A DNA template concentration of >30 ng/µl was desirable for input into the transcription. DNA templates prepared with lign'scribe was transcribed with T7 Megascript kit (Ambion) and DNA templates prepared from pGEM-T Easy plasmid cloning were transcribed either with SP6 or T7 Megascript kits (Ambion). A modified manufacturer's protocol was used: The RNA transcription was performed with a 5 µl reaction volume. The T7 reaction was composed of: template DNA (1 µl), 1x reaction buffer, ATP (7.5 mM),

CTP (7.5 mM), GTP (7.5 mM), UTP (4.8 mM), digoxigenin-11-UTP (2 mM) and T7 RNA polymerase (0.5 µl). The SP6 reaction was composed of: template DNA (1 µl), 1x reaction buffer, ATP (5 mM), CTP (5 mM), GTP (5 mM), UTP (3.2 mM), digoxigenin-11-UTP (1.4 mM) and SP6 RNA polymerase (0.5 µl). Both reactions were incubated overnight at 37 °C. The digoxigenin-11-UTP (Roche) used in the transcription was added so that approximately every fourth uridine incorporated into the RNA strand was digoxigenin labelled. Both sense and antisense riboprobes were synthesed for each target.

2.14.13 Riboprobe clean-up

After the completion of the transcription the reaction mixture was purified to remove the DNA template and unused digoxigenin-11-UTP which could increase the background signal in subsequent ISH. The procedure was: Molecule grade H_2O (96 µl), RLT (350 µl) and 100% ethanol (250 µl) were added to the transcription, mixed well and left for 10 min. The mixture was then applied to a Qiagen mini column and spun in a centrifuge at 13000 rpm for 15 s. The elute was collected and reapplied to the column and spun again at 13000 rpm for 15 s. This was repeated four times to maximise the amount of riboprobe sticking to the column matrix. RPE (500 µl) was then added to the column and spun at 13000 rpm for 15 s, the elute was discarded and RPE (500 µl) was again added to the column and spun for at 13000 rpm for 2 min. 30 µl of molecule grade H_2O was carefully added to the centre of the silica matrix, left for 1 min before being spun at 13000 rpm for 1 min. The elute was collected and stored at -20 °C until required. The riboprobes were quantified on a formaldehyde gel (see section 2.7.14).

2.14.14 Modified Braissant ISH Protocol

10 µm cryosections of AVN tissue were mounted on superfrost plus slides, stored -80 °C were fixed in 4 % paraformaldehyde for 10 min at room temperature and washed twice for 10 min in Acetic Anhydride/TEA solution. Acetylation of positively charged amino groups in the tissue sections decreases background labelling by reducing the electrostatic binding of the riboprobes to the tissue, and acetylation also inactivates endogenous RNases. A microwaving step is required to allow riboprobe tissue

penetration, which involves heating to boiling point in 10 mM Na Citrate pH 6 for 2.5 min. This step is repeated 3 times. This is followed by 15 min equilibration in 5x SSC (0.75 M NaCl, 75 mM Na Citrate, pH 7) before 2 hour prehybridisation at 58 °C, in 50 % formamide, 5x SSC, 40 µg/ml herring sperm DNA The prehybridisation was performed in a sealed moist chamber. Sections are hybridized for 40 to 64 hr at 58 °C, with 0.3 ng/µl of DIG-labelled probe, in 50 % formamide, 5x SSC, 40 µl/ml herring sperm DNA. Hybridisation was performed in a sealed moist chamber with parafilm covering the sections to prevent evaporation. Formamide counteracts RNA secondary structures by reducing the melting temperature of RNA-RNA hybrids thus allowing the riboprobe to bind, and also acts against non-specific hybridisation of the probe, SSC provides monovalent cations which stabilizes nucleic acid interactions and herring sperm DNA reduces background labeling by blocking non-specific riboprobe binding sites. The sections are washed for 30 min in 2x SSC, at room temperature, before two 1 hr washes at 65 °C, the first with 2x SSC and the second with 0.1x SSC. This is followed by RNase treatment, 0.5 µg/ml for 30 min, to degrade any unbound probe. The sections are twice washed in 2x SSC for 5 min, before a stringent wash, 0.5x SSC, 20% formamide at 60 °C for 10 min. The sections are twice washed in 2x SSC for 5 min. This is followed by washing in buffer 1 (100mM Tris, 150 mM NaCl, pH 7.5) for 5 min and buffer 2 (buffer1 with 1 % Boehringer blocking reagent) for 1 hour, before application for 2 hours of anti-DIG Fab-fragment, alkaline phosphatase coupled (Roche), 1:5000 in buffer 2. Unbound Fab-fragment was washed off by two 15 min DIG buffer 1 washes. The sections were incubated for 5 min in DIG buffer 3 (100mM Tris, 100mM NaCl, 50 mM $MgCl_2$, pH 9.5), before colour development in sealed coplin jars containing buffer 3, 10 % PVA (Sigma), 0.2 mM NBT (Roche) and 0.2mM BCIP (Roche). Signal development occurred overnight at room temperature. The staining reaction was stopped with three 15 min washes in stop buffer (0.1 M Tris, 1 mM EDTA, pH 8.0). The sections were embedded in Kaiser's gelatine (BDH).

Image capture and processing

Bright field images of the ISH labelling were taken using a Zeiss LSM 5 Pascal microscope, with Zeiss Axioscope software. Images underwent further processing using Adobe Photoshop 7.0 and Corel Photo-Paint 10 software.

2.14.15 Isolation of rabbit sequences

The rabbit nucleotide sequences for the majority of ion channel mRNAs were not available as entries on the Entrez-nucleotide database. These sequences were therefore obtained by PCR with degenerate primers. A sequence of approximately 1000 bp was optimal for riboprobe synthesis plus to have enough options for *real time* PCR primer design. A degenerate primer is a mixture of primers with similar sequences that vary at one or more positions. The principle underlying degenerate primer design is based on the fact that homologous genes have high levels of sequence similarity. PCR with degenerate primers is an established approach for the isolation of similar sequences (Nunberg *et al.*, 1989). For the design of degenerate primers the following steps were followed:

1. Sequences unique to the target were identified by running a BLAST search with the known sequence as many known vertebrate sequences as possible.
2. Sequences identified in step 1 were then aligned using ClustalW to identify areas of high homology suitable for primer design.
3. Stretches of approximately 30 bases were identified as potential primer sequences, the sequences chosen as primers followed the below criteria:
   a. At least 85 % similarity between the homologous sequences.
   b. No more than 50 % GC content, over 50 % would increase the chances of non-specific priming.
   c. The final two bases at the 3' end should not both be G or C, otherwise this could lead to mispriming.
   d. The final two bases at the 3' end should be completely homologous between all species. This is important as perfect binding of the 3' end of the primer to the target sequence is vital for the primer extension in the PCR.
   e. The final base at the 3' end of the primer should be the first or second base in the codon encoding for the amino acid, as the third base of the codon is most variable.
   f. Where a base varies between species, all possible bases should be included at that position in reference to the variation of the codon sequence.

A list of the degenerate primers used are shown in Table 2.4.

Chapter 3

Three-dimensional reconstruction of the rabbit atrioventricular node

3.1 Introduction

The tissues of the atrioventricular conduction axis lie within the confines of the triangle of Koch. Histological and electrophysiological studies (e.g. Anderson et al., 1974) to date have described multiple cell types and subcellular regions that vary from species to species and have a certain degree of ambiguity. How can the different cell types and regions be distinguished? Masson's trichrome staining allows the visualisation of distinct tissue subgroups due to differential attachment of dyes to certain tissue types. Cardiac myocytes (of the working myocardium as well as nodal cells) appear red and can be readily distinguished from connective tissue, which stains blue. The cardiac conduction system in rabbit can be delineated from normal working myocardium by using neurofilament-M (NF-M) as a marker; antibodies directed against the NF-M epitope have routinely been used for this purpose (Gorza et al., 1988; Dobrzynski et al., 2005). The propagation of impulses through cardiac tissue is largely dependent on the presence of gap junctions at the intercalated discs of adjacent myocytes. These are formed by connexins (Cx) of which there are multiple isoforms (Vozzi et al., 1999). Cx43 is the major cardiac gap junctional protein and can be used as a predictive marker of conduction properties in specific regions of cardiac tissue. Historically, the rabbit has been the animal of choice for investigations into the AVN. We aimed to 3-dimensionally reconstruct the rabbit AVN conduction axis by combining histology and immunhistochemical analysis of NF-M and Cx43 proteins to delineate the nodal tissue from the working myocardium and provide an understanding of conduction properties throughout the AVN conduction axis.

3.2 Methods

3.2.1 Histology and immunohistochemistry for Cx43 and neurofilament-M

A single rabbit AVN preparation was dissected (see section 2.1.2) and dehydrated through a series of alcohols and xylene. The preparation was then submerged in molten paraffin overnight and left to set (see section 2.2.2). 10 μm serial sections were cut using a standard microtome (see section 2.3.2). At 200 μm intervals, sections were either stained with Masson's trichrome (see section 2.4) or immunohistochemically labelled for Cx43 and NF-M (see section 2.5). Images of the sections were taken using a Zeiss LSM 5 Pascal microscope. The images were imported into Corel Draw 10 software and subcellular groups identified based on histological and/or immunological data, in order to build detailed two-dimensional schematic diagrams of each section (Fig. 3.1). Finally, two-dimensional schematic diagrams were imported into MATLAB software by Dr. Jue Li to generate a three-dimensional model of the AVN (Fig. 3.7; Li et al., 2004).

3.3 Results

The following cellular subgroups were chosen based on tissue location, histology and NF-M and/or Cx43 immunolabeling: ventricular muscle; connective tissue; adipose tissue; tendon of Todaro; upper nodal cells; lower nodal cells; loosely packed atrial muscle; atrial muscle; vein; ganglia/nerve. Figure 3.1A shows an example of a Masson's trichrome-stained section in which cardiac myocytes are stained red, connective tissue blue and adipose tissue as a grey/white colour; a large piece of ventricular muscle clearly makes-up the base of the section with the tricuspid valve attached on the endocardial surface; lying on the crest of the ventricular muscle is the central fibrous body which stains blue, and extending to the right from this is part of the mitral valve; lying immediately adjacent to the central fibrous body are the nodal cells which are hard to distinguish from the rest of the cardiac myocytes; superior to the nodal cells are bundles of densely packed atrial tissue running on the epicardial side towards the bulk of densely packed atrial muscle which lies upper most in the section; loosely packed atrial muscle occupies the region in between the densely packed atrial muscle and nodal cell region; finally, embedded within the loosely packed atrial muscle is a small blue area representing the tendon of Todaro. Figure 3.1B is a two-dimensional schematic with each cellular subgroup designated a specific colour in order to distinguish it from other structures; the large proportion of ventricular muscle is in light red; all connective tissue including the central fibrous body, mitral valve and tricuspid

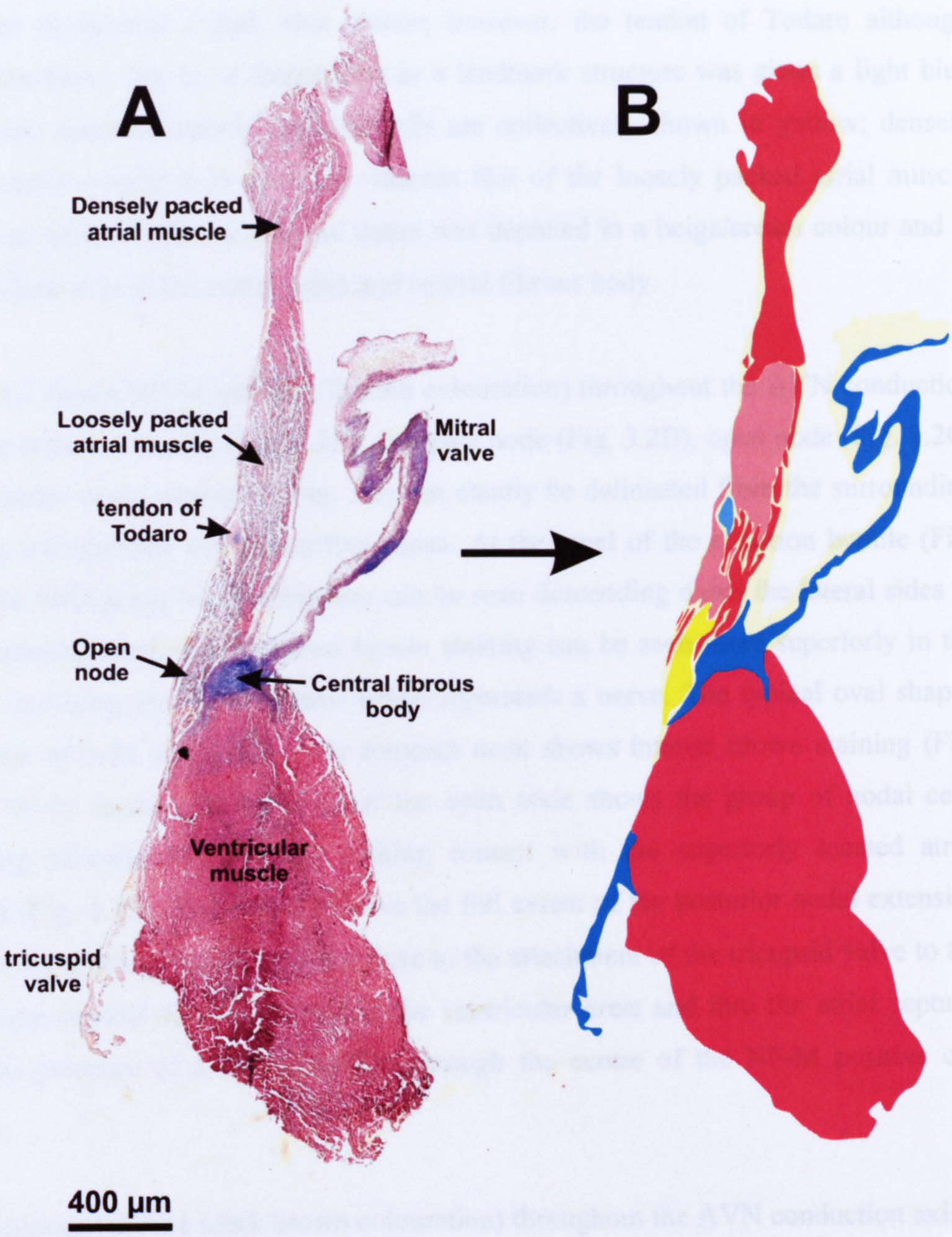

Figure 3.1 Transition from Masson's trichrome stained section to 2D schematic diagram with subcellular groups defined. Light red, ventricular muscle; Dark red, densely packed atrial muscle; Pink, loosely packed atrial muscle; light blue, tendon of Todaro; Dark blue, connective tissue including central fibrous body and tricuspid valve; cream, adipose tissue; yellow, neurofilament-M positive cells.

valve are designated a dark blue colour; however, the tendon of Todaro although connective tissue due to its importance as a landmark structure was given a light blue colour; the neurofilament-M positive cells are collectively shown in yellow; densely packed atrial muscle is in dark red whereas that of the loosely packed atrial muscle appears as pink; finally the adipose tissue was depicted in a beige/cream colour and is most evident around the mitral valve and central fibrous body.

Figure 3.2 shows NF-M labelling (brown colouration) throughout the AVN conduction axis: the common bundle (Fig. 3.2A), compact node (Fig. 3.2B), open node (Fig. 3.2C) and posterior nodal extension (Fig. 3D) can clearly be delineated from the surrounding working myocardium and connective tissue. At the level of the common bundle (Fig. 3.2A) the bifurcating bundle branches can be seen descending down the lateral sides of the ventricular crest; a less intense brown staining can be seen more superiorly in the section overlying the atrial septum which represents a nerve. The typical oval shaped collection of cells representing the compact node shows intense brown staining (Fig. 3.2B). NF-M staining at the level of the open node shows the group of nodal cells diverging towards and possibly making contact with the superiorly located atrial bundles (Fig. 3.2C). Figure 3.2D shows the full extent of the posterior nodal extension with NF-M staining extending from close to the attachment of the tricupsid valve to the ventricular muscle superiorly beyond the ventricular crest and into the atrial septum; note the presence of a vein travelling through the centre of the NF-M positive cell region.

Cx43 immunolabeling (dark brown colouration) throughout the AVN conduction axis is shown in Figure 3.3; Abundant immunolabeling of Cx43 is present in the atrial muscle (Fig. 3.3A), lower nodal cells (Fig. 3.3D), common bundle (Fig. 3.3B) and ventricular muscle (Fig. 3.3E). In contrast, sparse immunolabelling of Cx43 is present in the compact node (Fig. 3.3C) and open node (Fig. 3.3F).

Figure 3.4 shows the histology, together with the Cx43 immunolabelling, of different regions of the AVN conduction axis. Densely packed atrial muscle (Fig. 3.4A) and ventricular muscle (Fig. 3.4C) is densely packed with large cells with abundant Cx43 immunolabelling. Loosely packed atrial muscle (Fig. 3.4B) contains scattered cells with, however, a. abundant Cx43 immunolabelling. Figure 3.4G shows cells from the CB which are relatively tightly packed with abundant Cx43 immunolabelling. In

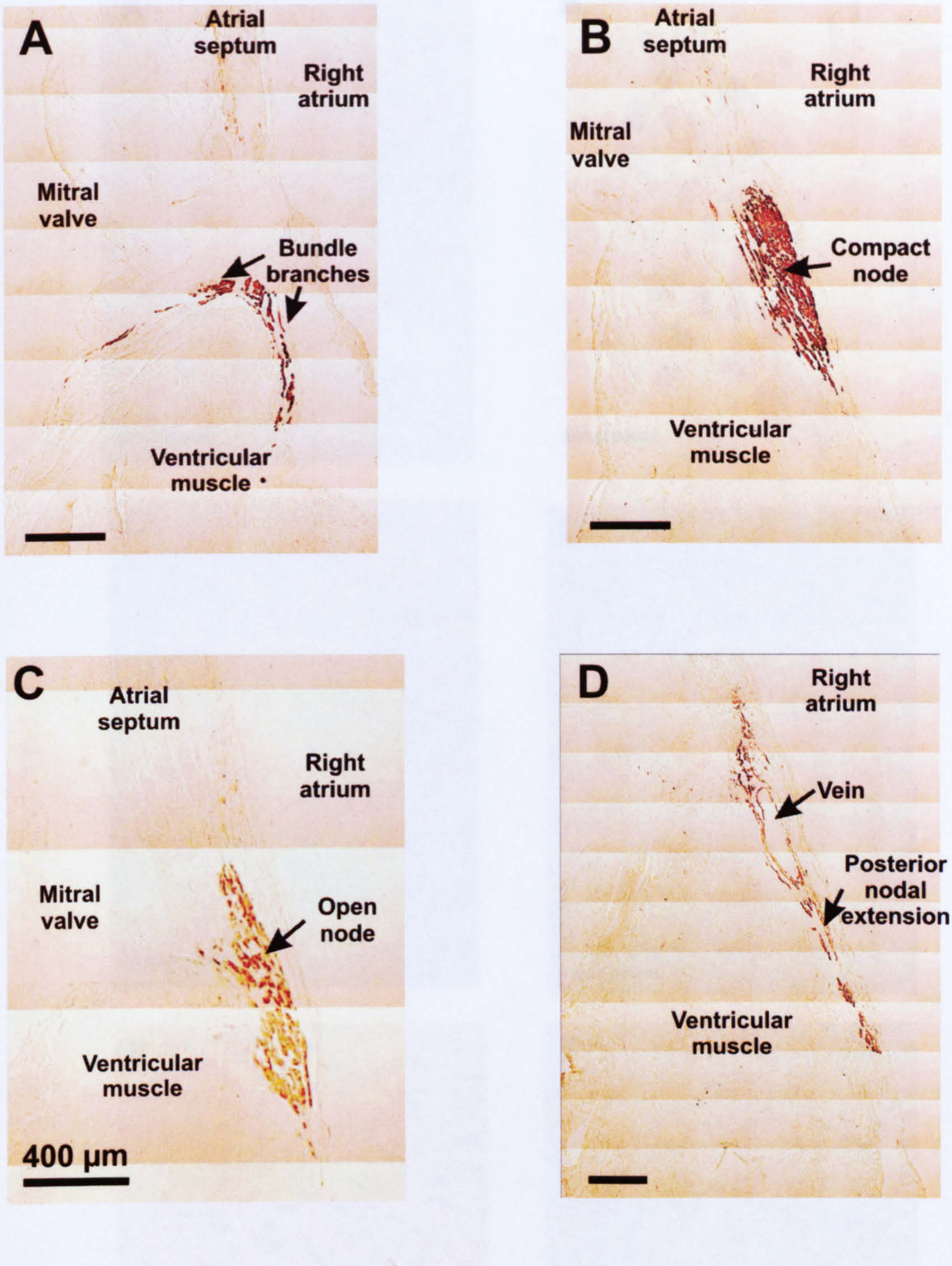

Figure 3.2 Neurofilament-M (NF-M) labelling at various levels of the AVN conduction axis. A, NF-M delineates the nodal tissue highlighting the bifurcation of the bundle branches. B, compact node. C, open node. D, posterior nodal extension. Scale bars, 400 µm.

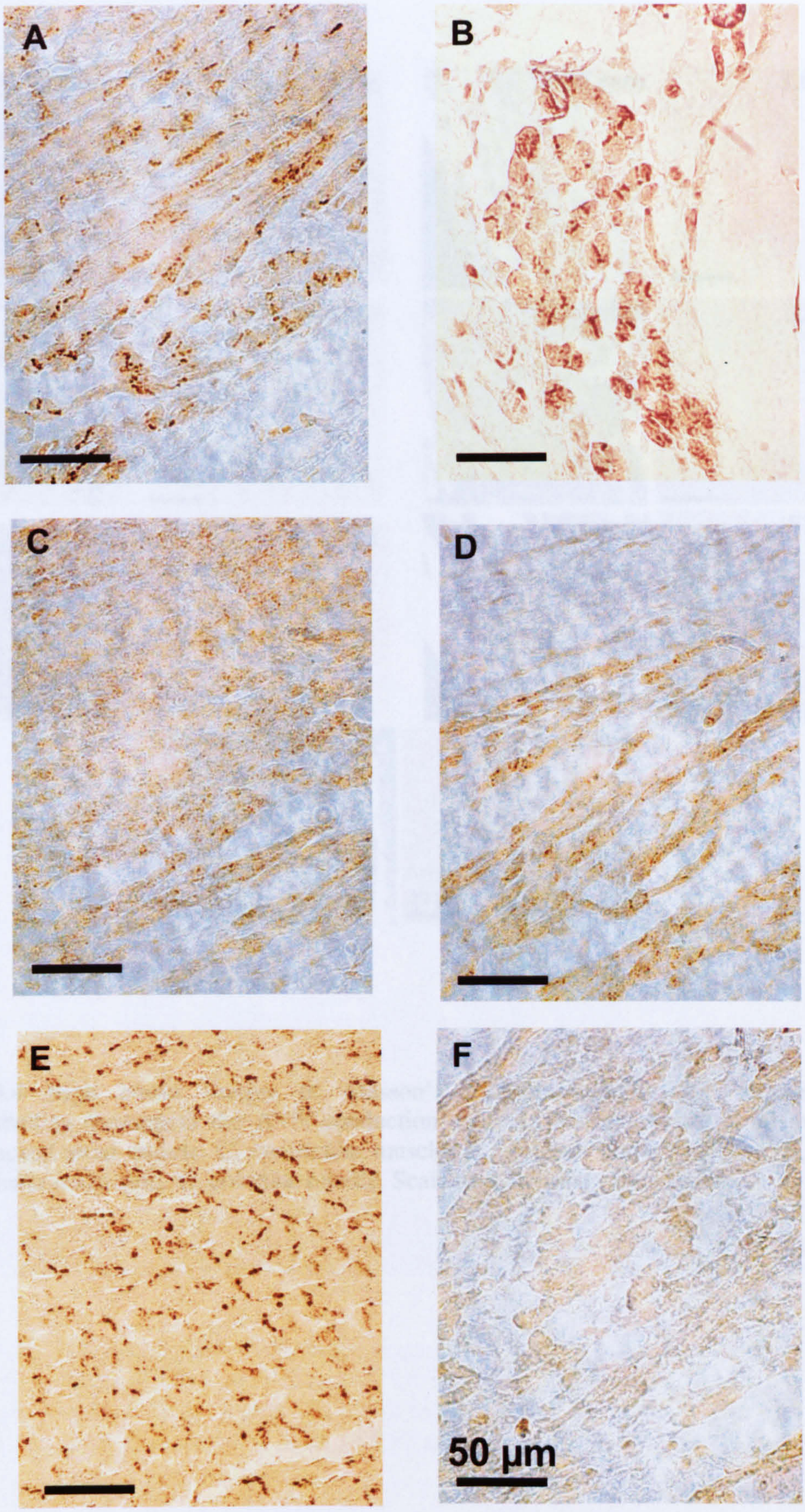

Figure 3.3 Immunolabelling of Cx43 throughout the AVN conduction axis. A, atrial muscle. B, common bundle. C, compact node. D, lower nodal cells. E, ventricular myocardium. F, posterior nodal extension. Scalebars, 50.

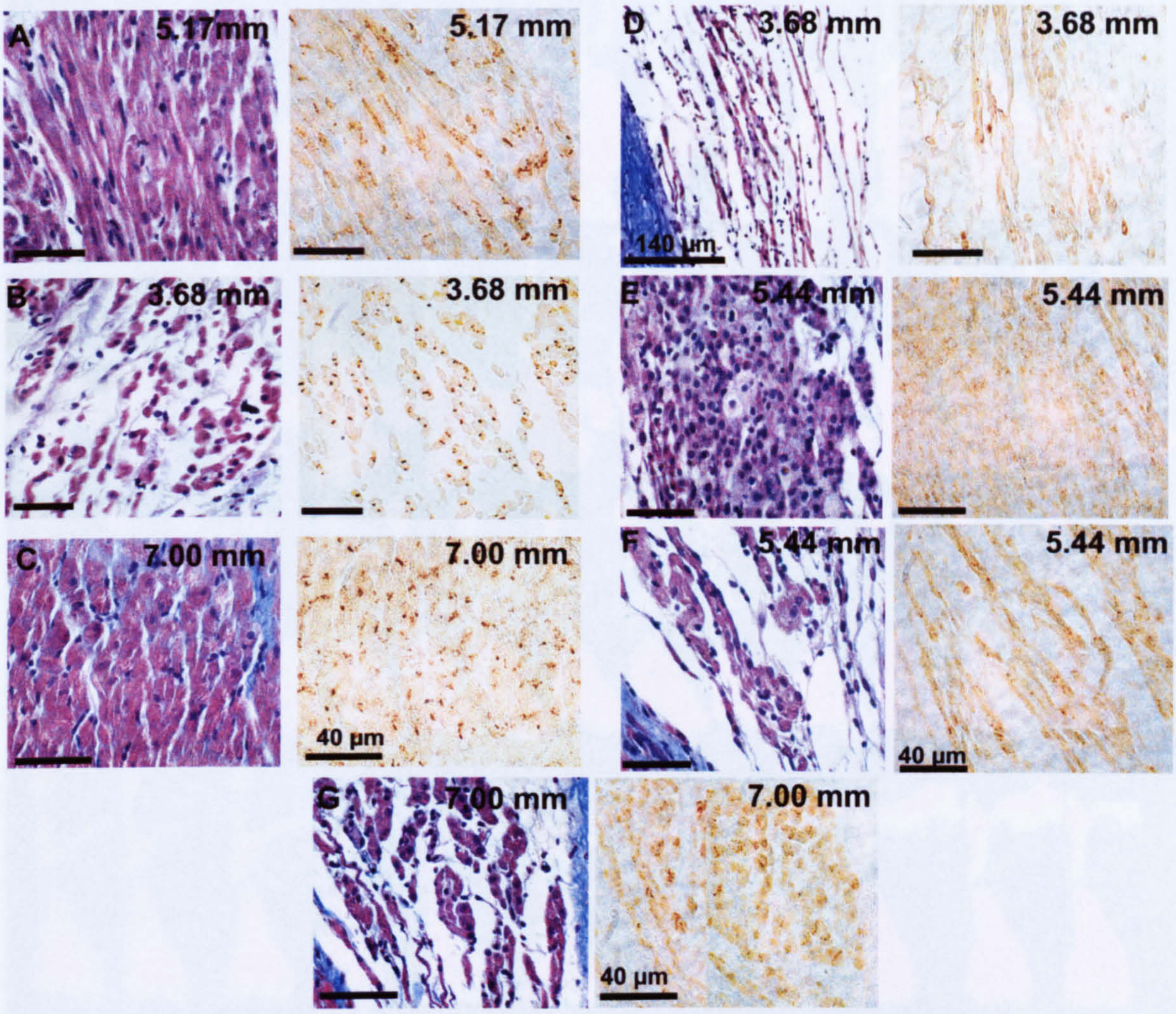

Figure 3.4 High power images of Masson's trichrome-staining and adjacent Cx43 immunolabelling throughout the AVN conduction axis. A, densely packed atrial muscle. B, loosely packed atrial muscle. C, ventricular muscle. D, posterior nodal extension. E, compact node. F, lower nodal cells. G, common bundle. Scale bars, 40 µm (unless stated).

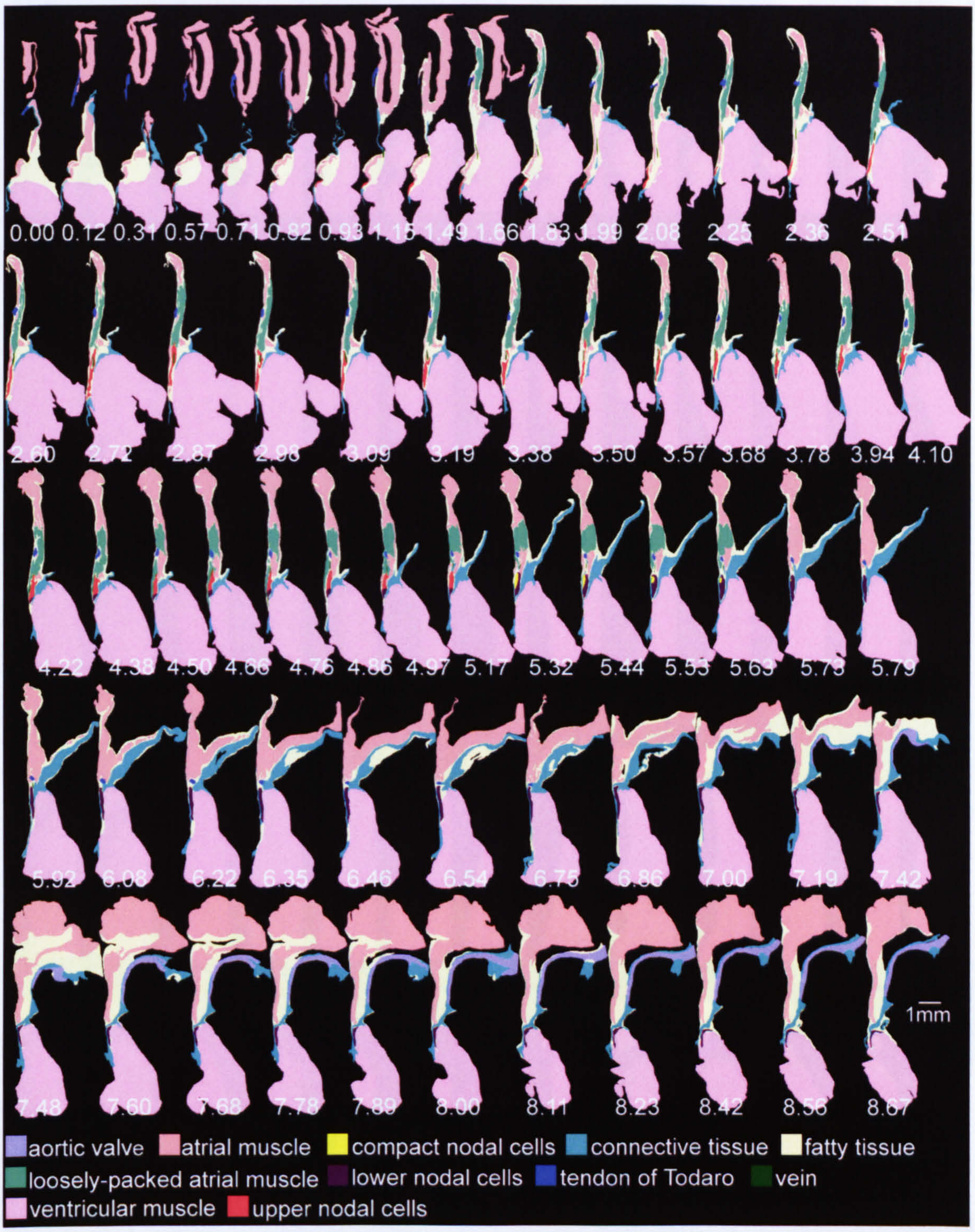

Figure 3.5 Two-dimensional schematic diagrams used to build the three-dimensional reconstruction of the AVN conduction axis. Numbers in white at the bottom of each two-dimensional schematic diagram represent the distance in "mm" along the AVN conduction axis from 0.00 mm, at its most posterior point, to 8.67 mm at its most anterior point.

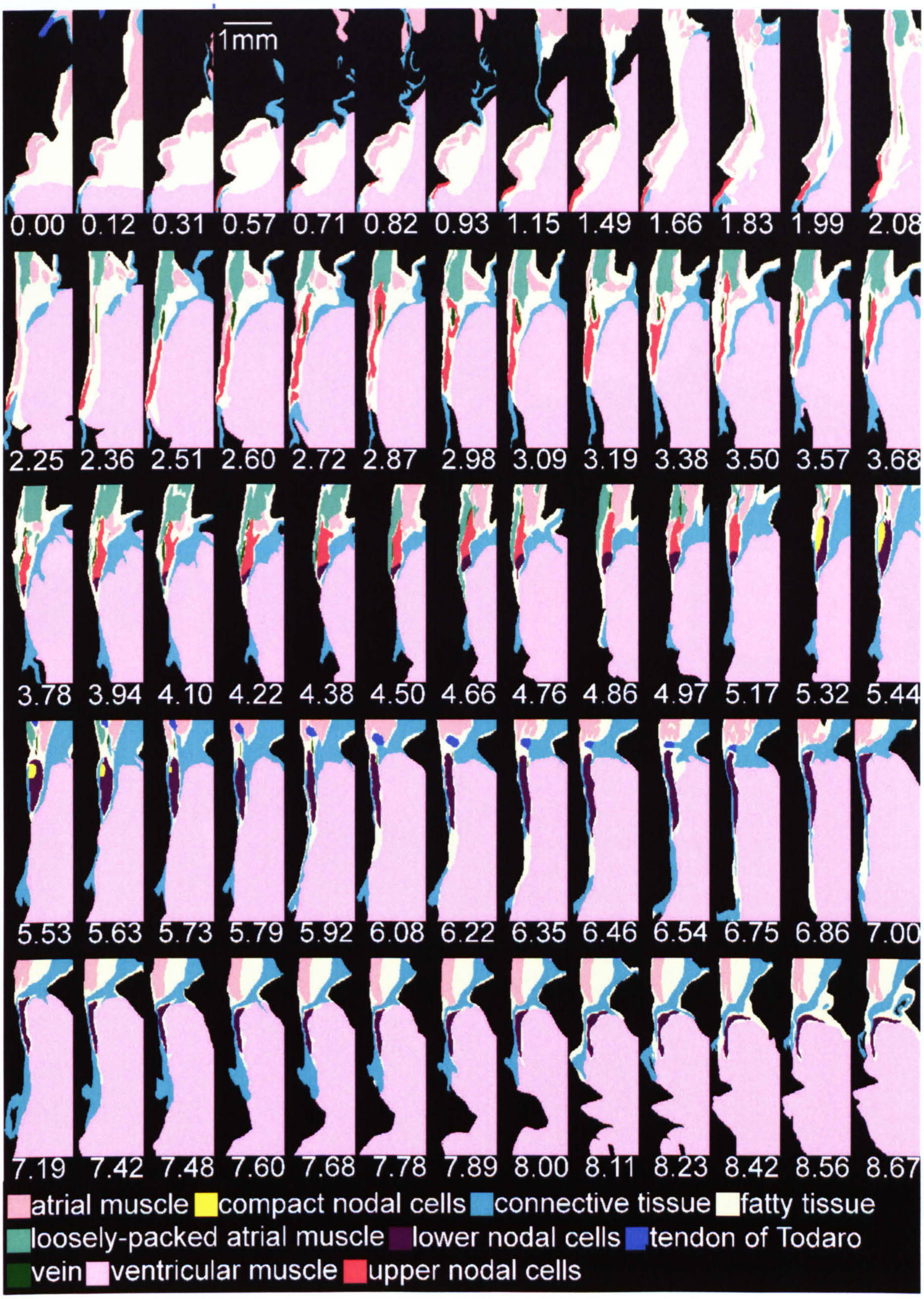

Figure 3.6 Higher magnification images to highlight the nodal regions of the two-dimensional schematic diagrams used to build the three-dimensional reconstruction of the AVN conduction axis. Numbers in white at the bottom of each two-dimensional schematic diagram represent the distance in "mm" along the AVN conduction axis from 0.00 mm, at its most posterior point, to 8.67 mm at its most anterior point.

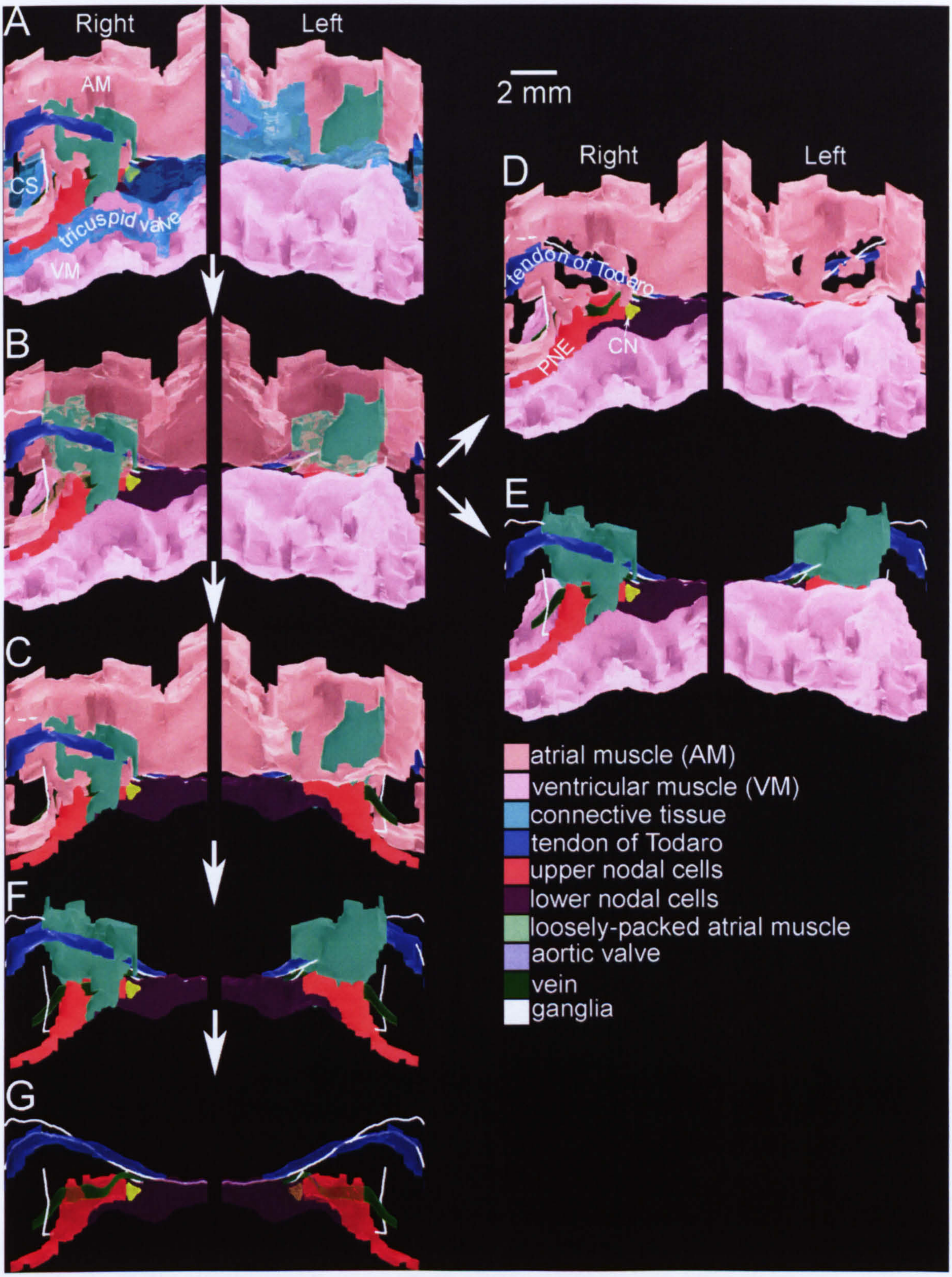

Figure 3.7 Three-dimensional reconstruction of the rabbit AVN conduction axis. A, full three-dimensional model showing views from the right and left atrium. B, same as A but with connective tissue removed. C, same as B but with ventricular muscle removed. D, three-dimensional model with loosely packed atrial muscle removed. E, three-dimensional model with densely packed atrial muscle removed. F, three-dimensional model with densely packed atrial and ventricular muscle removed. G, three-dimensional model with densely and loosely packed atrial and ventricular muscle removed.

contrast, cells of the PNE are scattered and appear "spindle" like with little or no Cx43 immunolabelling (Fig. 3.4D). Compact node cells are tightly packed but small in size with abundant nuclei and sparse Cx43 immunolabelling (Fig. 3.4E). Figure 3.4F shows lower nodal cells, which are relatively tightly packed with a mixture of "spindle" shaped cells and "ovoid" cells and abundant Cx43 immunolabelling.

Figure 3.5 (low magnification) and 3.6 (high magnification) shows the two-dimensional schematic diagrams, which were used to generate the final three-dimensional model. A total of 65 two-dimensional schematics from all levels were used to construct the three-dimensional model. The levels are numbered in Figure 3.5 and 3.6 from 8.67 at the most anterior point of the AVN conduction axis where the bifurcating bundle branches can be seen in purple, through the compact node area at level 5.32, and finally terminating at 0.00 toward the posterior end of the AVN conduction axis where nodal cells are absent.

Figure 3.6 shows images from all levels (8.67 to 0.00) at higher magnification to highlight the major nodal structures throughout the AVN conduction axis. Lower nodal cells are shown in purple, extending from 3.68 to 5.67, where they merge with cells of the common bundle. Compact node cells are shown in yellow from 5.73 to 5.32. Upper nodal cells merge with cells of the posterior nodal extension, shown as red, to extend for a large proportion of the AVN conduction axis from 5.17 to 0.82. Along the length of the upper nodal cells the transitional cells (green; 4.97 to 2.08) can be seen to comprise a large proportion of the atrial septum and contact the upper nodal cells at certain regions along their length (4.38 to 3.94).

The three-dimensional model of the rabbit AVN conduction axis is shown in series of images in Figure 3.7. Figure 3.7 "right" shows views from the right atrium/ventricle, whereas Figure 3.7A "left" shows views from the left atrium/ventricle. Figure 3.7A shows the complete model. The base of the model is made up largely of ventricular muscle (purple) and the bulk of the upper portion is made of densely packed atrial muscle (pink); the tendon of Todaro (blue region), located superiorly in the model, and the tricuspid valve annulus, located inferiorly, are clearly evident to demarcate the upper and lower margins of the triangle of Koch; within this area the anterior aspect of the AVN conduction axis shows a tract of cells (purple region) running toward the compact node; there is also a bulk of loosely packed atrial muscle (green region) which overlaps

the proximal portion of the posterior nodal extension; more posteriorly, the posterior nodal extension (red region) can be seen to extend to the level of the coronary sinus; the margins of the coronary sinus appear to made up of densely packed atrial muscle; and a nerve (white) appears to descend towards the mid-portion of the posterior nodal extension. Figure 3.7B is the same as Figure 3.7A, but with the connective tissue removed to highlight the major nodal regions of the conduction axis, in particular, the lower nodal cells (maroon), compact node (yellow), loosely packed atrial muscle (green), posterior nodal extension (red) and ventricular muscle (pink). After the removal of the loosely packed atrial muscle, a region of densely packed atrial muscle can be seen to progress from the anterior part of the posterior nodal extension towards the upper margins of the coronary sinus to connect to the bulk of densely packed atrial muscle (Figure 3.7D). Figure 3.7E shows the full extent of the loosely packed AM which appears to comprise a large portion of the upper part of the triangle of Koch. With the removal of the loosely packed atrial muscle, major nerves (shown in white), for example, running along the tendon of Todaro can be seen (Fig. 3.7G).

3.4 Discussion

Histological analysis of serial sections throughout the AVN conduction axis revealed atrial tissue which was either loosely arranged densely packed and this marked difference in appearance was used to divide the atrial tissue into two subgroups (Fig. 3.4A and B). The difference in organisation may have an influence on conduction properties: the densely packed tissue may conduct faster than the loosely arranged tissue. The term "transitional cells" has been used to describe the cells comprising the area between the compact node and "true" atrial cells. Transitional cells histologically appear intermediate in size and shape between those of typical nodal cells and true atrial cells (Anderson, 1972). It is possible that the loosely arranged atrial muscle is made of transitional cells.

The loosely arranged atrial muscle was extensive throughout the AVN conduction axis (Fig. 3.7; green), with this tissue comprising the whole thickness of the wall in places (Fig. 3.5; e.g. 2.87 mm). However, a small bundle of densely packed atrial tissue, was present in the region of the loosely arranged atrial muscle; it travelled horizontally from the anterior portion of the posterior nodal extension to the upper margins of the

coronary sinus to join with the bulk of densely packed atrial muscle (Figs. 3.7D and 3.5, 4.38 to 1.66 mm). This is the first description of this bundle of densely arranged atrial muscle in the rabbit AVN. It could be an additional input into the AVN (as opposed to the PNE and the more anterior atrial septal input). This bundle is similar to a Cx43-positive bundle at the AVN of the rabbit shown by Nikolski et al., (2003). Nikolski et al., (2003) suggested that this bundle is one of the dual pathways and plays a role in AVNRT.

Reconstruction of the three-dimensional distribution of NF-M positive cells (nodal cells) has revealed a tract of nodal cells running from the common bundle at the most anterior position (Fig. 3.7G, maroon), where it is embedded within the central fibrous body, to the oval shaped compact node (Fig. 3.7G; yellow), to the PNE at the most posterior position (Fig. 3.7G, red). This structure is remarkably similar to that described by Ko et al. (2004). Ko et al., (2004) used desmin expression as a marker of nodal cells. It is highly likely that this structure is the molecular substrate for slow pathway action potential propagation (Inoue and Becker, 1998). At the level of the open node, the group of NF-M positive nodal cells diverge towards bundles of loosely packed atrial tissue (Fig. 3.2C). This may allow entry of an action potential traversing the atrial septum into the AVN i.e. this may be the point of entry of the fast pathway. The PNE (NF-M positive nodal cells extending posteriorly from the compact node) appears to join with true atrial muscle at its most posterior point (Fig. 3.7B and G). This may be the entry point into the slow pathway. As already stated, the most anterior portion of the PNE lies adjacent to the loosely arranged atrial muscle (Fig. 3.7F). However, at the mid-portion of the PNE, the nodal cells are located below a vein, which appears to provide a barrier between the PNE cells and the loosely arranged atrial muscle (Fig. 3.7G). This is the first time this vein has been described. We have consistently seen this vein in multiple AVN preparations. Whether this structure is functionally significant (i.e. prevents action potential transmission from the PNE to the loosely arranged atrial muscle) remains to be seen. Finally, the PNE appears to be continuous with the lower nodal cells, which is in agreement with Ko et al., (2004).

Cx43 immunolabelling in the lower part of the compact node and also to a certain extent in the lower regions of the PNE (Figs. 3.3D and 3.4F). The cells positive for Cx43 in these areas were collectively referred to as "lower nodal cells".

The three-dimensional reconstruction showed that at the level of the common bundle the tract of NF-M positive nodal cells runs just above the ventricular crest (Fig. 3.5, 8.67-8.00 mm), at the level of the CN the tract of NF-M positive cells lies just below the crest of the ventricular septum on the right-hand side (Fig. 3.5, 5.17-4.22 mm) and at the level of the PNE the tract of NF-M positive cells occupies a region on the right side of the ventricular septum (Fig. 3.5, 3.94-0.92 mm). In the atrial septal wall, at the level of the coronary sinus, there is a progression from an abundance of loosely packed atrial muscle occupying the thickness of the wall, to the majority of this area being of densely packed atrial muscle (Fig. 3.5, 2.25-0.00 mm). The tricuspid valve lies just below the tract of NF-M positive nodal cells throughout the AVN conduction axis (Fig. 3.7A).

NF-M, as well as labelling myocytes of nodal origin, labels neuronal structures. This allowed us to track the pathway of certain nerves into the AVN conduction axis. Anteriorly, numerous ganglia were observed and appeared to innervate the anterior structures of the AVN conduction axis such as the compact node and common bundle (Fig. 3.7G). In addition, towards the mid-portion of the PNE a ganglia/nerve appeared to make contact with cells in this area. The nerve may influence pacemaker output from the AVN, because this region of the PNE has been shown in previous work from our laboratory to be the leading pacemaker site (Fig. 3.7G; Dobrzynski et al., 2003).

Chapter 4

Hyperpolarisation-activated, cyclic nucleotide-gated channels

4.1 Introduction

The pacemaker and conduction system of the heart, in particular the SAN and AVN, contains cells with the ability to show pacemaking and beat spontaneously. These "pacemaker cells" have a unique phase of slow diastolic depolarisation, which is driven by the "funny-current" (I_f) – so named due to its unusual features (DiFrancesco., 1993). One unusual feature is that it is activated at hyperpolarised potentials of about -40/-50 mV in SAN cells. Unlike most other currents, I_f is carried by both Na^+ and K^+ ions.

I_f possibly mediates the autonomic control of heart rate by the sympathetic and parasympathetic nervous systems. The sympathetic neurotransmitter noradrenaline once bound to β-adrenoceptors on the cell surface initiates a cascade of events that ultimately leads to a rise in intracellular concentration of cAMP. Upon binding to the COOH terminus of the channel it causes a shift in the activation curve of I_f to more positive potentials, thus allowing more current to be passed at diastolic potentials; this increases the slope of diastolic depolarisation without affecting any other phases of the action potential (Accili et al., 1997). On the other hand, acetylcholine released by parasympathetic nerve fibres, binds to muscarinic receptors and shifts the activation curve to more negative potentials, thereby allowing less current to pass during the diastolic range of potentials; this decreases the slope of diastolic depolarisation and thus slows the heart rate (Accili et al., 1997).

Underlying I_f are thought to be the hyperpolarisation-activated, cyclic nucleotide-gated channels. Four different isoforms (HCN1-4) have been cloned and shown to be expressed in a variety of tissues (for review see Accili et al., 2002). When expressed in heterologous (Ishii *et al.* 1999; Ludwig *et al.* 1999; Seifert *et al.* 1999; Moroni *et al.* 2000; Moosmang *et al.* 2001; Viscomi *et al.* 2001) and in homologous (Qu *et al.* 2001) systems, these channels exhibit properties typical of I_f, although differences exist in both the kinetics and the cAMP sensitivity (Santoro & Tibbs, 1999; Altomare *et al.* 2001; Kaupp & Seifert, 2001). The channel currents represented by the various isoforms

have different rates of activation and deactivation. HCN1 is the fastest followed by HCN2 and HCN4 (Altomare et al., 2001). Heteromeric assembly of HCN channels is thought to exist since single isoforms of HCN channels fail to fully reproduce native I_f (Chen et al., 2001; Ulens and Tytgat, 2001).

Evidence also exists suggesting HCN channel isoforms co-express with β-subunits, in particular, minK-related peptide 1 (MIRP1 or KCNE2); this subunit has been shown to increase the magnitude of expressed currents (Yu e al., 2001; Altomare et al., 2003).

HCN channels have a similar structure to most voltage-gated K^+ channels. They have six transmembrane domains, with a positively charged S4 domain, and the signature G-Y-G sequence which confers K^+ selectivity. In addition, they have a cyclic-nucleotide binding domain in their C-terminus (Accili et al., 2002).

All major isoforms of HCN channels have been shown to be expressed in the heart (Ludwig et al., 1998; Moosmang et al., 2001; Santoro et al., 1998). The SAN has been the tissue most studied for HCN channel isoform expression, because HCN4 was originally cloned from the SAN (Ishii et al., 1999) and because of its primary pacemaking role. The mouse SAN has been shown using *in situ* hybridisation to contain predominantly HCN4 mRNA but also low levels of HCN1 and HCN2 mRNA (Moosmang et al., 2001). Electrophysiological evidence from the rabbit SAN suggests heteromultimers may exist in this tissue because activation kinetics are intermediate between those of HCN1 and HCN4 (Moroni et al., 2001).

4.2 Methods

4.2.1 *Real time* PCR

Real time PCR was performed on HCN1 and HCN4 cDNAs generated from total RNA isolated from five rabbit AVN tissue types: atrial muscle, PNE, compact node, common bundle and ventricular muscle (n = 8 rabbits). *Real time* PCR was carried out using a Roche LightCycler 1.0.

4.2.2 *In situ* hybridisation

The riboprobes for HCN1 and HCN4 were designed by Dr. James Tellez using fragments cloned from rabbit SAN cDNA (Tellez, 2005).

4.3 Results

4.3.1 *Real time* PCR

Real time PCR revealed significantly ($P < 0.05$) higher amounts of HCN4 in the PNE (as compared to the ventricular muscle and common bundle) and compact node (as compared to the ventricular muscle) (Fig. 4.1). The compact node, common bundle and PNE showed significantly ($P < 0.05$) higher levels of HCN1 as compared to the ventricular muscle (Fig. 4.1).

4.3.2 *In situ* hybridisation

Perinuclear staining for HCN4 was most abundant in the PNE (Figs. 4.2C and 4.3). In contrast the atrial muscle, compact node, common bundle and ventricular muscle were completely negative for HCN4 labelling (Figs. 4.2A, B, D, E, 4.3-4.5). The riboprobe for HCN1 was tested but failed to produce a signal.

4.4 Discussion

I have shown abundant expression of HCN1 mRNA in the PNE, compact node and common bundle of the rabbit. In contrast, HCN4 mRNA was abundantly expressed only in the PNE (Figs. 4.2C and 4.3). The high level of HCN4 mRNA expression in the PNE is consistent with previous findings at the protein level and with the PNE being the origin of the pacemaking in the AVN (Dobrzynski et al., 2003).

The presence of HCN1 and HCN4 mRNA agrees with numerous electrophysiological studies which have shown spontaneously active AVN cells to contain I_f (Kokubun et al., 1980; Habuchi and Giles, 1993; Hancox and Levi, 1994; Munk et al., 1996).

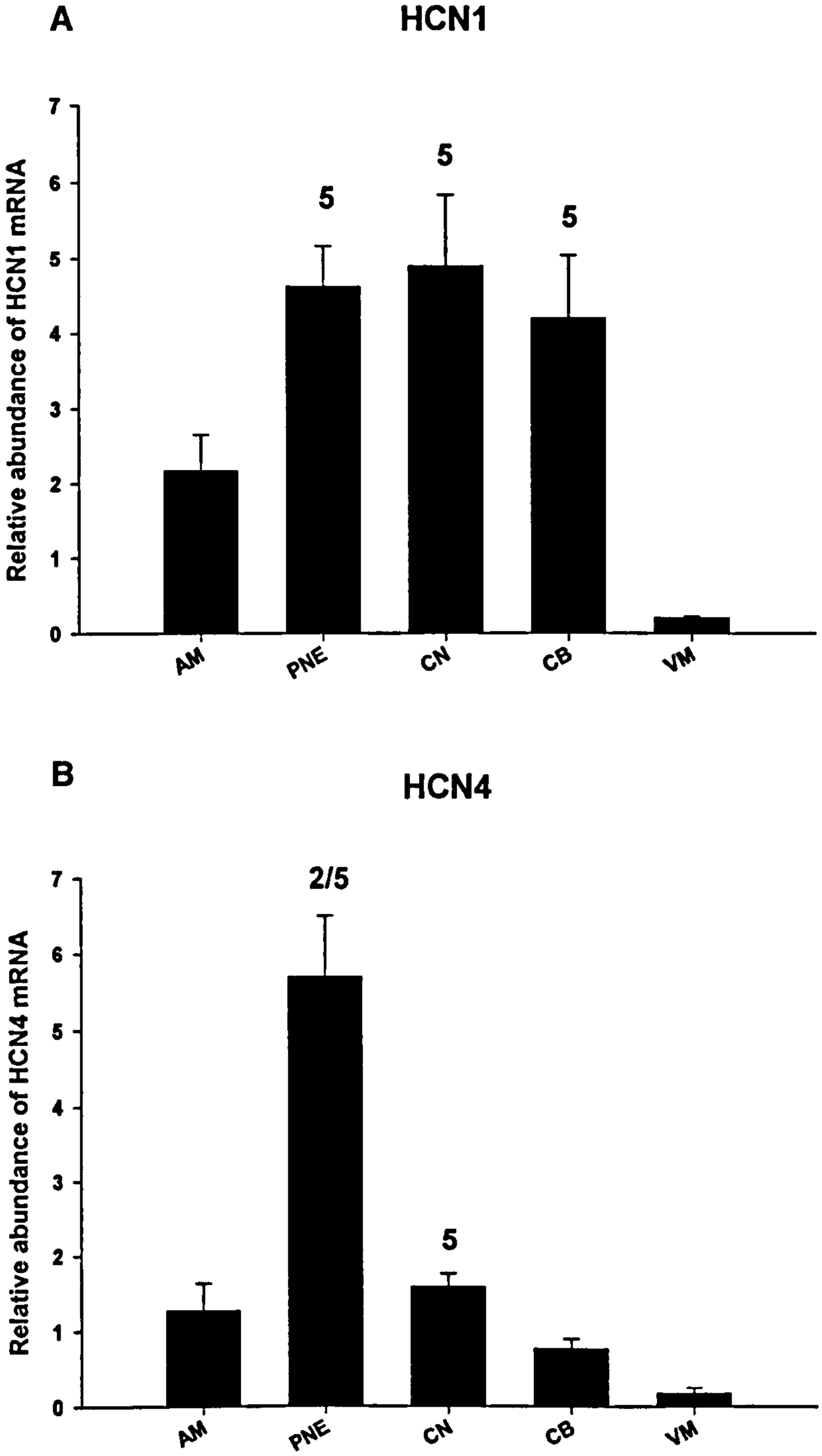

Figure 4.1 *Real time* PCR results for HCN channel mRNAs. 2 and 5, significantly different from common bundle and ventricular muscle, respectively ($P < 0.05$; one-way ANOVA); AM, atrial muscle; PNE, posterior nodal extension; CN, compact node; CB, common bundle; VM, ventricular muscle.

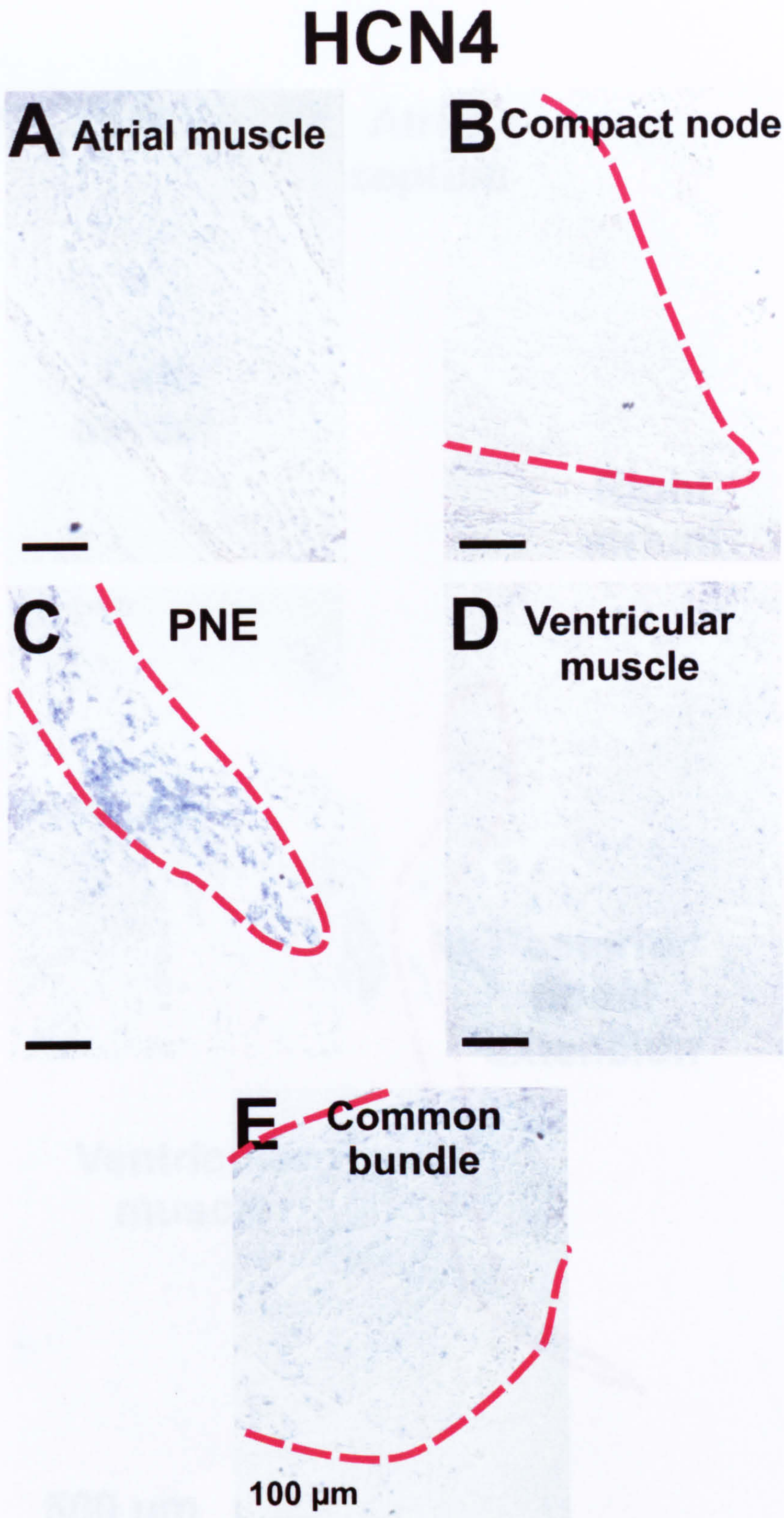

Figure 4.2 High power (x20 magnification) *in situ* hybridisation images for HCN4 mRNA. A, densely packed atrial muscle; B, loosely packed atrial muscle; C, common bundle; D, compact node; E, posterior nodal extension; F, ventricular muscle. Red dashed line outlines nodal cells.

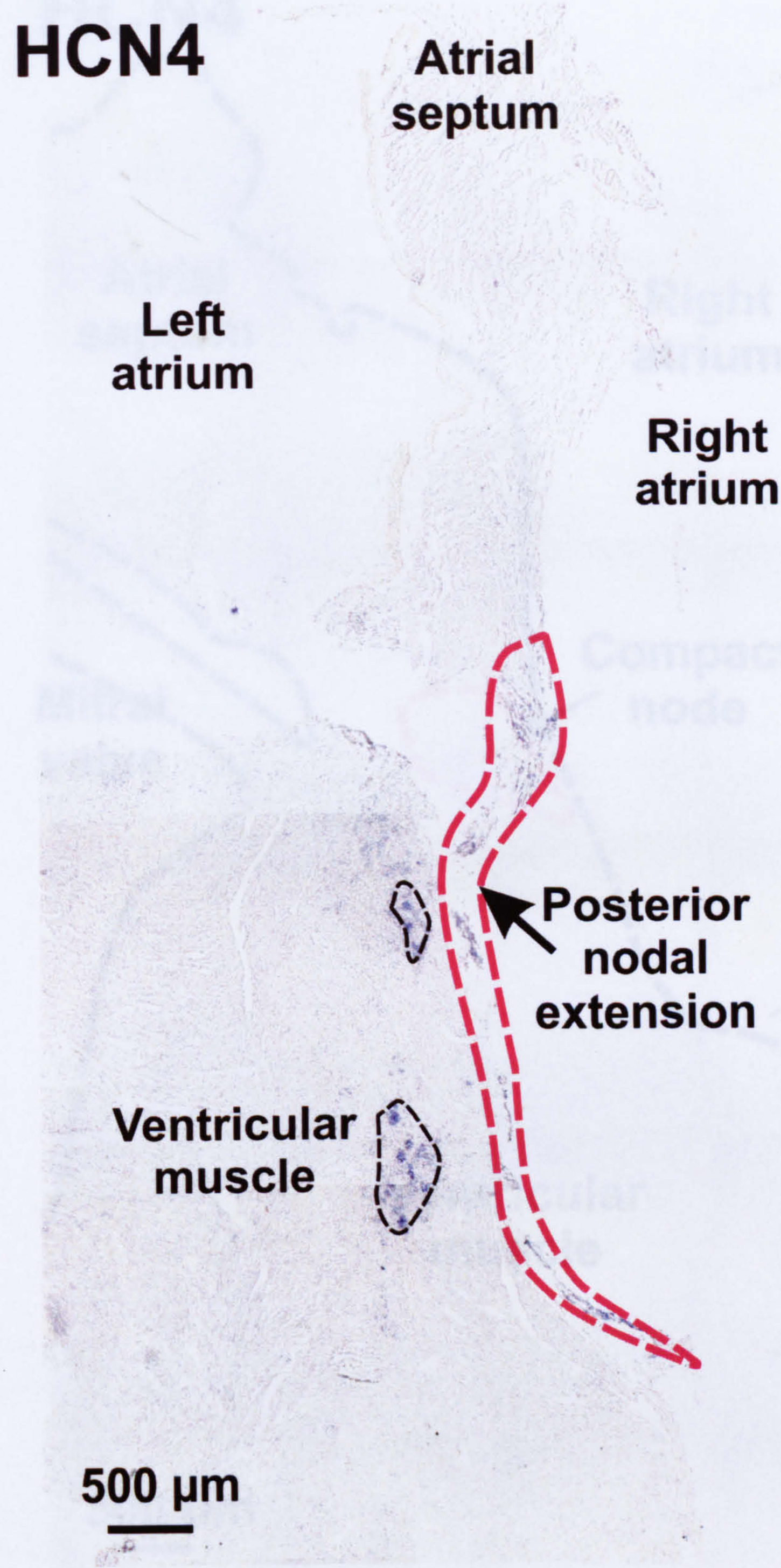

Figure 4.3 *In situ* hybridisation image for HCN4 mRNA at the level of the PNE. Red dashed line outlines cells comprising the PNE. Black dashed lines outline non-specific staining.

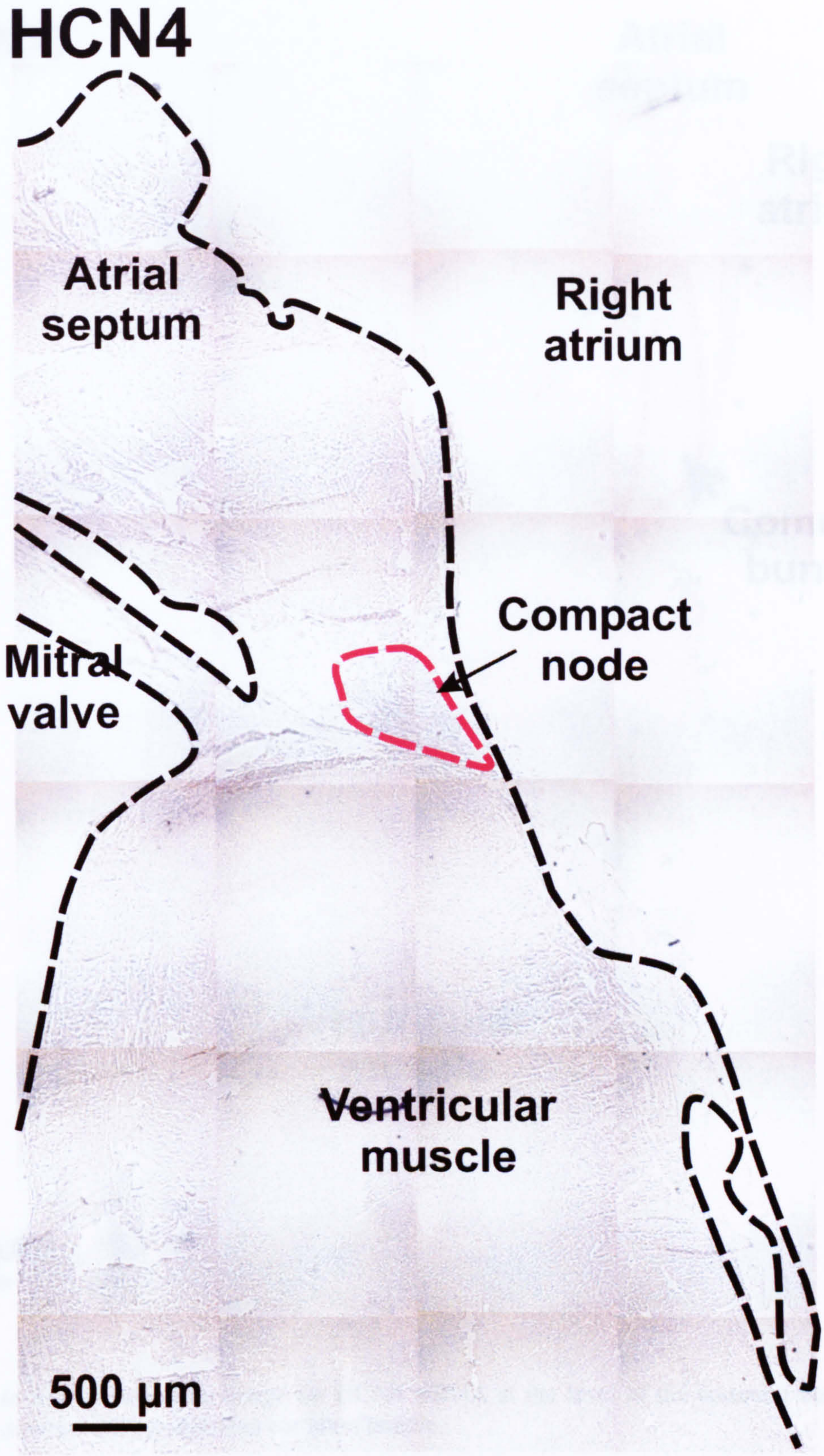

Figure 4.4 *In situ* hybridisation image for HCN4 mRNA at the level of the compact node. Red dashed line outlines cells comprising compact node. Black dashed line outlines tissue.

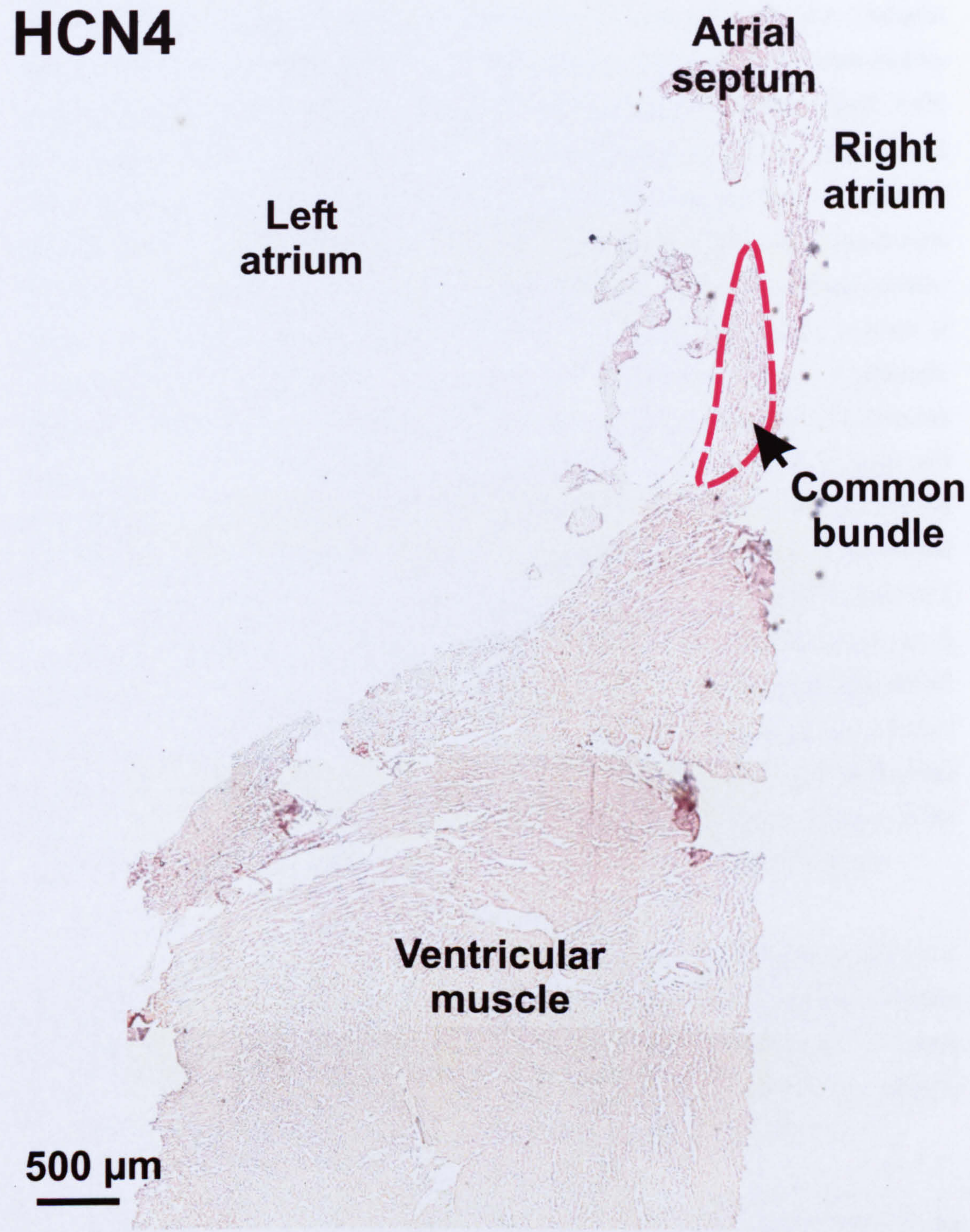

Figure 4.5 *In situ* hybridisation image for HCN4 mRNA at the level of the common bundle. Red dashed line outlines cells comprising common bundle.

However, Yuill and Hancox (2000), using guinea-pig AVN cells, measured a time-dependent inward current during hyperpolarising pulses from -40 mV, but the current in the diastolic depolarisation range of potentials was small, which suggests a negligible contribution of I_f to diastolic depolarisation in the AVN compared to the SAN (Habuchi et al., 1995). The contribution of I_f to pacemaking in the rabbit AVN was measured by Hancox and Levi (1994), who found 80-90 % of isolated single cells from rabbit AVN to be absent of I_f but still had the ability to generate spontaneous activity; they termed these cells "type-1". 10-20 % of cells did possess I_f, which was significantly enhanced by 100 nM isoprenaline; they termed these cells "type-2". It is likely that type-2 cells originate from the PNE, because I have shown these cells to contain significantly higher HCN4 mRNA levels than other cells within the AVN region. Furthermore, in terms of cell populations in the triangle of Koch area, the PNE cell population will be relatively small. In contrast, Munk et al. (1996) isolated two populations of single cells from the rabbit AVN: ovoid and rod shaped cells, and found I_f in the majority of both cell populations. I_f in ovoid cells was activated between -60 and -90 mV whereas I_f in rod shaped cells was activated at more negative potentials; the magnitude of I_f in ovoid cells was 25 times that in rod shaped cells (Munk et al., 1996). The activation threshold of I_f may provide insights into the different isoforms present in different cell populations: I_f activated at less negative voltages in ovoid cells and this could reflect the HCN1 isoform, which has been shown to have a half-maximal activation voltage of -73 mV; rod shaped cells have a more negative I_f activation range and this could reflect the HCN4 or even the HCN2 isoform, which have half-maximal activation voltages of -81 and -92 mV, respectively (Chen et al., 2001; Ishii et al., 1999; Accili et al., 2002).

These discrepancies regarding I_f from isolated single AVN cells (Hancox and Levi, 1994; Munk et al., 1996) could be the result of the harsh conditions of the cell isolation procedure leading to disruption of ionic currents and misleading results. Another limitation of these studies is that the exact location of the cells studied (type 1, type 2, ovoid, rod shaped) within the triangle of Koch cannot be determined.

Marionneau et al. (2005) have carried out similar mRNA expression analyses on the mouse AVN. HCN4 mRNA was found to be significantly higher in the SAN as compared to AVN, atrial muscle and ventricular muscle and ventricular muscle HCN4 mRNA was found to be were significantly lower than the SAN, AVN and atrial muscle. HCN1 mRNA was found to be significantly higher in the SAN compared to the AVN,

atrial muscle and ventricular muscle; ventricular muscle was found to have a significantly lower level of HCN1 mRNA (Marionneau et al., 2005). My finding of significantly low levels of HCN1 and HCN4 mRNA in the rabbit ventricular muscle (Figs. 4.1, 4.2D, 4.3-4.5) is consistent with the findings in mouse ventricular muscle. My findings of a higher expression of HCN4 mRNA in the PNE does not agree with the findings of Marionneau et al. (2005) who did not observe significantly higher amounts in the AVN compared to the atrial muscle and ventricular muscle. It is possible that a high level of HCN4 mRNA in the PNE of mouse in the study of Marionneau et al. (2005), was masked by the crude method of sampling tissue from the entire triangle of Koch region.

Chapter 5

Inward Na^+ current

5.1 Introduction

In the working myocardium the inward Na^+ current (I_{Na}) is responsible for the sharp upstroke of the action potential (phase 1). In contrast, the typical nodal action potential lacks a sharp upstroke. The rate of rise of a nodal action potential is about 5-10 V/s compared to >100 V/s for an atrial or ventricular action potential.

Na^+ channels are heteromeric complexes made up of a single, pore-forming, α-subunits together with two β-subunits. Ten α-subunits and four β-subunits (β1-4) have currently been identified (Caterall et al., 2000; Goldin et al., 2001). The β-subunits alter Na^+ channel gating, cell surface expression and function as cell adhesion molecules (Isom, 2001).

The α-subunit has four repeats, labelled I through IV. Each repeat contains six membrane-spanning regions labelled S1 through S6. The highly conserved S4 region acts as a voltage sensor, due to the presence of a positive amino acid at every third position, with hydrophobic residues inbetween. It is thought that when stimulated by a depolarisation of the membrane, this region moves within the membrane towards the extracellular side of the cell, causing the channel to become activated (i.e. open and permeable to Na^+ ions). On depolarisation, following activation of the channel, the channel is inactivated. The ability to inactivate is due to an inactivation gate (formed by a linker between domains III and IV), that blocks the inside of the channel shortly after it has been activated. The inactivation is removed when the membrane is hyperpolarised.

Rogart et al. (1989) cloned the first cardiac Na^+ channel from rat and named it rH1; in addition, a neuronal isoform was also detected but was not investigated further. A cardiac Na^+ channel isoform was also cloned from human heart (H1; Gellens et al., 1992). These channels were later identified as the major cardiac Na^+ channel isoform, $Na_v1.5$ (Malhotra et al., 2001). $Na_v1.5$ currents are resistant to nM concentrations of

tetrodotoxin (TTX), unlike neuronal isoforms ($Na_v1.1$, $Na_v1.2$, $Na_v1.3$ and $Na_v1.6$), and require μM concentrations for effective inhibition (Brown et al., 1981). In rat and mouse ventricular myocytes, $Na_v1.5$ is expressed at the intercalated disc, whereas $Na_v1.1$, $Na_v1.3$ and $Na_v1.6$ are expressed in the T-tubules (Maier et al., 2001). The function of neuronal Na^+ channels in the mammalian working myocardium is controversial: Maier et al. (2002) reported that nM concentrations of TTX caused a decrease in mouse left ventricular function, whereas Brette and Orchard (2006) detected no significant role for these channels in excitation-contraction coupling in isolated rat ventricular myocytes.

The role of Na^+ channels in pacemaker function is not clear. A TTX-sensitive current was detected in newborn rabbit SAN by Baruscotti et al. (1997). Half-maximal inhibition was achieved with a TTX concentration of 26 nM – this is characteristic of neuronal Na^+ channel isoforms, and it was thought this current was carried by $Na_v1.1$ channels. *In situ* hybridisation revealed expression of $Na_v1.1$ mRNA in newborn rabbit, although not in adult rabbit sinoatrial node (Baruscotti et al., 1997). Maier et al. (2003) showed that $Na_v1.1$ and $Na_v1.3$ are expressed in the adult mouse SAN and $Na_v1.1$ is expressed in the adult rat SAN. In addition, $Na_v1.5$ is not expressed in the adult mouse SAN. 100 nM TTX slowed the spontaneous activity of the adult mouse SAN (Maier et al., 2003). Interestingly, no effect of nM concentrations of TTX was seen on the P-R interval in adult mice suggesting a negligible role for neuronal Na^+ channels in AVN conduction (Maier et al., 2003).

The voltage-dependence of steady-state inactivation of $Na_v1.5$ is more negative than that of skeletal and neuronal isoforms (Makielski et al., 1996). Qu et al. (1995) using the rH1 Na^+ channel isoform investigated the effects of the β-1 subunit on cardiac Na^+ current, and found no alteration in the kinetics of the current, but up to six-fold increase in current expression.

Genetic mutations to SCN5A, the gene that encodes the $Na_v1.5$ channel, cause varying degrees of inactivity of the channel that manifest as different cardiac phenotypes. Long QT syndrome patients can have mutations in SCN5A that lead to impairments in inactivation of the channel (Wang et al., 1995). Schott et al. (1999) identified a mutation in SCN5A which was the underlying cause of Brugada syndrome. The patients showed a significant slowing of the heart rate (Schott et al., 1999). Papadatos et al. (2002)

generated a heterozygous SCN5A knockout mouse, SCN5A$^{+/-}$, which displayed an extreme prolongation of the P-R interval, and some cases of type II AVN block. Additional insights into the role of $Na_v1.5$ channels in AVN function have been gained from the identification of various mutations in the SCN5A gene that lead to varying degrees of AVN block and location of block (Brink et al., 1995; Schott et al., 1999; Tan et al., 2001; Wang et al., 2002; Viswanathan et al., 2003). Wang et al. (2002) describe two mutations in SCN5A that result in a decrease in the upstroke velocity in a simulation of the cardiac action potential. This would lead to a decrease in the conduction velocity during AVN conduction, possibly explaining the second degree AV block seen in patients with these mutations (Wang et al., 2002).

Kokubun et al. (1982) using microelectrode recordings from multicellular AVN preparations found 10 μM TTX to exert little effect on AVN upstroke velocity, which suggests that the Na^+ current does not play a major role in the AVN action potential. Hancox et al. (1993) also showed that the upstroke velocity of the AVN action potentials is slow suggesting a negligible role for the Na^+ current in the upstroke of the AVN action potential. Munk et al. (1996) reported that in isolated AVN cells, ovoid cells (possibly N-type cells) do not express Na^+ current, where rod cells (possibly AN-type or NH-type cells) do express Na^+ current. The aim of this chapter is to examine the expression of Na^+ channels in the rabbit AVN.

5.2 Methods

Real time PCR was performed using cDNA generated from total RNA isolated from five tissue types at the AV junction: atrial muscle, PNE, compact node, common bundle and ventricular muscle. A $Na_v1.1$ fragment was cross-species cloned using degenerate primers on rabbit cortex cDNA and a $Na_v1.5$ fragment was cross-species cloned using degenerate primers on rabbit whole heart cDNA. These fragments were sequenced and LightCycler primers were designed and optimised to amplify a fragment ~ 120-150 bp. Riboprobes were transcribed from pGEM T-easy vectors containing the specific $Na_v1.1$ and $Na_v1.5$ PCR fragments obtained using degenerate primers. In situ hybridisation was carried out using these riboprobes.

5.3 Results

5.3.1 *Real time* PCR

$Na_v1.1$ mRNA was significantly more abundant in the PNE, compact node and common bundle compared to the ventricular muscle ($p < 0.05$; Fig. 5.1A). There was also a tendency for $Na_v1.1$ mRNA to be more abundant in the nodal tissues compared to the atrial muscle (Fig. 5.1A). $Na_v1.5$ mRNA, in contrast, was more abundant in the atrial muscle compared with the PNE ($p <0.05$; Fig. 5.1B).

5.3.2 *In situ* hybridisation

In situ hybridisation for $Na_v1.5$ mRNA revealed an abundance of perinuclear staining in atrial muscle (Fig. 5.2A), compact node (Figs. 5.2C and 5.5) common bundle (Figs. 5.2D and 5.6) and ventricular muscle (Fig. 5.2F). At certain levels of the compact node and PNE some atrial muscle immediately anterior to the nodal tissue was devoid of $Na_v1.5$ perinuclear staining. The staining pattern in the compact node revealed an abundance of $Na_v1.5$ mRNA in the majority of this structure with a small group of cells (lower nodal cells) being largely devoid of $Na_v1.5$ perinuclear staining (Figs. 5.2D and 5.5). $Na_v1.5$ perinuclear staining in the PNE was largely absent (Figs. 5.3 and 5.4). However, in the proximal PNE (immediately adjacent to the CN), the cells lying endocardial most, were positive for $Na_v1.5$ mRNA, whereas those lying immediately adjacent to the ventricular crest were largely absent of $Na_v1.5$ perinuclear staining (Fig. 5.2E).

A riboprobe for $Na_v1.1$ mRNA was tested but failed to detect any mRNA in the AVN tissue sections. This $Na_v1.1$ riboprobe was tested on rabbit brain tissue sections and which produced strong perinuclear labelling in different brain regions. This demonstrates that the $Na_v1.1$ riboprobe is functional and thus the absence of $Na_v1.1$ staining at the AV junction is likely to be the result of a low abundance of $Na_v1.1$ mRNA.

5.4 Discussion

I have shown that mRNA for the cardiac Na^+ channel isoform, $Na_v1.5$, as well as the mRNA of the neuronal Na^+ channel isoform, $Na_v1.1$, is expressed at the rabbit AV junction.

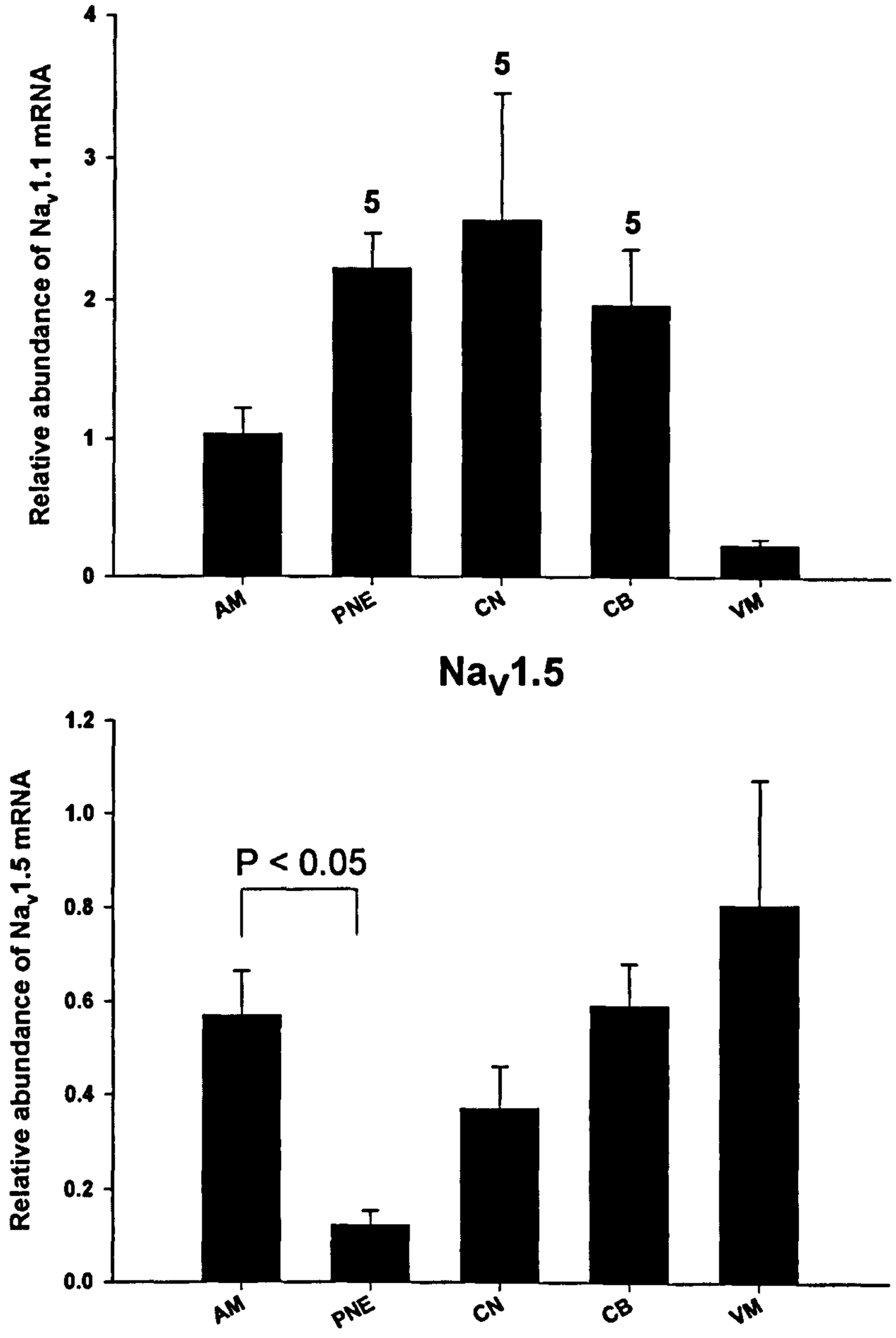

Figure 5.1 *Real time* PCR results for Na^+ channel mRNAs. 5, significantly different from VM ($p < 0.05$; one-way ANOVA). AM, atrial muscle; PNE, posterior nodal extension; CN, compact node; CB, common bundle; VM, ventricular muscle.

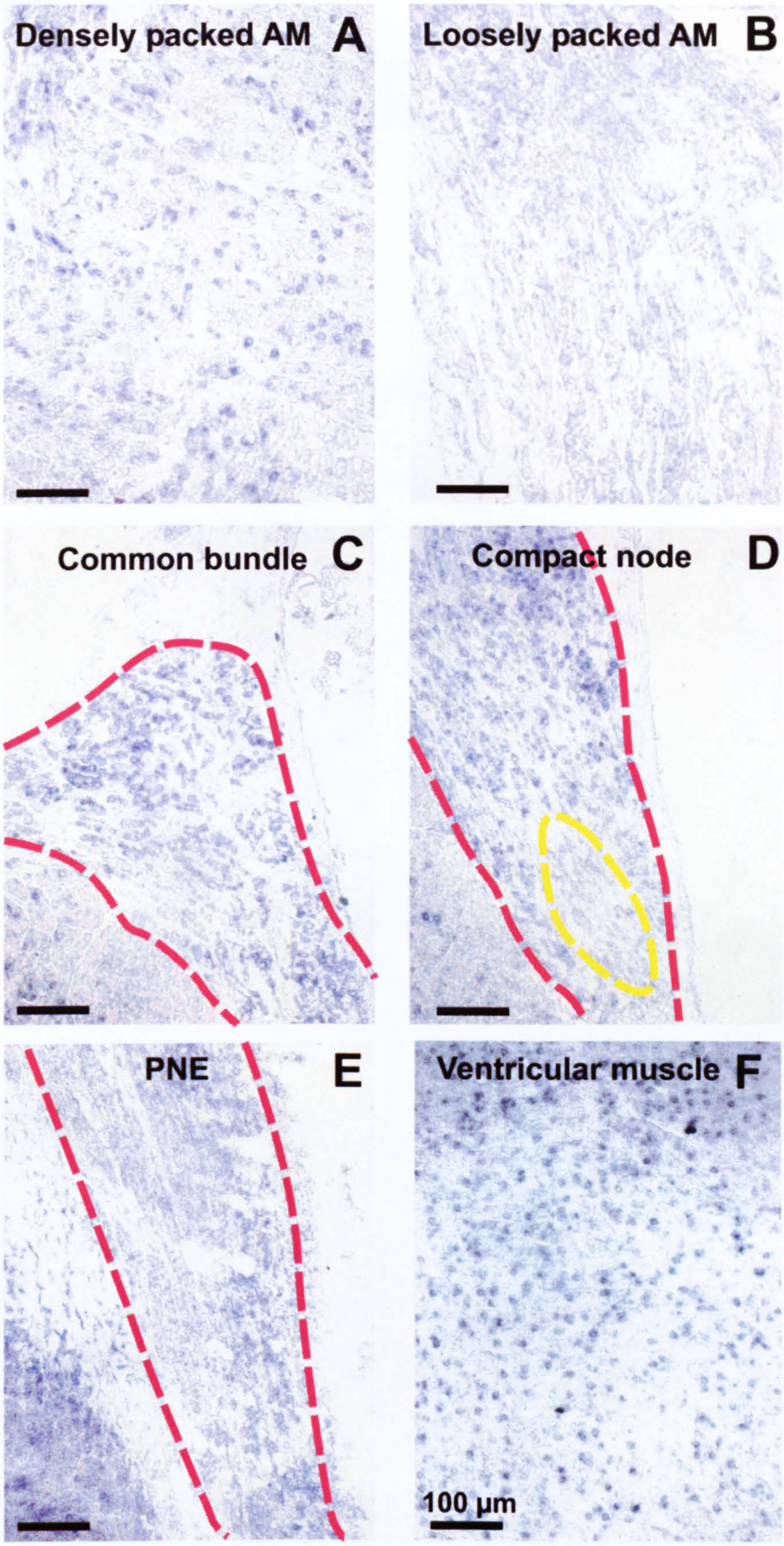

Figure 5.2 High power (x20 magnification) *in situ* hybridisation images for $Na_v1.5$ mRNA. A, densely packed atrial muscle; B, loosely packed atrial muscle; C, common bundle; D, compact node; E, posterior nodal extension; F, ventricular muscle. Red dashed lines outline nodal cells. Yellow dashed line outlines lower nodal cells.

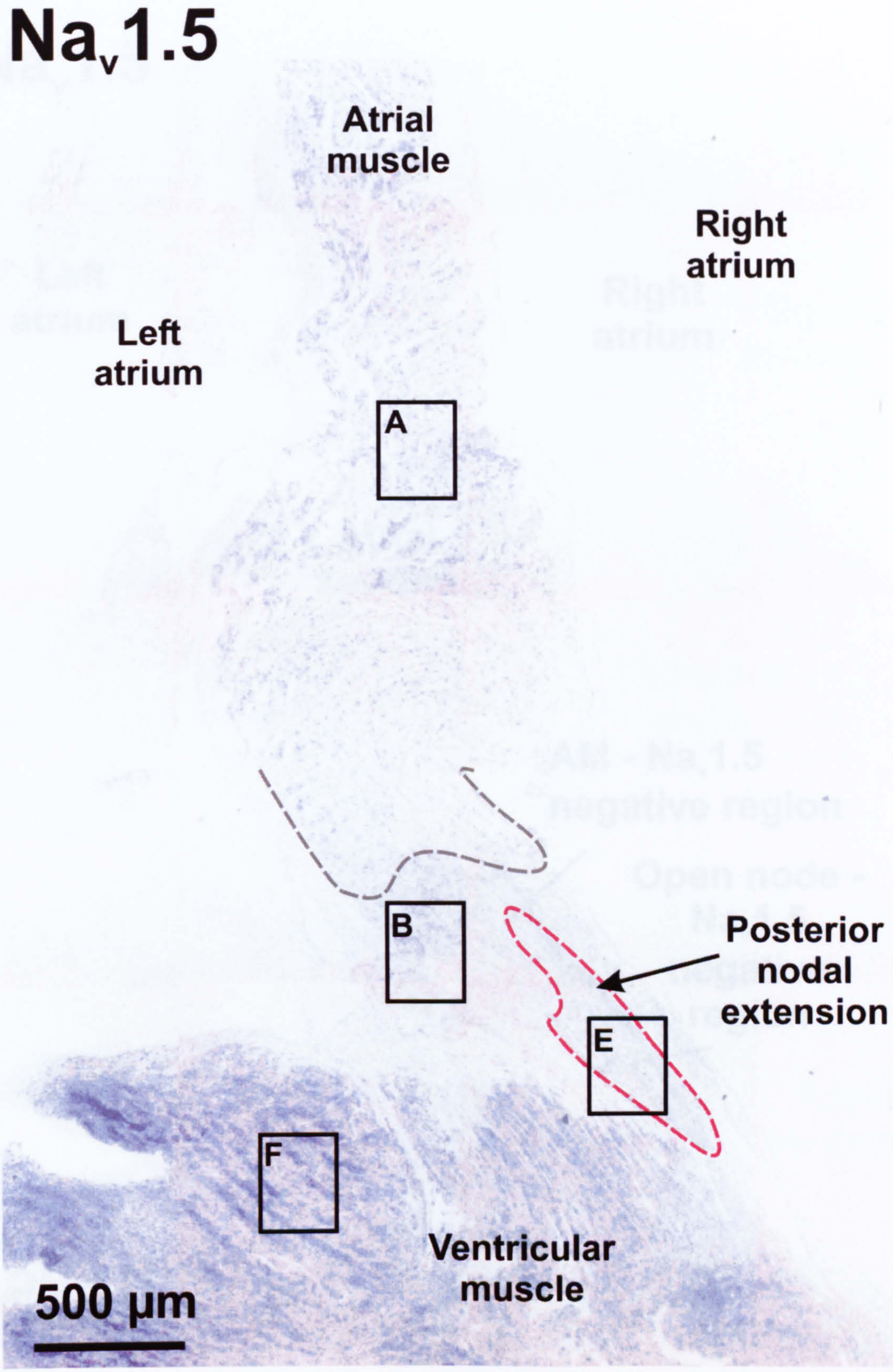

Figure 5.3 *In situ* hybridisation image for $Na_v1.5$ mRNA at the level of the PNE. Boxes indicate regions where the high power images in Fig. 5.2A, B, E and F were taken. Red dashed line outlines cells comprising PNE. Grey dashed line shows border of $Na_v1.5$ positive region (above the line).

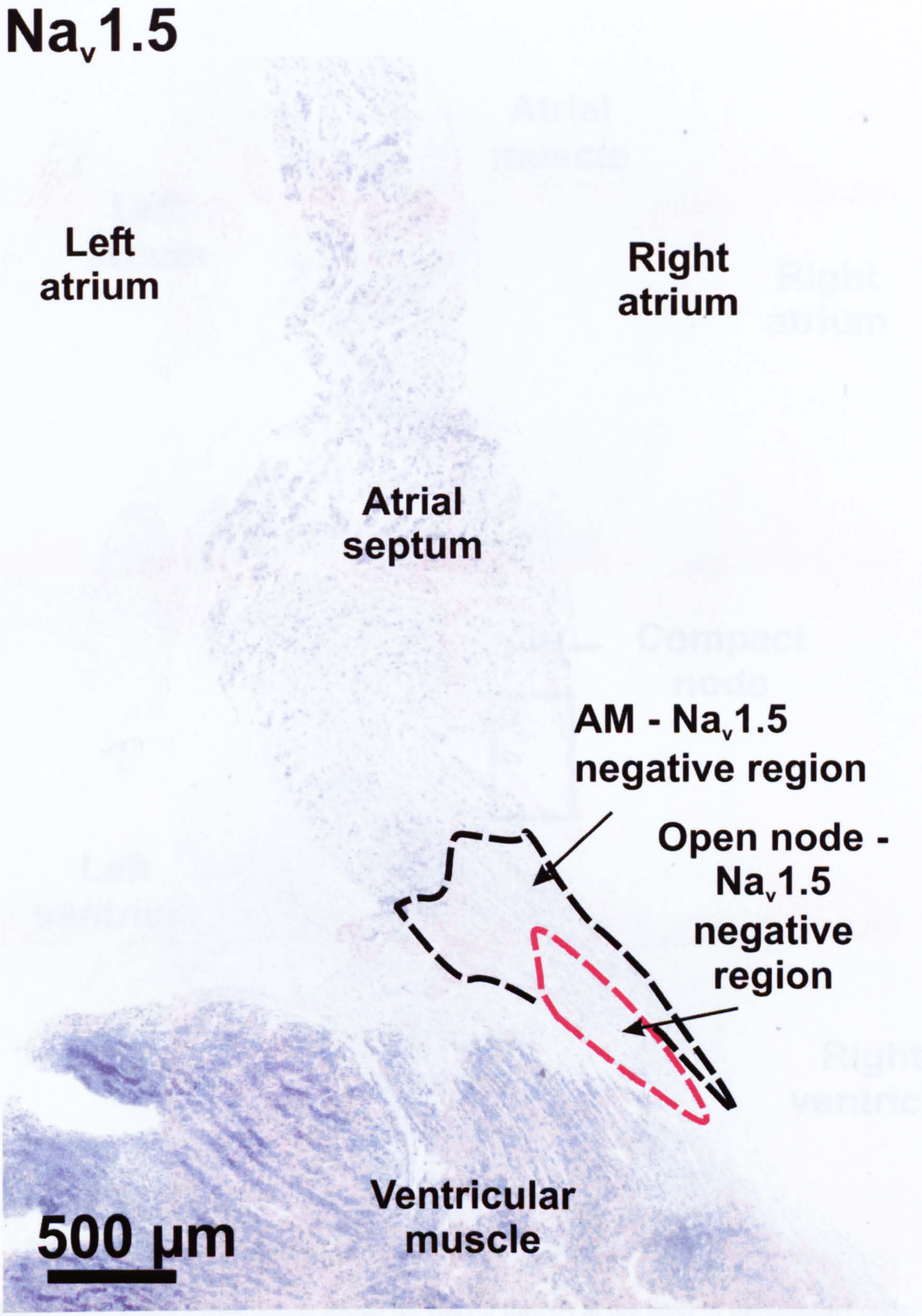

Figure 5.4 *In situ* hybridisation image for $Na_v1.5$ mRNA at the level of the open node. Red dashed line outlines cells comprising the open node. Black dashed line outlines $Na_v1.5$ negative area.

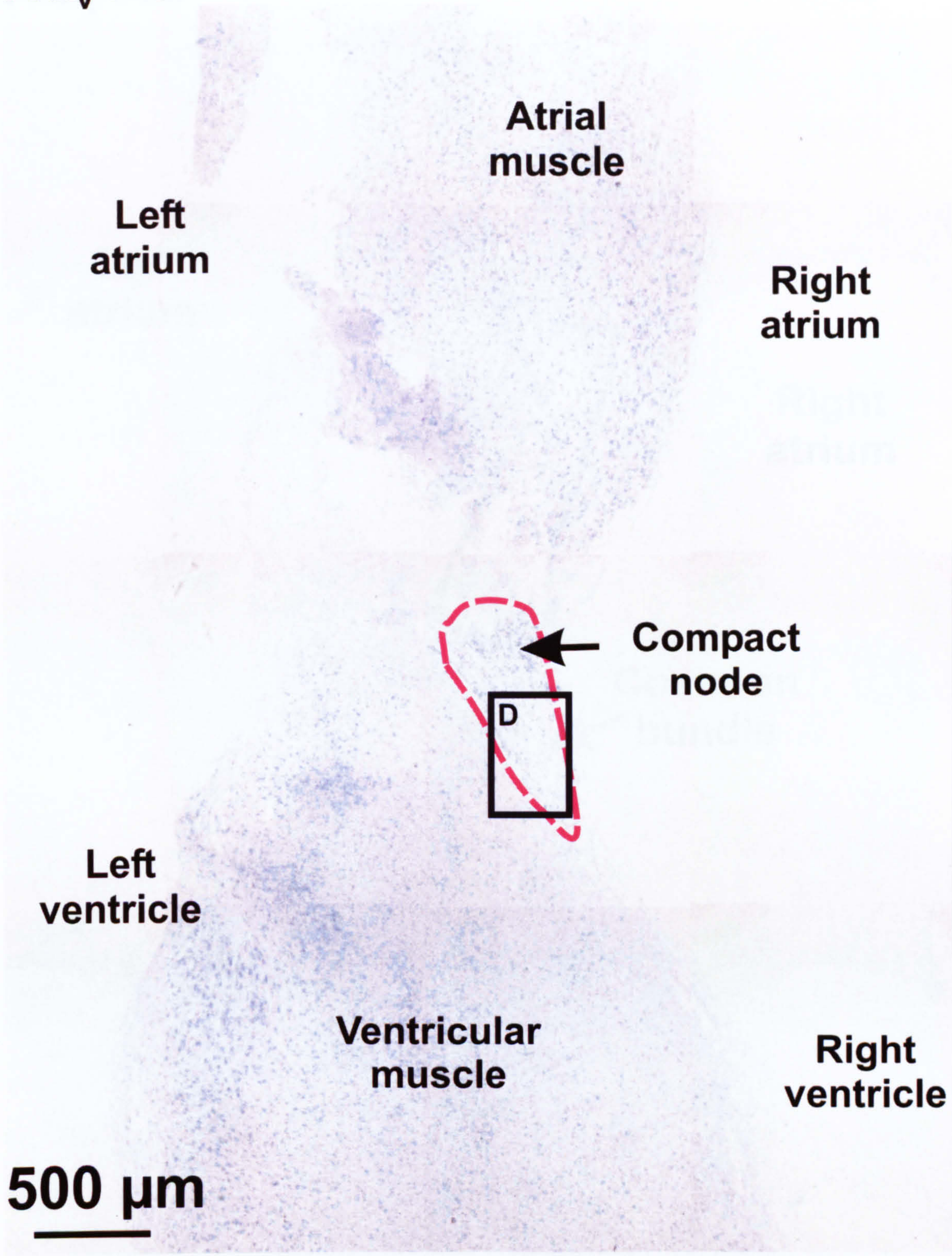

Figure 5.5 *In situ* hybridisation image for $Na_v1.5$ mRNA at the level of the compact node. Box indicates region where the high power image in Fig. 5.2D was taken. Red dashed line outlines cells comprising compact node.

$Na_v1.5$

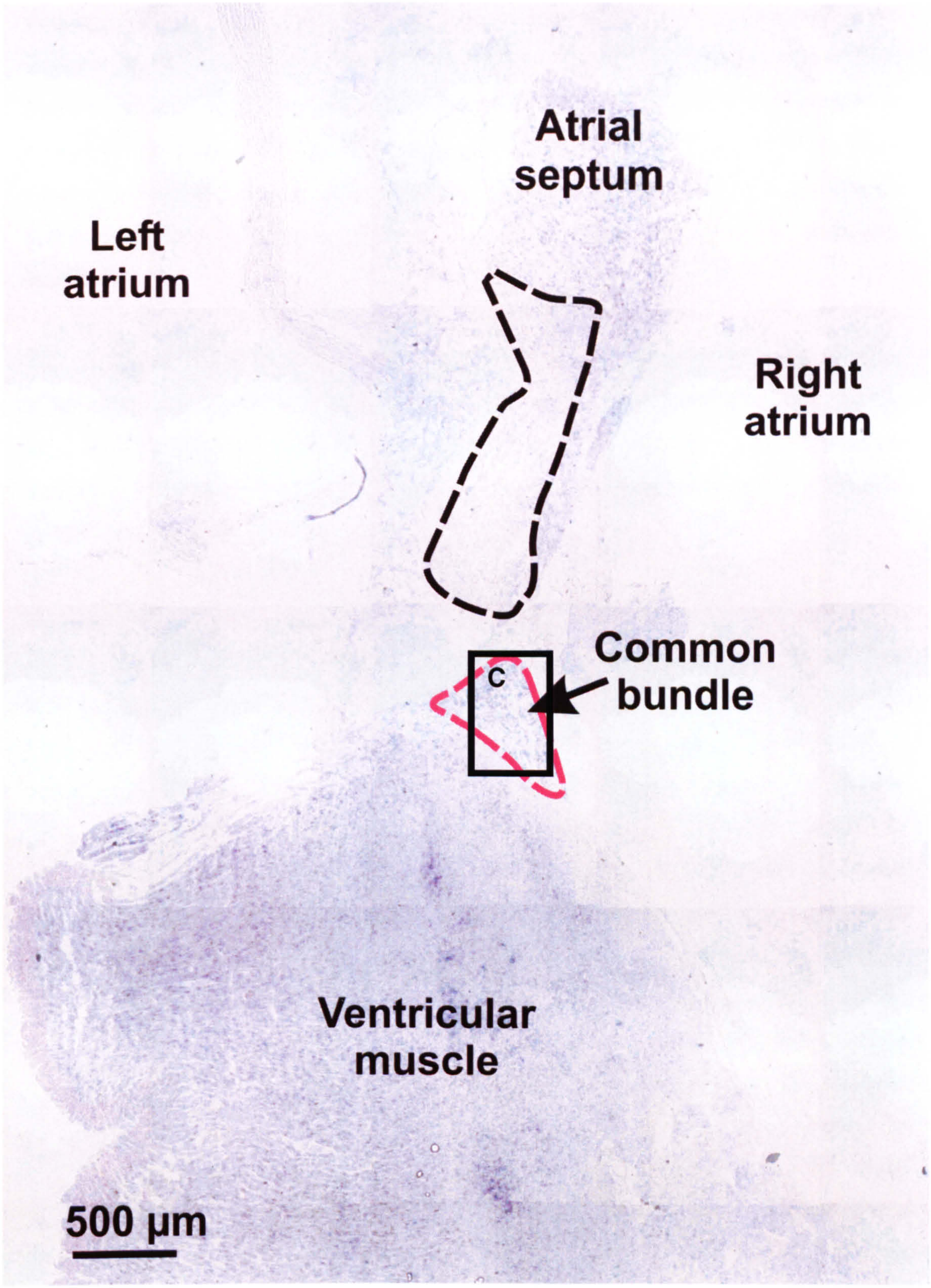

Figure 5.6 *In situ* hybridisation image for $Na_v1.5$ mRNA at the level of the common bundle. Box indicates region where high power image in Fig. 5.2C was taken. Red dashed line outlines cells comprising common bundle. Black dashed line indicates $Na_v1.5$ negative region.

The high abundance of $Na_v1.5$ mRNA in the AM and VM is consistent with previous findings showing that $Na_v1.5$ is the major isoform responsible for the Na^+ channel in the working myocardium (Rogart et al., 1989; Gellens et al., 1992; Petrecca et al., 1997; Malhotra et al., 2001). The presence of $Na_v1.5$ in the atrial and ventricular muscle is compatible with the more negative resting membrane potential (~ -80 mV) in these tissues, because the $Na_v1.5$ channels will be available for activation. In nodal tissues with a more positive membrane potential (~ -50 mV) $Na_v1.5$ channels will be largely inactivated.

The common bundle showed similar levels of $Na_v1.5$ mRNA as the atrial muscle, compatible with its fast conduction. These data suggest that the AVN delay occurs prior to the common bundle, because upon reaching the common bundle the action potential will be rapidly conducted towards the bundle branches and Purkinje fibres to eventually excite the ventricles.

Petrecca et al. (1997) using immunofluorescence labelling of Na^+ channels showed the rabbit compact node to express Na^+ channels. However, Petrecca et al. (1997) reported that the circumferential transitional cells showed labelling, whereas the 'mid-nodal' cells were largely devoid of labelling. Furthermore, using semi-quantitative immunofluorescent analysis, Petrecca et al. (1997) found similar levels of Na^+ channel expression in the circumferential transitional cells and lower nodal cells compared to ventricular muscle. The presence of Na^+ channels in the circumferential transitional cells is consistent with my observation of abundant $Na_v1.5$ mRNA in this region. However, I also show an abundance of $Na_v1.5$ mRNA in the cells described by Petrecca et al. (1997) as the mid-nodal cells. If the mid-nodal cells are largely devoid of Na^+ channels then it is likely that a post-transcriptional mechanism regulates the surface expression of Na^+ channels at the membrane in the mid-nodal cell region. The presence of Na^+ channel protein in the lower nodal cells (Petrecca et al., 1997) is in contrast to my finding of a lack of $Na_v1.5$ mRNA in this area. However, it must be stressed that in the study of Petrecca et al. (1997), the antibody used was targeted to an epitope in a highly conserved region of Na^+ channels and, therefore, the antibody will not discriminate between different Na^+ channel isoforms. It is, therefore, a possibility that the immunofluorescent labelling observed by Petrecca et al. (1997) in the lower nodal cells represents labelling of Na^+ channel isoform other than $Na_v1.5$, such as $Na_v1.1$ (I

show that $Na_v1.1$ mRNA to be higher in the compact node tissue compared to ventricular muscle and atrial muscle using *real time* PCR). Alternatively, the discrepancies between my findings and those of Petrecca et al. (1997) are possibly due to an alternative interpretation of the anatomy. For instance, they subclassify the area of the AVN I describe as the compact node into circumferential transitional cells, mid-nodal cells and lower nodal cells based on the histological definition first used by Anderson (1972). However, the group of cells they refer to as lower nodal cells appears in a section at the level of the compact node as an oval-shaped group of cells with abundant immunolabeling of Na^+ channels. However, this structure appears to be the whole compact node and not the small collection of cells in the lower region of the compact node; the abundance of fluorescent labelling throughout this structure (the compact node) contradicts their conclusions regarding an absence of Na^+ channel immunolabeling in the mid-nodal cells. Secondly, the cells they refer to as lower nodal cells appear to be located towards the middle of the oval-shaped group of cells rather than towards the tail of the compact node.

The lack of perinuclear staining for $Na_v1.1$ mRNA using *in situ* hybridisation suggests that, although *real time* PCR detected significantly more $Na_v1.1$ mRNA in the PNE, compact node and common bundle, than in the atrial and ventricular muscle, that mRNA levels are relatively low and, therefore, the role of the $Na_v1.1$ channel in AVN function is likely to be negligible. This agrees with previous work in mice in which nM concentrations of TTX had little effect on the P-R interval (Maier et al., 2003). The significantly higher amount of $Na_v1.1$ mRNA detected in the nodal regions (PNE, compact node and common bundle) is consistent with previous findings from mouse AVN, in which there was a significantly higher level of $Na_v1.1$ mRNA as compared to the SAN, AM and VM (Marionneau et al., 2005). In the study of Marionneau et al. (2005) the abundance of $Na_v1.1$ mRNA was than that of $Na_v1.5$ mRNA. In the study of Marionneau et al. (2005) there was a high level of $Na_v1.5$ mRNA in the AVN sample; this can be accounted for by the large contamination of the AVN sample with atrial myocytes (43 %). In the present study there was little or no contamination of the AVN samples because of the sampling technique used. In addition, Marionneau et al. (2005) also found significantly higher levels of mRNA for $Na_v1.7$, and the Na^+ channel β_1 and β_3 subunits. β_1 and β_2 subunits are known to speed up the normally slow inactivation of neuronal Na^+ channels (Tamkun et al., 1984; Hartshorne et al., 1985; Isom et al., 1992; Morgan et al., 2000). Studies involving familial mutations in the gene encoding the

$Na_v1.1$ channel, SCN1A, have focused on the profound CNS abnormalities that exist, such as epilepsy and febrile seizures (Escayg et al., 2000; Alekov et al., 2000). In these studies no mention is made of any cardiac abnormalities in these subjects. In the light of my findings, it would be interesting, however, to produce transgenic mice with similar loss of function mutations in SCN1A or complete gene knock-out to gain a better understanding of $Na_v1.1$ function in the AVN.

Dobrzynski et al., (2002) showed the leading pacemaker site in the AVN to be the PNE. The properties of this region can be compared to those of the leading pacemaker region in the SAN (SAN centre): in the SAN centre, there is little $Na_v1.5$ mRNA (or protein) (Tellez, 2005; Maier et al., 2004) as in the PNE. In the SAN centre, there is a greater abundance of $Na_v1.1$ mRNA (Tellez et al., 2005) as in the PNE.

Familial mutations in the SCN5A channels and mice heterozygous, $Na_v1.5^{+/-}$, for $Na_v1.5$ channels display profound AVN conduction disturbances. Why do mutations in the $Na_v1.5$ channel alter AVN conduction? Na^+ channels are responsible for the upstroke of the action potential and therefore determine upstroke velocity. In turn, upstroke velocity is a major contributor to conduction velocity. Our anatomical findings (see chapter 3) suggest that the PNE most likely represents the slow pathway since optical mapping of AVN preparations showing conduction along the slow pathway correlate with the anatomical boundaries for the PNE. Billette (1987) showed this area of the rabbit AVN to contain mainly NH cells which have an upstroke velocity of ~ 17 V/s, suggesting a lack of a Na^+ current. The findings of Billette (1987) agree with my findings at the PNE which I have shown to be largely absent of $Na_v1.5$ mRNA. Collectively, these findings indicate that an action potential would travel slowly along the slow pathway and that mutations in $Na_v1.5$ would be unlikely to effect conduction along the slow pathway. The entry point of the fast pathway into the AVN is from an anterior direction which most likely corresponds to loosely packed atrial muscle based upon our anatomical findings (chapter 3). Using *in situ* hybridisation I have shown an area of loosely packed atrial muscle to be largely absent of $Na_v1.5$ mRNA. Billette (1987) showed an area of transitional cells to contain mainly AN cells which have an upstroke velocity of ~ 40 V/s which, again, suggests a lack of a Na^+ current. These data indicate that mutations in $Na_v1.5$ would be unlikely to effect conduction through the loosely packed atrial muscle. The fast pathway most likely travels via densely packed atrial muscle. Atrial muscle has an action potential upstroke velocity of > 100 V/s and therefore is likely to contain

$Na_v1.5$ channels. I have shown densely packed atrial muscle to contain an abundance of $Na_v1.5$ mRNA. These data suggest that conduction through densely packed atrial muscle could be slowed due to a decrease in the upstroke velocity of atrial action potentials due to mutations in $Na_v1.5$ channels. I have shown the compact node and common bundle to contain an abundance of $Na_v1.5$ mRNA. Billette (1987) showed that the majority of cells comprising these areas were N and NH cells with upstroke velocities of ~ 18 V/s, which suggests an absence of Na^+ channels. The relatively low maximum diastolic potential of the N and NH cells (~ -60 mV; Billette, 1987) would inactivate $Na_v1.5$ channels. These data suggest that, although, I have shown $Na_v1.5$ mRNA to be abundant in the compact node and common bundle, $Na_v1.5$ channels are unlikely to play a significant role in conduction through these structures. Collectively, these data suggest that mutations in $Na_v1.5$ channels would impair action potential propagation at a point prior to its entry into the AVN.

There is the possibility that another Na^+ channel isoform such as, $Na_v1.1$, which I have shown the mRNA encoding this channel to be abundantly expressed in the PNE, compact node and common bundle, provides significant inward Na^+ current in these regions. Marionneau and colleagues (2005) showed in mouse AVN there to higher expression of $Na_v1.7$ mRNA compared to SAN, atrial muscle and ventricular muscle; in addition, they showed greater abundance of the Na^+ channel β-subunits, Na_v -β_1 and -β_3, which are known to speed up Na^+ channel current kinetics (Isom et al., 1992; Morgan et al., 2000). The combination of $Na_v1.1$ or $Na_v1.7$ with either of the β-subunits may be sufficient to provide an inward current for the upstroke of the action potential in the absence of $Na_v1.5$ channels. However, based on findings in the SAN, whereby μM concentrations of TTX have little effects on SAN spontaneous activity, it is likely that Na^+ channel contribution to AVN function is negligible.

Chapter 6

Ca^{2+} current

6.1 Introduction

Reuter (1967) was the first to detect an inward Ca^{2+} current (I_{Ca}) in sheep Purkinje fibres after the removal of extracellular Na^+ (Reuter, 1967). This current became known as the "slow" or "secondary inward" current (I_{si}) as opposed to the original fast activating and inactivating inward Na^+ current (Noble, 1984). Brown et al. (1979) found this current to be activated in the diastolic depolarisation range of pacemaker cells and to be significantly enhanced by adrenaline. Hagiwara et al. (1988) using rabbit SAN pacemaker cells dissected the Ca^{2+} current into two major components: the "transient", T-type, and the "long-lasting", L-type, Ca^{2+} currents based on their fast and slow inactivation, respectively. The T-type Ca^{2+} channels activate at ~ -50 mV, as opposed to ~ -40 mV for the L-type Ca^{2+} channels and have a smaller single channel conductance (T-type, 8 pS, L-type, 16 pS). The more negative voltage-dependence of T-type Ca^{2+} channels suggests a greater role for these channels during the diastolic depolarisation phase of pacemaker cells. Indeed, 40 μM Ni^{2+} (blocks T-type Ca^{2+} channels) leads to a reduction in the spontaneous activity of pacemaker tissue (Hagiwara et al., 1988). Huser et al. (2000) using cat pacemaker cells showed that T-type Ca^{2+} channels contribute to pacemaking by inducing subsarcolemmal Ca^{2+} release from SR stores, which in turn generates a net inward current via Na^+-Ca^{2+} exchange (I_{NCX}); inward I_{NCX} contributes to diastolic depolarisation. Three different α subunits for T-type Ca^{2+} channels exist: $Ca_v3.1$, $Ca_v3.2$ and $Ca_v3.3$. Of these channels, it appears $Ca_v3.1$ is the most abundant isoform, at least in the murine SAN (Bohn et al., 2000).

In mammals the α-subunit of the voltage-dependent L-type channel is encoded by four genes (Ertel et al., 2000): $Ca_v1.1$ (α1S), $Ca_v1.2$ (α1C), $Ca_v1.3$ (α1D) and $Ca_v1.4$ (α1F). L-type Ca^{2+} channels show very little inactivation in extracellular Ba^{2+} (Nowycky et al., 1985). However, in the presence of extracellular Ca^{2+}, L-type Ca^{2+} channels show Ca^{2+}-dependent inactivation (Soldatov et al., 1997). These channels are the target for downstream signalling complexes as a result of β-adrenoceptor stimulation. Activation of adenylate cyclase leads to rises in camp, which in turn stimulates protein kinase A-

mediated phosphorylation of L-type Ca^{2+} channels causing an enhancement of $I_{Ca,L}$ (Kemp and Hell, 2000; Qu et al.). $Ca_v1.2$ and $Ca_v1.3$ unlike the other members of the voltage-dependent Ca^{2+} channels show no G-protein mediated modulation (Bell et al., 2001). L-type Ca^{2+} current carried by the $Ca_v1.3$ α-subunit activates at voltages approximately 30 mV more hyperpolarized than that carried by $Ca_v1.2$. Additionally, $Ca_v1.3$-mediated currents show sensitivity to dihydropyridines in the μM range compared to nM concentrations for currents carried by $Ca_v1.2$ channels (Bell et al., 2001; Xu and Lipscombe, 2001; Mangoni et al., 2003). The relative negative voltage-dependence of activation of $Ca_v1.3$ channels suggests that they may contribute to inward current during the diastolic depolarisation phase in pacemaker cells. Zipes and Mendez (1973) first studied the role of $I_{Ca,L}$ in the AVN using Mn^{2+} as a blocker of $I_{Ca,L}$, they showed this current to be important for the action potential upstroke in AVN cells. Noma (1980) was first to make I_{Ca} recordings in AVN tissue. However, these findings have to be treated with caution since voltage-clamping multicellular preparations is difficult and can be inaccurate. Hancox and Levi (1994) using single AVN myocytes showed I_{Ca} to be greatly reduced by nifedipine. Steady-state activation and inactivation curves showed half-maximal activation at -3.6 mV and half-maximal inactivation at –25.8 mV; both, the time course of decay from a depolarising pulse and recovery from inactivation were biexponential (Hancox and Levi, 1994). Zipes and Fischer (1974) injected Ca^{2+} channel blockers into the AVN artery of dogs and saw a development of AVN block, suggestive of a major role for this current in AVN conduction.

In mouse SAN cells, $I_{Ca,L}$ is activated at –50 mV and peaks around –10 mV (Mangoni et al., 2003). Even though the sensitivities of $Ca_v1.2$ and $Ca_v1.3$ to the L-type Ca^{2+} channel blockers, 1,4-dihydropyridines (DHPs), is ~ 1000-fold different, L-type Ca^{2+} channel agonists such as BayK8644 fail to distinguish between the two isoforms. The lack of isoform specific agonists and antagonists, together with the advent of transgenic mice, has made the genetic alteration of genes encoding $Ca_v1.2$ and $Ca_v1.3$ channels the preferred approach to studying L-type Ca^{2+} channel function in the mouse heart, in particular, in the SAN and AVN. Seisenberger et al. (2000) generated heterozygous (+/-) and homozygous mice (-/-) for $Ca_v1.2$ and found there to be no difference in the frequency of cardiac contraction; other Ca_v1 channels were ruled out and it was suggested that a novel isoform of Ca_v1 channel may exist in the mouse heart.

Platzer et al. (2000) were the first to directly show a major functional role for $Ca_v1.3$-mediated L-type Ca^{2+} current in cardiac pacemaker tissue by generating a $Ca_v1.3$ knock-

out mouse. This displayed sinus bradycardia and a prolonged P-R interval (Platzer et al., 2000). Furthermore, Mangoni et al. (2003) using the same line of $Ca_v1.3$ null mice isolated single cells from the mouse SAN and found a slowing of pacemaker function and a tendency for irregular activity. Interestingly, a depolarising shift in the voltage-dependence of $I_{Ca,L}$ in $Ca_v1.3^{-/-}$ mice compared to wild-type $Ca_v1.3^{+/+}$ mice was recorded suggesting residual $I_{Ca,L}$, possibly carried by $Ca_v1.2$ channels. In addition, they provided evidence for the expression of $Ca_v1.3$ mRNA in the human AVN (Mangoni et al., 2003). In a similar study, again using transgenic mice with targeted disruption of the $Ca_v1.3$ gene, a slowing of the spontaneous firing rate, in particular the diastolic depolarisation phase in intact SA node preparations, was shown (Zhang et al. 2002). Moreover, Zhang et al. (2002) detected the presence of second-degree AV Block using ECG recordings in the $Ca_v1.3^{-/-}$ mice(Zhang et al., 2002). More recent evidence for the important role of $Ca_v1.3$ channels in AVN function comes from Matthes et al. (2004) again using homozygous $Ca_v1.3^{-/-}$ mice. Mathes et al. (2004) who found that the AVN conduction time (P-R interval) was significantly prolonged and could not be overcome with isoprenaline (unlike the SAN) (Matthes et al., 2004). The aim of this chapter is to examine the expression of L-type Ca^{2+} channels in the rabbit AVN.

6.2 Methods

6.2.1 *Real time* PCR

Real time PCR for $Ca_v1.2$, $Ca_v1.3$ and $Ca_v3.1$ was performed using cDNA generated from total RNA isolated from five rabbit AVN tissue types: atrial muscle, PNE, compact node, common bundle and ventricular muscle. (n = 8 rabbits). As described in chapter 2. *Real time* PCR was carried out using a Roche LightCycler 1.0. Primers were designed against $Ca_v1.2$ and $Ca_v1.3$ fragments which had been cross-species cloned from rabbit brain or whole heart cDNA by Dr. James Tellez.

6.2.2 *In situ* hybridisation

Riboprobes for $Ca_v1.2$ and $Ca_v1.3$ were generated by James Tellez using methods similar to those described in section 2 (Riboprobe Synthesis; Tellez et al., 2005).
In situ hybridisation was carried out using a modified version of the Braissant protocol, described in chapter 2 (n=2). No riboprobe was synthesised for $Ca_v3.1$.

6.3 Results:

6.3.1 *Real time* PCR

Real time PCR data for $Ca_v1.2$ mRNA showed no significant differences between different tissue regions (Fig. 6.1A). In contrast, *real time* PCR for $Ca_v1.3$ mRNA showed significantly ($P < 0.05$) higher amounts in the PNE, compact node and common bundle compared to ventricular muscle (Fig. 6.1B). In addition, atrial muscle showed a tendency for higher expression of $Ca_v1.3$ mRNA compared to ventricular muscle (Fig. 6.1B). $Ca_v3.1$ transcripts failed to be detected.

6.3.2 *In situ* hybridisation

In situ hybridisation revealed an abundance of $Ca_v1.3$ perinuclear staining in the PNE (Figs. 6.6C and 6.7), compact node (Figs. 6.6B and 6.8) and common bundle (Figs. 6.6A and 6.9). In contrast, the atria and ventricles were largely absent of $Ca_v1.3$ staining. The AM and VM showed an abundance of perinuclear staining for $Ca_v1.2$ mRNA (Figs. 6.2-6.5), whereas the PNE (Figs. 6.2E and 6.3), CN (Figs. 6.2C and 6.4) and CB (Figs. 6.2B and 6.5) were devoid of $Ca_v1.2$ mRNA. Interestingly, the small group of lower nodal cells at the level of the PNE and CN (Fig. 6.2D) showed abundant $Ca_v1.2$ perinuclear staining.

6.4 Discussion

My findings show that the predominant L-type Ca^{2+} channel isoform in the AVN is $Ca_v1.3$. These findings are consistent with a major role for this ion channel in the pacemaker action potential upstroke and for normal AVN conduction (Platzer et al., 2000; Zhang et al., 2002; Mangoni et al., 2003; Matthes et al., 2004; Zhang et al., 2005). I have shown the PNE and CN to be highly abundant for $Ca_v1.3$ mRNA which supports evidence from $Ca_v1.3^{-/-}$ mice which display a prolonged PR interval (Matthes et al., 2004). The detection of abundant $Ca_v1.3$ mRNA in the AVN tissues agrees with findings from human and mouse AVN tissue (Mangoni et al., 2003; Marionneau et al., 2005). This suggests that the $Ca_v1.3$ channel may be important in the rabbit, mouse and human AVN. In addition, separate studies using $Ca_v1.3^{-/-}$ mice show a slowing of

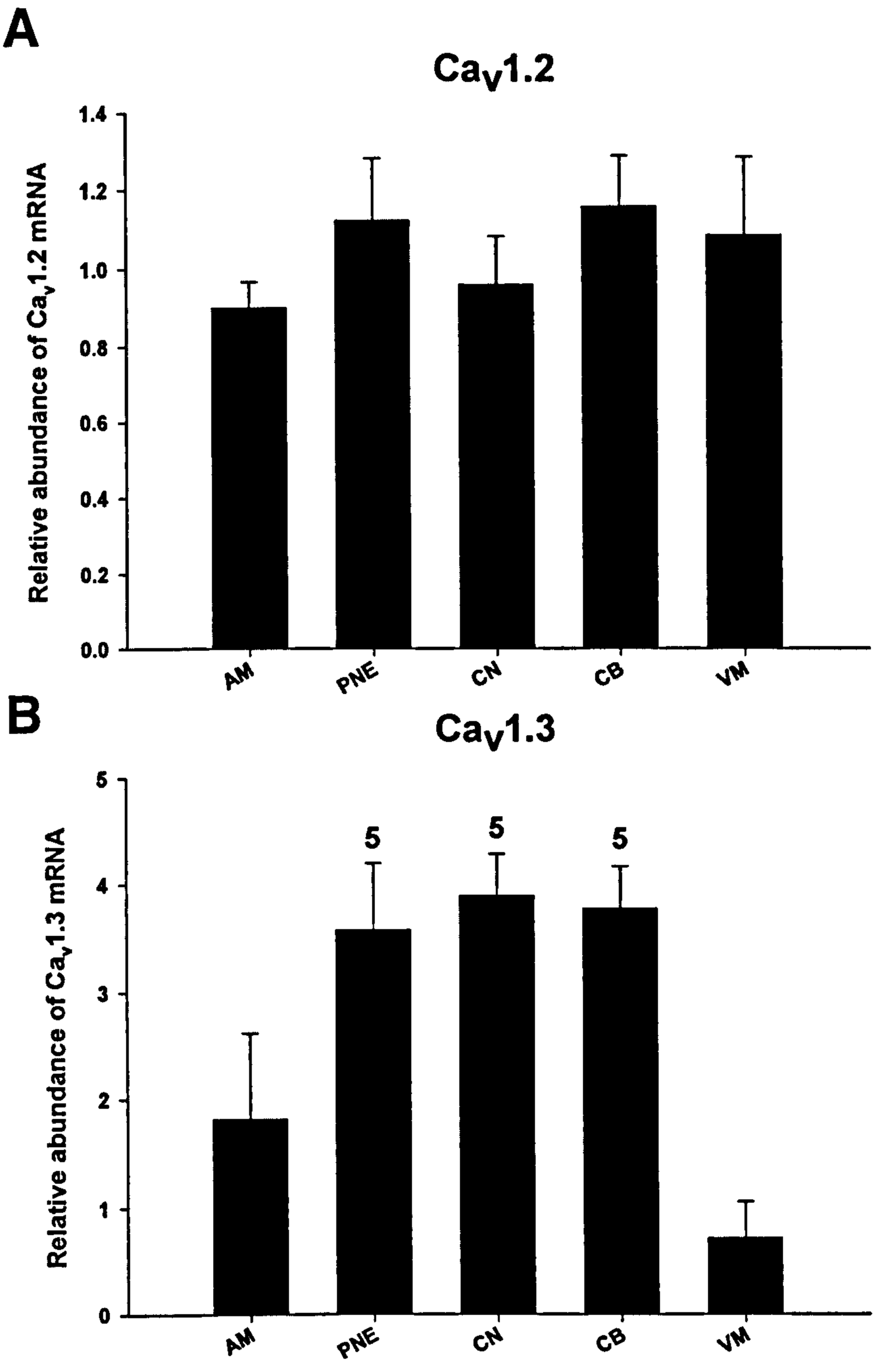

Figure 6.1 *Real-time* PCR results for Ca^{2+} channel mRNAs. The relative abundance of $Ca_v1.2$ (A) and $Ca_v1.3$ (B) mRNAs was quantified in AVN tissue samples. 5, significantly different from VM ($P < 0.05$; One-way ANOVA). AM, atrial muscle; PNE, posterior nodal extension; CN, compact node; CB, common bundle; VM, ventricular muscle.

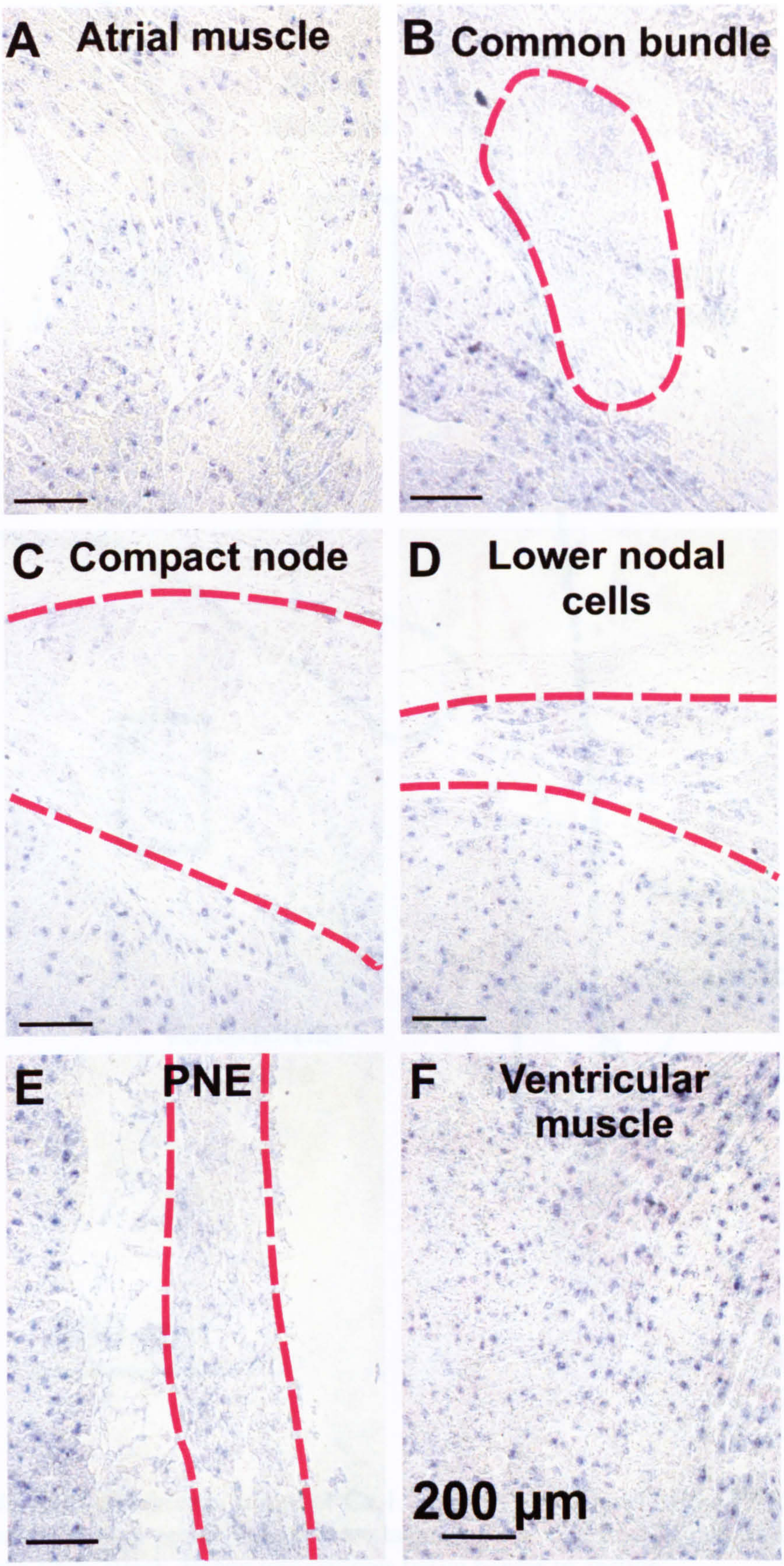

Figure 6.2 High power (x20 magnification) *in situ* hybridisation images of $Ca_v1.2$ mRNA. Dashed line outlines nodal cells.

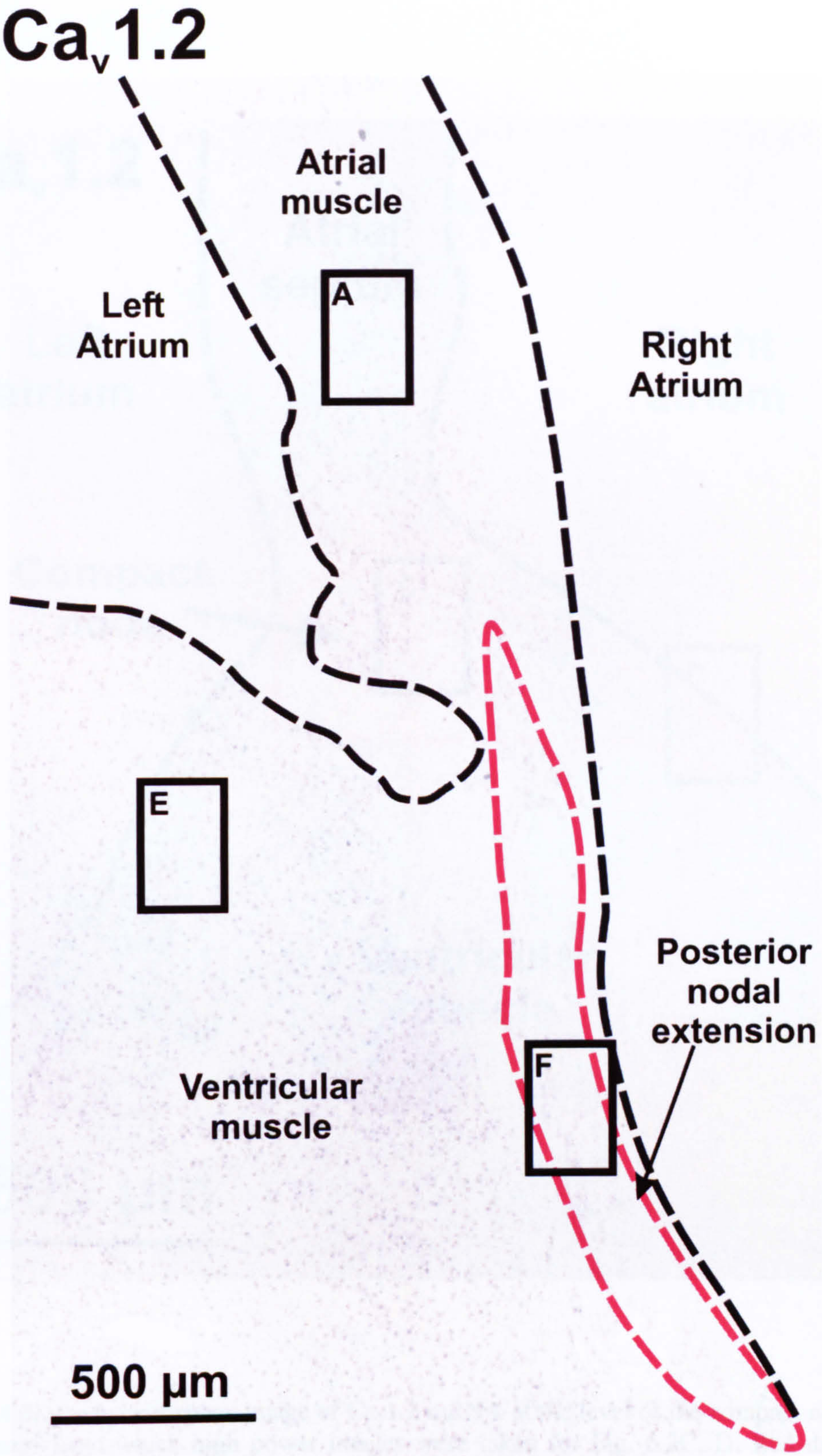

Figure 6.3 *In situ* hybridisation image of $Ca_v1.2$ mRNA at the level of the PNE. Boxes show regions from which high power images were taken for Fig. 6.2. Red dashed lines outline cells comprising the PNE. Black dashed line outlines tissue border of section.

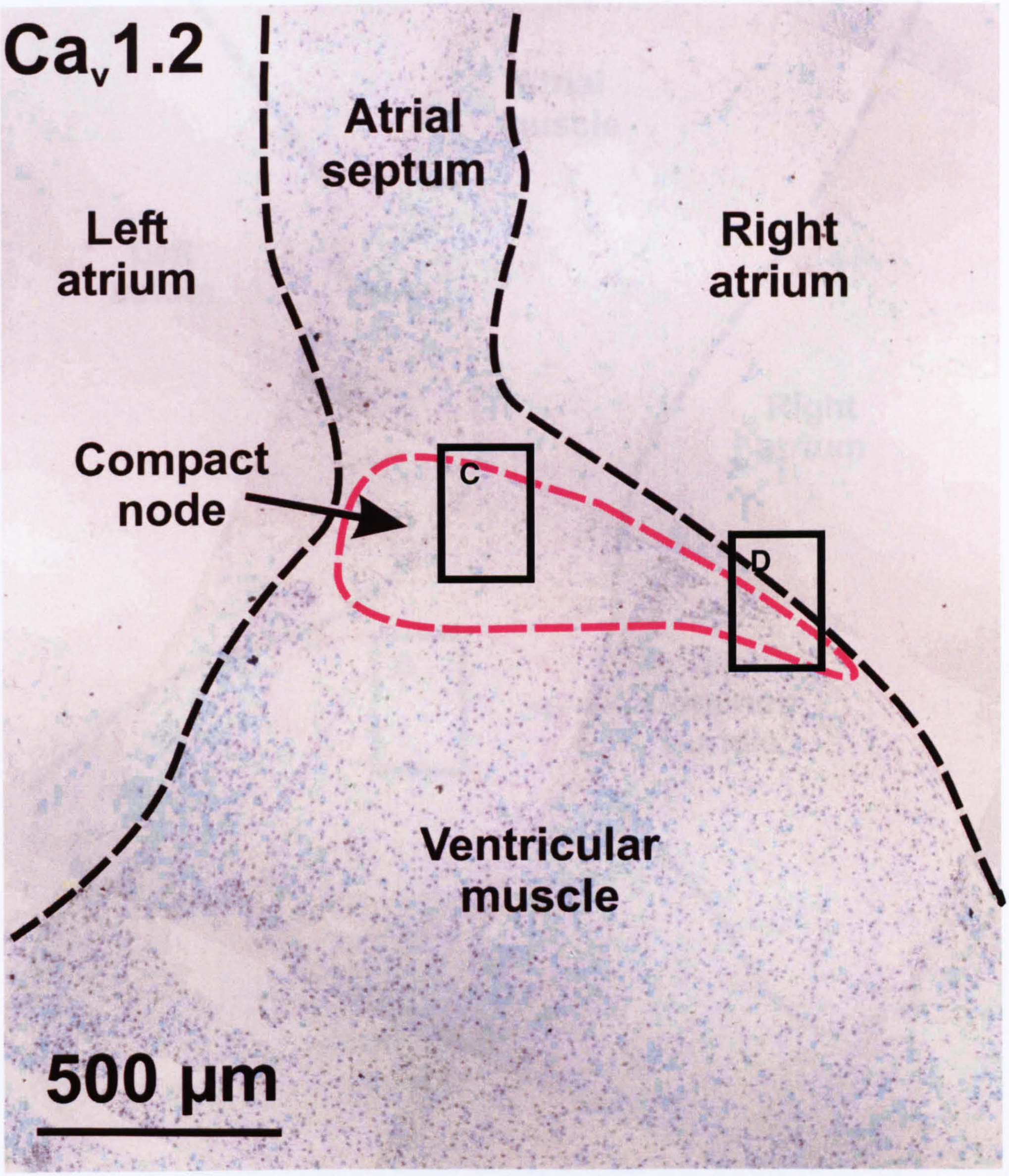

Figure 6.4 *In situ* hybridisation image of $Ca_v1.2$ mRNA at the level of the compact node. Boxes show regions from which high power images were taken for Fig. 6.2C, D. Red dashed lines outline cells comprising the compact node. Black dashed lines outline tissue border of section.

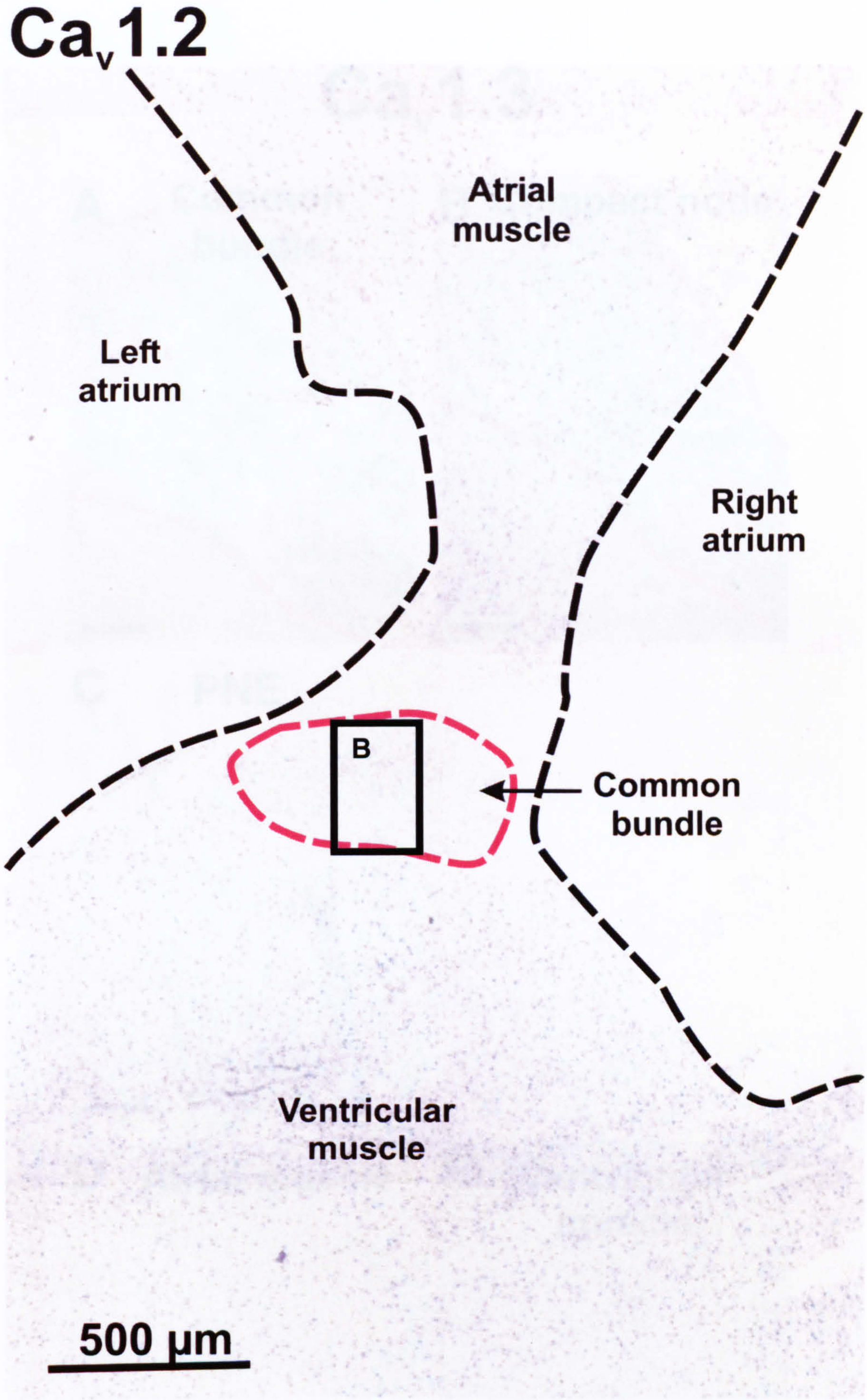

Figure 6.5 *In situ* hybridisation image of $Ca_v1.2$ mRNA at the level of the common bundle. Box indicates region from which a high power image was taken for Fig. 6.2B. Red dashed lines outline cells comprising the common bundle. Black dashed lines outline tissue border of section.

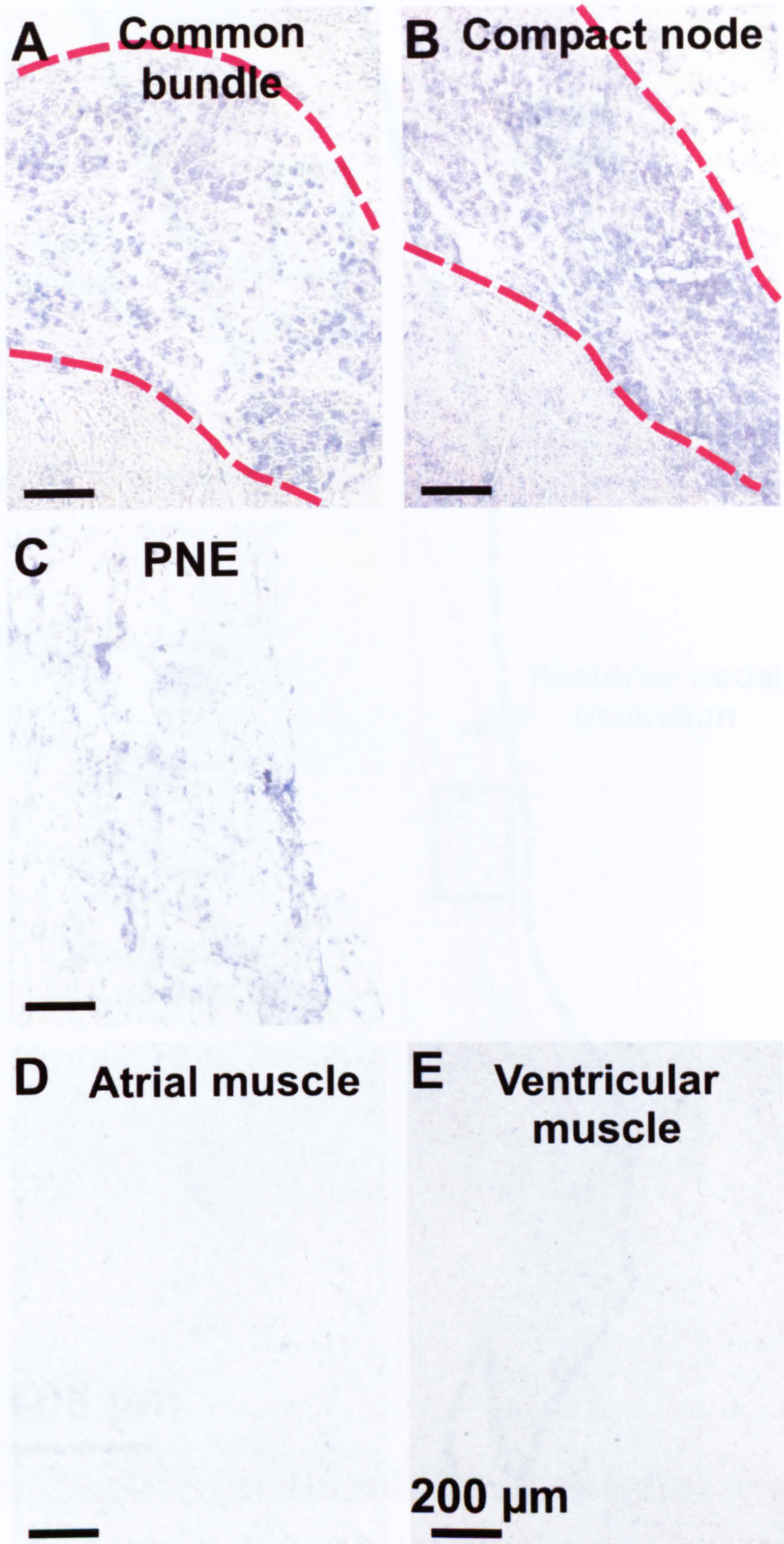

Figure 6.6 High power (x20 magnification) *in situ* hybridisation images of $Ca_v1.3$ mRNA Red dashed lines outline nodal cells.

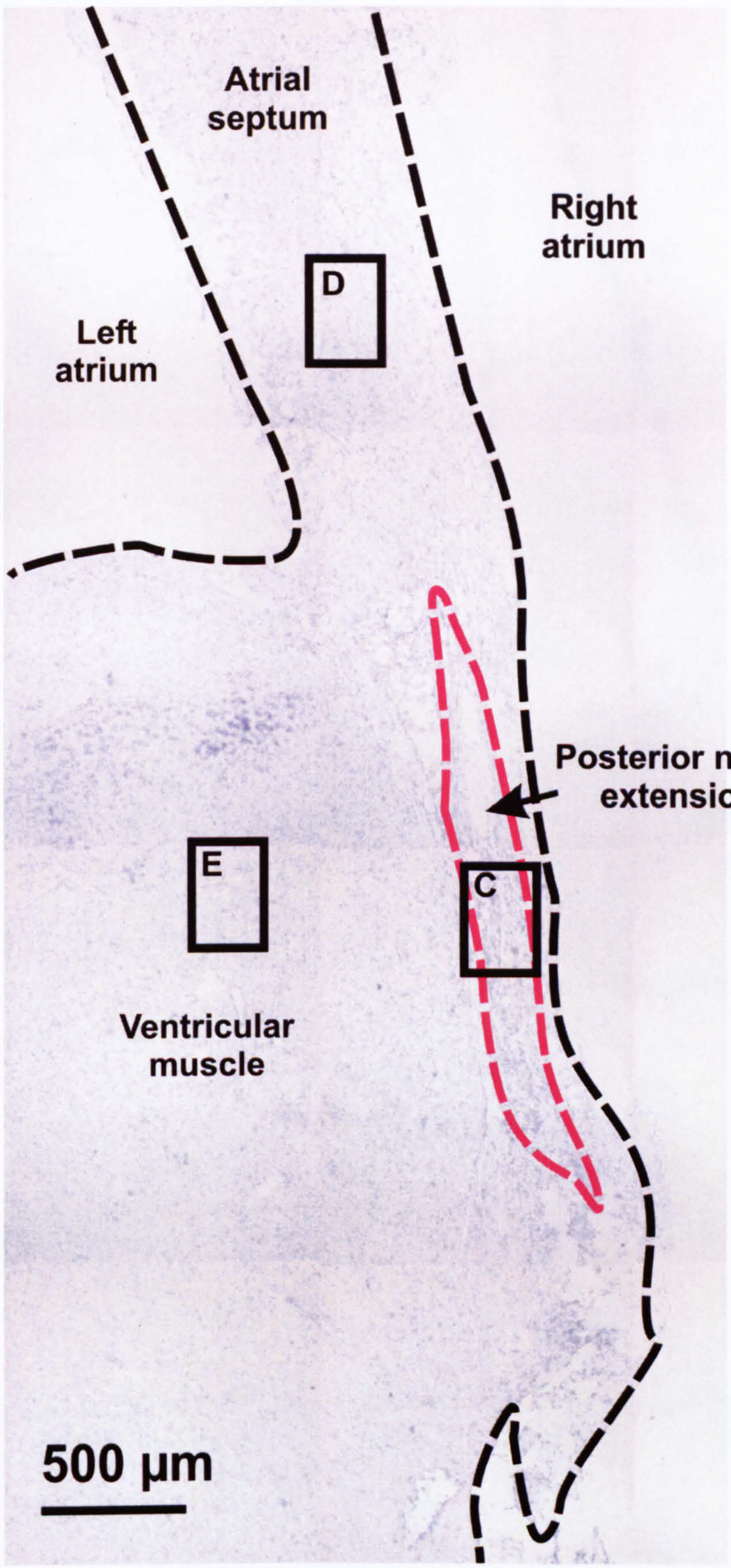

Figure 6.7 *In situ* hybridisation image of $Ca_v1.3$ mRNA at the level of the PNE. Boxes show region from which high power images were taken for Fig. 6.6C, D and E. Red dashed line outlines cells comprising the PNE. Black dashed line outlines tissue border of section.

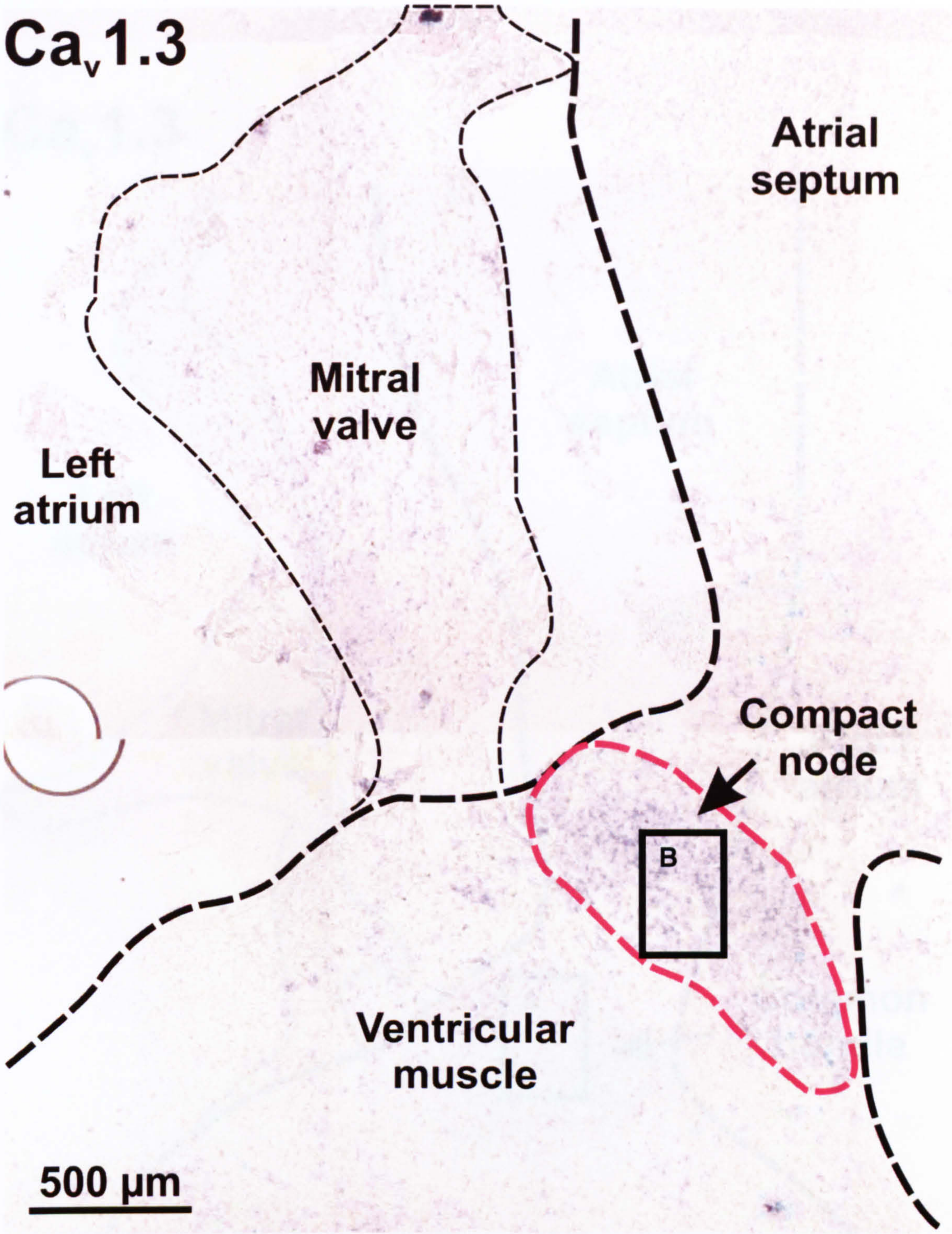

Figure 6.8 *In situ* hybridisation image of $Ca_v1.3$ mRNA at the level of the compact node. Box shows region from which a high power image was taken for Fig. 6.6B. Red dashed line outlines cells comprising the compact node. Thick black dashed line outlines tissue border of section. Thin black dashed line outlines mitral valve.

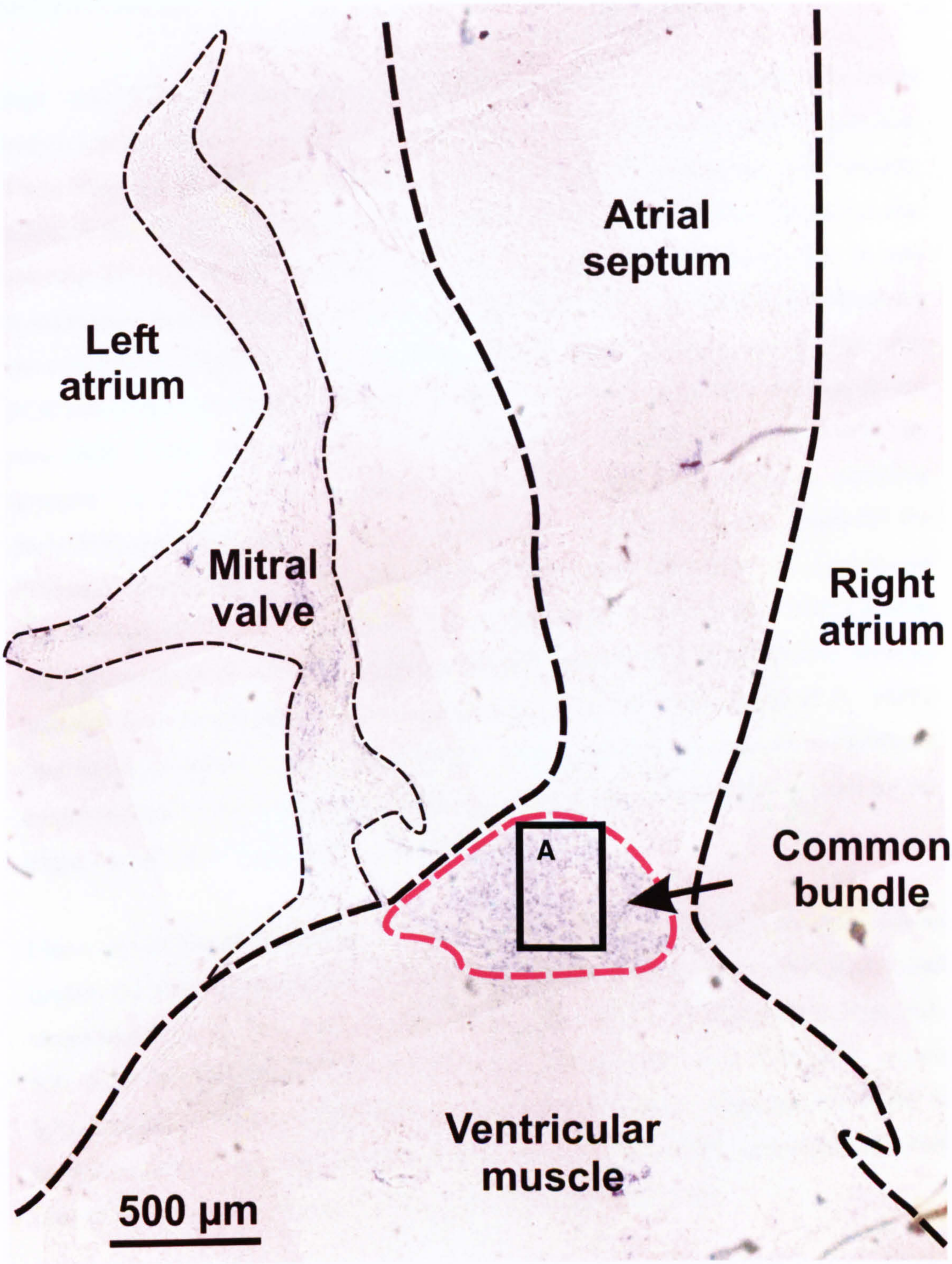

Figure 6.9 *In situ* hybridisation image of $Ca_v1.3$ mRNA at the level of the common bundle. Box shows region from which high power image was taken for Fig. 6.6A. Red dashed line outlines cells comprising the common bundle. Thick black dashed line outlines tissue border of section. Thin black dashed line outlines mitral valve.

spontaneous firing rate in SAN preparations suggestive of a major role for this channel in generating pacemaker activity. Therefore, it is highly likely that $Ca_v1.3$ channels are crucial for pacemaking in the AVN. The PNE has been shown to be the leading pacemaker site (Dobrzynski et al., 2003) and I have shown this region to be abundant for $Ca_v1.3$ mRNA.

Real time PCR measurements of $Ca_v1.2$ mRNA show no significant differences between tissue samples. This suggests of an important role for $Ca_v1.2$ in AVN function. These data are in agreement with the *in situ* hybridisation findings for atrial muscle, common bundle and ventricular muscle in which there is abundant $Ca_v1.2$ perinuclear staining for $Ca_v1.2$ mRNA (Figs. 6.2-6.5). However, they contradict the *in situ* hybridisation findings for the compact node and PNE. The most likely explanation for the conflicting findings for $Ca_v1.2$ mRNA in the PNE and compact node by *real time* PCR and *in situ* hybridisation is contamination from lower nodal cells in the case of *real time* PCR. I have shown using *in situ* hybridisation that the lower nodal cells are abundant in $Ca_v1.2$ mRNA. Unfortunately, during the microdissection sampling procedure, the lower nodal cells could not be removed from the tissue sample for the PNE and compact node due to the small size of the tissues. However, the positive *real time* PCR results for $Ca_v1.2$ mRNA in the compact node and PNE agree with a similar study on mouse AVN in which no significant difference in $Ca_v1.2$ mRNA was detected between atrial muscle, ventricular muscle, SAN and AVN (Marionneau et al., 2005). One limitation of the study of Marionneau et al. (2005), however, was a significant contamination of the AVN sample with AM cells (43 %), which could account for the larger expression of $Ca_v1.2$ mRNA in the nodal samples.

I have shown a tract of lower nodal cells at the level of the PNE and compact node to contain the same complement of L-type Ca^{2+} channel isoforms as the atrial muscle and ventricular muscle: $Ca_v1.2$ is the major isoform, but $Ca_v1.3$ is also present (Figs. 6.2-6.4; 6.6-6.8). This emphasises the need to combine *real time* PCR with *in situ* hybridisation to localise mRNA transcripts to specific cellular subgroups which fail to be distinguished from other structures with conventional sampling procedures for *real time* PCR especially in complex tissue structures such as the AVN.

I have shown the atrial muscle and ventricular muscle to predominantly express the $Ca_v1.2$ channel isoform. This is consistent with a wealth of functional and expression

data using atrial muscle and ventricular muscle tissues from a variety of species (Mangoni et al., 2005; Marrioneau et al., 2005).

Detection of $Ca_v1.3$ mRNA in the rabbit atria, albeit at a somewhat lower level than in nodal tissues (Fig. 6.1B), is in agreement with *real time* PCR data from rat, mouse, and human atria (Takimoto et al., 1997; Mangoni et al., 2003; Qu et al., 2005; Zhang et al., 2005). However, our *in situ* hybridisation data do not reveal an expression of $Ca_v1.3$ mRNA in the atria (Figs. 6.6-6.9), which contradicts the findings from mouse atrial tissue of Zhang et al. (2005) who used a similar *in situ* hybridisation protocol. Possible explanations for this difference is a species difference and also the region of atrial tissue sampling: I sampled atrial tissue immediately superior to the AVN whereas Zhang et al. (2005) may have sampled atrial tissue from the free-wall. It is possible that the atrial tissue that I sampled (in close proximity to the AVN) was composed of AN cells (Billette et al., 1987) with features intermediate between those of the compact node and atrial muscle.

The predominance of $Ca_v1.2$ mRNA in the common bundle is consistent with fast conduction properties in this region ($Na_v1.5$ mRNA is abundant here).

The overall importance of the L-type Ca^{2+} current in AVN function was shown by an investigation into congenital heart block: a mother with autoimmune disease produced antibodies that ultimately impaired the L-type Ca^{2+} current, including that mediated by $Ca_v1.3$ (Qu et al., 2003) in the newborn; the result was varying degrees of AV Block (Boutjdir, 2000).

With respect to the T-type Ca^{2+} channels, I was unable to detect $Ca_v3.1$ mRNA. This suggests a negligible role (if any) for $Ca_v3.1$ channels in rabbit AVN function. However, the mouse AVN was shown to express significantly higher amounts of $Ca_v3.1$ mRNA than the SAN, atrial muscle and ventricular muscle (Marionneau et al., 2005). Therefore, $Ca_v3.1$ currents could function during the diastolic depolarisation phase in the mouse AVN. The difference between this study and the study of Marionneau et al. (2005) could be a species difference in the expression of T-type Ca^{2+} channels in AVN function.

Chapter 7

Voltage-gated K^+ channels

7.1 Transient outward current

7.1.2 Introduction

The transient outward current is one of the major repolarizing currents of the heart. This current has two components: a Ca^{2+}-independent, 4-aminopyridine-sensitive component ($I_{to,1}$) and a Ca^{2+}-dependent, 4-aminopyridine-insensitive component ($I_{to,2}$) (Kenyon and Gibbons, 1979; Coraboeuf and Carmeliet, 1982). $I_{to,1}$ is carried by K^+ ions, whereas $I_{to,2}$ is carried by Cl^- ions.

Two components of $I_{to,1}$ have been described: a fast component, $I_{to,f}$ and a slow component, $I_{to,s}$, based on their recovery from inactivation. Both currents activate and inactivate rapidly. However, $I_{to,f}$ recovers from inactivation quickly, whereas $I_{to,s}$ shows slow recovery from inactivation (Xu et al., 1991).

Whereas, certain features of I_{to} are common to all species and cell-types, (e.g. activation kinetics) there are marked differences in some biophysical characteristics of I_{to} between species and cell types. For instance, the recovery from inactivation is rapid in rat (Apkon and Nerbonne, 1991) and human (Wettwer et al., 1993) ventricular myocytes, but slow in rabbit myocytes (Giles and Imaizumi, 1988). Furthermore, ventricular tissue shows profound regional differences in I_{to} density (Barry and Nerbonne, 1996). The species/regional differences in density and the biophysical nature of I_{to} are best explained by species/regional variations in expression of specific α- and β-channel isoforms.

The transient outward current is responsible for phase 1 or the spike-and-dome morphology of the atrial and ventricular action potentials. The SAN and AVN have also been shown to have I_{to} (Lei et al., 2000; Mitcheson and Hancox, 1999).

The molecular correlates of I_{to} have been extensively studied. The voltage-gated K^+ channel, $K_v1.4$ is related to the *Shaker* family of ion channels and was the first inactivating channel suggested to underlie I_{to} (Tseng-Crank et al., 1990; Comer et al., 1994). However, the kinetics of this current (the slow recovery from inactivation) fails to match those of I_{to} (Fermini et al., 1992).

Voltage-gated K^+ channels related to the *Shal* family mediate rapidly inactivating outward fast-recovering currents (K_v4) that can more closely resemble I_{to} (Fiset et al., 1997; Faivre et al., 1999).

$K_v4.2$ and $K_v4.3$ α-subunits have been shown to functionally exist as heteromers in HEK-293 cells, with gating properties that more closely resemble those of native mouse ventricular $I_{to,f}$ (Guo et al., 2002). tsa-201 cells expressing both $K_v4.2$ and $K_v4.3$ isoforms reproduce the fast recovering component measured in the right free wall of the rat ventricle (Wickenden et al., 1999). Additionally, $K_v4.2$ mRNA and protein expression correlated with I_{to} density in the right ventricular free-wall, whereas $K_v4.3$ was expressed uniformly. When $K_v1.4$ was expressed in tsa-201 cells, currents had recovery kinetics similar to the slow recovering component measured in the rat ventricular free-wall. $K_v1.4$ mRNA and protein also correlated with the density of the slow recovering component of I_{to} in the right ventricular free-wall and interventricular septum (Wickenden et al., 1999).

In intact rabbit SAN preparations, the I_{to} blocker, 4-aminopyridine (4-AP), exerts a number of effects: a shift in the leading pacemaker site and the abolition of the action potential notch in the periphery of the SAN (Boyett et al., 1998). The effects of 4-AP are greater on the periphery of the SAN than on the centre (Boyett et al., 1998). These data suggest a non-uniform distribution of I_{to} in the SAN (Boyett et al., 1998). Boyett et al. (1988) using single cells isolated from the rabbit SAN, measured recovery of I_{to} from inactivation and showed recovery occurred over a double-exponential time-course with time constants of 43 and 1434 ms. These kinetics resemble those of $K_v4.2/K_v4.3$ and $K_v1.4$ α-subunits, respectively. Similar effects of 4-AP were seen in single AVN cells; 5 mM 4-AP abolished spontaneous pacemaker activity in some cells (Mitcheson and

Hancox, 1999). Mitcheson and Hancox (1999) suggested that I_{to} in the AVN could contribute to action potential repolarization.

K_v-channel interacting proteins (KChIP) proteins were first described in neurones in which they have various functions. They act as Ca^{2+} sensors that bind to the N-terminus of K_v4 channels; they modulate surface expression of the channel; they hasten the onset of inactivation and increase the rate of recovery from inactivation (An et al., 2000; Decher et al., 2001). In humans and dogs (Litovsky and Antzelevitch, 1988) there is a transmural gradient of KChIP2 that correlates with a transmural gradient in I_{to}, whereas in rodents there is a transmural gradient in K_v4 that correlates with the transmural gradient in I_{to} (Rosati et al., 2001). Seven different splice variants of KChIP2 have now been cloned and shown to exhibit differing modulatory properties (Deschens et al., 2002; Patel et al., 2002; Decher et al., 2004).

In addition, a group of voltage-gated K^+ channel β-subunits ($K_v\beta$) can exert modulatory effects on K^+ channels (Pongs et al., 1999). Three genes encoding Kvβ subunits (Kvβ1, Kvβ2, Kvβ3) exist, which also give rise to splice variants (Leicher et al., 1998). Marionneau et al. (2005) using mouse AVN mRNA showed higher expression of the $K_v\beta1$ subunit compared to SAN. Moreover, Marionneau et al. (2005) also showed higher expression in mouse AVN of the neuronal α-subunit isoforms, $K_v1.1$ and $K_v1.6$; these isoforms are known to have slow inactivation kinetics (Klump et al., 1991), but in the presence of $K_v\beta1$ become rapidly inactivating (Jing et al., 1999).

The K^+ channel chaperone protein, KChAP, also exists, but fails to modulate current kinetics. It may alter cell surface expression of K_v-channel α-subunits (Wible et al., 1998).

The aim of this investigation was to determine the relative expression of α- and β-subunits responsible for I_{to} throughout the tissues of the AVN conduction system and relate this to previous AVN electrophysiological findings.

7.1.3 Methods

7.1.3.1 *Real time* PCR

Real time PCR was performed on Kv1.5, Kv4.2, Kv4.3 and KChIP2 cDNAs generated from total RNA isolated from five rabbit AVN tissue types: atrial muscle, PNE, compact node, common bundle and ventricular muscle (n = 8 rabbits). *Real time* PCR was carried out using a Roche LightCycler 1.0.

7.1.3.2 *In situ* hybridisation

The riboprobe for KChIP2 was generated by Dr. Gillian Graham using a PCR fragment cloned from rabbit whole heart cDNA. The KChIP2 PCR product used for riboprobe synthesis was in a conserved region for KChIP2 mRNA sequences.

7.1.4 Results

7.1.4.1 *Real time* PCR

The relative expression of mRNA transcripts encoding α- (K_v1.4, K_v4.2 and K_v4.3) and β- (KChIP2) subunits of I_{to} in the heart were investigated. K_v1.4 expression was significantly higher in the atrial and ventricular muscle ($P < 0.05$) compared to the PNE (Fig. 7.1A). In contrast, K_v4.2 (Fig. 7.1C) and K_v4.3 (Fig. 7.1B) expression levels were found not to be significantly different between tissues. The K_v4.x β-subunit, KChIP2, was found to be significantly lower in the compact node compared to the atrial and ventricular muscle ($P<0.05$; Fig. 7.1D).

7.1.4.2 *In situ* hybridisation

In situ hybridisation for KChIP2 revealed a more complex staining pattern than anticipated. The rabbit atrial muscle was largely positive for KChIP2 in the most superior regions (Figs. 7.2A and 7.3–7.6). However, a region of negative staining was apparent in the atrial muscle immediately adjacent to the nodal tissue at the level of the PNE and compact node (Figs. 7.3-7.5). The ventricular muscle showed a unique pattern of KChIP2 staining; a transmural gradient was apparent with an abundance of positive staining on one side and no staining on the other (Figs. 7.3–7.6). In contrast, the PNE,

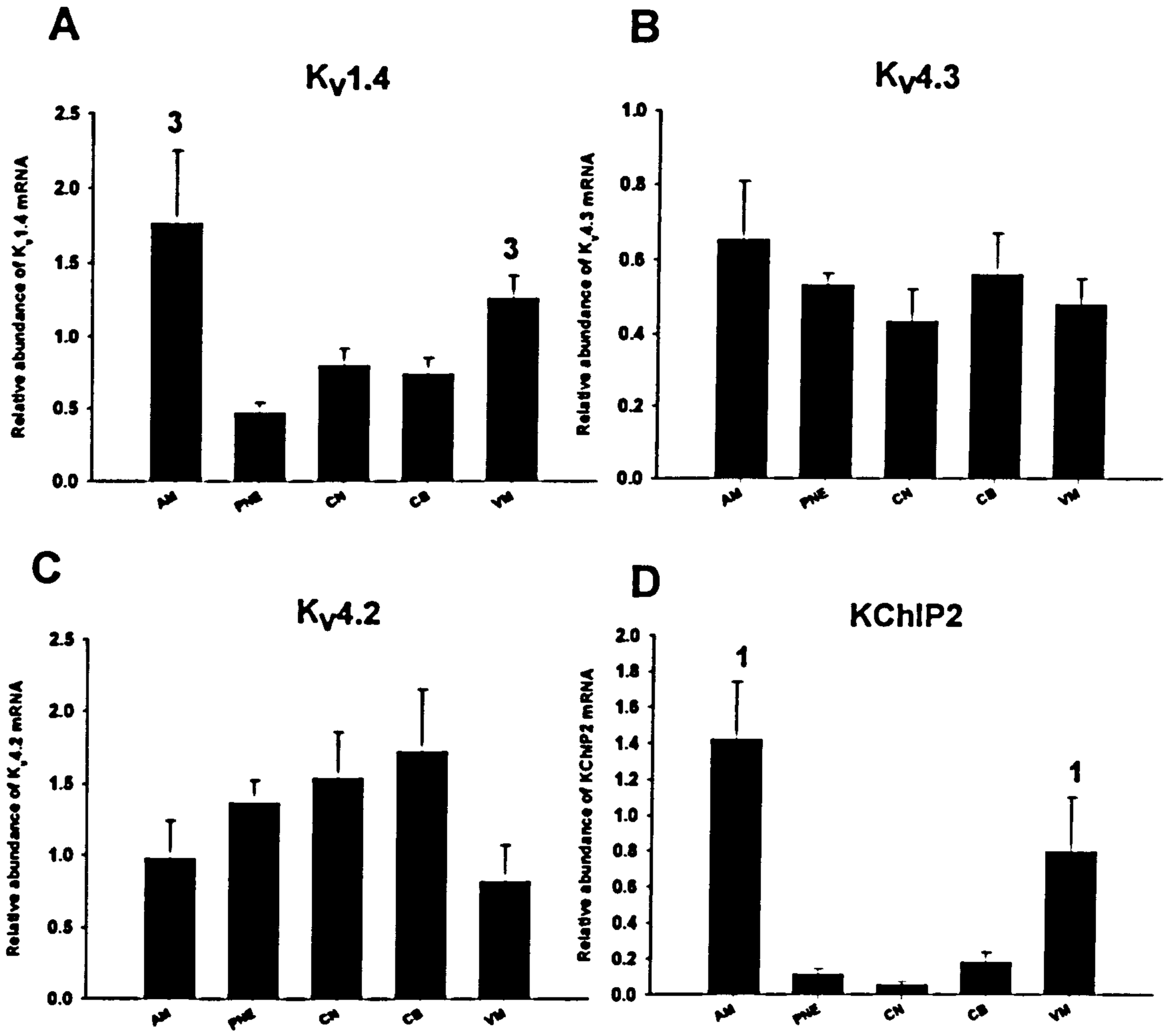

Figure 7.1 *Real time* PCR results for I_{to} mRNAs. A, Kv1.4; B, Kv4.3; C, Kv4.2; D, KChIP2. 1 and 3, denote significantly different from CN and PNE, respectively ($P < 0.05$; one-way ANOVA). AM, atrial muscle; PNE, posterior nodal extension; CN, compact node; CB, common bundle; VM, ventricular muscle.

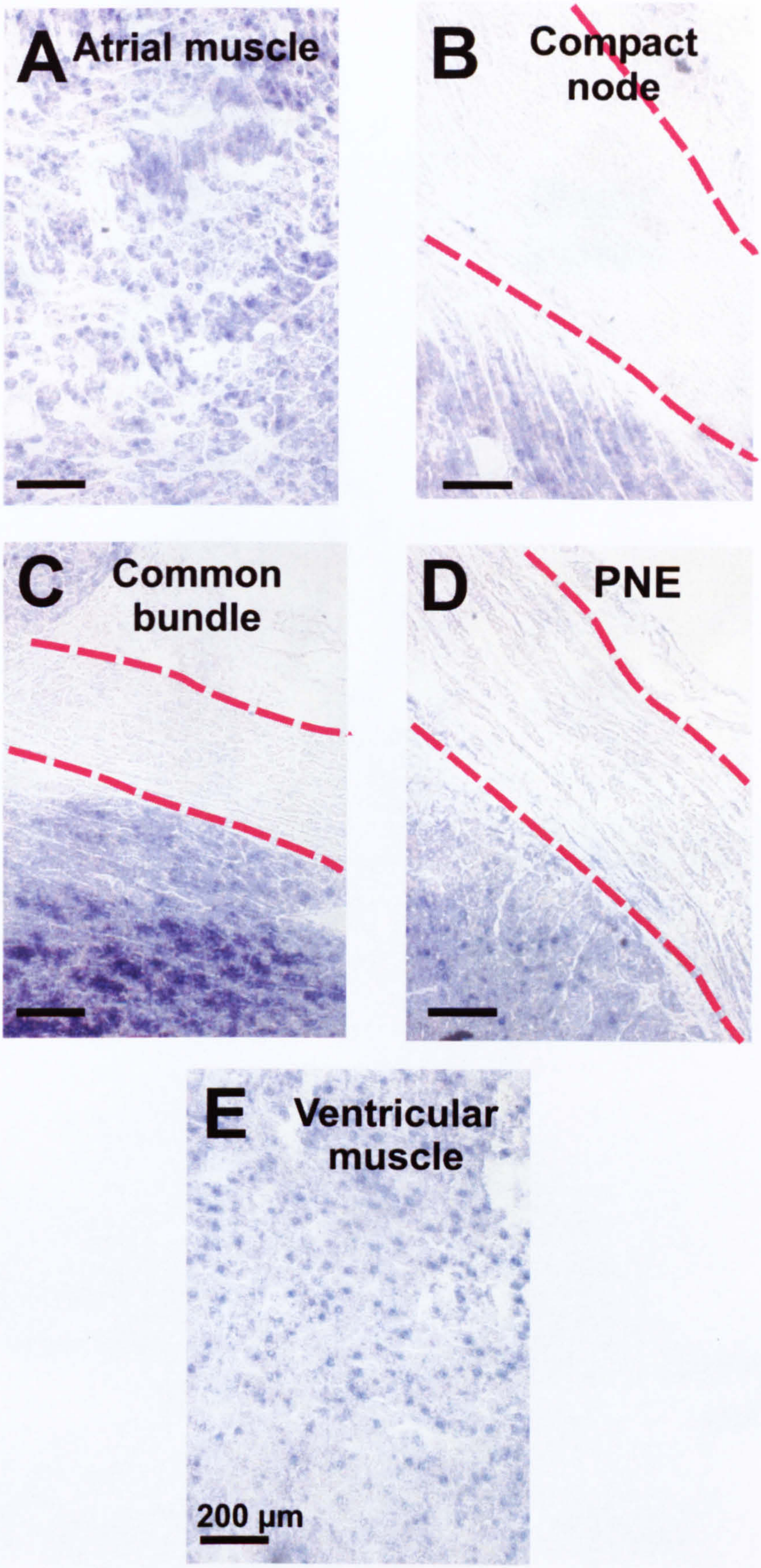

Figure 7.2 High power (x20 magnification) *in situ* hybridisation images of KChIP2 mRNA. A, atrial muscle; B, compact node; C, common bundle; D, PNE; E, ventricular muscle. Red dashed line outlines nodal cells.

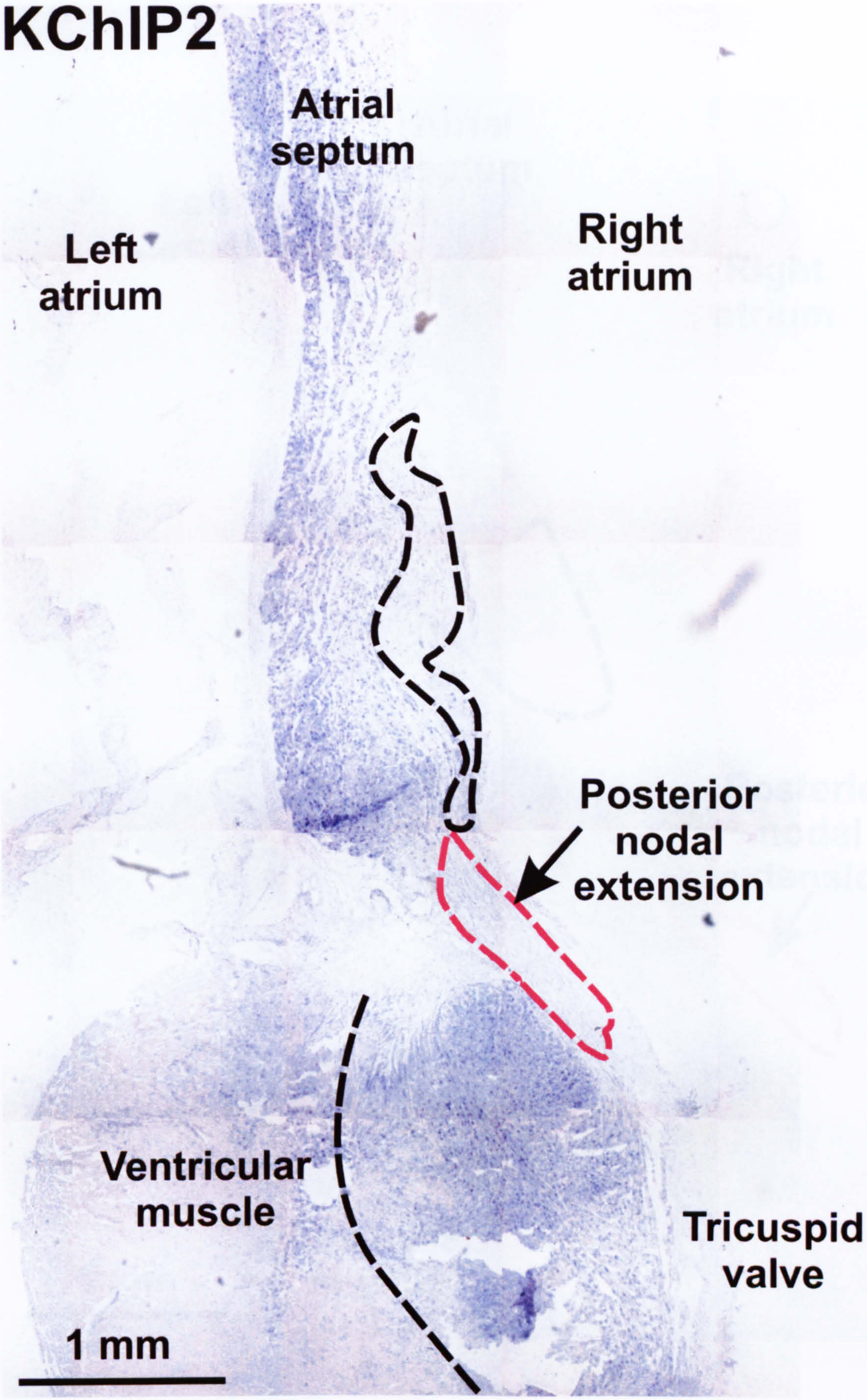

Figure 7.3 *In situ* hybridisation image of KChIP2 mRNA at the level of the PNE (distal). Red dashed line outlines cells comprising PNE (distal). Upper black dashed line outlines KChIP2-negative region. Lower black dashed line separates KChIP2-positive region from KChIP2-negative region in the ventricle.

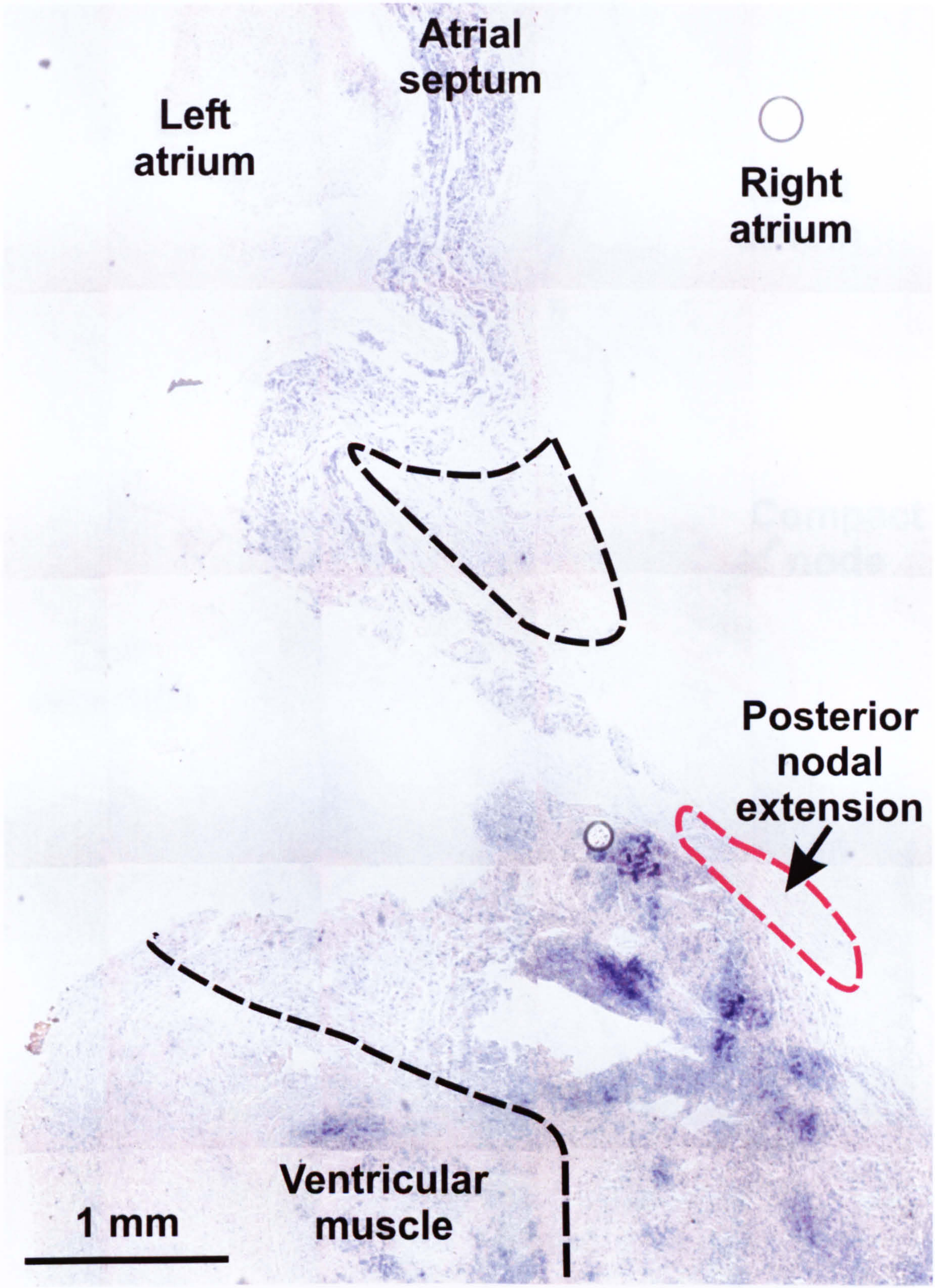

Figure 7.4 *In situ* hybridisation image of KChIP2 mRNA at the level of the PNE (proximal). Red dashed line outlines cells comprising PNE (proximal). Upper black dashed line outlines KChIP2-negative region. Lower black dashed line separates KChIP2-positive region from KChIP2-negative region in the ventricle.

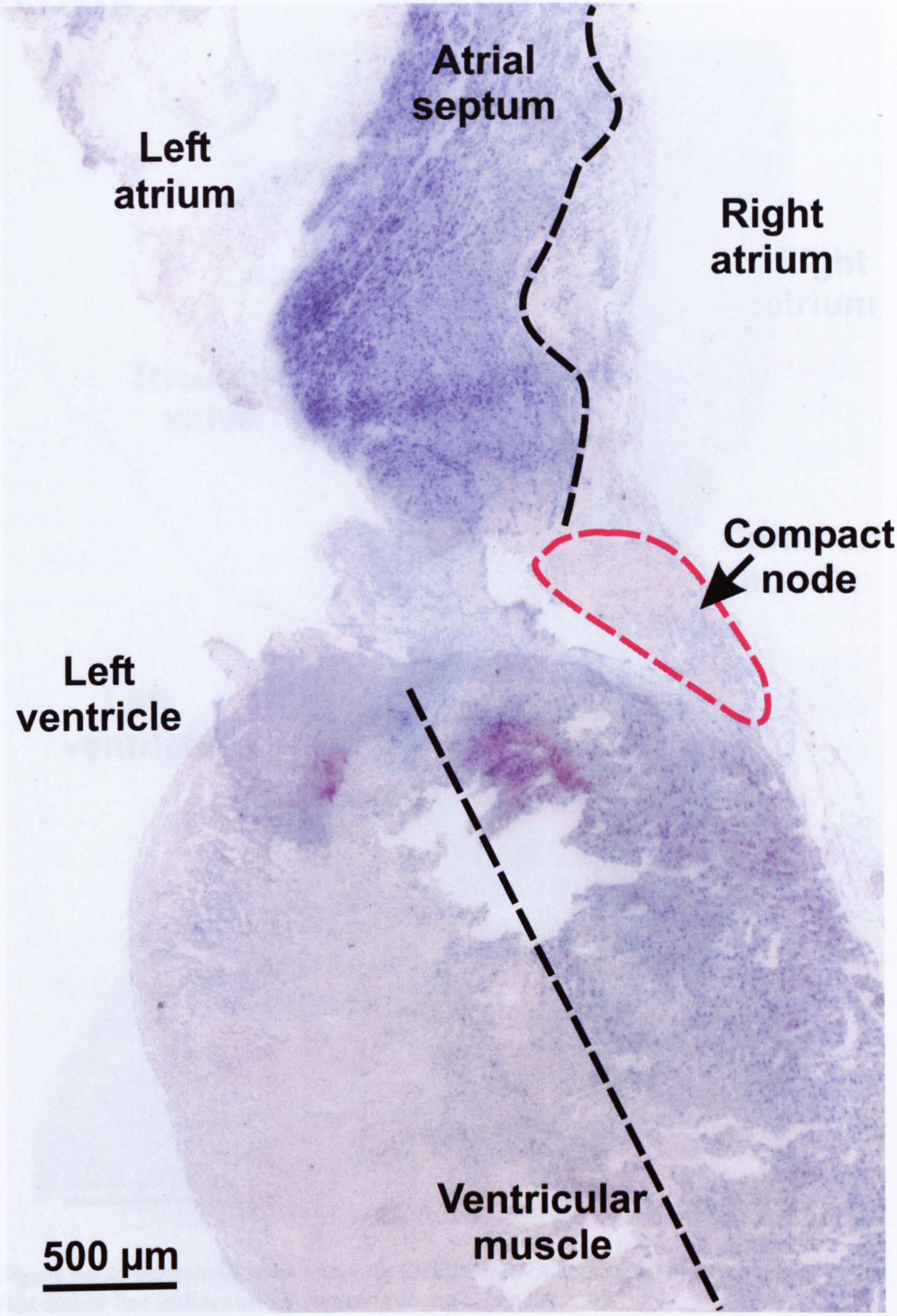

Figure 7.5 *In situ* hybridisation image of KChIP2 mRNA at the level of the compact node. Red dashed line outlines cells comprising compact node. Black dashed line separates KChIP2-positive region from KChIP2-negative region.

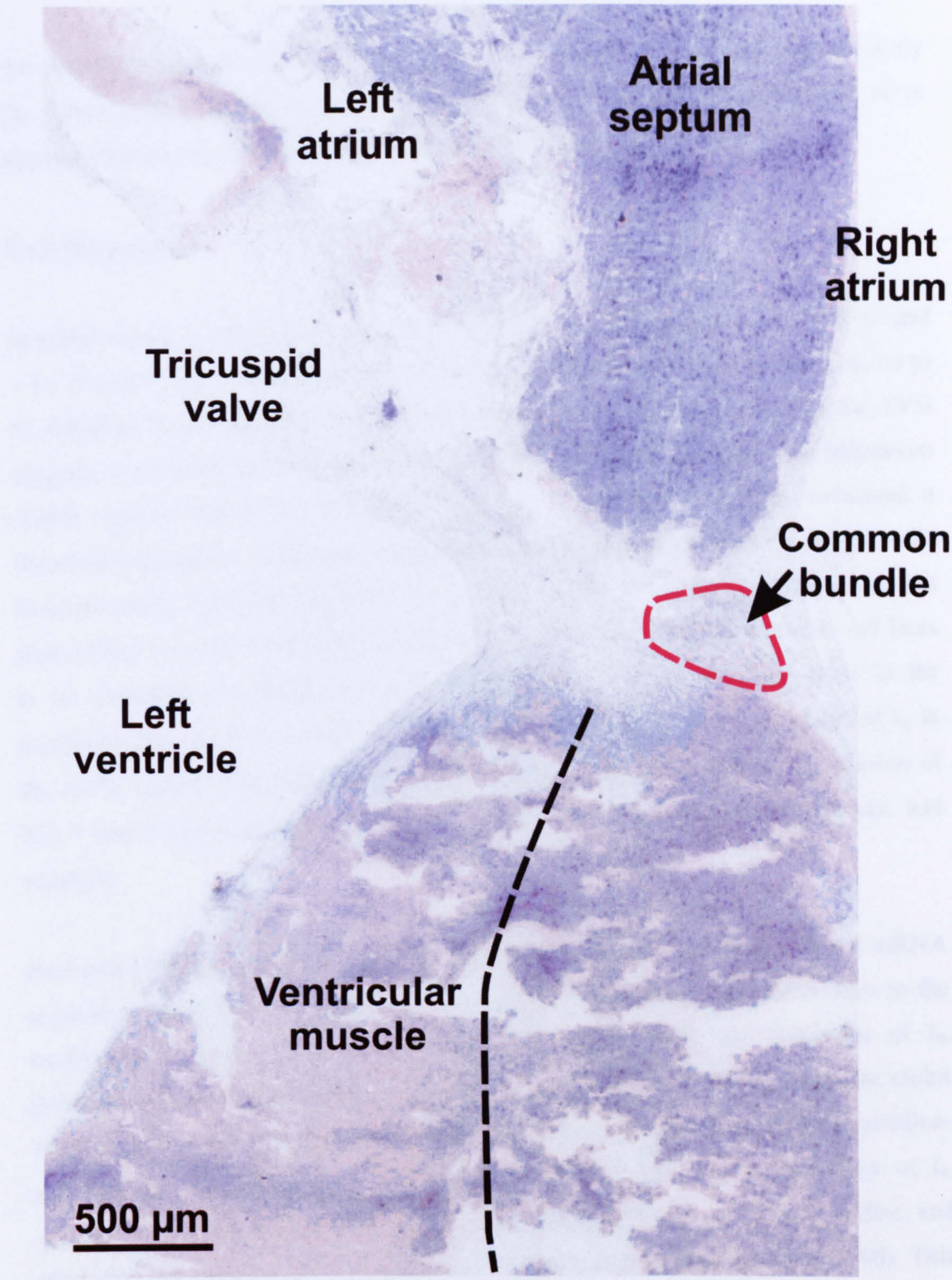

Figure 7.6 *In situ* hybridisation image for KChIP2 mRNA at the level of the common bundle. Red dashed line outlines cells comprising common bundle.

compact node and common bundle were negative for KChIP2 staining (Figs. 7.2B, C, D, and 7.3–7.6).

An attempt to generate riboprobes for $K_v1.4$, $K_v4.2$ and $K_v4.3$ was made previously by Dr. James Tellez. The riboprobes were tested, but were unsuccessful. Therefore, no *in situ* hybridisation results for $K_v1.4$, $K_v4.2$ and $K_v4.3$ mRNAs were obtained.

7.1.5 Discussion

In rabbit atrium, I_{to} recovers slowly from activation with time constants of ~ 650 ms and ~ 8 s (Fermini et al., 1992). This is characteristic of $K_v1.4$ and Fig. 7.1A shows $K_v1.4$ to be abundant in the atrial muscle. A low expression level of $K_v1.4$ mRNA in the AVN suggests this current has a small role to play in I_{to} in the AVN. Hancox and Mitcheson (1999) showed that I_{to} in the rabbit AVN has two components. They measured a flecainide-insensitive component with slow recovery from inactivation in single cells from the rabbit AVN and suggested $K_v1.4$ could be the molecular correlate, because it shows slow recovery from inactivation and it has been shown in mammalian cell lines to be insensitive to flecainide (Yeola and Snyders, 1997). However, there is the possibility that other K_v1 channel isoforms could underlie the slow component of I_{to} in the AVN. Indeed, Marionneau et al. (2005) showed significantly higher expression of $K_v1.1$ and $K_v1.6$ channel isoforms in the murine AVN compared to atrium and ventricle.

Real time PCR data presented here suggest a role for $K_v4.2$ in AVN I_{to} – Kv4.2 mRNA is present and there is a suggestion that it is more abundant in the AVN than in the working myocardium (Fig. 7.1C). This is consistent with the properties of I_{to} (Mitcheson and Hancox, 1999; Munk et al., 1996) in single cells isolated from the rabbit AVN. $K_v4.2$ when expressed in mammalian cell lines was shown to be both quinidine- and flecainide-sensitive (Yeola and Snyders, 1997). The major component of I_{to} measured in single rabbit AVN cells is also very sensitive to both quinidine and flecainide and recovers rapidly from inactivation (Mitcheson and Hancox, 1999). This suggests that Kv4.2 does play a substantial role in I_{to} in the rabbit AVN.

Atrial and ventricular expression patterns of mRNAs encoding cardiac I_{to} α-subunits appear relatively similar according to *real time* PCR (Fig. 7.1). This is consistent with the findings of Imaizumi and Giles (1987) they showed that the sensitivity of rabbit atrial and ventricular I_{to} to quinidine is similar (IC_{50}, 7 μM).

In the AVN, there is the possibility that other subunits are involved in I_{to}: MIRP1 has been shown to interact with $K_v4.2$ in Xenopus oocytes and slow the rate of activation and inactivation as well as shifting the voltage-dependence of activation and inactivation to more positive potentials (Zhang et al., 2001). In addition, Deschenes and Tomaselli (2002) using HEK-293 cells demonstrated modulating effects of MIRP1 on $K_v4.3$ channels. Finally, there is substantial evidence for the existence of additional modulatory K_v4 channel subunits known as dipeptidyl-aminopeptidase-like proteins (DPPX) in neurones. They are thought to form ternary complexes with $K_v4.2$/$K_v4.3$ and KChIPs to produce subthreshold A-type currents (Nadal et al., 2003). Furthermore, Radicke et al. (2005) using *real time* PCR showed high expression of DPPX-6 in the human ventricle and found it to produce a current closely resembling human cardiac I_{to} when expressed with $K_v4.3$ and KChIP2a in CHO cells.

7.2 Delayed rectifier current

7.2.1 Introduction

Cardiac delayed rectifier K^+ currents are the major repolarizing currents in the heart. Specifically, they are responsible for repolarisation during phase 3 of the atrial and ventricular action potential (Yue et al., 1996; Mitcheson and Hancox, 1999). Two types of delayed rectifier K^+ current were first described in guinea-pig atrial cells (Horie et al., 1990; Sanguinetti and Jurkiewicz, 1991). These were termed "rapid" ($I_{K,r}$) and "slow" ($I_{K,s}$) based on their time- and voltage-dependent properties. In addition, a further rapidly activating component termed the "ultra-rapid" ($I_{K,ur}$) delayed recitifier has been described in the heart, predominantly, in atrium (Wang et al., 1993). During electrophysiological studies, delayed rectifier K^+ currents can be seen as deactivating

outward "tail" currents apparent upon depolarization of a cell to positive test potentials (-20 to +40 mV) followed by repolarization back to the holding potential (generally -40 mV).

The slow component of the delayed rectifier K^+ current becomes apparent after application of the class III antiarrhythmic or I_{Kr} blockers, E-4031 or ibutilide, when small tail currents remain (Howarth et al., 1996; Sato et al., 2000).

Single cells isolated from the guinea-pig AVN show both I_{Kr} and I_{Ks} (Yuill and Hancox, 2002). Sato et al. (2000) using ibutilide, a class III anti-arrhythmic agent and specific blocker of I_{Kr}, on single SAN and AVN cells showed evidence for the presence of $I_{K,r}$ in both SAN and AVN cells, but found $I_{K,s}$ only to be present in SAN cells.

I_{Kr} is likely to contribute to repolarisation in the SAN and AVN. Deactivation of I_{Kr} is also likely to contribute to the depolarisation of the membrane during the pacemaker potential (the 'I_K delay' hypothesis). This will be helped by the high input resistance of AVN cells (Hancox et al., 1993; Munk et al. 1996).

Mitcheson and Hancox (1999) have suggested that I_{Kr} could vary between the SAN and AVN: I_{Kr} in AVN myocytes activates at -30 to -20 mV (Mitcheson and Hancox, 1999), whereas it activates at -60 to -40 mV in SAN myocytes (Ono and Ito, 1995). The molecular make-up of the channel underlying I_{Kr} in these tissues may, therefore, be different.

The α-subunit underlying I_{Kr}, ERG, was originally cloned from human brain (Trudeau et al., 1995). However, the time constants of activation and deactivation of ERG are four to 10 times slower than those of native $I_{K,r}$ in guinea pig and mouse cardiac myocytes (Sanguinetti and Jurkiewicz, 1990). Abbott et al. (1999) identified a β-subunit for ERG, minK-related peptide 1 (MIRP1), and found complexes of ERG and MIRP1 to closely reproduce properties of cardiac $I_{K,r}$ (the time constants of activation and deactivation are more similar).

To add to electrophysiological complexity, evidence for splice variants of ERG exist. Lees-Miller et al. (1997) cloned a truncated NH_2-terminal isoform of ERG from mouse AT-1 cDNA library and showed it to be highly expressed in mouse and human heart.

minK was originally cloned from rat kidney (Takumi et al., 1988) and later found to be expressed in the heart (Folander et al., 1990). The small size of the mink protein (130 amino acids in length) with one transmembrane domain suggests it is likely to be a regulatory β-subunit rather than major pore forming unit (Goldstein and Miller, 1991). Sanguinetti et al. (1996) identified the α-subunit underlying $I_{K,s}$, K_vLQT1, using positional cloning techniques. When K_vLQT1 is co-expressed with minK the resulting current closely resembles native $I_{K,s}$.

The biophysical characteristics and high-sensitivity of $I_{K,ur}$ to 4-AP are similar to these of K_v1.5 (Fedida et al., 1993; Wang et al., 1993) suggesting that this subunit underlies $I_{K,ur}$ in cardiac tissue. Indeed, K_v1.5 mRNA has been shown to be highly abundant in pacemaker and working myocardial tissue of mouse hearts, in particular in ventricular tissue (Marionneau et al., 2005).

7.2.2 Methods

7.2.2.1 *Real time* PCR

Real time PCR was performed using cDNA generated from total RNA isolated from five rabbit AVN tissue types: atrial muscle, PNE, compact node, common bundle and ventricular muscle (n = 8 rabbits). Primers for ERG and K_v1.5 were designed and optimised by Dr. James Tellez (Tellez, 2005). See Chapter 2 for detailed methods of primer design and optimisation of K_vLQT1 and mink primers. Only a partial mRNA coding sequence for rabbit MIRP1 exists. Attempts were made to optimise primers using this sequence but unfortunately the primer pairs tested had a tendency for primer-dimer formation and were not used.

7.2.2.2 *In situ* hybridisation

The riboprobe for rabbit ERG mRNA was generated by Dr. James Tellez using a clone obtained from Professor Harry Witchell (Tellez, 2005).

7.2.3 Results:

7.2.3.1 *Real time* PCR

The relative expression of mRNA transcripts encoding α- (K_v1.5, ERG and K_vLQT1) and β- (minK) subunits of the delayed rectifier K^+ currents was investigated in tissues of the AVN conduction system, as well as surrounding atrial and ventricular tissue. Expression levels for K_v1.5, ERG, K_vLQT1 and the β-subunit minK, were found not to be significantly different between experimental groups (Fig. 7.7).

7.2.3.2 *In situ* hybridisation

The *in situ* hybridisation results for ERG showed an abundance of perinuclear staining in the PNE, compact node and common bundle (Figs. 7.8-7.10). There was an absence of perinuclear staining for ERG mRNA in the atria and ventricles (Figs. 7.8-7.10). Attempts to obtain *in situ* hybridisation results for K_v1.5, K_vLQT1 and minK riboprobes were undertaken by Dr. James Tellez; however, no signal was detected.

7.2.4 Discussion

The *real time* PCR data presented here provide evidence for the existence of α- and β-subunits comprising $I_{K,ur}$, $I_{K,r}$ and $I_{K,s}$ in all tissue types. However, the *real time* PCR technique only allows the relative abundance of mRNAs in diffeent tissues to be assessed; it does not measure the absolute abundance of mRNAs. Using single cells isolated from rabbit AVN, Howarth et al. (1996) and Mitcheson and Hancox (1999) observed only a single exponential time constant for deactivation of delayed rectifier K^+ current. The data suggest only the presence of $I_{K,r}$ in rabbit AVN. However, in multicellular rabbit AVN preparations, Kokubun et al. (1982) observed a bi-exponential decline of the current tail with time constants of 133 and 1234 ms. This could be consistent with the presence of both $I_{K,r}$ and $I_{K,s}$ in rabbit AVN. With investigations involving single cells isolated from the AVN, it is impossible to determine exactly

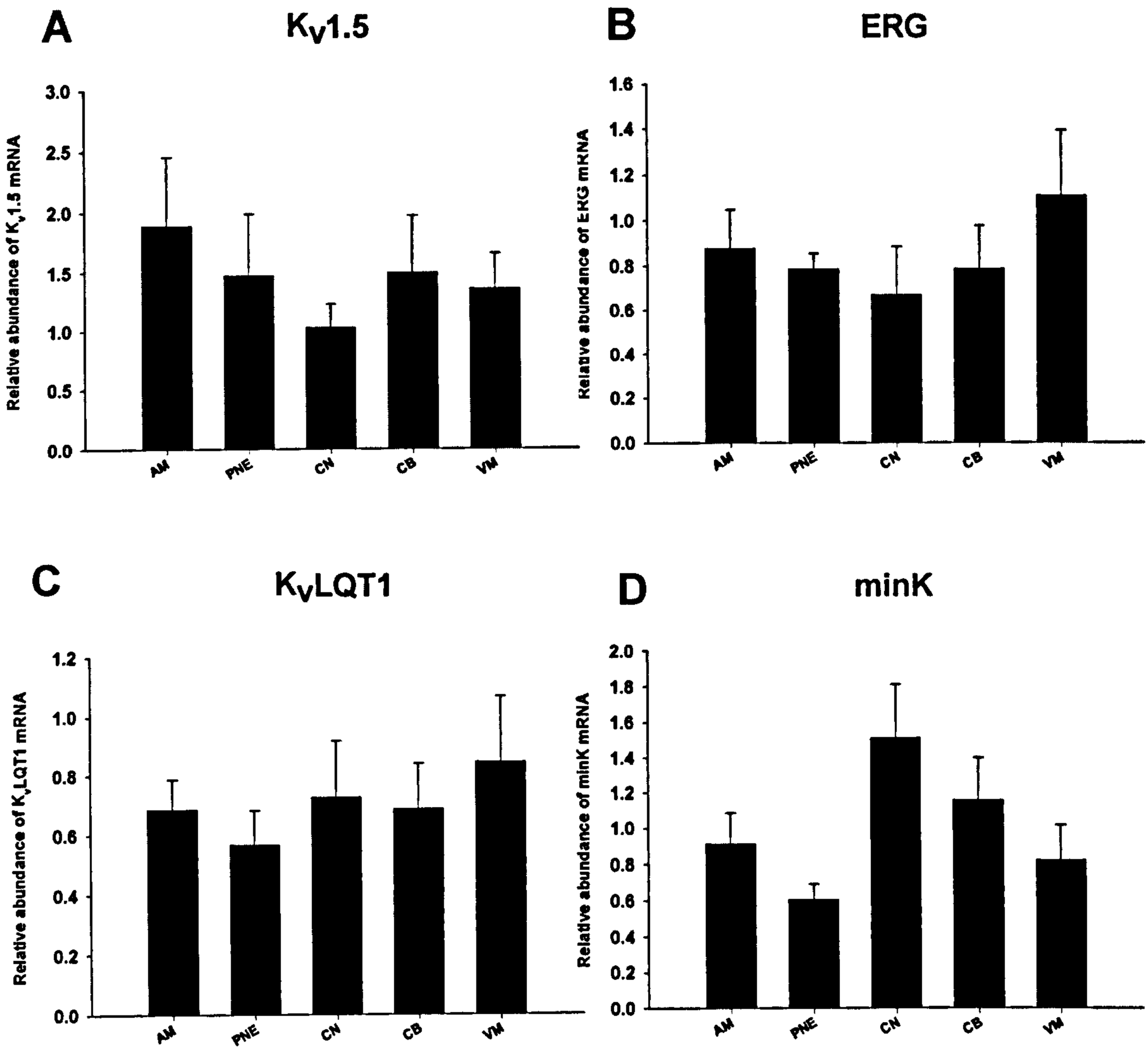

Figure 7.7 *Real time* PCR results for delayed rectifier current mRNAs. A, $K_v1.5$; B, ERG; C, K_vLQT1; D, minK. AM, atrial muscle; PNE; CN, compact node; CB, common bundle; VM, ventricular muscle.

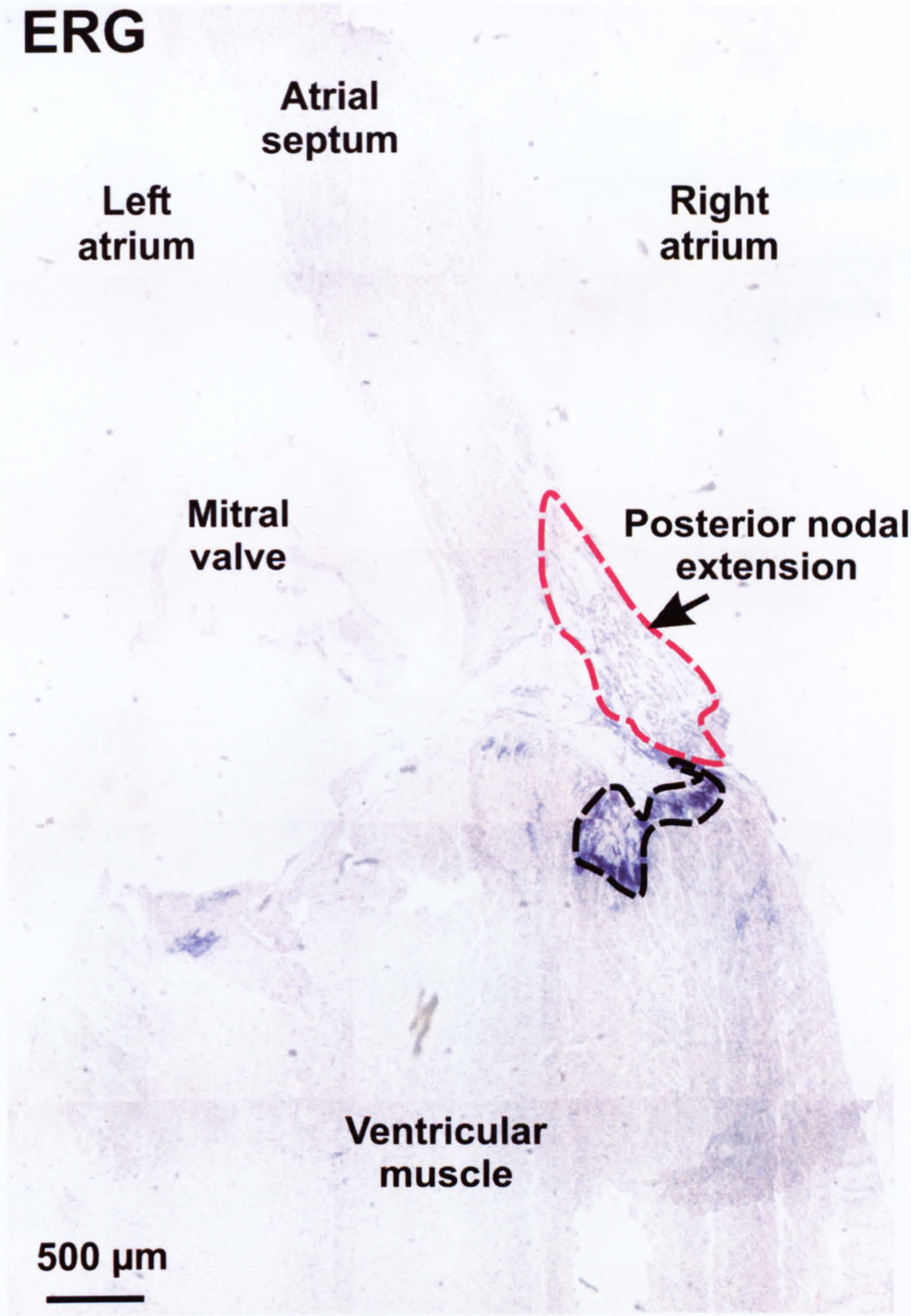

Figure 7.8 *In situ* hybridisation image of ERG mRNA at the level of the PNE. Red dashed line outlines cells comprising PNE. Black dashed line shows region of *non-specific* staining.

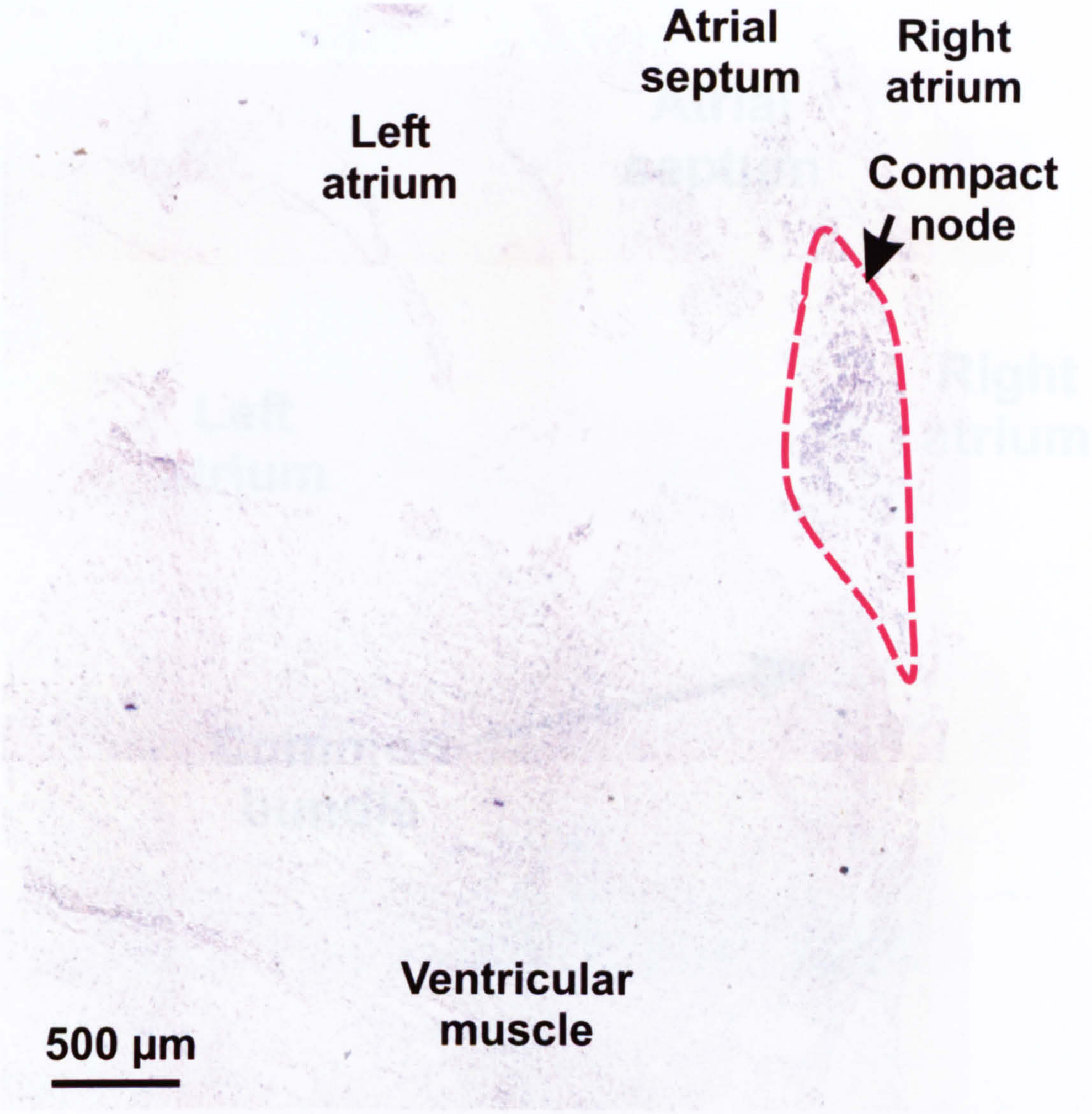

Figure 7.9 *In situ* hybridisation image of ERG mRNA at the level of the compact node. Red dashed line outlines cells comprising compact node.

ERG

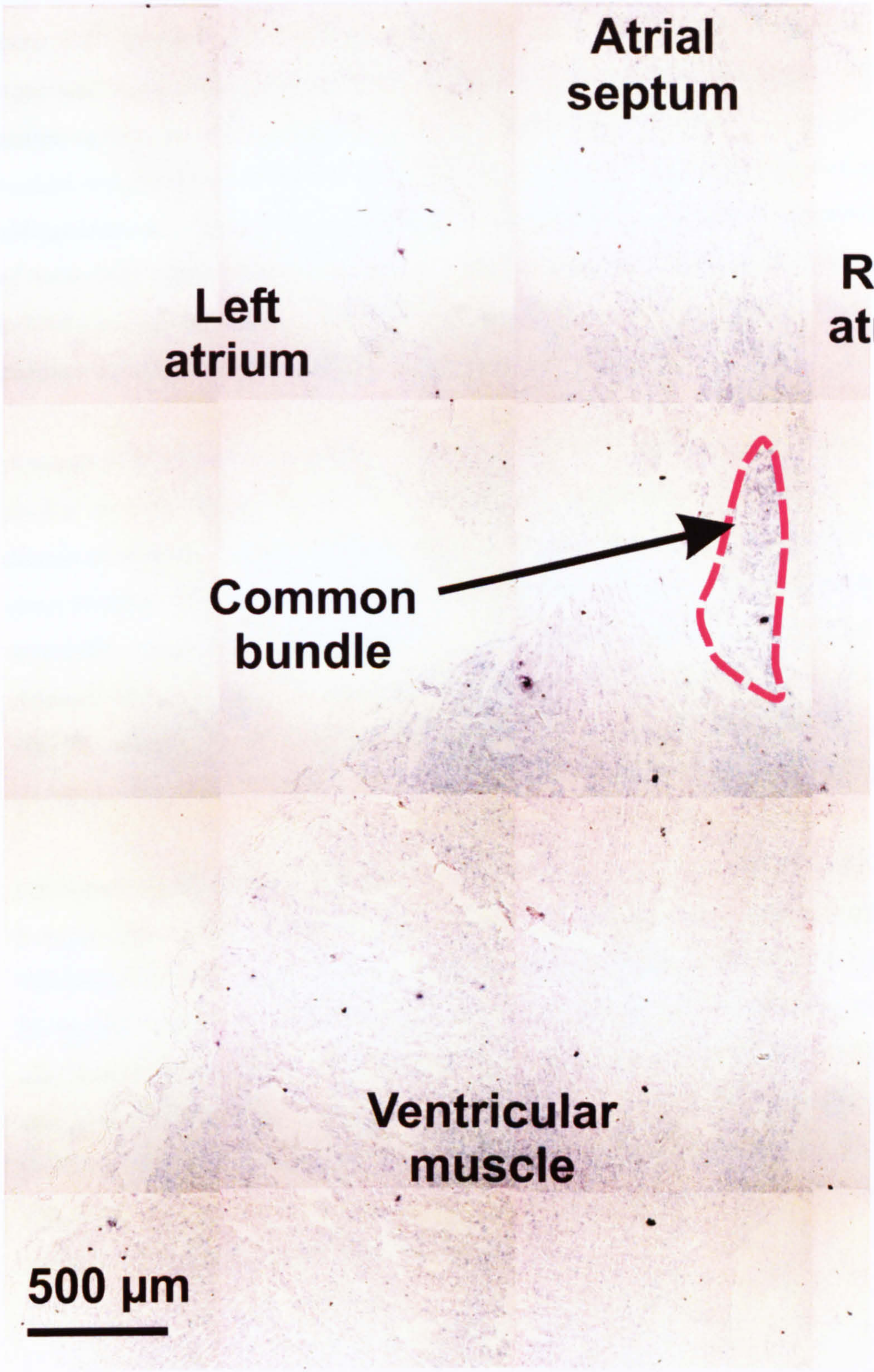

Figure 7.10 *In situ* hybridisation image of ERG mRNA at the level of the common bundle. Red dashed line outlines cells comprising common bundle.

where single cells originate from within the confines of the triangle of Koch and given the complex electrical heterogeneity of the rabbit AVN the cells retaining morphology and function in these studies may originate from an area other than the PNE, compact node or common bundle. In addition, it is possible that the cells not expressing $I_{K,s}$ are more Ca^{2+} tolerant and therefore more likely to survive. Indeed, Yue et al. (1996) suggested that I_K is sensitive to the isolation methods used to isolate single cells. Using canine atrium, they found only 4 % of cells isolated using "chunk" pieces of tissue to contain recordable I_K compared to 99 % of cells obtained using arterial perfusion of a collagenase-containing solution. Multicellular preparations may allow a greater survival of those cells expressing both $I_{K,r}$ and $I_{K,s}$. On the other hand, it is possible that, although mRNAs encoding K_vLQT1 and mink are present in the AVN (Fig. 7.7C), they fail to produce functional protein complexes needed to generate $I_{K,s}$.

Howarth et al. (1996) using single cells from rabbit AVN and ventricle showed $I_{K,r}$ to be similar in both tissues (in terms of steady state activation for example). However, deactivation of tail currents upon repolarization was more rapid in cells from the AVN (time constant, 230 ms) than ventricle (time constant, 480 ms). This suggests a different molecular composition of the rabbit AVN $I_{K,r}$ channel compared to the ventricular $I_{K,r}$ channel. One possibility is that in the AVN there is a modulatory β-subunit, such as MIRP1, which could possibly confer faster deactivation than in the ventricle. Unfortunately, I was unable to optimise primers for MIRP1 to test this possibility.

I observed no significant differences of K_v1.5 mRNA levels throughout the AVN tissue. It is possible that $I_{K,ur}$ is present in all AVN tissues. This is in contrast to the study of Marrionneau et al. (2005) who showed significantly higher levels of K_v1.5 mRNA in the mouse ventricle compared to atrial muscle, SAN and AVN. Immunocytochemistry and Western blot for K_v1.5 protein have shown it to be present in the SAN of guinea-pig and ferret (Dobrzynski et al., 2000). However, there is no electrophysiological (or protein expression) evidence supporting the existence of functional $I_{K,ur}$ in the AVN. The contrasting findings of Marrioneau et al. (2005) could be due to species differences in the expression patterns of K_v1.5 mRNA.

7.3 Inward rectifier K^+ current, $I_{K,1}$

7.3.1 Introduction

The channels for inward rectifier K^+ current were first described in skeletal muscle (Katz et al., 1949) and later found in Purkinje fibres (Weidmann, 1955). They determine the resting membrane potential in cardiac cells and also contribute to repolarization. Depolarisation causes a reduction in conductance. The term inward rectification refers to the fact that these channels conduct K^+ ions into the cell (at hyperpolarized potentials) more readily than out of the cell (at depolarised potentials). This is because the conductance of the channels is high at hyperpolarized potentials, but low at depolarised potentials. Inward rectification occurs at voltages between -60 and -20 mV and is the result of block of the channel pore by intracellular Mg^{2+} and polyamines, such as spermine.

There are currently six K_{ir} subfamilies ($K_{ir}1$ to $K_{ir}6$) classified according to similarities in amino acid sequence The inward rectifier K^+ channels contain two-transmembrane domains and a pore-forming loop (P-loop). These channels assemble as tetramers to form functional channels (Nichols and Lopatin, 1997).

The first of the $K_{ir}2.x$ subfamily of inward rectifier K^+ channels was cloned from mouse macrophages and when expressed heterologously was shown to closely resemble properties of native I_{K1} (Kubo et al., 1993). Recombinant $K_{ir}2.1$ channels have single channel conductances of 20-29 pS, which closely matches that of native $I_{K,1}$ channels (28 pS; Burnashev at al., 1986). Like all K^+ channels, the $K_{ir}2.x$ subfamily contains the G-Y-G signature sequence, which confers K^+ selectivity.

Further molecular insights into the α-subunits encoding $I_{K,1}$ was provided by Zaritsky et al. (2001) using a transgenic mouse with targeted deletion of the $K_{ir}2.1$ gene. Zaritsky et al. (2001) showed $I_{K,1}$ to be absent from ventricular myocytes from the knock-out mice. However, there was a residual current present, which suggests that alternative isoforms are also present. When they knocked-out $K_{ir}2.2$, there was a 50 % reduction in $I_{K,1}$ which suggests that there are contributions from both isoforms. Various studies using

electrophysiological and molecular biological approaches have investigated $I_{K,1}$ in the heart and shown $K_{ir}2.1$ and $K_{ir}2.2$ to be the major isoforms underlying $I_{K,1}$, with a negligible contribution from $K_{ir}2.3$ (Wang et al., 1998; Liu et al., 2001; Zobel et al., 2003).

Single cells isolated from the AVN fail to display inwardly rectifying K^+ currents (Hancox et al., 1993; Hancox and Levi, 1994). SAN cells also do not possess $I_{K,1}$ (Boyett et al., 2000).

7.3.2 Methods

7.3.2.1 *Real time* PCR

Real time PCR was performed on $K_{ir}2.1$ and $K_{ir}2.2$ cDNAs generated from total RNA isolated from five rabbit AVN tissue types: atrial muscle, PNE, compact node, common bundle and ventricular muscle (n = 8 rabbits). *Real time* PCR was carried out using a Roche LightCycler 1.0. Primers for $K_{ir}2.1$ and $K_{ir}2.2$ were designed and optimised by Dr. James Tellez (Tellez, 2005).

7.3.2.2 *In situ* hybridisation

The riboprobe for $K_{ir}2.1$ mRNA was designed by Dr. James Tellez (Tellez, 2005).

7.3.3 Results

7.3.3.1 *Real time* PCR

The relative expression of mRNA transcripts encoding the α-subunits, $K_{ir}2.1$ and $K_{ir}2.2$, were investigated in the tissues of the AVN conduction system, as well as surrounding atrial and ventricular tissue.

The expression level of $K_{ir}2.1$ mRNA was significantly higher in the ventricle compared to the PNE, compact node, common bundle and atrial muscle ($P < 0.05$; Fig. 7.11A). In

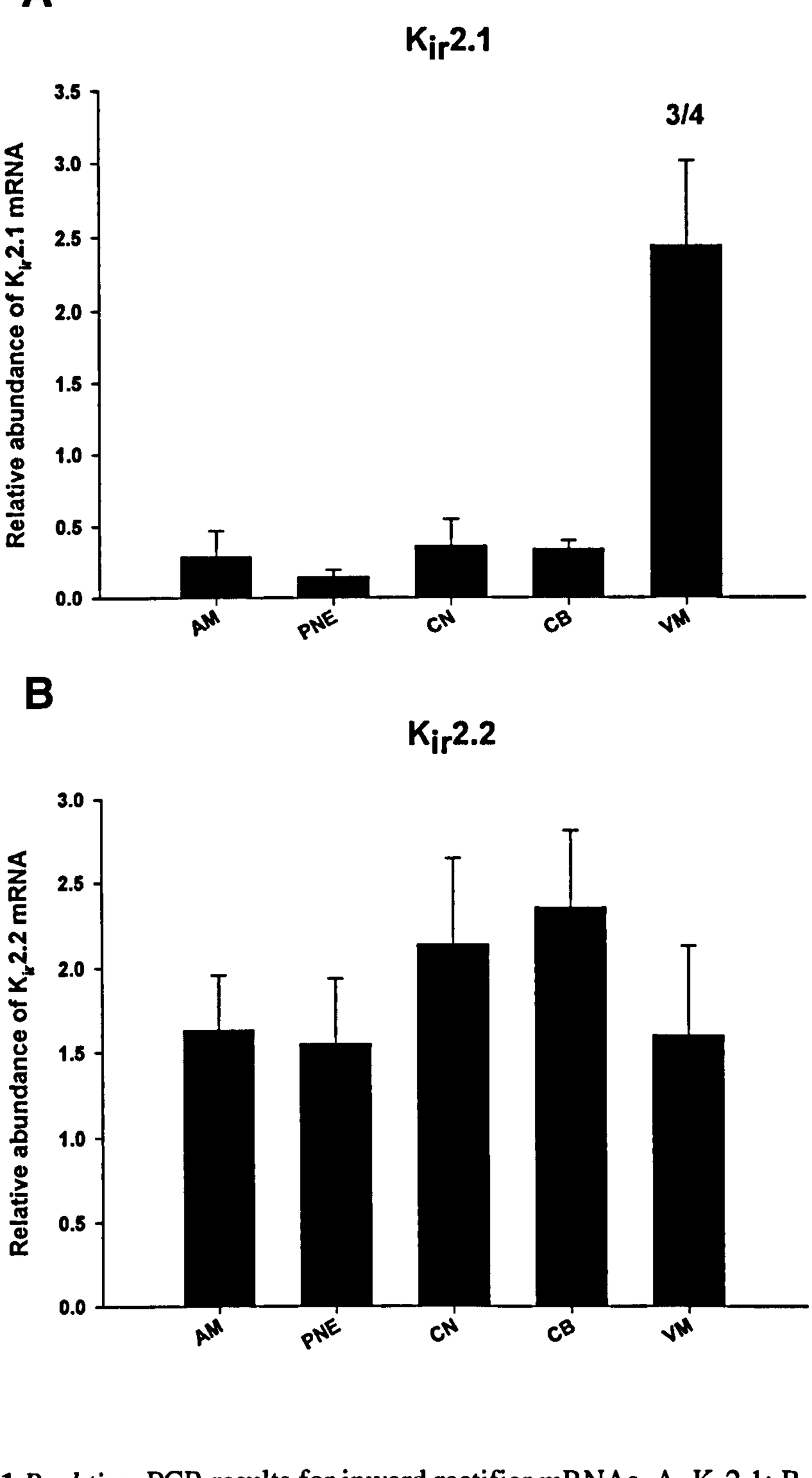

Figure 7.11 *Real time* PCR results for inward rectifier mRNAs. A, $K_{ir}2.1$; B, $K_{ir}2.2$. 3 and 4 denote significantly different from PNE and atrial muscle, respectively ($p < 0.05$; one-way ANOVA); AM, atrial muscle; PNE, posterior nodal extension; CN, compact node; CB, common bundle; VM, ventricular muscle.

contrast, there were no significant differences among the expression levels of $K_{ir}2.2$ mRNA in the different tissues (Fig. 7.11B).

7.3.3.2 *In situ* hybridisation

In situ hybridisation for $K_{ir}2.1$ mRNA revealed an abundance of perinuclear staining for $K_{ir}2.1$ in the ventricular muscle (Figs. 7.12-7.15). In contrast, the atrial muscle, PNE, compact node and common bundle were largely absent of $K_{ir}2.1$ perinuclear staining (Figs. 7.12-7.15).

7.3.4 Discussion

The *real time* PCR data (Fig. 7.11) show the presence of both $K_{ir}2.1$ and $K_{ir}2.2$ in the ventricles, which is consistent with the presence in the ventricles of a negative resting potential of ~ -80 mV and a sharp repolarization phase at the end of the plateau. In the atrial muscle, both $K_{ir}2.1$ and $K_{ir}2.2$ were also present, but $K_{ir}2.1$ was less abundant than in the ventricular muscle. The density of $I_{K,1}$ is known to be less in the atria than in the ventricles (Bouchard et al., 2004) and this may be the result of the lower expression of $K_{ir}2.1$ in the atria.

Our findings are consistent with those of previous studies: Ishii et al. (1994) cloned an inward rectifier K^+ channel from rabbit heart with homology to $K_{ir}2.1$ and showed it to be highly abundant in the rabbit ventricle and absent from rabbit atrium using RNA blot analysis. Zobel et al. (2003) showed the expression of both $K_{ir}2.1$ and $K_{ir}2.2$ protein with Western blots in rabbit ventricular tissue. Furthermore, dominant-negative constructs of both $K_{ir}2.1$ and $K_{ir}2.2$, resulted in a 70 % reduction in $I_{K,1}$, suggesting that both $K_{ir}2.1$ and $K_{ir}2.2$ carry $I_{K,1}$.

The *real time* PCR data for $K_{ir}2.2$ show it to be present in the PNE, compact node and common bundle as well as the working myocardium. This is somewhat surprising, because $I_{K,1}$ is known not to be present in the AVN. However, the absolute abundance of $K_{ir}2.2$ mRNA is not known and it may not be sufficient to result in significant $I_{K,1}$ in the AVN. As expected, the level of $K_{ir}2.1$ mRNA was low in the AVN (Figs. 7.11 and 7.12-7.15). Unexpectedly, however, the level of $K_{ir}2.1$ and $K_{ir}2.2$ mRNA was the same

$K_{ir}2.1$

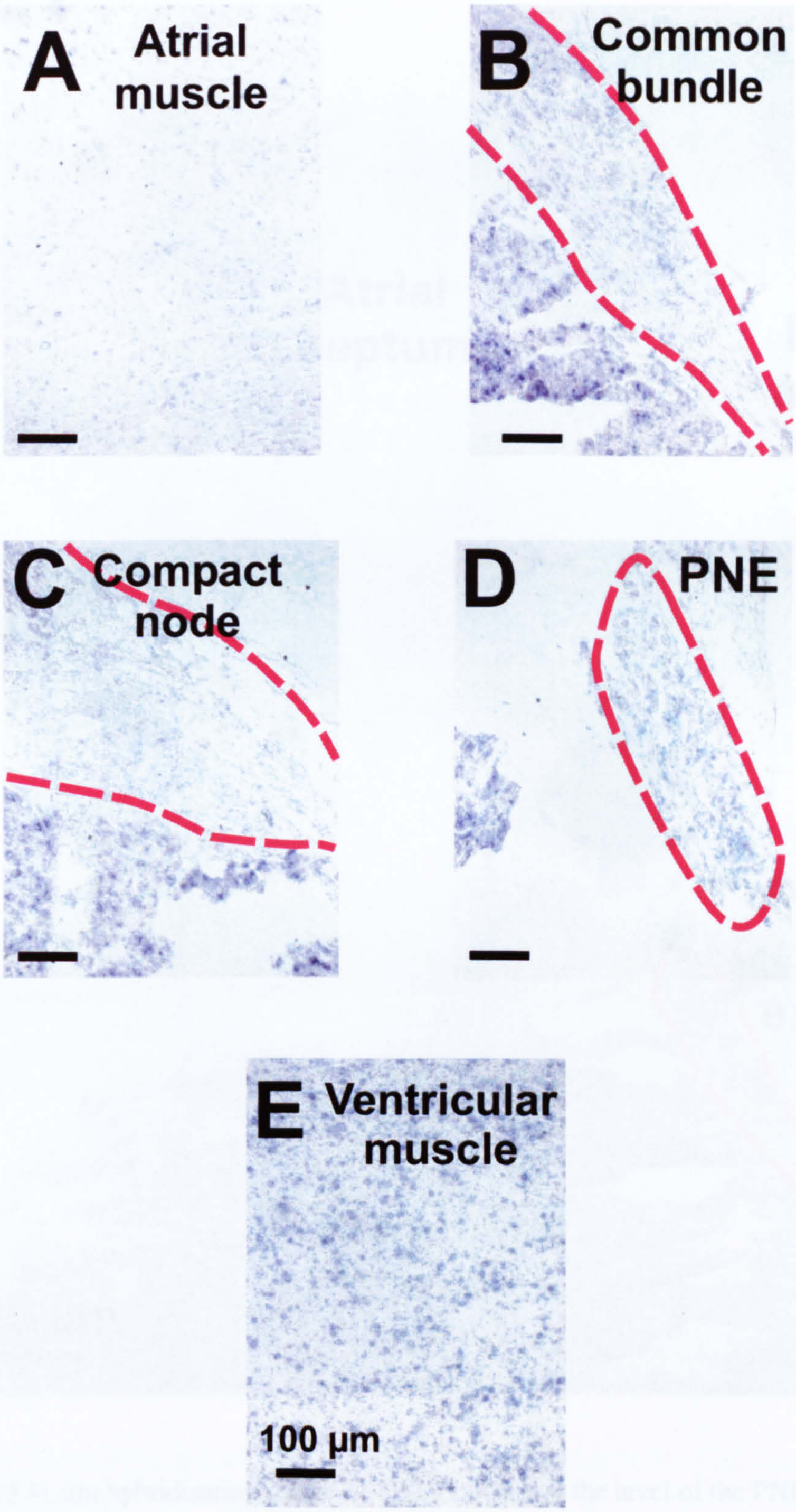

Figure 7.12 High power (x20 magnification) *in situ* hybridisation images of $K_{ir}2.1$ mRNA. A, atrial muscle; B, common bundle; C, compact node; D, PNE; E, ventricular muscle. Red dashed line outlines nodal cells.

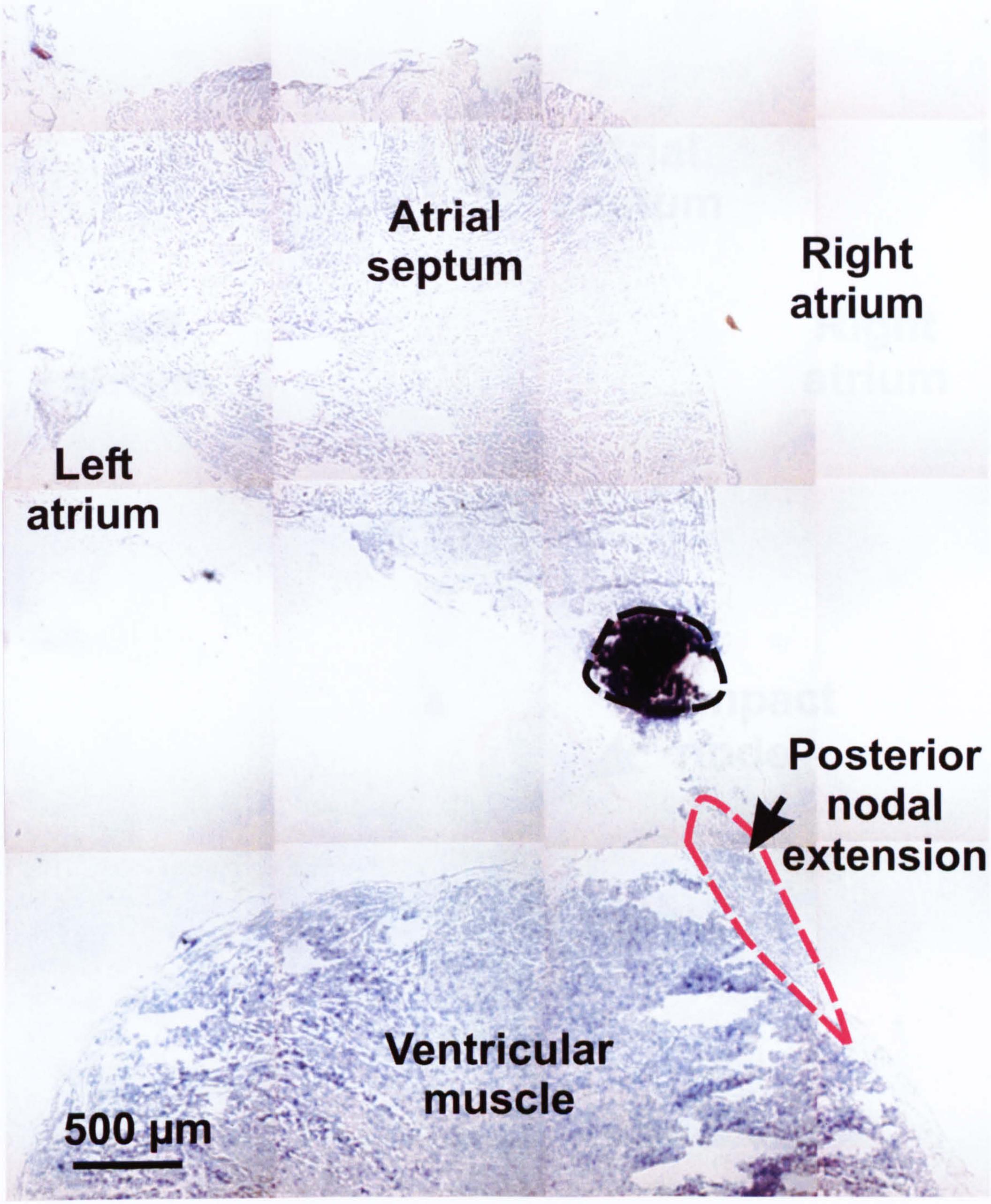

Figure 7.13 *In situ* hybridisation image of $K_{ir}2.1$ mRNA at the level of the PNE. Red dashed line outlines cells comprising PNE. Black dashed line shows region of *non-specific* staining.

$K_{ir}2.1$

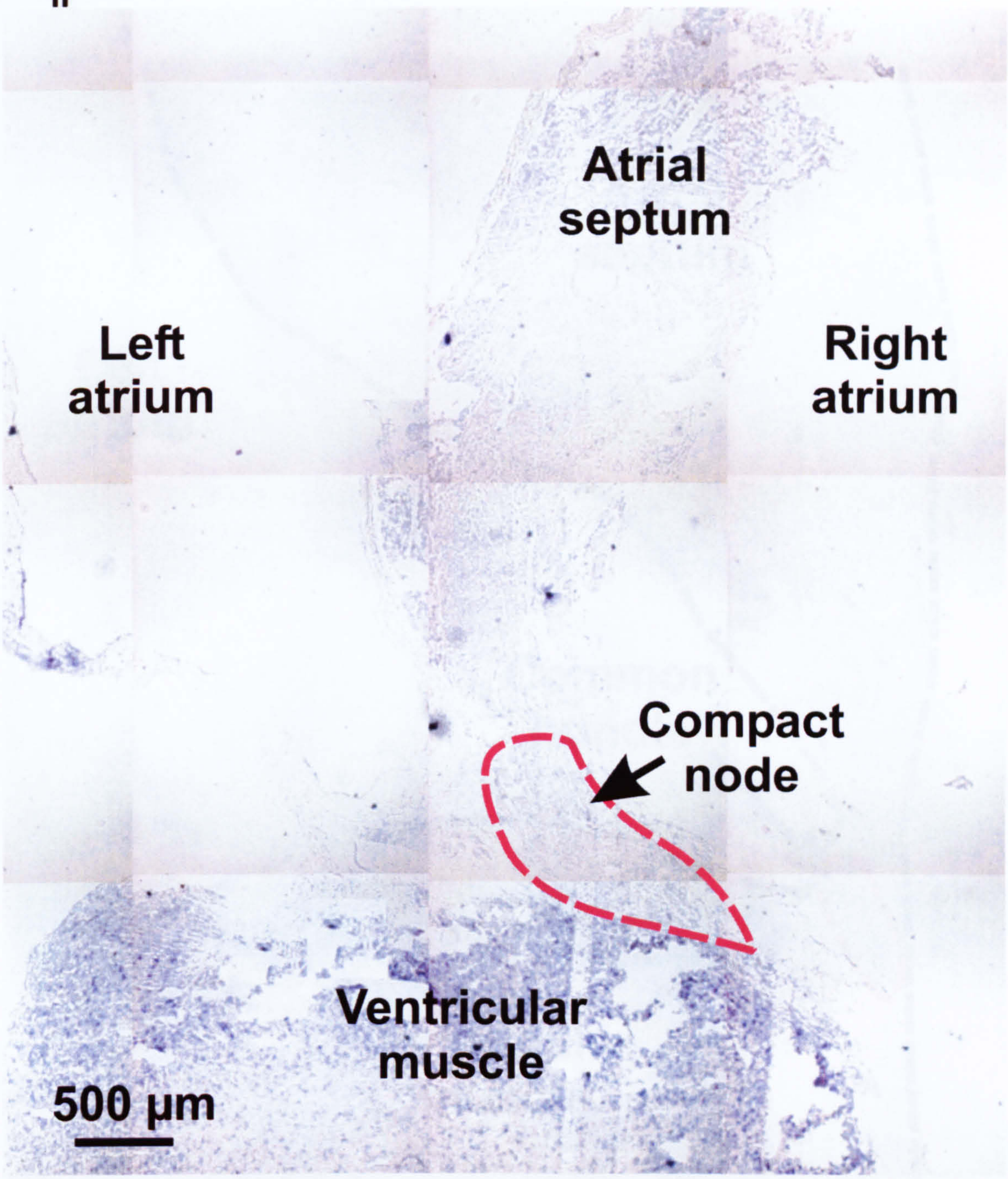

Figure 7.14 *In situ* hybridisation image of $K_{ir}2.1$ mRNA at the level of the compact node. Red dashed line outlines cells comprising compact node.

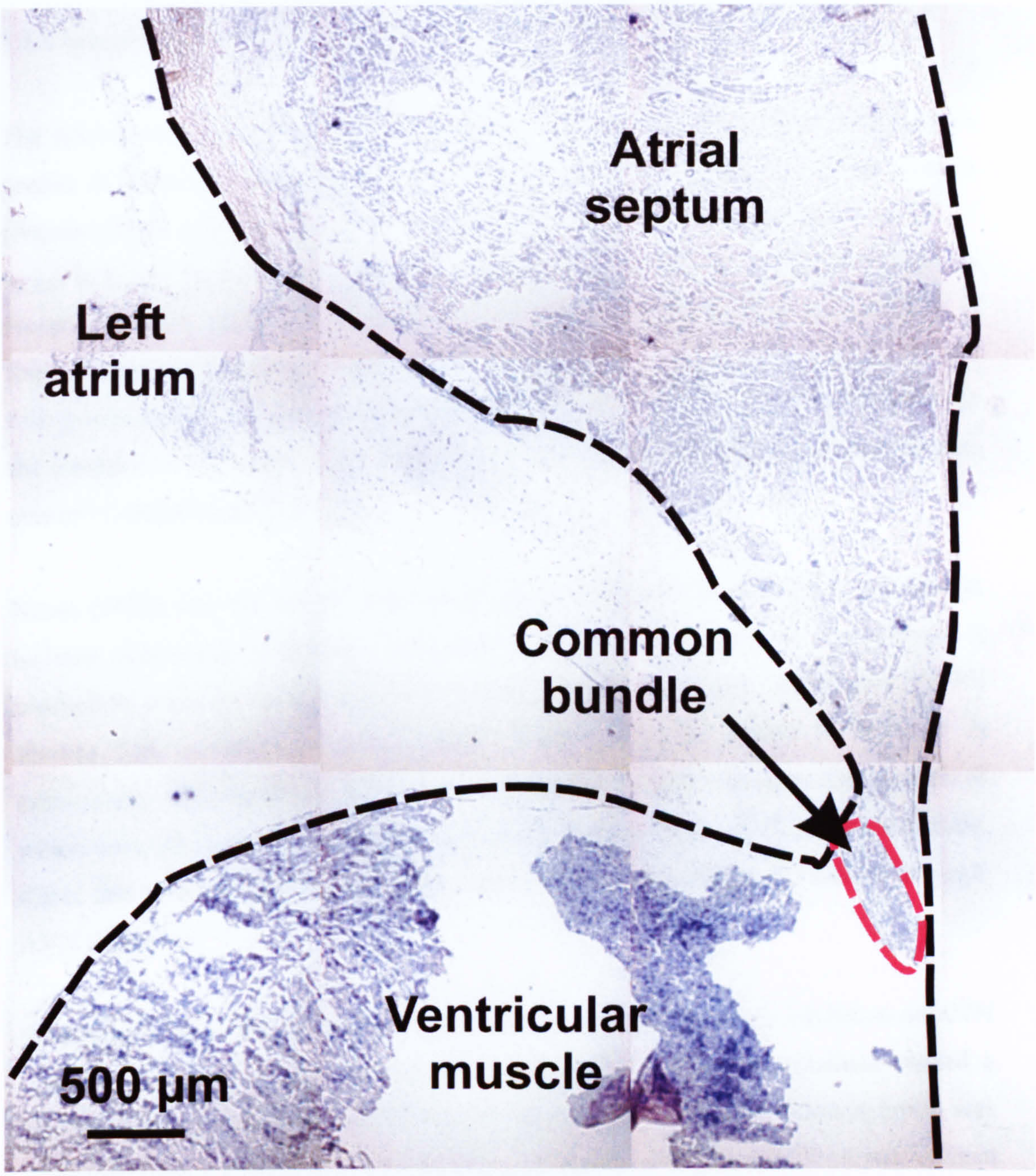

Figure 7.15 *In situ* hybridisation image of $K_{ir}2.1$ mRNA at the level of the common bundle. Red dashed line outlines cells comprising common bundle. Black dashed line outlines tissue.

in the AVN and atrial muscle. Perhaps $K_{ir}2.3$ mRNA is present in the atrial muscle, but not the AVN.

7.4 ATP-sensitive potassium current ($IK_{,ATP}$)

7.4.1 Introduction

The adenosine-tri-phosphate (ATP) sensitive K^+ current ($I_{K,ATP}$) is present in various organs of mammals including the heart, brain, pancreas, kidney and blood vessels (Aguilar-Bryan and Bryan, 1999). In the heart, the major pore-forming α-subunit of $I_{K,ATP}$ is $K_{ir}6.2$. $K_{ir}6.2$ forms a complex with a β-subunit known as the sulphonylurea receptor, SUR2A (Babenko et al., 1998; Haider et al., 2005). The channel complex is formed with the following stoichiometry: four α-subunits ($K_{ir}6.x$) are combined with four β-subunits (SUR). During normal physiological conditions, I_{KATP} is inactive due to the presence of ATP; only upon removal of ATP during ischemia does the channel pass current (Goldhaber et al., 1991).

Noma (1983) was the first to demonstrate the existence of an outward K^+ current in isolated guinea-pig ventricular myocytes under hypoxic conditions; the current is blocked by a rise in intracellular ATP (Noma, 1983). Furthermore, Wilde et al. (1990) showed that ischaemia-induced opening of these channels caused an increase in extracellular K^+ concentration and shortening of the cardiac action potential, both of which were prevented by the application of the specific $I_{K,ATP}$ blocker, glibenclamide. Kakei and Noma (1984) showed the presence of an ATP-sensitive K^+ current in single AVN myocytes.

Samanbori et al. (1995) studied the effects of hypoxia and metabolic inhibition on AVN conduction properties and the induction of AV block. Hypoxic solutions caused a prolongation of AVN conduction time (A-H interval). However, when hypoxia was combined with a glucose-free solution, second-degree or higher AV block was evident possibly suggesting an effect of $I_{K,ATP}$ on AVN function under these conditions. However, the role of $I_{K,ATP}$ in normal AVN function is probably negligible.

7.4.2 Methods

7.4.2.1 *Real time* PCR

Real time PCR was performed using cDNA generated from total RNA isolated from five rabbit AVN tissue types: atrial muscle, PNE, compact node, common bundle and ventricular muscle (n = 8 rabbits). Primers for $K_{ir}6.2$ and SUR2A were designed and optimised by Dr. James Tellez (Tellez, 2005).

7.4.2.2 *In situ* hybridisation

A riboprobe against $K_{ir}6.2$ or SUR2A was not generated and therefore no *in situ* hybridisation results are present for these transcripts.

7.4.3 Results

7.4.3.1 *Real time* PCR

The relative expression of mRNA transcripts encoding the α-subunit, $K_{ir}6.2$, and the β-subunit, SUR2A, of the $I_{K,ATP}$ were investigated in the tissues of the AVN conduction system, as well as the surrounding atrium and ventricle. Expression levels for SUR2A mRNA were significantly higher in the ventricle than in the PNE (Fig. 7.16B). No significant differences among $K_{ir}6.2$ mRNA levels were detected (Fig. 7.16A). However, there was a tendency for higher expression of this transcript in atrium and ventricle compared to the PNE, compact node and common bundle (Fig. 7.16A).

7.4.4 Discussion

The greater level of SUR2A in the ventricle suggests a greater expression of K_{ATP} channels in the ventricles versus other tissues since SUR2A subunits are necessary for $K_{ir}6.2$ subunits to traffic to the membrane and form functional channels. However, it could be that there is a surplus of SUR2A in the ventricle as opposed to other tissues and that the levels of SUR2A do not directly reflect the levels of functional channels formed with SUR2A – this has been suggested previously (Van Bever et al., 2004). If,

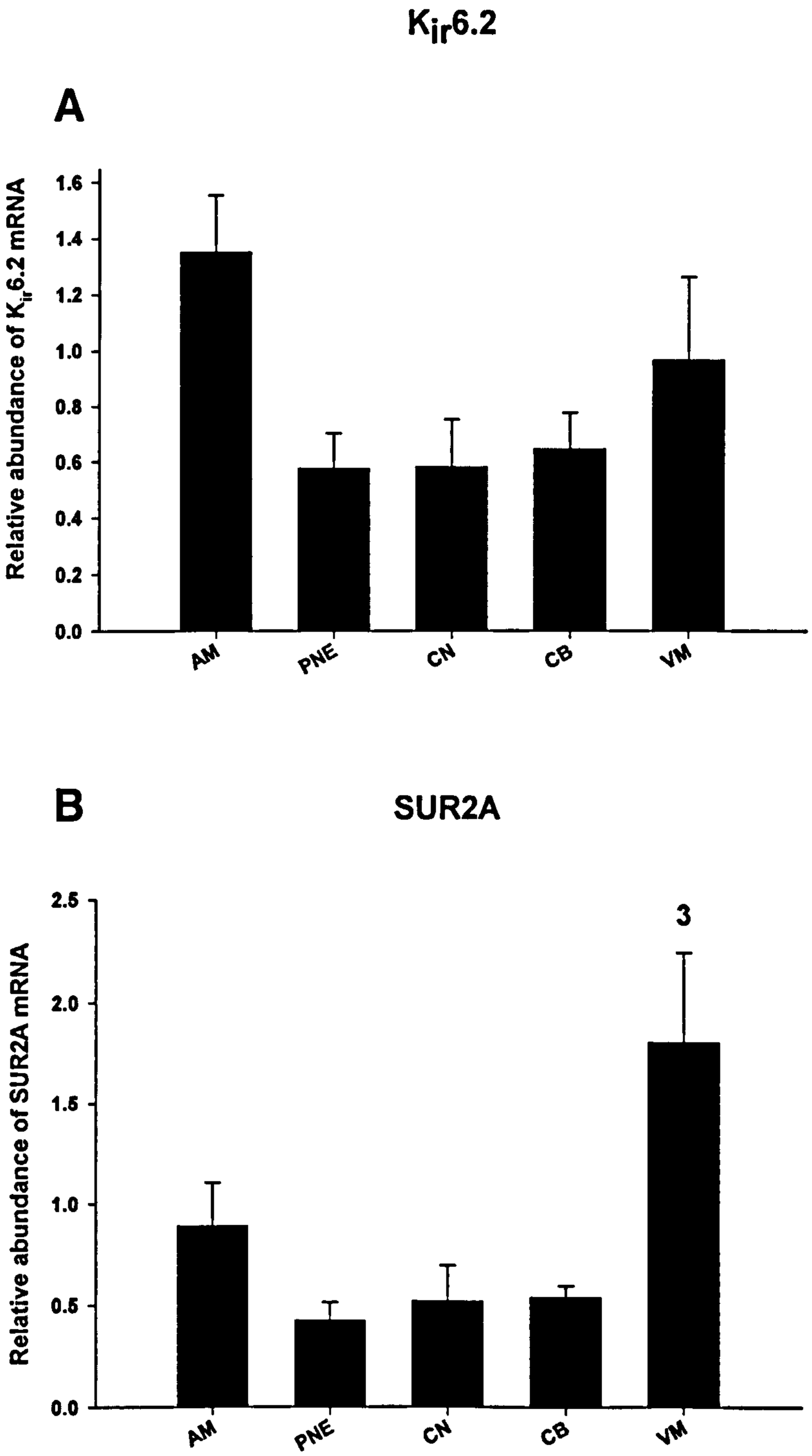

Figure 7.16 *Real time* PCR results for ATP sensitive current mRNAs. A, $K_{ir}6.2$; B, SUR2A. 3 denotes significantly different from PNE ($P < 0.05$; one-way ANOVA); AM, atrial muscle; PNE; CN, compact node; CB, common bundle; VM, ventricular muscle.

indeed, the greater level of SUR2A mRNA in the ventricle as compared to the atria do reflect a greater abundance of functional channels at the membrane, then these data are in contrast to experimental findings: the atria (as compared to the ventricles) have been shown to be more sensitive to metabolic inhibition, diazoxide-induced opening and propafenone-induced blockade; collectively, the functional data suggest that the atria have a greater sensitivity to ischaemia than the ventricles (Poitry et al., 2003; Christie et al., 1999). The presence of $K_{ir}6.2$ mRNA in the ventricle is consistent with previous findings in rabbit ventricular myocytes: it has been shown that adenoviral-mediated transduction of mutated $K_{ir}6.1$ channels has no effect on $I_{K,ATP}$ in ventricular myocytes (Seharaseyon et al., 2000).

The detection of $K_{ir}6.2$ and SUR2A mRNA in the common bundle, compact node and PNE, albeit at lower levels than in the working myocardium, is consistent with electrophysiological findings showing the presence of $I_{K,ATP}$ in the rabbit AVN (Kakei and Noma, 1984). However, there is the possibility that $K_{ir}6.1$ α-subunit is expressed in these tissues, because the measured single channel conductance of $I_{K,ATP}$ in the investigation of Kakei and Noma (1984) was ~40 pS, which is intermediate between that of $K_{ir}6.2$ homotetramers (67 pS) and $K_{ir}6.1$ homotetramers (34 pS; Kono et al., 2000).

Our data suggest there is a tendency for lower levels of I_{KATP} in the rabbit AVN conduction tissue, which is consistent with previous findings from our laboratory: rabbits were shown to have lower level of $K_{ir}6.2$ mRNA in the SAN (unpublished data).

Chapter 8

Ca^{2+}-handling proteins

8.1 Introduction

8.1.1 Ca^{2+} release

Ca^{2+} handling in cardiac muscle involves Ca^{2+}-release units (CRUs) (Franzini-Armstrong et al., 2005). CRUs consist of SR, L-type Ca^{2+} channels, ryanodine receptors, triadin and junctin. In addition to CRUs, important Ca^{2+} handling proteins include SERCA2a, Ca^{2+}-ATPase, Na^{+}-Ca^{2+} exchanger (NCX), plasma membrane Ca^{2+}-ATPase (PMCA), calsequestrin and inositol 1.4.5-triphosphate (IP_3) receptors. Ca^{2+} release from the SR occurs via ryanodine (Inui et al., 1987) or IP_3 receptors (Berridge and Irvine, 1989).

The cardiac SR can be divided into three: 1) "dyads" (junctional SR forms a close association with the T-tubules of the myocyte) 2) peripheral SR which lies immediately adjacent to the surface membrane/sarcolemma and 3) corbular SR which fails to form any associations with the membrane and is located deep in the cytosol (Franzini-Armstrong et al., 2005). Calsequestrin binds Ca^{2+} in the SR and effectively acts as a Ca^{2+} sink. Triadin and junctin are important proteins in the SR since they form quarternary structures with ryanodine receptors and calsequestrin (for review see Niggli, 1999).

Technological advances in confocal imaging, in particular laser scanning confocal microscopy with improved resolution concomitant with developments in Ca^{2+}-dependent fluorescent dyes (Minta et al., 1989) took us from Ca^{2+} waves (Takamatsu and Wier, 1990) and to the phenomena of "Ca^{2+} sparks" (Fig. 8.1). Ca^{2+} sparks are subcellularly localized releases of Ca^{2+}, which have a short duration (100 ms), an amplitude of ~170 nM and limited spatial diffusion (Cheng et al., 1993; Lipp and Niggli, 1994). Ca^{2+} sparks most likely represent the opening of one or a few ryanodine receptors (Cheng et al., 1993). However, during excitation-contraction coupling, Ca^{2+}

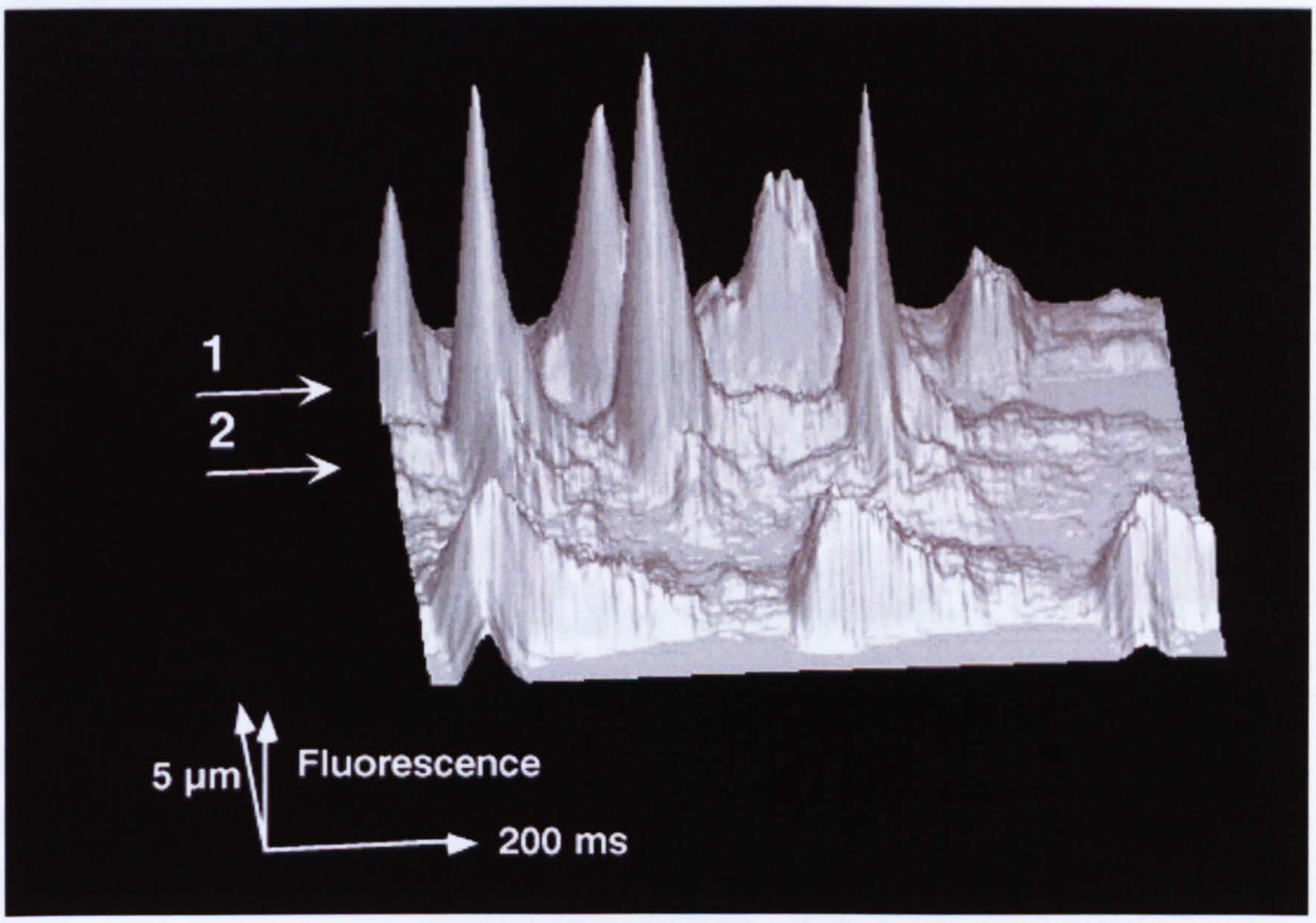

Figure 8.1 An example of Ca^{2+} sparks from a rat cardiac myocyte. A surface plot of fluo-3 fluorescence (a measure of intracellular Ca^{2+}) was constructed from a confocal line scan image. Localized Ca^{2+} signals are shown along one spatial dimension whereas the other dimension corresponds to time. From Niggli (1999).

sparks summate to produce the overall Ca^{2+} transient, which is detected with more coarse measurements of Ca^{2+} concentration (Cheng et al., 1995). Ca^{2+} sparks are linked to the opening of single L-type Ca^{2+} channels.

Removal of Ca^{2+} from the cytosol is achieved predominantly via two mechanisms: 1) a Ca^{2+} ATP-ase located on the SR (SERCA2a) and 2) a Na^{+}-Ca^{2+} exchanger (NCX) located on the plasma membrane/sarcolemma. Ryanodine receptors, once excited, become refractory and this explains various phenomena: 1) Ca^{2+}-induced Ca^{2+} release (CICR) can be described as positive feedback and ryanodine receptor refractoriness prevents uncontrollable Ca^{2+} release and 2) if two propagating Ca^{2+} waves collide there is an annhilation of the waves (Cheng et al., 1996).

Major differences between atrial and ventricular EC coupling exist. Di-2-ANEPEQ staining of ventricular cells reveals, in addition to strong sarcolemmal staining, a network of T-tubules, whereas staining atrial cells shows only sarcolemmal staining indicating a lack of T-tubules in atrial myocardium (Tanaka et al., 2001). The sensitivity of contractile force in rat (Tanaka et al., 2001), guinea-pig (Agata et al., 1994) and rabbit (Bers, 1989) to ryanodine is greater in atrial compared to ventricular cells. This suggests that the SR plays a greater role in atrial as compared to ventricular cells. SR architecture in SAN and AVN tissue lacks the organized structural make-up of the working myocardium (Shimada et al., 1986).

8.1.2 Sarcoplasmic/endoplasmic reticulum Ca^{2+} ATPase (SERCA2a)

The sarco(endo)plasmic reticulum Ca^{2+}-ATPase (SERCA) family of proteins is encoded by three separate genes: SERCA1, SERCA2 and SERCA3. Each of these isoforms shows tissue specific expression. Furthermore, alternative splicing results in six different splice variants: SERCA1a is predominant in fast-twitch skeletal muscle (Stewart and Maclennan, 1976); SERCA2a is mainly found in cardiac muscle and slow-twitch skeletal muscle (Brandl et al., 1986); SERCA2b is expressed ubiquitously (Lytton et al., 1989); and SERCA3 is found predominantly in non-muscle cells (Papp et al., 1992). SERCA2a is responsible for the removal of accumulated cytosolic Ca^{2+} (as a result of myocyte depolarization) back into the lumen of the SR for use in a subsequent contraction. SERCA2a lies adjacent to a protein called phospholamban (PLB), which exerts an inhibitory influence on SERCA2a whereby SERCA2a's affinity for Ca^{2+} is

reduced. This is the result of direct protein interaction (Caroni and Carafoli, 1981). Furthermore, if PLB becomes phosphorylated as a result of protein kinase activity, it loses its ability to inhibit SERCA2a and therefore Ca^{2+} pumping efficiency is improved (Toyofuku et al., 1994). Ji et al. (2000) showed in transgenic mice heterozygous for a null mutation in SERCA2a profound decreases in contraction and relaxation properties; compensatory upregulation of NCX was also detected. Minajeva et al. (1997) investigated Ca^{2+} handling in rabbit atria and ventricles and found relative abundance of SERCA2a mRNA to be 38% higher in the atria compared to ventricles.

8.1.3.1 Na^{+}-Ca^{2+} Exchanger (NCX)

Reuter and Seitz (1968) were the first to report the presence of a Na^{+} and Ca^{2+} exchange mechanism in cardiac muscle (Reuter and Seitz, 1968). Kieval et al. (1992) showed that the expression level of NCX in the sarcolemma was the same in the T-tubules, the surface membrane and intercalated discs in rat and guinea-pig myocytes (Kieval et al., 1992). In contrast, rabbit ventricular myocytes have been suggested to contain more NCX protein in the T-tubules (Chen et al., 1995). The discrepancies between the two studies may be accounted for by greater folding of the T-tubules compared to the surface membrane and limitations in the resolution of confocal microscopy (Kieval et al., 1992). Bridge et al. (1993) using a rapid solution exchange system and specific blockers of NCX estimated the Ca^{2+} entering the cells from I_{Ca} upon membrane depolarisation was extruded via the NCX. Bassani et al. (1994) using rat and rabbit myocytes estimated that ~7 % and ~25-30 %, respectively, of the decay of the Ca^{2+} transient was due to removal of Ca^{2+} from the cytosol via NCX (Bassani et al., 1994). NCX can influence EC coupling profoundly, since NCX determines the level of intracellular Ca^{2+}. The NCX has ~10-fold less affinity for Ca^{2+} than the sarcolemmal Ca^{2+}-ATPase (PMCA) but has a 40- to 50-fold greater turnover rate (Bassani et al., 1994).

8.1.3.2 Role of the NCX during cardiac action potential

As explained above NCX is located in the sarcolemma and is a major mediator of Ca^{2+} extrusion from cardiac myocytes. However, it also has the capability to generate a current, I_{NCX}. The current-voltage relationship for I_{NCX} indicates that the reversal potential, E_{NCX}, is between -10 and -50 mV under diastolic conditions. During the initial

phase of myocyte depolarization during the action potential the membrane potential becomes more positive than E_{NCX} and, therefore, a brief outward current (corresponding to Ca^{2+} influx) is generated. Eventually, the intracellular Ca^{2+} level rises as a result of CICR. This causes E_{NCX} to become more positive than the membrane potential and, therefore, an inward current (corresponding to Ca^{2+} efflux) is generated by NCX.

Atrial cells display two plateau phases: a high plateau and a low plateau. Using mathematical models, Hilgemann and Noble (1987) showed that the low plateau of the atrial action potential is generated by inward I_{NCX}, which is activated by the Ca^{2+} transient (Hilgemann and Noble, 1987). Experimentally, Earm et al. (1990) showed in isolated rabbit atrial myocytes that the inward I_{NCX} current was prevented when the Ca^{2+} transient was abolished with EGTA (Earm et al., 1990). Furthermore, substituting extracellular Na^+ by Li^+ (which cannot be transported by NCX) reduced the duration of the low plateau in rabbit and human atrial cells (Earm et al., 1990; Coraboeuf and Nargeot, 1993).

The role of I_{NCX} during the ventricular action potential is less important than during the atrial action potential. The plateau phase in the ventricular action potential and peak of the Ca^{2+} transient occur at relatively positive voltages. For this reason, the driving force for inward I_{NCX} is weak. Janvier et al. (1997) using ferret ventricular cells estimated inward I_{NCX} (BAPTA-sensitive current) to be ~0.16 nA in amplitude; when this current was blocked by BAPTA or by replacing Na^+ with Li^+ the ventricular action potential was significantly shortened, indicating this current has a significant role to play in the ventricular action potential (Janvier et al., 1997). Furthermore, Leitch and Brown (1996) using a BAPTA-AM detected no change in inactivation of I_{Ca} and found a significant shortening of guinea-pig action potential duration, which they attributed to a reduction in inward I_{NCX}.

8.1.5 Role of I_{NCX} in pacemaker function

Inward I_{NCX} is known to play a role in pacemaker activity in the SAN (Bogdanov et al., 2001). Convery and Hancox (2000) investigated I_{NCX} in rabbit AVN and ventricular cells; similar densities of I_{NCX} were detected in AVN and ventricular cells.

8.1.6 Molecular properties of NCX

NCX was first cloned from dog heart (Nicoll et al., 1990). Since then, three genes have been shown to encode NCX in mammals: NCX1, NCX2 and NCX3 (Nicoll et al., 1996). Regional expression patterns of the three different isoforms indicate that NCX1 is the major isoform expressed in the heart (Kofuji et al., 1992). In contrast, NCX2 and NCX3 appear to be restricted to the brain and skeletal muscle (Li et al., 1994; Nicoll et al., 1996). All three isoforms share structural similarities, with 11 transmembrane domains and a large intracellular loop between transmembrane domains 5 and 6. This large intracellular loop is responsible for regulatory Ca^{2+} binding (Levitsky et al., 1994) and alternative splicing, giving rise to tissue specific splice variants (Kofuji et al., 1994).

8.1.7 Ryanodine receptor

Ryanodine receptors (RYRs) belong to a superfamily of Ca^{2+} release channels, which also includes the inositol 1,4,5-triphosphate receptor (IP_3Rs). RYRs form functional complexes as tetramers (Lai et al., 1989). They play an important role in excitation-contraction coupling in the heart (Berridge et al., 2000). Three genes have been cloned which encode the three RYR isoforms: RYR1, RYR2 and RYR3. RYR1 is predominantly found in skeletal muscle, RYR2 is mostly found in cardiac (Anderson et al., 1989) and brain tissues and RYR3 is found in a variety of tissues such as brain, diaphragm and smooth muscle (Franzini-Armstrong and Protasi, 1997). However, more recent findings have revealed further complexity, whereby some tissues express all three receptor isoforms (Giannini et al., 1995).

Xiao et al. (2002) using HEK293 cells demonstrated the ability of ryanodine receptors to form heteromers, in particular RYR1 with RYR2 and RYR2 with RYR3. Moreover, in vascular smooth muscle cells that have been shown to express all three RYR isoforms, antisense removal of either RYR1 or RYR2 prevented Ca^{2+} sparks and a global Ca^{2+} response; in the same study removal of RYR3 had no effect on depolarization- or caffeine-induced Ca^{2+} responses (Coussin et al., 2000). It appears that RYR3 only plays a role, at least in vascular smooth muscle cells, during SR Ca^{2+} overload (Marionneau et al., 2001). However, immunoprecipitation studies using extracts from various tissues have failed to show co-expression of any two isoforms (Murayama and Ogawa, 1996).

Munch et al. (2000) using explanted human hearts to investigate the expression of the three RYR isoforms found protein levels for RYR2 to be significantly lower in the right ventricle as compared to other chambers of the heart. In contrast, RYR1 and RYR3 protein levels were found to be equally abundant in all chambers (Munch et al., 2000). In contrast to the findings of Munch et al. (2000), Cote et al. (2000) using a [^{3}H]ryanodine binding assay found the density of binding 4.5 times lower in human atrial versus ventricular tissue. Masumiya et al. (2003) using an RNase protection assay and *in situ* hybridization on mouse SAN tissue showed RYR2 mRNA to be abundantly expressed in all regions of the heart, whereas RYR3 mRNA expression was predominant in the SAN and right atrium with low levels in the right ventricle.

Until recently, investigations into SR function in cardiac tissue have focused on working myocardium. However, recent work has implicated the SR (as well as NCX – see above) in pacemaker function. Bogdanov et al. (2001) and Vinogradova et al. (2002) using single cells isolated from rabbit SAN have suggested that RYRs play a major role in pacemaking in the heart. However, Honjo et al. (2003) demonstrated with both multicellular preparations and single cells that ryanodine had caused a ~20 % reduction in spontaneous beating rate in both preparations; this is less than that showed by Bogdanov et al. (2001) and Vinogradova et al. (2002) but still significant.

8.2 Methods

8.2.1 *Real time* PCR

Real time PCR was performed using cDNA generated from total RNA isolated from five rabbit AVN tissue types: atrial muscle, PNE, compact node, common bundle and ventricular muscle (n = 8 rabbits). Primers for NCX1, SERCA2a, RYR2 and RYR3 were designed and optimised by Dr. James Tellez (Tellez, 2005).

8.2.2 *In situ* hybridisation

No riboprobes for NCX1 and SERCA2a were generated. Riboprobes for RYR2 and RYR3 were generated; however, upon testing they failed to produce a good signal and were, therefore, not used.

8.3 Results

8.3.1 *Real time* PCR

The relative expression of mRNA encoding isoform 1 of NCX (NCX1), SERCA2a, and the cardiac and neuronal ryanodine receptors (RYR2 and RYR3)were investigated in tissues of the AVN conduction system, as well as the surrounding atrial and ventricular muscle (Fig. 8.2). Expression levels for SERCA2a mRNA were significantly higher in the atrial muscle and ventricular muscle compared to the compact node ($P < 0.05$; Fig. 8.2). No significant differences among NCX1, RYR2 and RYR3 mRNAs were seen between tissues (Fig. 8.2).

8.4 Discussion:

Similar levels of NCX mRNA were detected in all tissues (Fig. 8.2A), which is consistent with the important role of this protein in both Na^+ and Ca^{2+} regulation and generating current during the action potential and pacemaker potential of both working myocardium and pacemaker tissue (Janvier and Boyett, 1996; Reuter et al., 2005). This finding is consistent with the study of Convery and Hancox (2000) who found little difference in I_{NCX} density between rabbit AVN and ventricular cells. The isolation technique used by Convery and Hancox (2000) fails to identify the exact location within the triangle of Koch region of the cells isolated. However, because the study of Dobrzynski et al. (2003) showed the leading pacemaker site to be in the PNE, it is likely that the spontaneously active cells used in their study originate, at least in part, from the PNE (Dobrzynski et al., 2003).

I have shown SERCA2a to be significantly higher in the atrial muscle compared to the compact node (Fig. 8.2B). In addition, there was a tendency for SERCA2a mRNA levels to be higher in the working myocardium than in all the nodal tissues. This suggests that the dependence of the Ca2+ transient on the SR will be less in nodal cells than in atrial and ventricular cells; instead, in nodal cells the Ca^{2+} transient will be more dependent on NCX and Ca^{2+} movement across the sarcolemma. However, Hancox et al. (1994) using FURA-2 measurement of $[Ca^{2+}]_i$ showed that the Ca^{2+} transient was

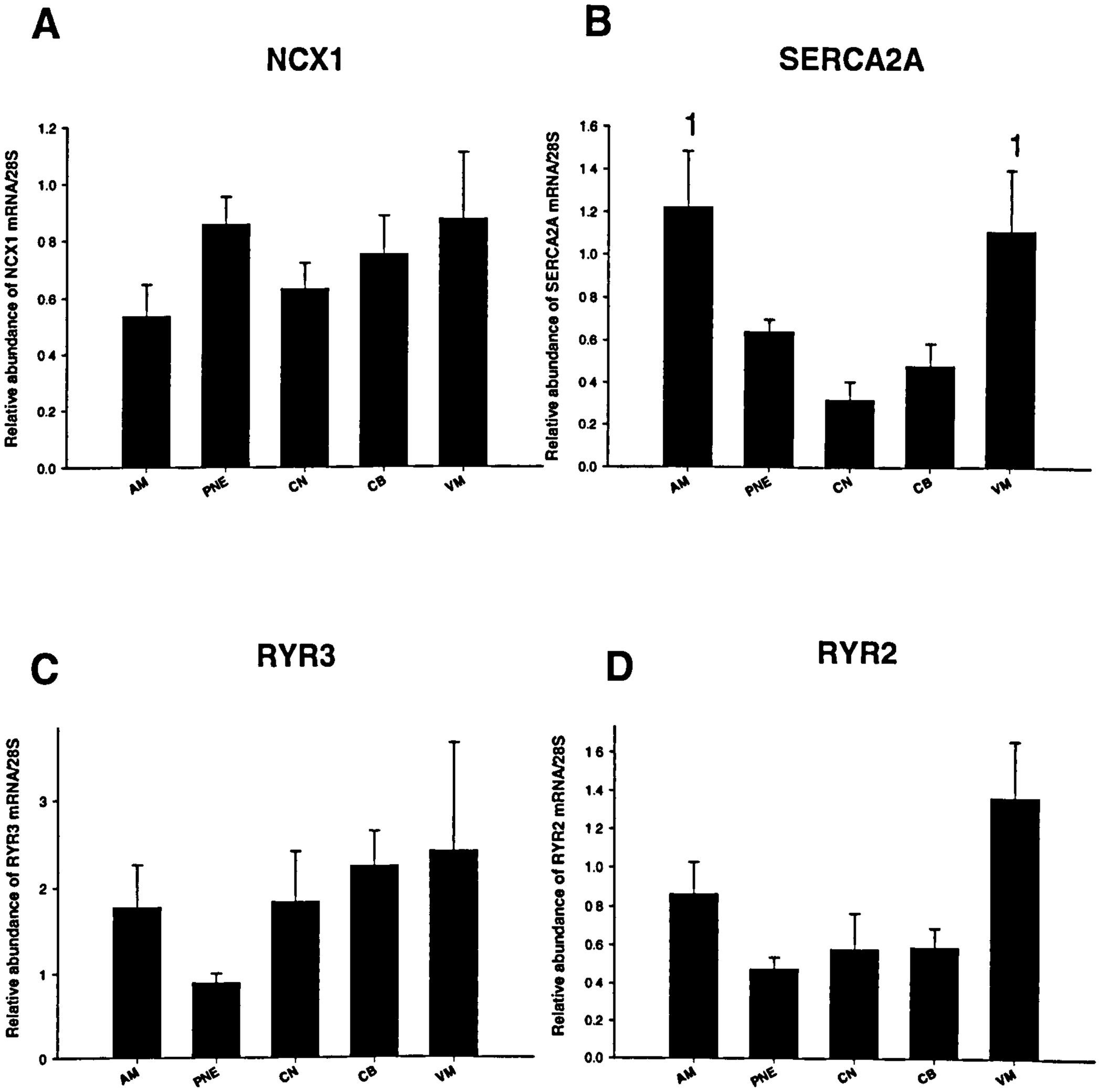

Figure 8.2 *Real time* PCR results for Ca^{2+} handling protein mRNAs. The relative abundance of NCX1 (A), SERCA2A (B), RYR3 (C) and RYR2 (D) mRNAs was quantified in AVN tissue samples. 1, significantly different from compact node ($P < 0.05$; one-way ANOVA). AM, atrial muscle; PNE; CN, compact node; CB, common bundle; VM, ventricular muscle.

abolished by ryanodine (demonstrating that the role of the SR in the AVN is still important).

The presence of SERCA2a mRNA in the working myocardium is consistent with previous findings from rabbit heart (Mearow et al., 1993). However, Mearow et al. (1993) found greater levels of SERCA2A mRNA in the atrium compared to the ventricle.

I have shown that the AVN expresses RYR2 and RYR3 mRNA, albeit at lower levels than in the atrial and ventricular tissue (Fig. 8.2C and D). These data are consistent with the ability of ryanodine to abolish the Ca^{2+} transient in isolated AVN cells (Hancox et al., 1994). Because I have shown both RYR2 and RYR3 are expressed in nodal tissue and working myocardium, it is possible that the channels exist as heteromers with different Ca^{2+} release properties to the homomers.

Vinogradova et al. (2004) have recently suggested that rhythmical release of Ca^{2+} from the SR of SAN cells plays a major role in the generation of spontaneous activity. If this is the case, then based on the mRNA levels detected here for the Ca^{2+} handling proteins it is possible that NCX, SERCA2a, RYR2 and RYR3 all are involved in the generation of spontaneous activity in the leading pacemaking region of the PNE. The relative expression levels I have shown here are similar to those described by Tellez (2005): in the rabbit SAN, Tellez (2005) observed significantly higher levels of RYR3 mRNA in the centre of the SAN compared to SAN periphery and right atrium; RYR2 mRNA, on the other hand, was more abundant in the right atrium compared to SAN centre and periphery.

In conclusion, Ca^{2+} handling in the AVN is likely to be qualtitatively similar to that in the working myocardium. For example, in rabbit AVN cells there is a Ca^{2+} transient and this is largely the result of SR Ca^{2+} release via ryanodine receptors triggered by $I_{Ca,L}$ or I_{NCX} (Hancox et al., 1994). However, there are likely to be differences in Ca^{2+} handling between the AVN and working myocardium, because of the differences in Ca^{2+} handling proteins between the two tissues (Fig. 8.2) as well as the less organized nature of the SR in the AVN as compared to the working myocardium (Shimada et al., 1986).

Chapter 9

Gap junctions and markers

9.1.1 Gap junctions

Gap junctions are channels linking the cytoplasms of neighbouring cells, which enable the diffusion of small molecular weight substances that are important for many cellular activities, including cell-cell communication and conduction in a longitudinal direction (Goodenough et al., 1996; Kumar & Gilula, 1996; Alexander & Goldberg, 2003). These structures are essential for the heart to function as a syncytium. Cardiac myocytes are held together by intercalated discs which contain gap junctions. These gap junctions allow propagation of the action potential. They provide low electrical resistance pathways between adjacent cells.

These junctions can be closed by acidosis (protons) and high cytosolic Ca^{2+}. Such conditions are encountered during ischaemia, e.g. due to coronary occlusion. Closure of gap junctions during ischaemia can be a protective mechanism, because it isolates damaged cells. Closure of gap junctions impairs the normal conduction of the action potential. Propagation of the action potential is accelerated due to ATP and protein-kinase phosphorylation, which open these channels.

A gap junction channel is formed by the docking of two hemichannels (connexons) from opposing cells. Each connexon consists of six connexin (Cx) subunits, which are the sole proteins required to form functional gap junctions. A connexin spans the plasma membrane four times, and contains two extracellular loops, a cytoplasmic N-terminal region, and a cytoplasmic C-terminal region. The most significant differences between connexin isoforms are in the lengths and sequences of the N- and C-terminal regions, which are thought to be important in connexin regulation i.e. by phosphporylation (Lampe and Lau, 2004). The connexin gene family has been reported to contain at least 20 members in the human and 19 in the mouse.

The discontinuous nature of conduction in cardiac tissue is thought to be due to delays in gap junctions (Spach et al., 1985). Decreased gap junctional coupling can lead to

slow propagation of electrical impulses through cardiac tissue (Shaw and Rudy, 1997; Rohr et al.,1998).

It is well known that the gap junctions in the SAN and AVN are very small and sparse compared to those in the atria, ventricles or bundle branches (Severs, 1990). Cx43 is the major cardiac isoform in the mammalian heart. However, additional isoforms have been shown to be expressed: Cx37, Cx40, Cx45 and Cx46 (Davis et al., 1995; Verheule et al., 1997). Recently, the slowest conducting of all gap junctional proteins, Cx30.2, has also been shown to be highly expressed in the mouse conduction system (Kreuzberg et al., 2005).

Davis et al. (1995) showed that the human AVN contains Cx40, Cx43 and Cx45. Cx45 has been shown to be abundantly expressed in the AVN and common bundle of rats (Coppen et al., 1999). In the study of Gourdie et al. (1993), an increase in the expression levels of Cx40 from the AVN to His bundle has been reported; Cx40 and Cx43 were colocalised in the AVN.

Insights into the role of gap junctions in AVN function have been gained from transgenic mice engineered to lack the gap junctional protein, Cx40; the mice have a prolonged P-R interval, suggesting a major role for Cx40 in the formation of gap junctions in the AVN and propagation of the action potential through the AVN (Simon et al., 1998). In addition, there is the Holt-Oram syndrome, in which there is a genetic defect in the homeobox gene, Tbx 5, which leads to a lack of Cx40 and manifests as first-degree AV block and/or prolonged P-R interval (Bruneau et al., 2001). Pollack (1976), using a fluorescent tracer dye to measure intercellular coupling in the rabbit heart, showed that the passage of dye in the AVN is three orders of magnitude slower as compared to other areas of the heart.

9.1.2 AVN markers

Expressional analysis requires the use of tissue markers in order to differentiate between tissue types. The conduction tissue of the heart has been shown to express certain genes at significantly different levels than the surrounding atrial and ventricular tissue (Gourdie et al., 2003).

9.1.3 Atrial natriuretic peptide

Atrial natriuretic peptide/atrial natriuretic factor (ANP/ANF) is specifically expressed in the atrial tissue of cardiac muscle and can therefore act as a positive marker of atrial tissue (de Bold, 1985). ANP is a peptide hormone which is released from the atrial cells in response to stresses (predominantly an increase in blood pressure) placed upon the atria. ANP in turn, reduces blood volume and increases Na^+ secretion and excretion by its actions on the kidney. Specifically, ANP decreases Na^+ resorption in the distal convoluted tubule and cortical collecting duct. All the actions of ANP are mediated by the transmembrane form of ANP receptor, via cGMP generated by the guanylyl cyclase in the cytosolic domain of the receptor. In addition, ANP causes vasodilatation and fluid volume reduction by direct actions on vascular smooth muscle cells, and inhibition of secretion of hormones, such as aldosterone from the adrenal cortex and norepinephrine. Since ANP expression is limited to the atrial muscle under normal conditions, it can be used as a positive marker of atrial tissue.

9.1.4 Neurofilament-M

There are three neurofilament isoforms with molecular weights of 115 kDa (NF-H), 95 kDa (NF-M), and 68 kDa (NF-L). NF-M is a neuronal cytoskeletal protein found predominantly in the brain. However, using an anti-NF-M antibody, this protein has been shown to delineate the conduction system of the rabbit heart (Gorza *et al.*, 1988; Gorza & Vitadello, 1989). NF-M can, therefore, be used as a positive marker of conduction system tissue in the rabbit heart.

9.1.5 Housekeeper genes: 28S/GAPDH/NaK pump

When quantifying cDNA from different tissue samples by *real time* PCR, it is vital that the mRNA input into each reverse transcription reaction is the same. However, quantification of RNA can be prone to inaccuracies. Therefore, in order to allow for variations in mRNA input, the quantities of the transcripts measured can be normalised to the quantities of a housekeeper transcript that is equally distributed throughout tissue. The suitability of two housekeeper genes was assessed in this study: glyceraldehyde 3 phosphate dehydrogenase (GAPDH) and 28S rRNA, which are both established housekeeper genes (Thellin et al., 1999; Zhong & Simons, 1999; Bustin, 2000).

9.2 Methods

9.2.1 *Real time* PCR

Real time PCR was performed using cDNA generated from total RNA isolated from five rabbit AVN tissue types: atrial muscle, PNE, compact node, common bundle and ventricular muscle. (n = 8 rabbits). The Roche LightCycler was used to measure 28S, ANP and NF-M transcripts, whereas the ABI 7900 HT was used to measure GAPDH transcripts.

9.2.2 *In situ* hybridisation

Riboprobes for NF-M, ANP and GAPDH were generated by Dr. James Tellez (Tellez, 2005). A modification of the Braissant protocol was used as described in chapter 2 (n=4 rabbits).

9.3 Results

9.3.1 *Real time* PCR

Real time PCR showed for Cx40 and Cx45 no significant differences between tissues (Fig. 9.1A and 9.1C); Cx43 was significantly higher in the atrial muscle compared to PNE and compact node ($P < 0.05$; Fig. 9.1B). NF-M mRNA was significantly more abundant in the PNE, compact node and common bundle compared to the ventricular and atrial muscle ($P < 0.05$; Fig. 9.6A). ANP mRNA was significantly more abundant in the atrial muscle compared to the other tissues ($P <0.05$; Fig. 9.6B). GAPDH and 28S mRNA levels showed no significant differences between tissues (data not shown).

9.3.2 *In situ* hybridisation

Cx43 perinuclear staining was abundant in the atrial and ventricular muscle throughout the AVN conduction axis (Figs. 9.2-9.5). In addition, there was abundant Cx43 perinuclear staining in the common bundle (Figs. 9.2B and 9.5) with progressively less staining in the compact node (Figs. 9.2C and 9.4) and little in the PNE (Fig. 9.3).

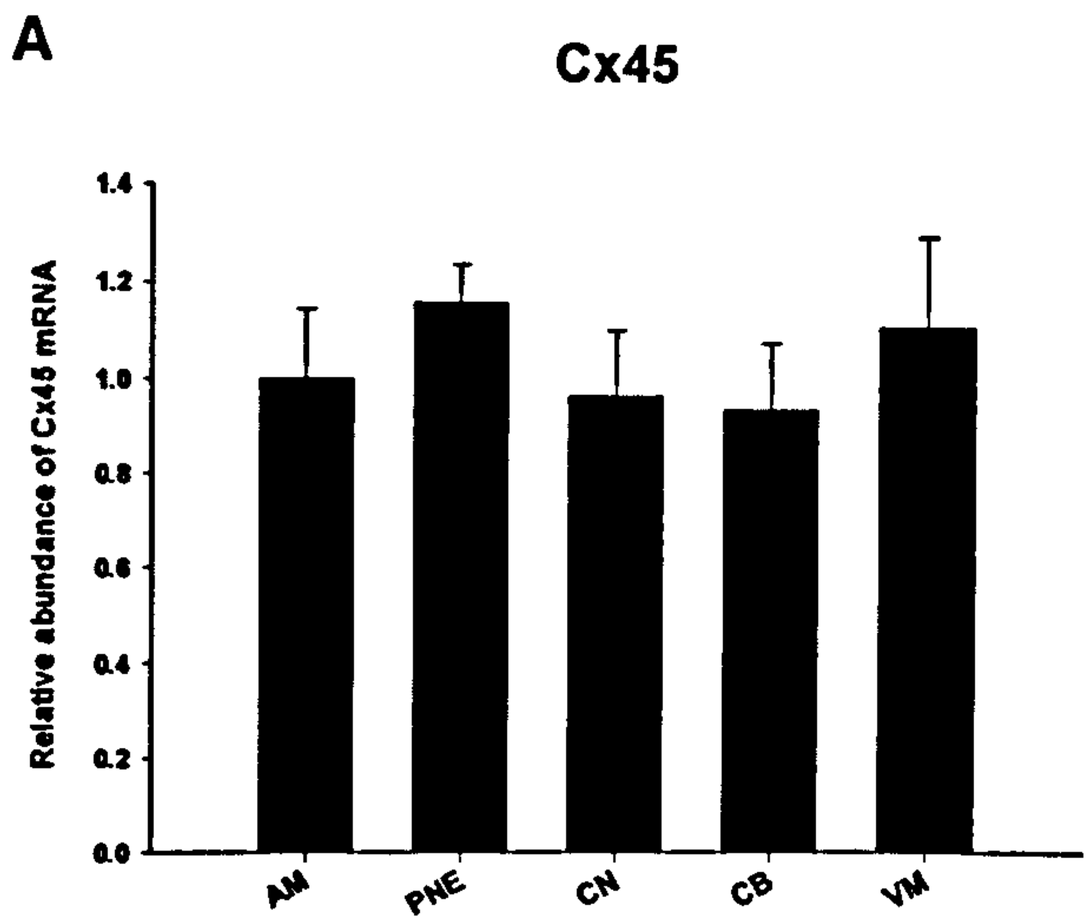

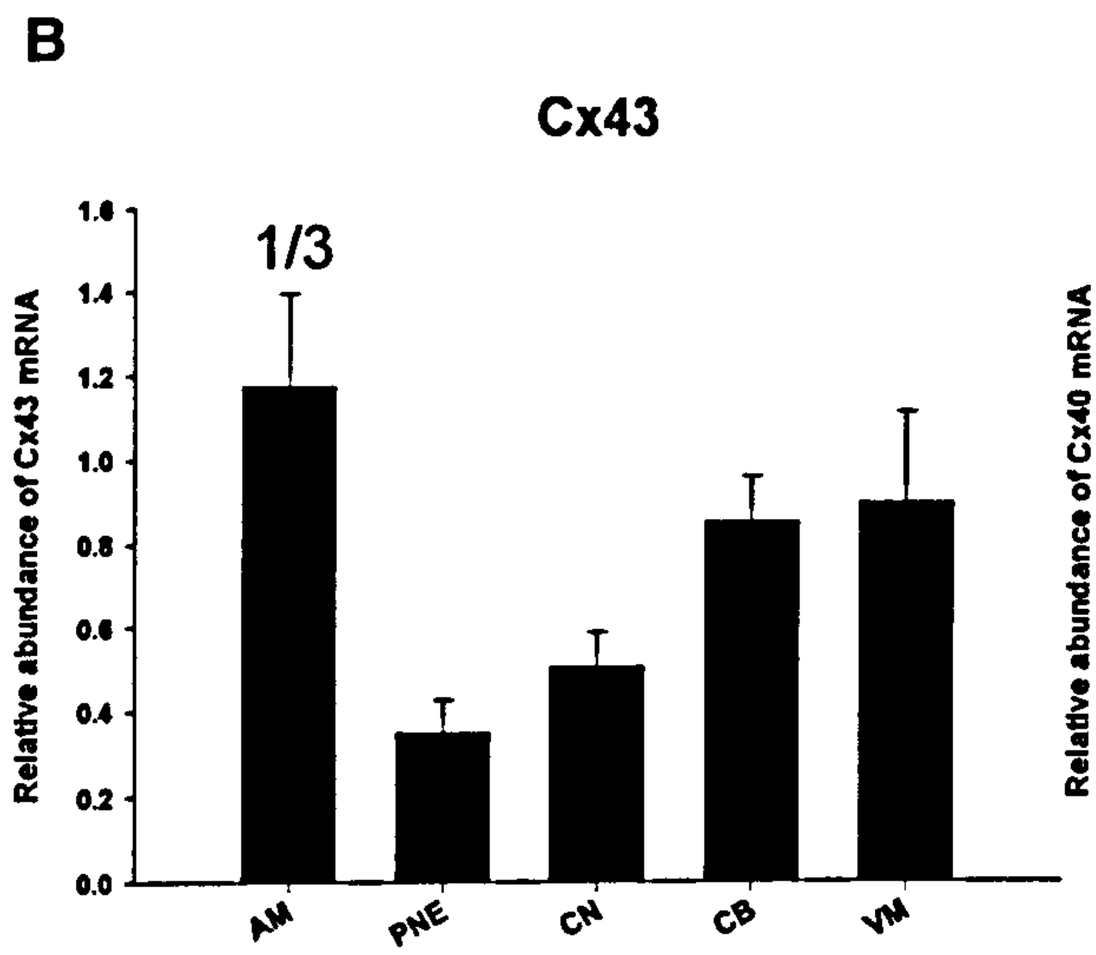

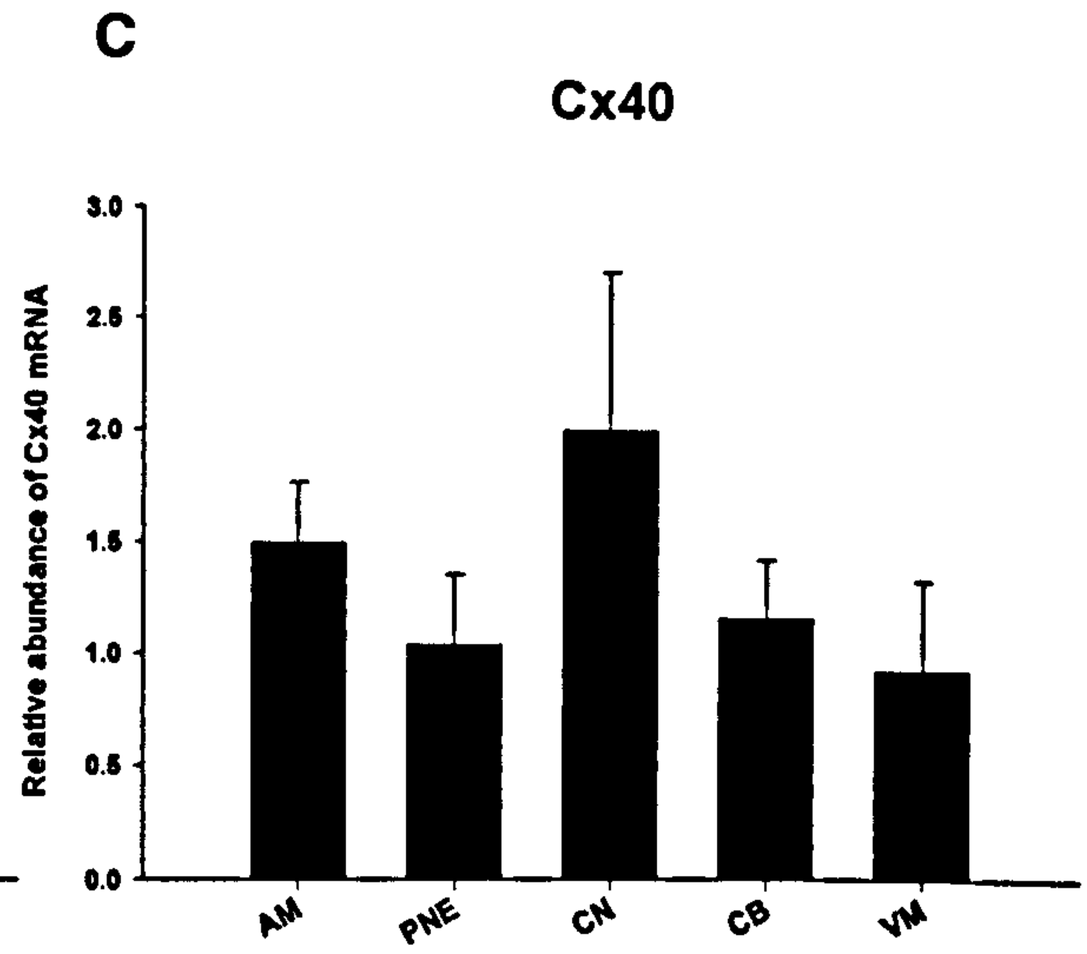

Figure 9.1 *Real time* PCR results for connexin mRNAs. A, Cx45. B, Cx43. C, Cx40. 1 & 3, denote significantly different from CN ($p < 0.05$; One-way ANOVA); AM, atrial muscle; PNE, posterior nodal extension; CN, compact node; CB, common bundle; VM, ventricular muscle.

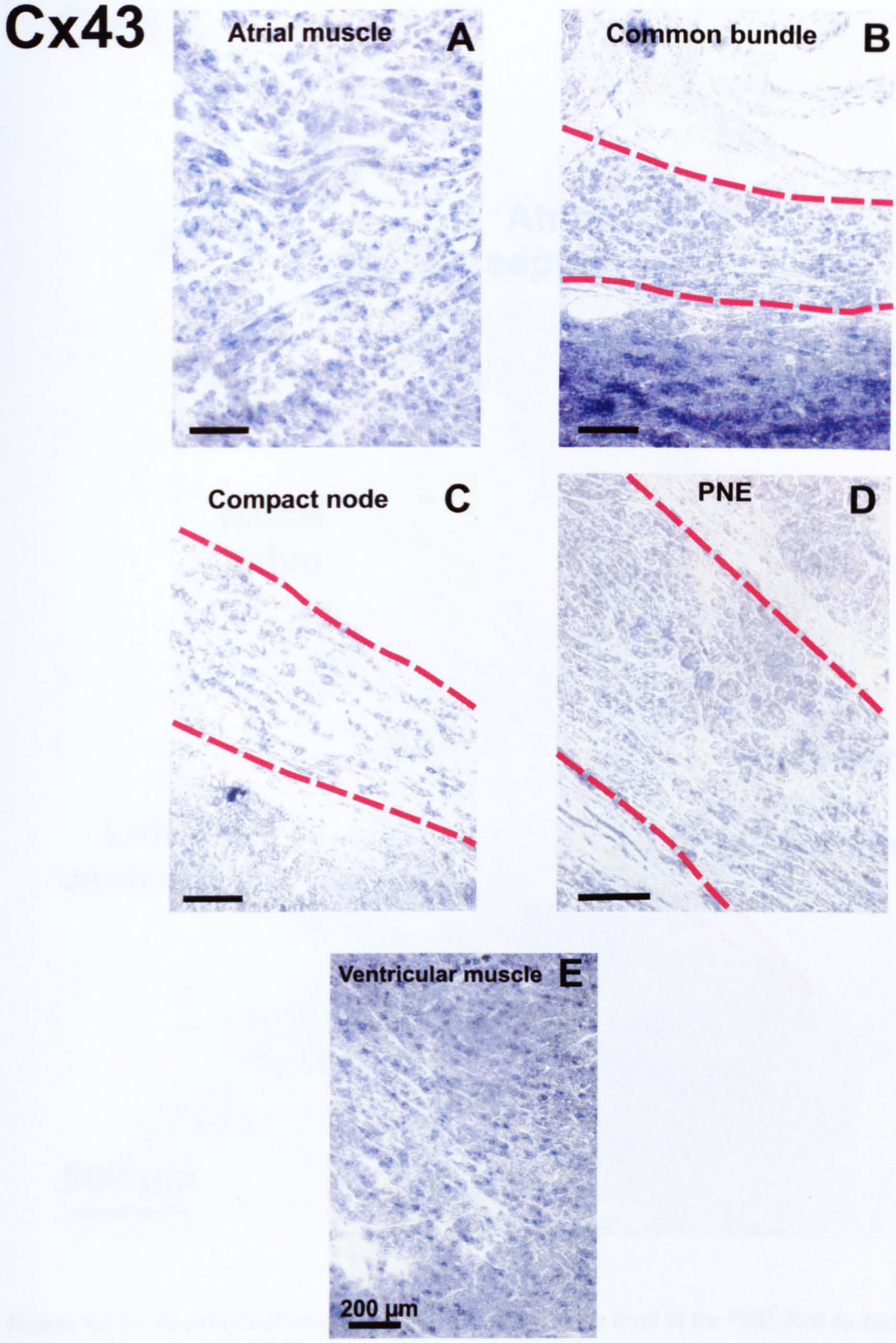

Figure 9.2 High power (x20 magnification) *in situ* hybridisation images for Cx43 mRNA. A, atrial muscle; B, common bundle; C, compact node; D, posterior nodal extension; E, ventricular muscle. Red dashed line outlines nodal cells.

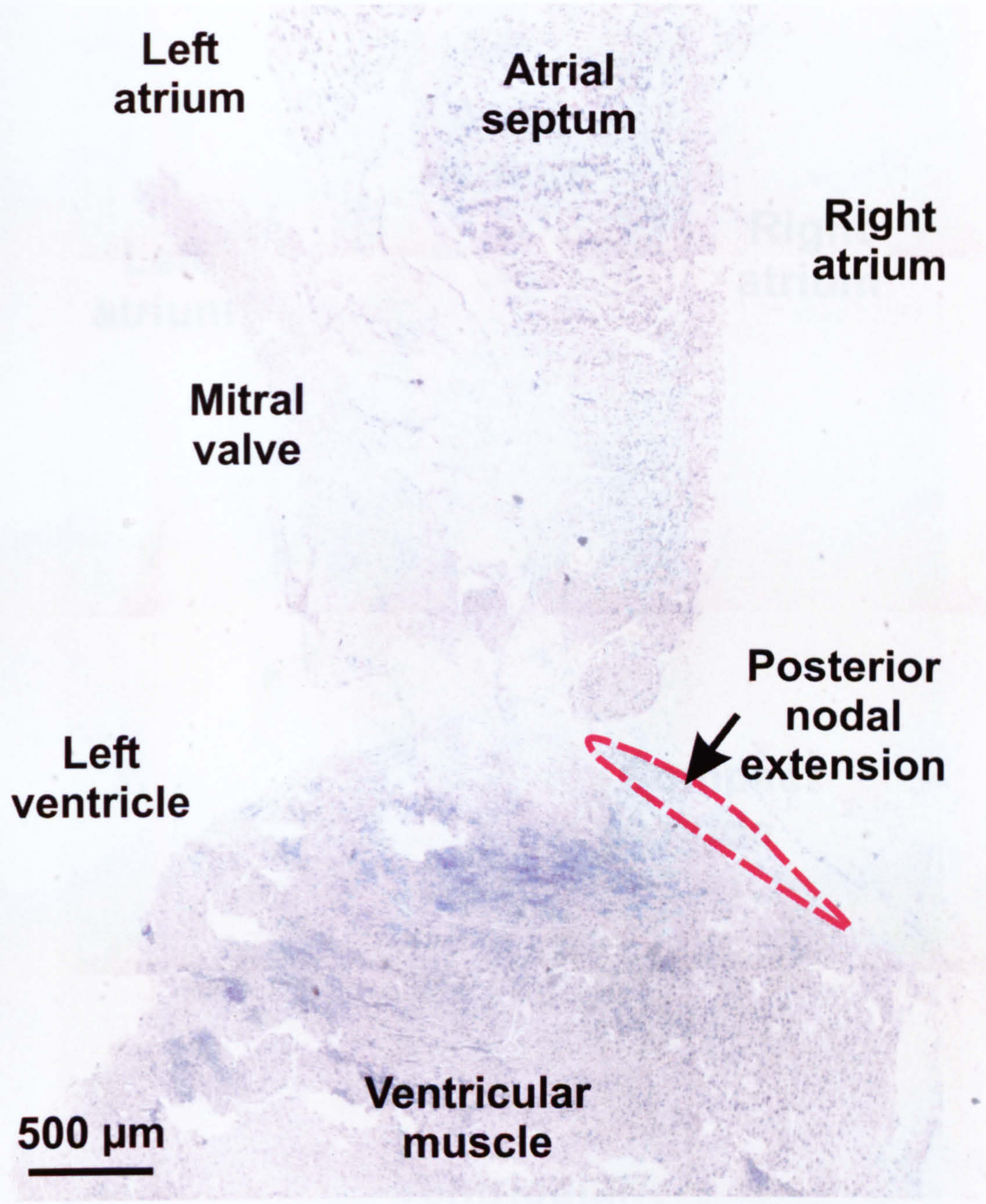

Figure 9.3 *In situ* hybridisation image for Cx43 mRNA at the level of the PNE. Red dashed line outlines cells comprising PNE.

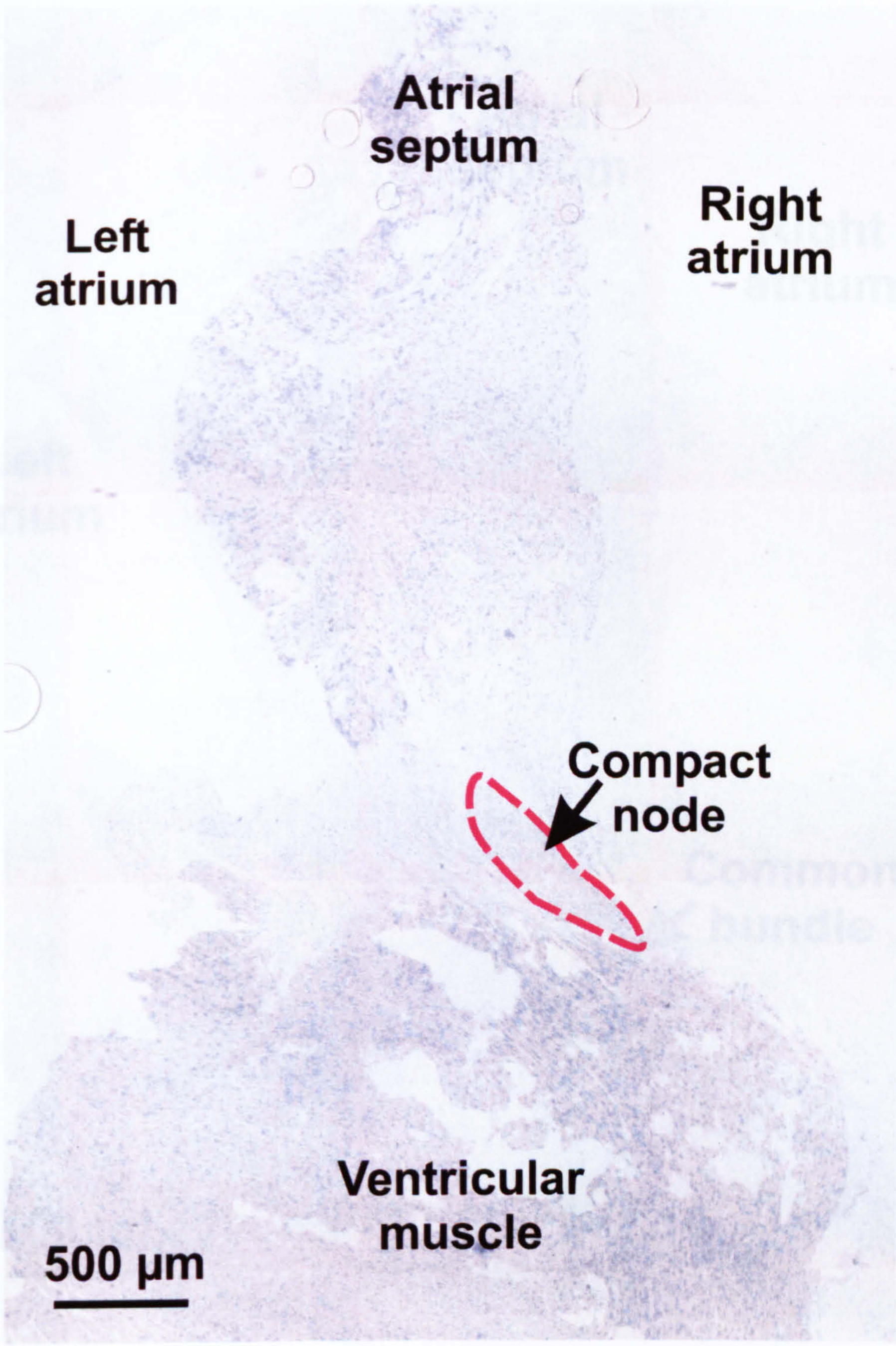

Figure 9.4 *In situ* hybridisation image for Cx43 mRNA at the level of the compact node. Red dashed line outlines cells comprising compact node.

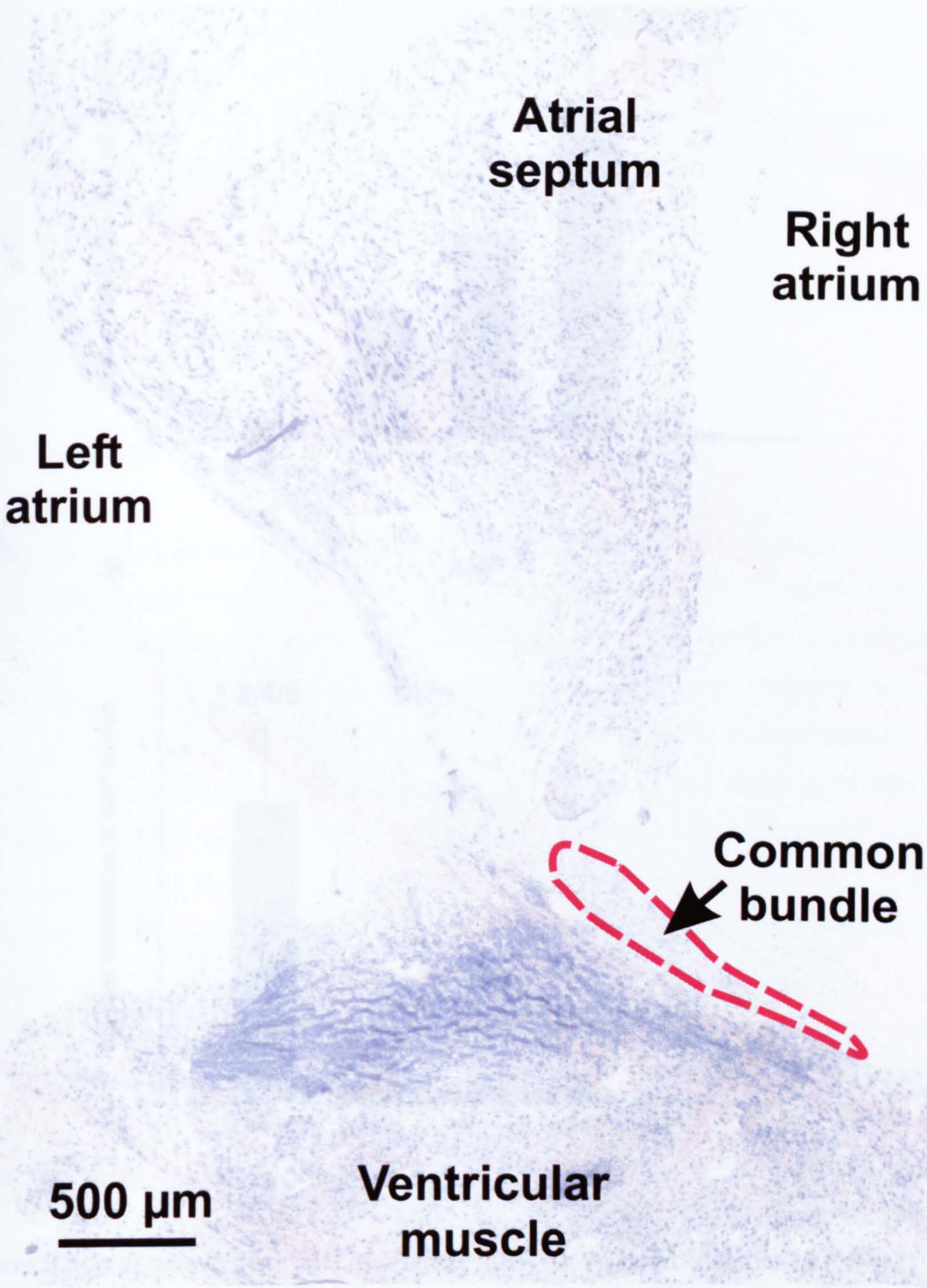

Figure 9.5 *In situ* hybridisation image for Cx43 mRNA at the level of the common bundle. Red dashed line outlines cells comprising common bundle.

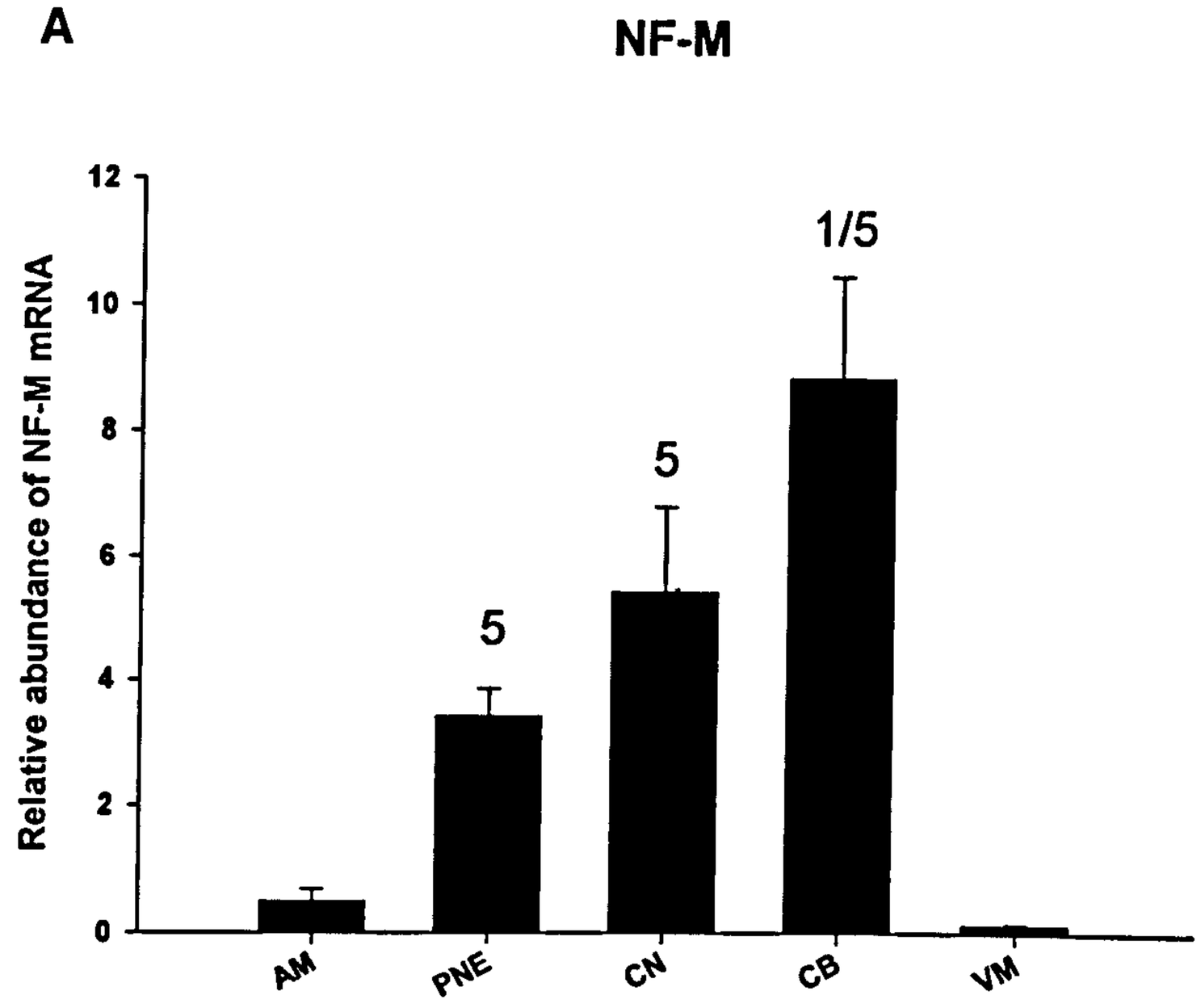

Figure 9.6 *Real time* PCR results for marker mRNAs. A, neurofilament-M (NF-M). B, atrial natriuretic peptide (ANP). 1 & 3, denote significantly different from CN ($p < 0.05$; One-way ANOVA); AM, atrial muscle; PNE, posterior nodal extension; CN, compact node; CB, common bundle; VM, ventricular muscle.

In situ hybridisation for NF-M mRNA revealed an abundance of perinuclear staining at the levels of the PNE (Fig. 9.7), compact node (Fig. 9.8) and common bundle (Fig. 9.9); this clearly delineated these nodal structures.

Strong perinuclear staining of ANP mRNA was detected in the atrial septum region of the tissue sections throughout the AVN conduction axis (Figs. 9.10-9.12); at the level of the PNE this labelling was strongest on the left of the septum with cells on the right being largely negative for ANP perinuclear staining (Fig. 9.10). The opposite was seen at the level of the compact node where cells on right contained abundant ANP mRNA and the cells on the left were largely negative for ANP staining (Fig. 9.11).

Perinuclear staining for GAPDH was uniform throughout tissue sections at all levels of the AVN conduction axis (Fig. 9.13).

9.4 Discussion

Real time PCR showed no differences for Cx40 between tissue samples (Fig. 9.1); this is consistent with a major role for this gap junctional protein in AVN function (Simon et al., 1998; Bruneau et al., 2001). In contrast, Severs et al. (2004) found no Cx40 protein expression along the rabbit AVN conduction axis; the discrepancy between our data at the mRNA level and the findings of Severs et al. (2004) at the protein level could be due to: 1) a post-transcriptional regulatory mechanism for Cx40, preventing the production of protein at the cell surface, or 2) the use of a suboptimal antibody concentration for Cx40; in the study of Severs et al. (2004) the authors fail to comment on whether a strong signal was detected in the surrounding atrial or ventricular septal tissue where Cx40 should be present (Ko et al., 2004).

The abundance of Cx45 mRNA in all regions (PNE, compact node, common bundle) of the rabbit AVN conduction axis (Fig. 9.1C) agrees with protein observations from mice, rat and rabbit AVN (Coppen et al., 1998; Coppen et al., 1999; Ko et al., 2004). More specifically, the abundant Cx45 mRNA in the PNE (Fig. 9.1A) is consistent with findings at the protein level in rabbit (Dobrzynski et al., 2003; Ko et al., 2004).

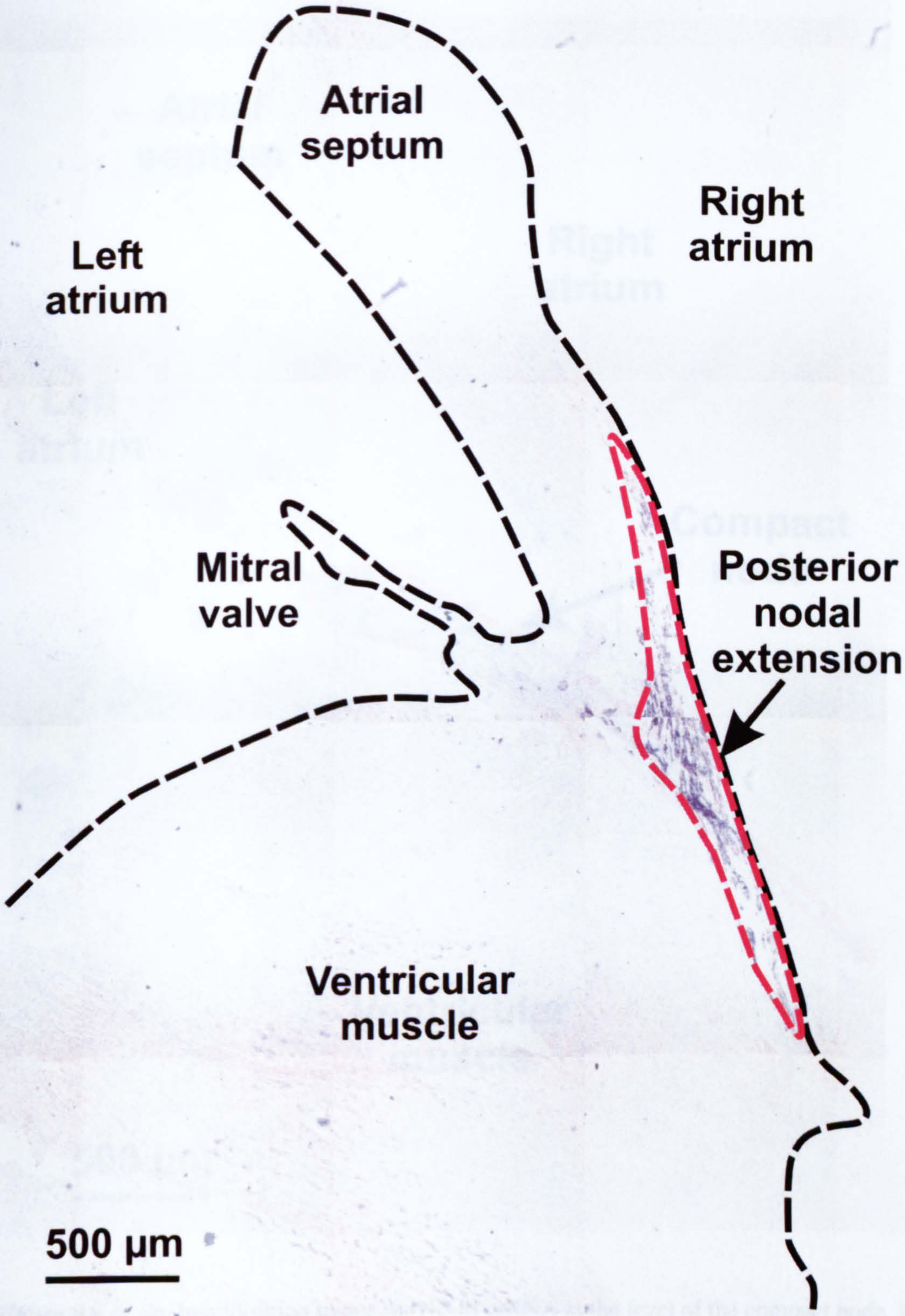

Figure 9.7 *In situ* hybridisation image for NF-M mRNA at the level of the PNE. Red dashed line outlines cells comprising PNE.

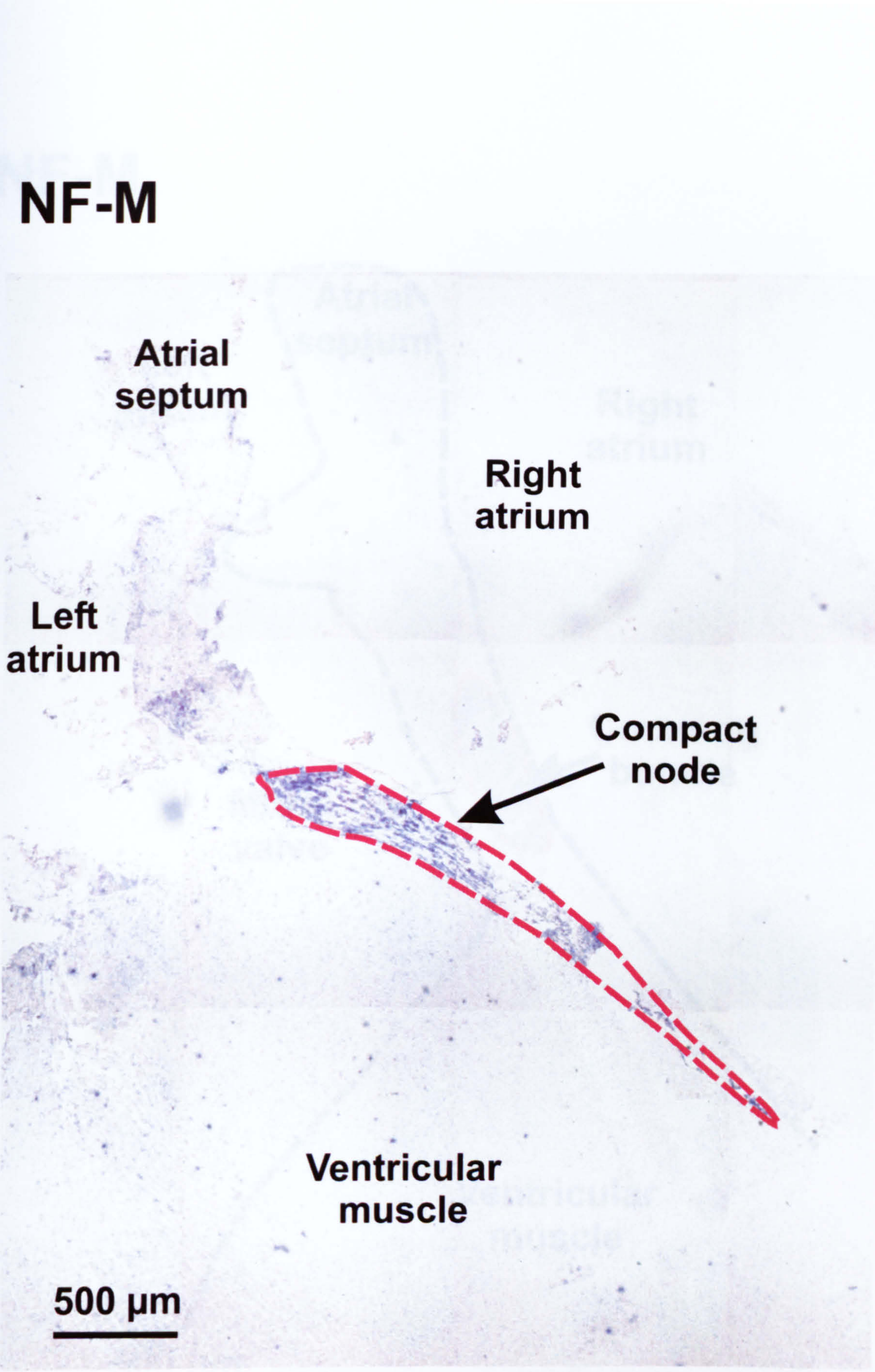

Figure 9.8 *In situ* hybridisation image for NF-M mRNA at the level of the compact node. Red dashed line outlines cells comprising compact node.

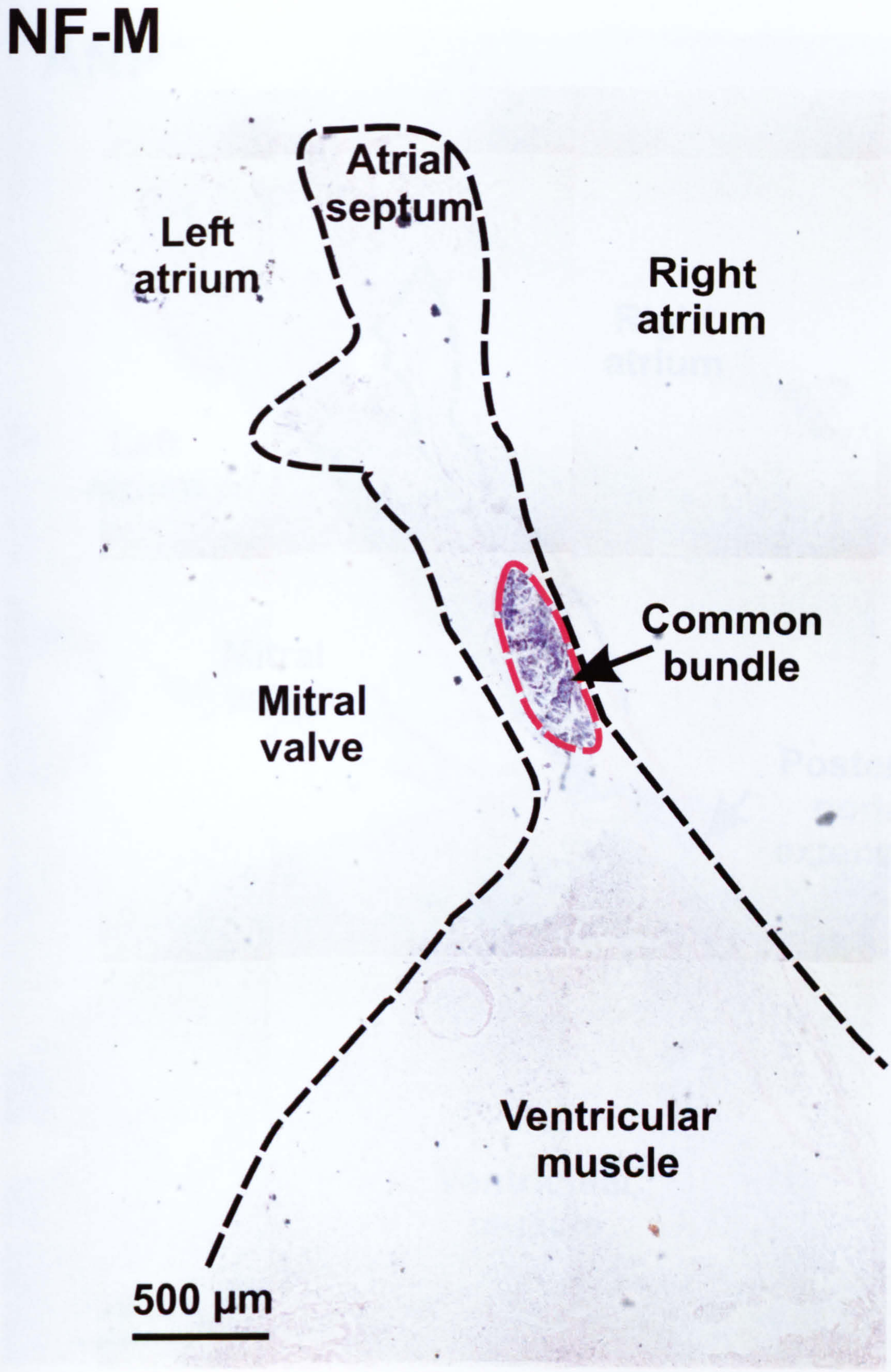

Figure 9.9 *In situ* hybridisation image for NF-M mRNA at the level of the common bundle. Red dashed line outlines cells comprising common bundle.

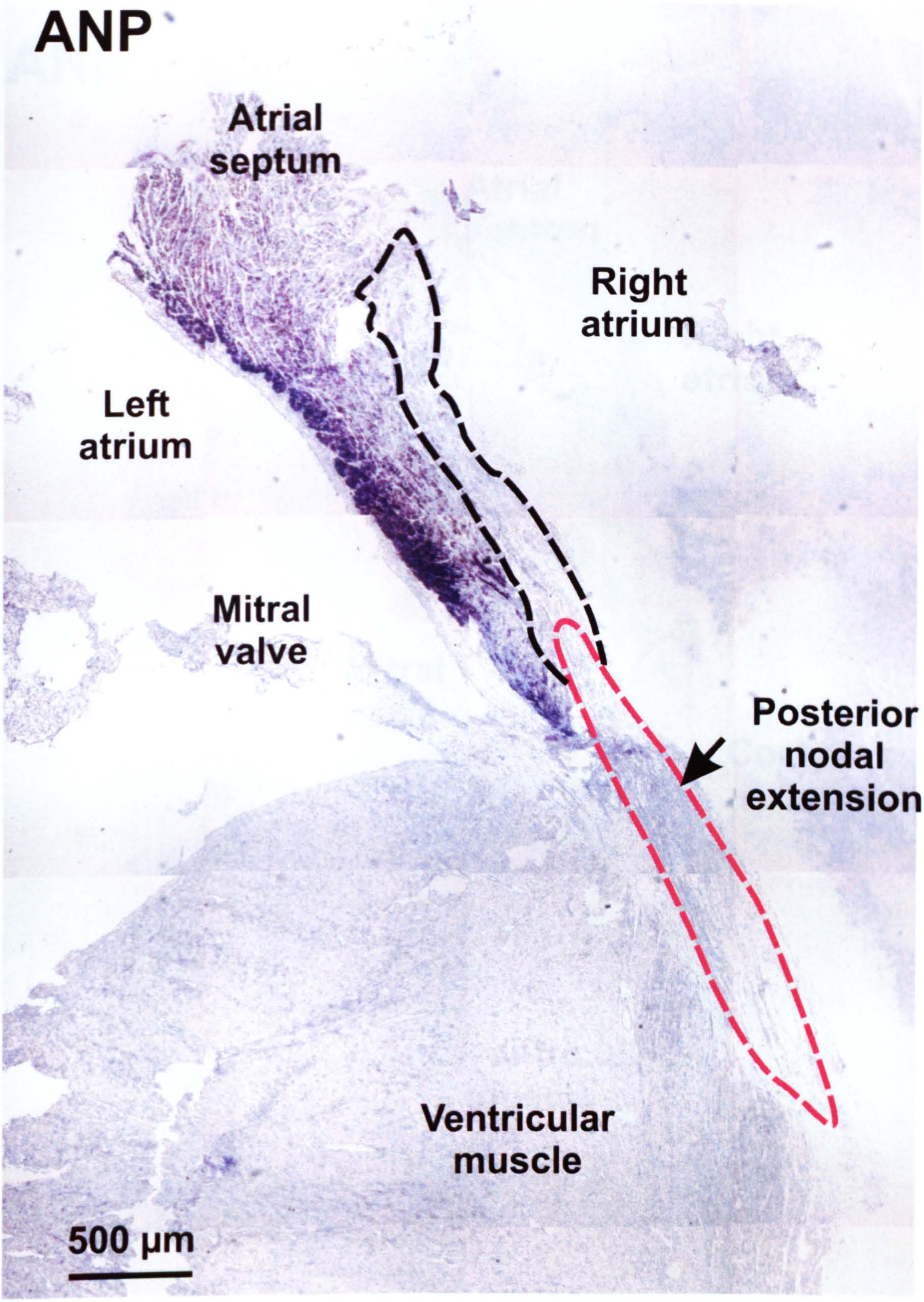

Figure 9.10 *In situ* hybridisation image for ANP mRNA at the level of the PNE. Red dashed line outlines cells comprising PNE.

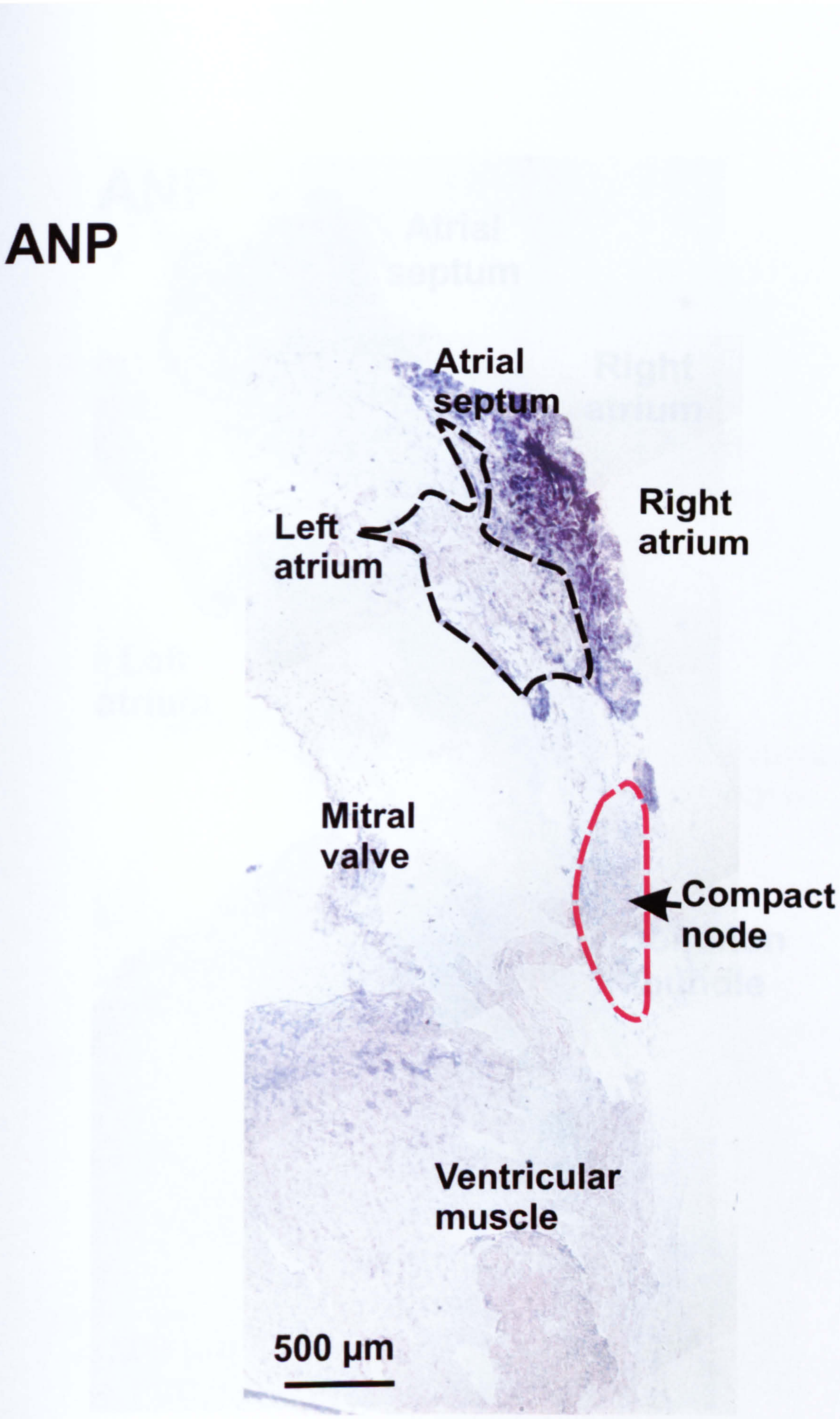

Figure 9.11 *In situ* hybridisation image for ANP mRNA at the level of the compact node. Red dashed line outlines cells comprising compact node.

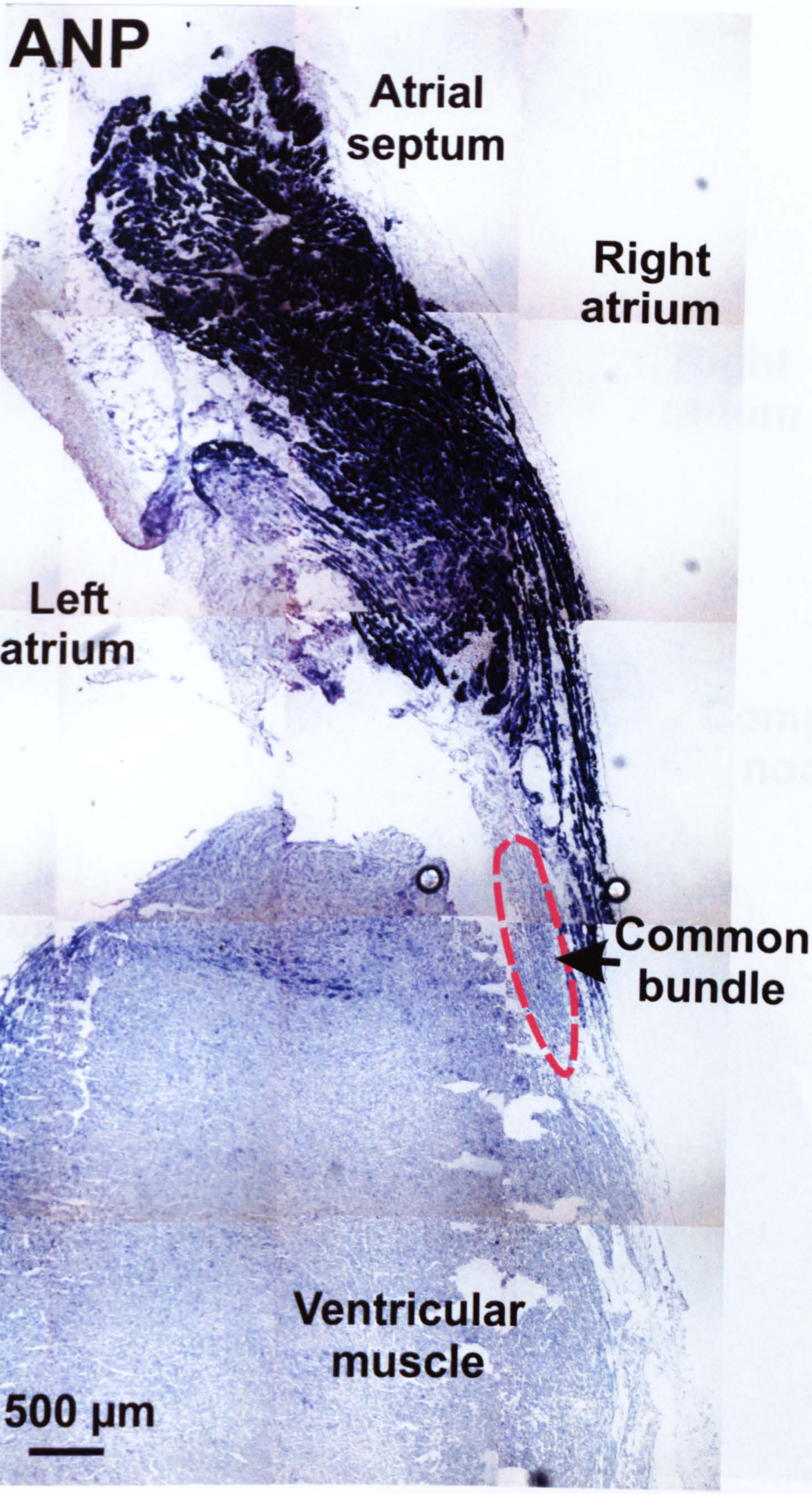

Figure 9.12 *In situ* hybridisation image for ANP mRNA at the level of the common bundle. Red dashed line outlines cells comprising common bundle.

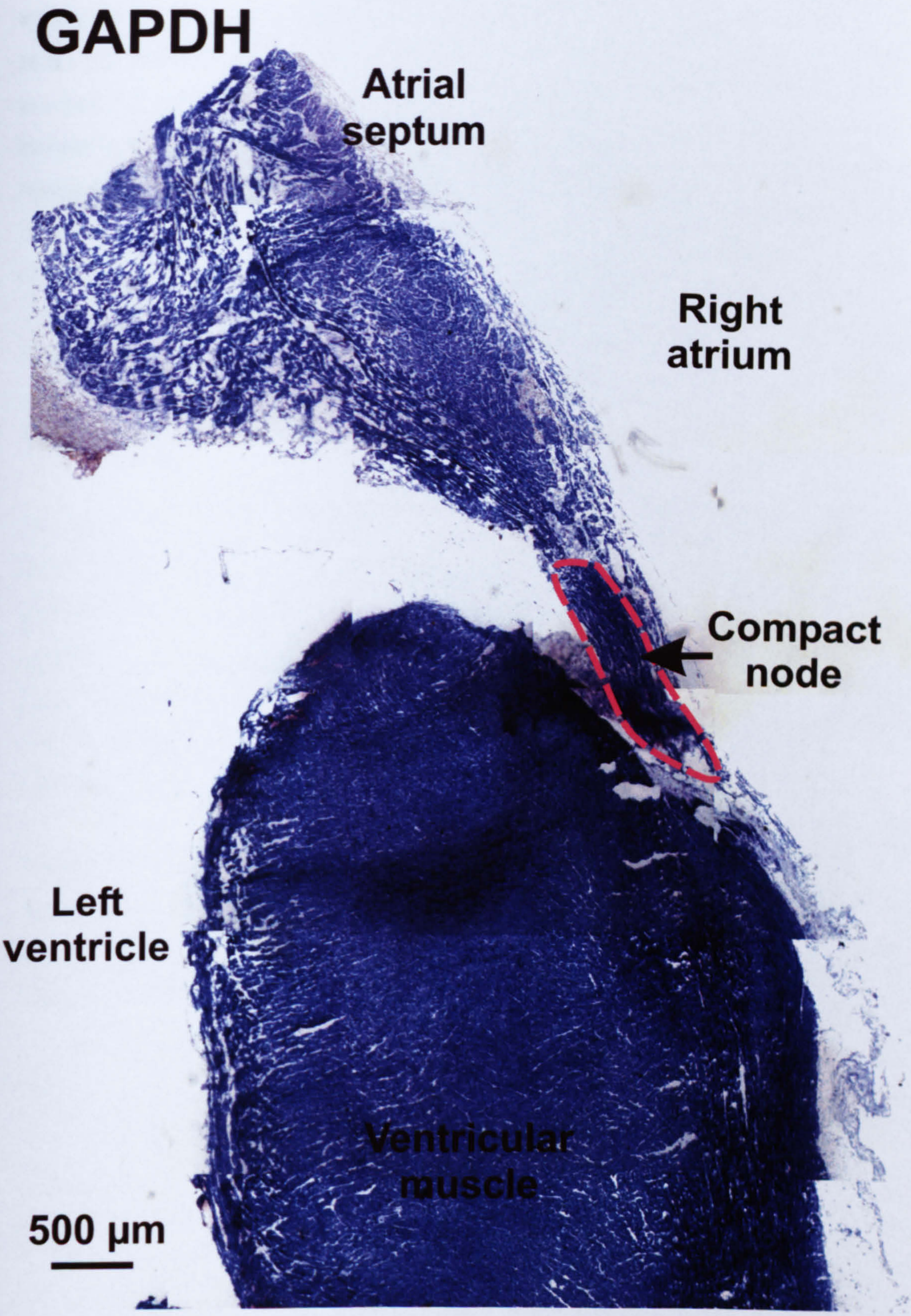

Figure 9.13 *In situ* hybridisation image of GAPDH mRNA at the level of the compact node. Red dashed line outlines cells comprising compact node.

In situ hybridisation for Cx43 mRNA revealed an abundance of staining in the ventricular and atrial tissue at all levels throughout the AVN conduction axis, consistent with its role as the major cardiac gap junctional protein (Gourdie et al., 1991; Verheule et al., 1997). The abundance of Cx43 mRNA perinuclear staining in the common bundle is consistent with fast conduction through this structure. The presence of Cx43 mRNA perinuclear staining in the compact node, albeit at lower level than in the common bundle, is in agreement with the immunohistochemical findings described in Chapter 3. It is possible that conduction through the common bundle is faster than through the compact node. The significantly lower amount of Cx43 mRNA in the PNE (Fig. 9.1B) is consistent with slow conduction through this tissue (Nikolski and Efimov, 2001). The apparent gradient in Cx43 mRNA expression from common bundle>compact node>PNE agrees with a similar study investigating the levels of Cx43 protein throughout the AVN conduction axis (Ko et al., 2004).

The presence of Cx40, Cx43 and Cx45 in all tissues of the AVN conduction axis (with the exception of Cx43, which is absent from the PNE) possibly suggests that the gap junctions exist as heteromers with different conduction properties the homomer i.e. gap junctions. Co-expression localisation of Cx43 and Cx45 has been detected in the rabbit SAN (Coppen et al., 1999). This would add to the already complex architecture of the node and would allow for subtle variations in speed of impulse propagation within the confines of the triangle of Koch.

The *real time* PCR findings for ANP mRNA were as predicted, with abundant expression of mRNA in the atrial muscle and virtually no detection of ANP mRNA in the other tissue samples (Fig. 9.2B) confirming its role as a negative marker for the rabbit conduction system (Gorza et al., 1988; Gorza and Vitadello, 1989). These findings are consistent with previous studies (Mercadier et al., 1989; Sharma et al., 2003). *In situ* hybridisation for ANP mRNA, however, revealed a greater complexity of ANP mRNA expression, at the level of the PNE: the atrial tissue lying on the left side of the atrial septum possessed abundant ANP mRNA perinuclear staining, whereas the tissue lying on the right was negative for ANP mRNA (Fig. 9.10). At the level of the compact node, the reverse was seen, with abundant ANP mRNA perinuclear staining on the right side of the atrial septum whereas the atrial tissue lying on the left was largely negative for ANP mRNA (Fig. 9.11). The ANP-positive tissue could be "true" atrial tissue, whereas the ANP-negative tissue could represent a region occupied by

transitional cells. If correct, ANP would be a good marker in AVN experiments to distinguish between "true" atrial muscle and transitional cells.

NF-M mRNA staining of the AVN tissues (Figs. 9.7-9.9) was remarkably similar with our findings at the protein level described in Chapter 3; the PNE appears as a thin elongated collection of cells positive for NF-M mRNA (Fig. 9.7); the compact node appears as a typical oval-shaped collection of cells (Fig. 9.8) and the common bundle Fig. 9.9), as a more cylindrical bundle of positively stained cells lying near the crest of the ventricle.

I have shown GAPDH and 28S to be uniformly distributed throughout the various tissues. This justifies their use as housekeepers in *real time* PCR experiments.

Chapter 10

Summary

Electrophysiology studies of the AVN of various species have described various electrophysiological phenomena including reentry, concealed conduction, facilitation and fatigue, amongst others. In addition, single cell studies and microelectrode studies have described a multitude of action potentials and cell types. Both of these electrophysiological means of studying the AVN show that the electrical activity of the AVN in all mammalian species is complex and heterogeneous. On the other hand, morphological studies have shown that the structure of the AVN is also heterogeneous and complex. To date, electrophysiological and morphological investigations, alone or combined (Anderson et al., 1976), have failed to provide detailed information regarding the electrophysiological properties of the specific sub-cellular compartments – which ultimately determine the overall function of the node. Therefore, by investigating the mRNA encoding ion channels and membrane proteins, and localising these mRNAs to specific subdomains by *real time* PCR analysis and *in situ* hybridisation I have provided further insights into the electrophysiological properties of specific regions of the rabbit atrioventricular node and therefore to overall AVN function.

By grouping tissue types based on histological appearance, Cx43- and neurofilament-M labelling and subsequent three-dimensional reconstruction of these regions, I have provided a simplified understanding of AVN structure. Moreover, I have shown the full extent of the PNE, in contrast to the study of Ko et al. (2005), by using an antibody against neurofilament-M, which delineates conduction system tissue in the rabbit (Chapter 3 - Fig. 3). Previous studies have failed to provide a distinct anatomical entity representing the fast-pathway. However, I have shown that the atrial septum immediately above the compact node is composed of densely- and loosely-packed atrial tissue and this area would likely contribute to fast pathway conduction. In addition, the three-dimensional reconstruction also acts as a mathematical model which can be used to study re-entry properties of the node (for example see Boyett et al. 2006). Furthermore, this accurate three-dimensional model can be built upon to ultimately produce a virtual heart which would act as a valuable anatomical educational tool for relating cardiac anatomy to function.

The posterior nodal extension has been implicated in the genesis of AVNRT and has been suggested to be the molecular substrate for slow pathway conduction (Inoue and Becker, 2000). It is of major importance, therefore, to elucidate ion channel expression patterns throughout this structure in order to provide insights into the ion channels governing the electrical properties of this structure such as the shorter effective refractory period compared to the fast-pathway and the relatively slow conduction (7 cm/sec) of an action potential through this tissue.

I have provided for the first time clues as to the electrical nature of the fast pathway by showing that 1) the atrial septal tissue likely to be the substrate for the fast-pathway is composed of both densely- and loosely-packed atrial tissue and 2) regions of this atrial septal tissue have a heterogeneous mRNA distribution for certain ion channels (for instance there are regions which are positive and negative for KChIP2 and $Na_v1.5$ mRNAs). These insights into electrical properties of the pathway could explain the longer refractory period of this pathway compared to the slow-pathway and could lead to pharmacological interventions for the cessation of re-entry.

Additional re-entry pathways other than the fast- and slow-pathways have been shown electrophysiologically to enter the AVN from the superior margins of the coronary sinus. I have shown for the first time a bundle of densely packed, Cx43-positive, atrial tissue travelling from the region of the compact node to the superior margins of the coronary sinus which would provide an ideal molecular substrate for such a pathway. This structure was not mentioned by Ko et al. (2005). A possible explanation for this discrepancy could be due to the fact that both studies are based on a single heart and that there could be inter-individual variation, especially since this electrophysiologically determined pathway fails to be seen in every patient/preparation.

There has been very little in the way of uncovering ion channel expression patterns in the atrioventricular node. Petrecca et al. (1997) using an antibody against a common region of sodium channels used immunohistochemistry to show Na^+ channel expression in the compact node of the rabbit. Marionneau et al. (2005) carried out a *real time* PCR study on mouse AVN but, however, their sampling procedure for the AVN was crude and there was a significant amount of atrial contamination (47 %) which could lead to misleading results regarding AVN function. An additional limitation of the study of

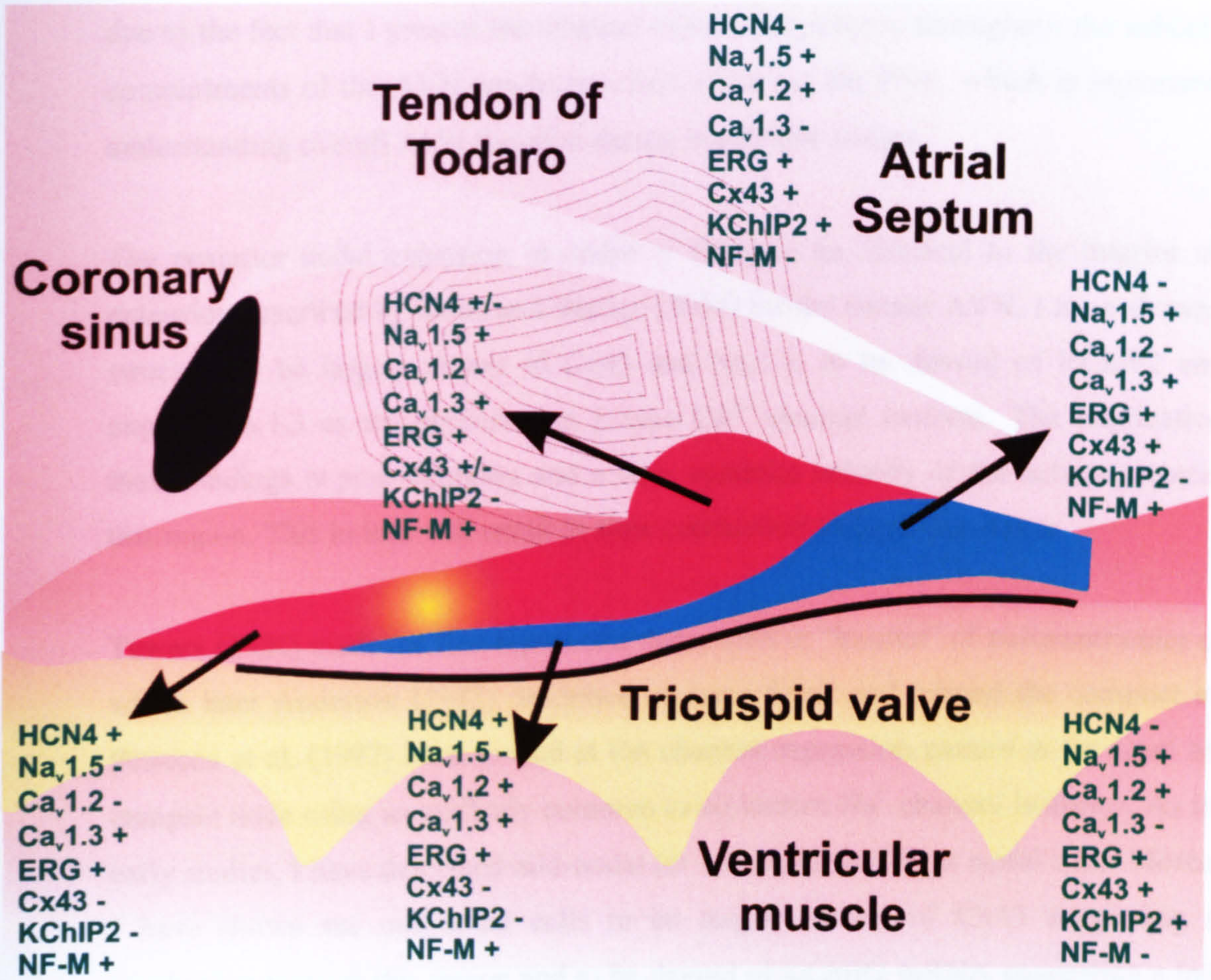

Figure 10.1 A schematic diagram to summarise the *in situ* hybridisation findings from the various AVN tissue regions. Arrows show the region where *in situ* hybridisation data was gathered. Contours show loosely packed muscle. Blue region, cells comprising the common bundle and lower nodal cells. Red region, cells comprising PNE and compact node. Yellow, leading pacemaker region in the PNE. +, means positive for given mRNA. -, means negative for given mRNA. +/-, means this tissue was positive in some regions and negative in others for the given mRNA.

Marionneau et al. (2005) is that the sampling procedure failed to take into account the complex architecture of the node and there was no information regarding subcellular structures within the AVN conduction axis. Therefore, the work I present here is novel due to the fact that I present ion channel expression patterns throughout the subcellular compartments of the AVN conduction axis including the PNE, which is important for understanding overall AVN function during health and disease.

The posterior nodal extension in rabbit is likely to be identical to the inferior nodal extension described by Inoue and Becker (2000) for the human AVN. I have shown this structure to be largely absent of Cx43 and $Na_v1.5$, to be devoid of KChIP2 and to express $Ca_v1.3$ as the predominant L-type Ca^{2+} channel isoform. The implication of these findings is poor coupling and a slow upstroke velocity of the action potential in this region. This in turn will result in slow conduction through this tissue.

Tawara (1906) made the first report of a dense knot or "knoten" of atrioventricular cells, which later Anderson (1972) described in more detail and termed the compact node. Petrecca et al. (1997) have looked at ion channel expression pattern at the level of the compact node using an antibody common to all known Na^+ channel isoforms. As in the early studies, I have described mid-nodal (or compact) and lower nodal cells. Moreover, I have shown the mid-nodal cells to be largely absent of Cx43 suggesting slow conduction through this region and to be devoid of KChIP2 mRNA suggesting a lack of or altered I_{to} in this region. These data suggest that a component of AVN delay could occur when an action potential reaches the compact node.

Lower nodal cells, which lie in close proximity to cells of the PNE, have been suggested to act as a current sink for action potentials travelling along the PNE which would effectively slow conduction. In addition, these cells have been shown to display fully formed action potentials even when most of the tissue around these cells is refractory. The electrical properties allowing such activity to date has been unknown. I have shown these cells to have a unique ion channel expression profile, in that, both $Ca_v1.2$ and $Ca_v1.3$ mRNA are expressed and they are absent of $Na_v1.5$ and KChIP2 mRNA.

This work has uncovered the expression of the major ion channel subunits throughout functionally distinct areas of the AVN conduction axis. These data provide a better understanding of AVN function than previous studies (Petrecca et al. 1997).

The AVN has been described using the words of Sir Winston Churchill as "a riddle, wrapped in a mystery, inside an enigma". I would like to think that my work has contributed towards solving the "riddle", "mystery" and "enigma".

Reference List

Abbott, G. W., Sesti, F., Splawski, I., Buck, M. E., Lehmann, M. H., Timothy, K. W., Keating, M. T., & Goldstein, S. A. (1999). MiRP1 forms IKr potassium channels with HERG and is associated with cardiac arrhythmia. *Cell* 97, 175-187.

Accili, E. A., Redaelli, G., & DiFrancesco, D. (1997). Differential control of the hyperpolarization-activated current (i(f)) by cAMP gating and phosphatase inhibition in rabbit sino-atrial node myocytes. *Journal of Physiology-London* 500, 643-651.

Accili, E. A., Proenza, C., Baruscotti, M., & DiFrancesco, D. (2002). From funny current to HCN channels: 20 years of excitation 4. *News Physiol Sci* 17, 32-37.

Agata, N., Tanaka, H., & Shigenobu, K. (1994). Inotropic effects of ryanodine and nicardipine on fetal, neonatal and adult guinea-pig myocardium. *Eur J Pharmacol* 260, 47-55.

Aguilar-Bryan, L. & Bryan, J. (1999). Molecular biology of adenosine triphosphate-sensitive potassium channels. *Endocr.Rev.* 20, 101-135.

Alexander, D. B. & Goldberg, G. S. (2003). Transfer of biologically important molecules between cells through gap junction channels. *Curr.Med.Chem.* 10, 2045-2058.

Altomare, C., Bucchi, A., Camatini, E., Baruscotti, M., Viscomi, C., Moroni, A., & DiFrancesco, D. (2001). Integrated allosteric model of voltage gating of HCN channels. *J.Gen.Physiol* 117, 519-532.

Altomare, C., Terragni, B., Brioschi, C., Milanesi, R., Pagliuca, C., Viscomi, C., Moroni, A., Baruscotti, M., & DiFrancesco, D. (2003). Heteromeric HCN1-HCN4 channels: a comparison with native pacemaker channels from the rabbit sinoatrial node. *J.Physiol* 549, 347-359.

An, W. F., Bowlby, M. R., Betty, M., Cao, J., Ling, H. P., Mendoza, G., Hinson, J. W., Mattsson, K. I., Strassle, B. W., Trimmer, J. S., & Rhodes, K. J. (2000). Modulation of A-type potassium channels by a family of calcium sensors. *Nature* 403, 553-556.

Anderson, K., Lai, F. A., Liu, Q. Y., Rousseau, E., Erickson, H. P., & Meissner, G. (1989). Structural and functional characterization of the purified cardiac ryanodine receptor-Ca2+ release channel complex. *J Biol.Chem.* 264, 1329-1335.

Anderson, R. H. (1972). Histologic and histochemical evidence concerning the presence of morphologically distinct cellular zones within the rabbit atrioventricular node. *Anat.Rec.* 173, 7-23.

Anderson, R. H., Janse, M. J., van Capelle, F. J., Billette, J., Becker, A. E., & Durrer, D. (1974). A combined morphological and electrophysiological study of the atrioventricular node of the rabbit heart. *Circ Res* 35, 909-922.

Anderson, R. H., Ho, S. Y., Gillette, P. C., & Becker, A. E. (1996). Mahaim, Kent and abnormal atrioventricular conduction. *Cardiovasc.Res* 31, 480-491.

Anderson, R. H. & Ho, S. Y. (1998). The architecture of the sinus node, the atrioventricular conduction axis, and the internodal atrial myocardium. *J Cardiovasc.Electrophysiol.* 9 , 1233-1248.

Anderson, R. H. & Ho, S. Y. (1998). The morphology of the atrial approaches to the AV node. *J Cardiovasc.Electrophysiol.* 9, 336-337.

Anderson, R. H. & Ho, S. Y. (2003). The morphology of the cardiac conduction system. *Novartis.Found.Symp.* 250, 6-17.

Apkon, M. & Nerbonne, J. M. (1991). Characterization of two distinct depolarization-activated K+ currents in isolated adult rat ventricular myocytes. *J Gen Physiol* 97, 973-1011.

Arguello, C., Alanis, J., & Valenzuela, B. (1988). The early development of the atrioventricular node and bundle of His in the embryonic chick heart. An electrophysiological and morphological study. *Development* 102, 623-637.

Aschoff L 1910 Referat uber die Herzstorungen in ihren Beziehungen zu den Spezifischen Muskelsystem des Herzens. Verh Dtsch Pathol Ges 14:3-35.

Babenko, A. P., Gonzalez, G., Aguilar-Bryan, L., & Bryan, J. (1998). Reconstituted human cardiac KATP channels: functional identity with the native channels from the sarcolemma of human ventricular cells. *Circ Res* 83, 1132-1143.

Barry, D. M. & Nerbonne, J. M. (1996). Myocardial potassium channels: electrophysiological and molecular diversity. *Annu.Rev.Physiol* 58, 363-394.

Barry, W. H. & Bridge, J. H. (1993). Intracellular calcium homeostasis in cardiac myocytes *Circulation* 87, 1806-1815.

Baruscotti, M., Westenbroek, R., Catterall, W. A., DiFrancesco, D., & Robinson, R. B. (1997). The newborn rabbit sino-atrial node expresses a neuronal type I-like Na+ channel. *J Physiol* 498 (Pt 3), 641-648.

Bassani, R. A. & Bers, D. M. (1994). Na-Ca exchange is required for rest-decay but not for rest-potentiation of twitches in rabbit and rat ventricular myocytes *J Mol Cell Cardiol* 26, 1335-1347.

Basson, C. T., Solomon, S. D., Weissman, B., MacRae, C. A., Poznanski, A. K., Prieto, F., Ruiz, d. l. F., Pease, W. E., Levin, S. E., Holmes, L. B., & . (1995). Genetic heterogeneity of heart-hand syndromes. *Circulation* 91, 1326-1329.

Bell, D. C., Butcher, A. J., Berrow, N. S., Page, K. M., Brust, P. F., Nesterova, A., Stauderman, K. A., Seabrook, G. R., Nurnberg, B., & Dolphin, A. C. (2001). Biophysical properties, pharmacology, and modulation of human, neuronal L-type (alpha(1D), Ca(V)1.3) voltage-dependent calcium currents. *J Neurophysiol.* 85, 816-827.

Bers, D. M. & Bridge, J. H. (1989). Relaxation of rabbit ventricular muscle by Na-Ca exchange and sarcoplasmic reticulum calcium pump. Ryanodine and voltage sensitivity *Circ Res* 65, 334-342.

Bers, D. M. & Stiffel, V. M. (1993). Ratio of ryanodine to dihydropyridine receptors in cardiac and skeletal muscle and implications for E-C coupling. *Am.J Physiol* 264, C1587-C1593.

Billette, J., Janse, M. J., van Capelle, F. J., Anderson, R. H., Touboul, P., & Durrer, D. (1976). Cycle-length-dependent properties of AV nodal activation in rabbit hearts. *Am.J Physiol* 231, 1129-1139.

Billette, J. (1987). Atrioventricular nodal activation during periodic premature stimulation of the atrium. *Am.J Physiol* 252, H163-H177.

Billeter, R., Weber, H., Lutz, H., Howald, H., Eppenberger, H. M., & Jenny, E. (1980). Myosin types in human skeletal muscle fibers. *Histochemistry* 65, 249-259.

Blaustein, M. P. & Lederer, W. J. (1999). Sodium/calcium exchange: its physiological implications. *Physiol Rev.* 79, 763-854.

Bogdanov, K. Y., Vinogradova, T. M., & Lakatta, E. G. (2001). Sinoatrial nodal cell ryanodine receptor and Na(+)-Ca(2+) exchanger: molecular partners in pacemaker regulation *Circ Res* 88, 1254-1258.

Bohn, G., Moosmang, S., Conrad, H., Ludwig, A., Hofmann, F., & Klugbauer, N. (2000). Expression of T- and L-type calcium channel mRNA in murine sinoatrial node. *FEBS Lett.* 481, 73-76.

Boutjdir, M. (2000). Molecular and ionic basis of congenital complete heart block. *Trends Cardiovasc.Med.* 10, 114-122.

Boyett, M. R., Honjo, H., Yamamoto, M., Nikmaram, M. R., Niwa, R., & Kodama, I. (1998). Regional differences in effects of 4-aminopyridine within the sinoatrial node. *Am.J Physiol* 275, H1158-H1168.

Boyett, M. R., Honjo, H., & Kodama, I. (2000). The sinoatrial node, a heterogeneous pacemaker structure. *Cardiovasc.Res* 47, 658-687.

Boyett, M. R., Inada S. Yoo, S., Li, J., Liu, J., Tellez, J., Greener., I.D., Honjo, H., Billeter, R., Lei, M., Zhang, H., Efimov, I., Dobrzynski, H. (2006). Connexins in the sinoatrial and atrioventricular nodes. *Advances in Cardiology* 42; 175-197.

Brand T. Heart development: molecular insights into cardiac specification and early morphogenesis. Dev Biol 2003; 258:1-19

Brandl, C. J., Green, N. M., Korczak, B., & MacLennan, D. H. (1986). Two Ca2+ ATPase genes: homologies and mechanistic implications of deduced amino acid sequences. *Cell* 44, 597-607.

Brechenmacher, C., Courtadon, M., Jourde, M., Yermia, J. C., Cheynel, J., & Voegtlin, R. (1976). [Wolff-Parkinson-White syndrome caused by association of atrio-hisian fibers and Mahaim's fibers. Comparison between the electrophysiology and histology. *Arch.Mal Coeur Vaiss.* 69, 1275-1283.

Brette, F. & Orchard, C. H. (2006). No apparent requirement for neuronal sodium channels in excitation-contraction coupling in rat ventricular myocytes. *Circ Res* 98, 667-674.

Brown, A. M., Lee, K. S., & Powell, T. (1981). Sodium current in single rat heart muscle cells. *J Physiol* 318, 479-500.

Bru-Mercier, G., Deroubaix, E., Capuano, V., Ruchon, Y., Rucker-Martin, C., Coulombe, A., & Renaud, J. F. (2003). Expression of heart K+ channels in adrenalectomized and catecholamine-depleted reserpine-treated rats. *J Mol.Cell Cardiol.* 35, 153-163.

Bruneau, B. G., Nemer, G., Schmitt, J. P., Charron, F., Robitaille, L., Caron, S., Conner, D. A., Gessler, M., Nemer, M., Seidman, C. E., & Seidman, J. G. (2001). A murine model of Holt-Oram syndrome defines roles of the T-box transcription factor Tbx5 in cardiogenesis and disease. *Cell* 106, 709-721.

Burnashev, N. A. & Zilberter, Y. (1986). Two types of single inward rectifying potassium channels in rat myocardial cells. *Gen Physiol Biophys.* 5, 495-504.

Bustin, S. A. (2002). Quantification of mRNA using real-time reverse transcription PCR (RT-PCR): trends and problems. *J Mol Endocrinol.* **29**, 23-39.

Bustin, S. A. (2000). Absolute quantification of mRNA using real-time reverse transcription polymerase chain reaction assays. *J Mol.Endocrinol.* 25, 169-193.

Campbell, D. L., Rasmusson, R. L., Qu, Y., & Strauss, H. C. (1993). The calcium-independent transient outward potassium current in isolated ferret right ventricular myocytes. I. Basic characterization and kinetic analysis. *J Gen Physiol* 101, 571-601.

Caroni, P. & Carafoli, E. (1981). Regulation of Ca2+-pumping ATPase of heart sarcolemma by a phosphorylation-dephosphorylation Process *J Biol Chem* 256, 9371-9373.

Catterall, W. A. (2000). From ionic currents to molecular mechanisms: the structure and function of voltage-gated sodium channels. *Neuron* 26, 13-25.

Chen, F., Mottino, G., Klitzner, T. S., Philipson, K. D., & Frank, J. S. (1995). Distribution of the Na+/Ca2+ exchange protein in developing rabbit myocytes *Am J Physiol* 268, C1126-C1132.

Chen, S., Wang, J., & Siegelbaum, S. A. (2001). Properties of hyperpolarization-activated pacemaker current defined by coassembly of HCN1 and HCN2 subunits and basal modulation by cyclic nucleotide *J Gen.Physiol* 117, 491-504.

Cheng, H., Lederer, W. J., & Cannell, M. B. (1993). Calcium sparks: elementary events underlying excitation-contraction coupling in heart muscle *Science* 262, 740-744.

Cheng, H., Cannell, M. B., & Lederer, W. J. (1995). Partial inhibition of Ca2+ current by methoxyverapamil (D600) reveals spatial nonuniformities in [Ca2+]i during excitation-contraction coupling in cardiac myocytes *Circ Res* 76, 236-241.

Cheng, H., Lederer, M. R., Lederer, W. J., & Cannell, M. B. (1996). Calcium sparks and [Ca2+]i waves in cardiac myocytes. *Am J Physiol* 270, C148-C159.

Christie, P. D., Edelberg, J. M., Picard, M. H., Foulkes, A. S., Mamuya, W., Weiler-Guettler, H., Rubin, R. H., Gilbert, P., & Rosenberg, R. D. (1999). A murine model of myocardial microvascular thrombosis. *J Clin.Invest* 104, 533-539.

Comer, M. B., Campbell, D. L., Rasmusson, R. L., Lamson, D. R., Morales, M. J., Zhang, Y., & Strauss, H. C. (1994). Cloning and characterization of an Ito-like potassium channel from ferret ventricle. *Am.J Physiol* 267, H1383-H1395.

Convery, M. K. & Hancox, J. C. (2000). Na+-Ca2+ exchange current from rabbit isolated atrioventricular nodal and ventricular myocytes compared using action potential and ramp waveforms *Acta Physiol Scand.* 168, 393-401.

Coppen, S. R., Dupont, E., Rothery, S., & Severs, N. J. (1998). Connexin45 expression is preferentially associated with the ventricular conduction system in mouse and rat heart. *Circ Res* 82, 232-243.

Coppen, S. R., Severs, N. J., & Gourdie, R. G. (1999). Connexin45 (alpha 6) expression delineates an extended conduction system in the embryonic and mature rodent heart. *Dev.Genet.* 24, 82-90.

Coraboeuf, E. & Carmeliet, E. (1982). Existence of two transient outward currents in sheep cardiac Purkinje fibers. *Pflugers Arch.* 392, 352-359.

Coraboeuf, E. & Nargeot, J. (1993). Electrophysiology of human cardiac cells *Cardiovasc Res* 27, 1713-1725.

Cosio, F. G., Anderson, R. H., Kuck, K. H., Becker, A., Borggrefe, M., Campbell, R. W., Gaita, F., Guiraudon, G. M., Haissaguerre, M., Rufilanchas, J. J., Thiene, G., Wellens, H. J., Langberg, J., Benditt, D. G., Bharati, S., Klein, G., Marchlinski, F., & Saksena, S. (1999). Living anatomy of the atrioventricular junctions. A guide to electrophysiologic mapping. A Consensus Statement from the Cardiac Nomenclature Study Group, Working Group of Arrhythmias, European Society of Cardiology, and the Task Force on Cardiac Nomenclature from NASPE. *Circulation* 100, e31-e37.

Cote, K., Proteau, S., Teijeira, J., & Rousseau, E. (2000). Characterization of the sarcoplasmic reticulum k(+) and Ca(2+)-release channel-ryanodine receptor-in human atrial cells. *J Mol.Cell Cardiol.* 32, 2051-2063.

Coussin, F., Macrez, N., Morel, J. L., & Mironneau, J. (2000). Requirement of ryanodine receptor subtypes 1 and 2 for Ca(2+)-induced Ca(2+) release in vascular myocytes. *J Biol.Chem.* 275, 9596-9603.

Crespo, L. M., Grantham, C. J., & Cannell, M. B. (1990). Kinetics, stoichiometry and role of the Na-Ca exchange mechanism in isolated cardiac myocytes *Nature* 345, 618-621.

Daggett, W. M., Bianco, J. A., Powell, W. J., Jr., & Austen, W. G. (1970). Relative contributions of the atrial systoleventricular systole interval and of patterns of ventricular activation to ventricular function during electrical pacing of the dog heart. *Circ Res* 27, 69-79.

Davis, L. M., Rodefeld, M. E., Green, K., Beyer, E. C., & Saffitz, J. E. (1995). Gap junction protein phenotypes of the human heart and conduction system. *J Cardiovasc.Electrophysiol.* 6, 813-822.

de Bold, A. J. (1985). Atrial natriuretic factor: a hormone produced by the heart. *Science* 230, 767-770.

de CARVALHO, A. & de ALMEIDA, D. (1960). Spread of activity through the atrioventricular node. *Circ Res* 8, 801-809.

De Jong, F., Opthof, T., Wilde, A. A., Janse, M. J., Charles, R., Lamers, W. H., & Moorman, A. F. (1992). Persisting zones of slow impulse conduction in developing chicken hearts. *Circ Res* 71, 240-250.

Decher, N., Uyguner, O., Scherer, C. R., Karaman, B., Yuksel-Apak, M., Busch, A. E., Steinmeyer, K., & Wollnik, B. (2001). hKChIP2 is a functional modifier of hKv4.3 potassium channels: cloning and expression of a short hKChIP2 splice variant. *Cardiovasc.Res* 52, 255-264.

Decher, N., Barth, A. S., Gonzalez, T., Steinmeyer, K., & Sanguinetti, M. C. (2004). Novel KChIP2 isoforms increase functional diversity of transient outward potassium currents. *J Physiol* 557, 761-772.

Delorme, B., Dahl, E., Jarry-Guichard, T., Briand, J. P., Willecke, K., Gros, D., & Theveniau-Ruissy, M. (1997). Expression pattern of connexin gene products at the early developmental stages of the mouse cardiovascular system. *Circ Res* 81, 423-437.

Denes, P., Wu, D., Dhingra, R., Leon, F., Wyndham, C., & Rosen, K. M. (1975). Dual atrioventricular nodal pathways. A common electrophysiological response. *Br Heart J* 37, 1069-1076.

Deschenes, I., DiSilvestre, D., Juang, G. J., Wu, R. C., An, W. F., & Tomaselli, G. F. (2002). Regulation of Kv4.3 current by KChIP2 splice variants: a component of native cardiac I(to)? *Circulation* 106, 423-429.

Deschenes, I. & Tomaselli, G. F. (2002). Modulation of Kv4.3 current by accessory subunits. *FEBS Lett.* 528, 183-188.

Dhar, M. J., Chen, C., Rivolta, I., Abriel, H., Malhotra, R., Mattei, L. N., Brosius, F. C., Kass, R. S., & Isom, L. L. (2001). Characterization of sodium channel alpha- and beta-subunits in rat and mouse cardiac myocytes. *Circulation* 103, 1303-1310.

DiFrancesco, D. (1993). Pacemaker mechanisms in cardiac tissue. *Annu.Rev.Physiol* 55, 455-472.

Dixon, J. E. & McKinnon, D. (1994). Quantitative analysis of potassium channel mRNA expression in atrial and ventricular muscle of rats. *Circ Res* 75, 252-260.

Dobrzynski, H., Rothery, S. M., Marples, D. D., Coppen, S. R., Takagishi, Y., Honjo, H., Tamkun, M. M., Henderson, Z., Kodama, I., Severs, N. J., & Boyett, M. R. (2000). Presence of the Kv1.5 K(+) channel in the sinoatrial node. *J Histochem.Cytochem.* 48, 769-780.

Dobrzynski, H., Nikolski, V. P., Sambelashvili, A. T., Greener, I. D., Yamamoto, M., Boyett, M. R., & Efimov, I. R. (2003). Site of origin and molecular substrate of atrioventricular junctional rhythm in the rabbit heart. *Circ Res* 93, 1102-1110.

Dreifus, L. S. & Watanabe, Y. (1971). Localization and significance of atrioventricular block. *Am.Heart J* 82, 435-438.

Earm, Y. E., Ho, W. K., & So, I. S. (1990). Inward current generated by Na-Ca exchange during the action potential in single atrial cells of the rabbit *Proc R.Soc.Lond B Biol Sci* 240, 61-81.

Ertel, E. A., Campbell, K. P., Harpold, M. M., Hofmann, F., Mori, Y., Perez-Reyes, E., Schwartz, A., Snutch, T. P., Tanabe, T., Birnbaumer, L., Tsien, R. W., & Catterall, W. A. (2000). Nomenclature of voltage-gated calcium channels. *Neuron* 25, 533-535.

Fedida, D., Wible, B., Wang, Z., Fermini, B., Faust, F., Nattel, S., & Brown, A. M. (1993). Identity of a novel delayed rectifier current from human heart with a cloned K+ channel current. *Circ Res* 73, 210-216.

Fermini, B., Wang, Z., Duan, D., & Nattel, S. (1992). Differences in rate dependence of transient outward current in rabbit and human atrium. *Am.J Physiol* 263, H1747-H1754.

Folander, K., Smith, J. S., Antanavage, J., Bennett, C., Stein, R. B., & Swanson, R. (1990). Cloning and expression of the delayed-rectifier IsK channel from neonatal rat heart and diethylstilbestrol-primed rat uterus. *Proc.Natl.Acad.Sci.U.S.A* 87, 2975-2979.

Frank, K. F., Bolck, B., Erdmann, E., & Schwinger, R. H. (2003). Sarcoplasmic reticulum Ca2+-ATPase modulates cardiac contraction and relaxation *Cardiovasc Res* 57, 20-27.

Franzini-Armstrong, C. & Protasi, F. (1997). Ryanodine receptors of striated muscles: a complex channel capable of multiple interactions. *Physiol Rev.* 77, 699-729.

Franzini-Armstrong, C., Tijskens, P., & Jones, L. R. (2004). Protein interactions within calcium release units of muscle *J Muscle Res Cell Motil.* 25, 586-587.

Franzini-Armstrong, C., Protasi, F., & Tijskens, P. (2005). The assembly of calcium release units in cardiac muscle *Ann N Y Acad Sci* 1047, 76-85.

Galper, J. B. & Catterall, W. A. (1978). Developmental changes in the sensitivity of embryonic heart cells to tetrodotoxin and D600. *Dev.Biol.* 65, 216-227.

Gellens, M. E., George, A. L., Jr., Chen, L. Q., Chahine, M., Horn, R., Barchi, R. L., & Kallen, R. G. (1992). Primary structure and functional expression of the human cardiac tetrodotoxin-insensitive voltage-dependent sodium channel. *Proc.Natl.Acad.Sci.U.S.A* 89, 554-558.

Giannini, G. & Sorrentino, V. (1995). Molecular structure and tissue distribution of ryanodine receptors calcium channels. *Med.Res Rev.* 15, 313-323.

Giles, W. R. & Imaizumi, Y. (1988). Comparison of potassium currents in rabbit atrial and ventricular cells. *J Physiol* 405, 123-145.

Goldberger, J., Brooks, R., & Kadish, A. (1992). Physiology of "atypical" atrioventricular junctional reentrant tachycardia occurring following radiofrequency catheter modification of the atrioventricular node. *Pacing Clin.Electrophysiol.* 15, 2270-2282.

Goldhaber, J. I., Parker, J. M., & Weiss, J. N. (1991). Mechanisms of excitation-contraction coupling failure during metabolic inhibition in guinea-pig ventricular myocytes. *J Physiol* 443, 371-386.

Goldin, A. L. (2001). Resurgence of sodium channel research. *Annu.Rev.Physiol* 63, 871-894.

Goldstein, S. A. & Miller, C. (1991). Site-specific mutations in a minimal voltage-dependent K+ channel alter ion selectivity and open-channel block. *Neuron* 7, 403-408.

Goodenough, D. A., Goliger, J. A., & Paul, D. L. (1996). Connexins, connexons, and intercellular communication. *Annu.Rev.Biochem.* 65, 475-502.

Gorza, L., Schiaffino, S., & Vitadello, M. (1988). Heart conduction system: a neural crest derivative? *Brain Res* 457, 360-366.

Gorza, L. & Vitadello, M. (1989). Distribution of conduction system fibers in the developing and adult rabbit heart revealed by an antineurofilament antibody. *Circ Res* 65, 360-369.

Gorza, L., Menabo, R., Vitadello, M., Bergamini, C. M., & Di Lisa, F. (1996). Cardiomyocyte troponin T immunoreactivity is modified by cross-linking resulting from intracellular calcium overload. *Circulation* 93, 1896-1904.

Gourdie, R. G., Green, C. R., & Severs, N. J. (1991). Gap junction distribution in adult mammalian myocardium revealed by an anti-peptide antibody and laser scanning confocal microscopy. *J Cell Sci.* 99 (Pt 1), 41-55.

Gourdie, R. G., Severs, N. J., Green, C. R., Rothery, S., Germroth, P., & Thompson, R. P. (1993). The spatial distribution and relative abundance of gap-junctional connexin40 and connexin43 correlate to functional properties of components of the cardiac atrioventricular conduction system. *J Cell Sci.* 105 (Pt 4), 985-991.

Gourdie, R. G., Mima, T., Thompson, R. P., & Mikawa, T. (1995). Terminal diversification of the myocyte lineage generates Purkinje fibers of the cardiac conduction system. *Development* 121, 1423-1431.

Gourdie, R. G., Harris, B. S., Bond, J., Edmondson, A. M., Cheng, G., Sedmera, D., O'Brien, T. X., Mikawa, T., & Thompson, R. P. (2003). His-Purkinje lineages and development. *Novartis.Found.Symp.* 250, 110-122.

Guo, W., Li, H., Aimond, F., Johns, D. C., Rhodes, K. J., Trimmer, J. S., & Nerbonne, J. M. (2002). Role of heteromultimers in the generation of myocardial transient outward K+ currents. *Circ Res* 90, 586-593.

Habets, P. E., Moorman, A. F., Clout, D. E., van Roon, M. A., Lingbeek, M., van Lohuizen, M., Campione, M., & Christoffels, V. M. (2002). Cooperative action of Tbx2 and Nkx2.5 inhibits ANF expression in the atrioventricular canal: implications for cardiac chamber formation. *Genes Dev.* 16, 1234-1246.

Hagiwara, N., Irisawa, H., & Kameyama, M. (1988). Contribution of two types of calcium currents to the pacemaker potentials of rabbit sino-atrial node cells. *J Physiol* 395, 233-253.

Haider, S., Antcliff, J. F., Proks, P., Sansom, M. S., & Ashcroft, F. M. (2005). Focus on Kir6.2: a key component of the ATP-sensitive potassium channel. *J Mol.Cell Cardiol.* 38, 927-936.

Hall, C. E., Hurtado, R., Hewett, K. W., Shulimovich, M., Poma, C. P., Reckova, M., Justus, C., Pennisi, D. J., Tobita, K., Sedmera, D., Gourdie, R. G., & Mikawa, T. (2004).

Hemodynamic-dependent patterning of endothelin converting enzyme 1 expression and differentiation of impulse-conducting Purkinje fibers in the embryonic heart. *Development* 131, 581-592.

Hancox, J. & Levi, A. (1994). The hyperpolarisation-activated current, I(f), is not required for pacemaking in single cells from the rabbit atrioventricular node *Pflugers Arch.* 427, 121-128.

Hancox, J. C., Levi, A. J., Lee, C. O., & Heap, P. (1993). A method for isolating rabbit atrioventricular node myocytes which retain normal morphology and function. *Am.J Physiol* 265, H755-H766.

Hancox, J. C. & Levi, A. J. (1994). L-type calcium current in rod- and spindle-shaped myocytes isolated from rabbit atrioventricular node *Am J Physiol* 267, H1670-H1680.

Hancox, J. C., Levi, A. J., & Brooksby, P. (1994). Intracellular calcium transients recorded with Fura-2 in spontaneously active myocytes isolated from the atrioventricular node of the rabbit heart *Proc Biol Sci* 255, 99-105.

Hilgemann, D. W. & Noble, D. (1987). Excitation-contraction coupling and extracellular calcium transients in rabbit atrium: reconstruction of basic cellular mechanisms *Proc R.Soc.Lond B Biol Sci* 230, 163-205.

Hiroi, Y., Kudoh, S., Monzen, K., Ikeda, Y., Yazaki, Y., Nagai, R., & Komuro, I. (2001). Tbx5 associates with Nkx2-5 and synergistically promotes cardiomyocyte differentiation. *Nat.Genet.* 28, 276-280.

Hirota, A., Fujii, S., & Kamino, K. (1979). Optical monitoring of spontaneous electrical activity of 8-somite embryonic chick heart. *Jpn.J Physiol* 29, 635-639.

His W, Jr 1893 Die Thätigkeit des embryonalen Herzens und deren Bedeutung für die Lehre von der Herzbewegung beim Erwachsenen. Arb aus d med Klinik zu Leipzig 1:14-49.

Hocini, M., Loh, P., Ho, S. Y., Sanchez-Quintana, D., Thibault, B., de Bakker, J. M., & Janse, M. J. (1998). Anisotropic conduction in the triangle of Koch of mammalian hearts: electrophysiologic and anatomic correlations. *J Am.Coll.Cardiol.* 31, 629-636.

HOFFMAN, B. F., DE CARVALHO, A. P., & DE MELLO, W. C. (1958). Transmembrane potentials of single fibres of the atrio-ventricular node. *Nature* 181, 66-67.

Hogan, P. G., Chen, L., Nardone, J., & Rao, A. (2003). Transcriptional regulation by calcium, calcineurin, and NFAT. *Genes Dev.* 17, 2205-2232.

Honjo, H., Kodama, I., Zang, W. J., & Boyett, M. R. (1992). Desensitization to acetylcholine in single sinoatrial node cells isolated from rabbit hearts *Am J Physiol* 263, H1779-H1789.

Honjo, H., Inada, S., Lancaster, M. K., Yamamoto, M., Niwa, R., Jones, S. A., Shibata, N., Mitsui, K., Horiuchi, T., Kamiya, K., Kodama, I., & Boyett, M. R. (2003). Sarcoplasmic reticulum Ca2+ release is not a dominating factor in sinoatrial node pacemaker activity. *Circ Res* 92, e41-e44.

Horie, M., Hayashi, S., & Kawai, C. (1990). Two types of delayed rectifying K+ channels in atrial cells of guinea pig heart. *Jpn.J Physiol* 40, 479-490.

Howarth, F. C., Levi, A. J., & Hancox, J. C. (1996). Characteristics of the delayed rectifier K current compared in myocytes isolated from the atrioventricular node and ventricle of the rabbit heart. *Pflugers Arch.* 431, 713-722.

Huser, J., Blatter, L. A., & Lipsius, S. L. (2000). Intracellular Ca2+ release contributes to automaticity in cat atrial pacemaker cells. *J Physiol* 524 Pt 2, 415-422.

Iinuma, H., Dreifus, L. S., Mazgalev, T., Price, R., & Michelson, E. L. (1983). Role of the perinodal region in atrioventricular nodal reentry: evidence in an isolated rabbit heart preparation. *J Am.Coll.Cardiol.* 2, 465-473.

Inoue, S. & Becker, A. E. (1998). Posterior extensions of the human compact atrioventricular node: a neglected anatomic feature of potential clinical significance. *Circulation* 97 , 188-193.

Inui, M., Saito, A., & Fleischer, S. (1987). Isolation of the ryanodine receptor from cardiac sarcoplasmic reticulum and identity with the feet structures *J Biol Chem* 262 , 15637-15642.

Ishii, K., Yamagishi, T., & Taira, N. (1994). Cloning and functional expression of a cardiac inward rectifier K+ channel. *FEBS Lett.* 338, 107-111.

Ishii, T. M., Takano, M., Xie, L. H., Noma, A., & Ohmori, H. (1999). Molecular characterization of the hyperpolarization-activated cation channel in rabbit heart sinoatrial node. *J.Biol.Chem.* 274, 12835-12839.

Isom, L. L. (2001). Sodium channel beta subunits: anything but auxiliary. *Neuroscientist.* 7, 42-54.

Jackman, W. M., Beckman, K. J., McClelland, J. H., Wang, X., Friday, K. J., Roman, C. A., Moulton, K. P., Twidale, N., Hazlitt, H. A., Prior, M. I., & . (1992). Treatment of supraventricular tachycardia due to atrioventricular nodal reentry, by radiofrequency catheter ablation of slow-pathway conduction. *N.Engl.J Med.* 327, 313-318.

Janse, M. J. (1969). Influence of the direction of the atrial wave front on A-V nodal transmission in isolated hearts of rabbits. *Circ Res* 25, 439-449.

Janvier, N. C. & Boyett, M. R. (1996). The role of Na-Ca exchange current in the cardiac action potential *Cardiovasc Res* 32, 69-84.

Janvier, N. C., McMorn, S. O., Harrison, S. M., Taggart, P., & Boyett, M. R. (1997). The role of Na(+)-Ca2+ exchange current in electrical restitution in ferret ventricular cells 1. *J Physiol* 504 (Pt 2), 301-314.

Ji, Y., Lalli, M. J., Babu, G. J., Xu, Y., Kirkpatrick, D. L., Liu, L. H., Chiamvimonvat, N., Walsh, R. A., Shull, G. E., & Periasamy, M. (2000). Disruption of a single copy of the SERCA2 gene results in altered Ca2+ homeostasis and cardiomyocyte function *J Biol Chem* 275, 38073-38080.

Jing, J., Chikvashvili, D., Singer-Lahat, D., Thornhill, W. B., Reuveny, E., & Lotan, I. (1999). Fast inactivation of a brain K+ channel composed of Kv1.1 and Kvbeta1.1 subunits modulated by G protein beta gamma subunits. *EMBO J* 18, 1245-1256.

Kagiyama, Y., Hill, J. L., & Gettes, L. S. (1982). Interaction of acidosis and increased extracellular potassium on action potential characteristics and conduction in guinea pig ventricular muscle. *Circ Res* 51, 614-623.

Kakei, M. & Noma, A. (1984). Adenosine-5'-triphosphate-sensitive single potassium channel in the atrioventricular node cell of the rabbit heart. *J Physiol* 352, 265-284.

Kamp, T. J. & Hell, J. W. (2000). Regulation of cardiac L-type calcium channels by protein kinase A and protein kinase C. *Circ Res* 87, 1095-1102.

KATZ, B. (1949). The electric response at a sensory nerve ending. *J Physiol* 109, roc, 9.

Kaupp, U. B. & Seifert, R. (2001). Molecular diversity of pacemaker ion channels. *Annu Rev Physiol* 63, 235-257.

Kawai, M., Hussain, M., & Orchard, C. H. (1999). Excitation-contraction coupling in rat ventricular myocytes after formamide-induced detubulation. *Am J Physiol* 277, H603-H609.

Kawano, S., Hirayama, Y., & Hiraoka, M. (1995). Activation mechanism of Ca(2+)-sensitive transient outward current in rabbit ventricular myocytes. *J Physiol* 486 (Pt 3), 593-604.

Kenyon, J. L. & Gibbons, W. R. (1979). 4-Aminopyridine and the early outward current of sheep cardiac Purkinje fibers. *J Gen Physiol* 73, 139-157.

Kieval, R. S., Bloch, R. J., Lindenmayer, G. E., Ambesi, A., & Lederer, W. J. (1992). Immunofluorescence localization of the Na-Ca exchanger in heart cells *Am J Physiol* 263, C545-C550.

Kimura, J., Miyamae, S., & Noma, A. (1987). Identification of sodium-calcium exchange current in single ventricular cells of guinea-pig 11. *J Physiol* 384, 199-222.

Ko, Y. S., Yeh, H. I., Ko, Y. L., Hsu, Y. C., Chen, C. F., Wu, S., Lee, Y. S., & Severs, N. J. (2004). Three-dimensional reconstruction of the rabbit atrioventricular conduction axis by combining histological, desmin, and connexin mapping data. *Circulation* 109, 1172-1179.

Kofuji, P., Hadley, R. W., Kieval, R. S., Lederer, W. J., & Schulze, D. H. (1992). Expression of the Na-Ca exchanger in diverse tissues: a study using the cloned human cardiac Na-Ca exchanger *Am J Physiol* 263, C1241-C1249.

Kofuji, P., Lederer, W. J., & Schulze, D. H. (1994). Mutually exclusive and cassette exons underlie alternatively spliced isoforms of the Na/Ca exchanger. *J Biol.Chem.* 269, 5145-5149.

Kokubun, S., Nishimura, M., Noma, A., & Irisawa, H. (1980). The spontaneous action potential of rabbit atrioventricular node cells. *Jpn.J Physiol* 30, 529-540.

Kokubun, S., Nishimura, M., Noma, A., & Irisawa, H. (1982). Membrane currents in the rabbit atrioventricular node cell. *Pflugers Arch.* 393, 15-22.

Kono, Y., Horie, M., Takano, M., Otani, H., Xie, L. H., Akao, M., Tsuji, K., & Sasayama, S. (2000). The properties of the Kir6.1-6.2 tandem channel co-expressed with SUR2A. *Pflugers Arch.* 440, 692-698.

Kreuzberg, M. M., Sohl, G., Kim, J. S., Verselis, V. K., Willecke, K., & Bukauskas, F. F. (2005). Functional properties of mouse connexin30.2 expressed in the conduction system of the heart. *Circ Res* 96, 1169-1177.

Kubo, Y., Baldwin, T. J., Jan, Y. N., & Jan, L. Y. (1993). Primary structure and functional expression of a mouse inward rectifier potassium channel. *Nature* 362, 127-133.

Kumar, N. M. & Gilula, N. B. (1996). The gap junction communication channel. *Cell* 84, 381-388.

Kuro-o M, Tsuchimochi, H., Ueda, S., Takaku, F., & Yazaki, Y. (1986). Distribution of cardiac myosin isozymes in human conduction system. Immunohistochemical study using monoclonal antibodies. *J Clin.Invest* 77, 340-347.

Lai, F. A., Misra, M., Xu, L., Smith, H. A., & Meissner, G. (1989). The ryanodine receptor-Ca2+ release channel complex of skeletal muscle sarcoplasmic reticulum. Evidence for a cooperatively coupled, negatively charged homotetramer. *J Biol.Chem.* 264, 16776-16785.

Lamers, W. H., De Jong, F., De Groot, I. J., & Moorman, A. F. (1991). The development of the avian conduction system, a review. *Eur J Morphol.* 29, 233-253.

LANGENDORF, R. & PICK, A. (1956). Concealed conduction further evaluation of a fundamental aspect of propagation of the cardiac impulse. *Circulation* 13, 381-399.

Leblanc, N. & Hume, J. R. (1990). Sodium current-induced release of calcium from cardiac sarcoplasmic reticulum *Science* 248, 372-376.

Lees-Miller, J. P., Kondo, C., Wang, L., & Duff, H. J. (1997). Electrophysiological characterization of an alternatively processed ERG K+ channel in mouse and human hearts. *Circ Res* 81, 719-726.

Lei, M., Honjo, H., Kodama, I., & Boyett, M. R. (2000). Characterisation of the transient outward K+ current in rabbit sinoatrial node cells. *Cardiovasc.Res* 46, 433-441.

Lei, M., Cooper, P. J., Camelliti, P., & Kohl, P. (2002). Role of the 293b-sensitive, slowly activating delayed rectifier potassium current, i(Ks), in pacemaker activity of rabbit isolated sino-atrial node cells. *Cardiovasc.Res* 53, 68-79.

Leicher, T., Bahring, R., Isbrandt, D., & Pongs, O. (1998). Coexpression of the KCNA3B gene product with Kv1.5 leads to a novel A-type potassium channel. *J Biol.Chem.* 273, 35095-35101.

Leitch, S. P. & Brown, H. F. (1996). Effect of raised extracellular calcium on characteristics of the guinea-pig ventricular action potential. *J Mol Cell Cardiol* 28, 541-551.

Levitsky, D. O., Nicoll, D. A., & Philipson, K. D. (1994). Identification of the high affinity Ca(2+)-binding domain of the cardiac Na(+)-Ca2+ exchanger. *J Biol.Chem.* 269, 22847-22852.

Li, Z., Matsuoka, S., Hryshko, L. V., Nicoll, D. A., Bersohn, M. M., Burke, E. P., Lifton, R. P., & Philipson, K. D. (1994). Cloning of the NCX2 isoform of the plasma membrane Na(+)-Ca2+ exchanger. *J Biol.Chem.* 269, 17434-17439.

Lin, L. J., Billette, J., Medkour, D., Reid, M. C., Tremblay, M., & Khalife, K. (2001). Properties and substrate of slow pathway exposed with a compact node targeted fast pathway ablation in rabbit atrioventricular node. *J Cardiovasc.Electrophysiol.* 12, 479-486.

Lipp, P. & Niggli, E. (1994). Modulation of Ca2+ release in cultured neonatal rat cardiac myocytes. Insight from subcellular release patterns revealed by confocal microscopy *Circ Res* 74, 979-990.

Lipp, P., Laine, M., Tovey, S. C., Burrell, K. M., Berridge, M. J., Li, W., & Bootman, M. D. (2000). Functional InsP3 receptors that may modulate excitation-contraction coupling in the heart. *Curr.Biol.* 10, 939-942.

Litovsky, S. H. & Antzelevitch, C. (1988). Transient outward current prominent in canine ventricular epicardium but not endocardium. *Circ Res* 62, 116-126.

Liu, G. X., Derst, C., Schlichthorl, G., Heinen, S., Seebohm, G., Bruggemann, A., Kummer, W., Veh, R. W., Daut, J., & Preisig-Muller, R. (2001). Comparison of cloned Kir2 channels with native inward rectifier K+ channels from guinea-pig cardiomyocytes. *J Physiol* 532, 115-126.

Lopez-Lopez, J. R., Shacklock, P. S., Balke, C. W., & Wier, W. G. (1995). Local calcium transients triggered by single L-type calcium channel currents in cardiac cells *Science* 268, 1042-1045.

Ludwig, A., Zong, X., Jeglitsch, M., Hofmann, F., & Biel, M. (1998). A family of hyperpolarization-activated mammalian cation channels. *Nature* 393, 587-591.

Lytton, J., Zarain-Herzberg, A., Periasamy, M., & MacLennan, D. H. (1989). Molecular cloning of the mammalian smooth muscle sarco(endo)plasmic reticulum Ca2+-ATPase *J Biol Chem* 264, 7059-7065.

Ma, D., Zerangue, N., Lin, Y. F., Collins, A., Yu, M., Jan, Y. N., & Jan, L. Y. (2001). Role of ER export signals in controlling surface potassium channel numbers. *Science* 291, 316-319.

Maier, S. K., Westenbroek, R. E., Schenkman, K. A., Feigl, E. O., Scheuer, T., & Catterall, W. A. (2002). An unexpected role for brain-type sodium channels in coupling of cell surface depolarization to contraction in the heart. *Proc.Natl.Acad.Sci.U.S.A* 99, 4073-4078.

Maier, S. K., Westenbroek, R. E., Yamanushi, T. T., Dobrzynski, H., Boyett, M. R., Catterall, W. A., & Scheuer, T. (2003). An unexpected requirement for brain-type sodium channels for control of heart rate in the mouse sinoatrial node. *Proc.Natl.Acad.Sci.U.S.A* 100, 3507-3512.

Makielski, J. C. (1996). The heart sodium channel phenotype for inactivation and lidocaine block. *Jpn.Heart J* 37, 733-739.

Mangoni, M. E., Couette, B., Bourinet, E., Platzer, J., Reimer, D., Striessnig, J., & Nargeot, J. (2003). Functional role of L-type Cav1.3 Ca2+ channels in cardiac pacemaker activity. *Proc.Natl.Acad.Sci.U.S.A* 100, 5543-5548.

Marionneau, C., Couette, B., Liu, J., Li, H., Mangoni, M. E., Nargeot, J., Lei, M., Escande, D., & Demolombe, S. (2005). Specific pattern of ionic channel gene expression associated with pacemaker activity in the mouse heart. *J Physiol* 562, 223-234.

Masumiya, H., Yamamoto, H., Hemberger, M., Tanaka, H., Shigenobu, K., Chen, S. R., & Furukawa, T. (2003). The mouse sino-atrial node expresses both the type 2 and type 3 Ca(2+) release channels/ryanodine receptors. *FEBS Lett.* 553, 141-144.

MATSUDA, K., HOSHI, T., & KAMEYAMA, S. (1958). Action potential of the atrio-ventricular node (Tawara). *Tohoku J Exp.Med.* 68, 8.

Matthes, J., Yildirim, L., Wietzorrek, G., Reimer, D., Striessnig, J., & Herzig, S. (2004). Disturbed atrio-ventricular conduction and normal contractile function in isolated hearts from Cav1.3-knockout mice. *Naunyn Schmiedebergs Arch.Pharmacol* 369, 554-562.

McDonald, R. L., Colyer, J., & Harrison, S. M. (2000). Quantitative analysis of Na+-Ca2+ exchanger expression in guinea-pig heart. *Eur J Biochem.* 267, 5142-5148.

McGuire, M. A., de Bakker, J. M., Vermeulen, J. T., Moorman, A. F., Loh, P., Thibault, B., Vermeulen, J. L., Becker, A. E., & Janse, M. J. (1996). Atrioventricular junctional tissue. Discrepancy between histological and electrophysiological characteristics. *Circulation* 94, 571-577.

Mearow, K. M., Thilander, B. G., Khan, I., Garfield, R. E., & Grover, A. K. (1993). In situ hybridization and immunocytochemical localization of SERCA2 encoded Ca2+ pump in rabbit heart and stomach *Mol Cell Biochem* 121, 155-165.

Medkour, D., Becker, A. E., Khalife, K., & Billette, J. (1998). Anatomic and functional characteristics of a slow posterior AV nodal pathway: role in dual-pathway physiology and reentry. *Circulation* 98, 164-174.

Meijler, F. L. & Janse, M. J. (1988). Morphology and electrophysiology of the mammalian atrioventricular node. *Physiol Rev.* 68, 608-647.

Mendez, C. & MOE, G. K. (1966). Demonstration of a dual A-V nodal conduction system in the isolated rabbit heart. *Circ Res* 19, 378-393.

Mercadier, J. J., Samuel, J. L., Michel, J. B., Zongazo, M. A., de la, B. D., Lompre, A. M., Wisnewsky, C., Rappaport, L., Levy, B., & Schwartz, K. (1989). Atrial natriuretic factor gene expression in rat ventricle during experimental hypertension. *Am.J Physiol* 257, H979-H987.

Minajeva, A., Kaasik, A., Paju, K., Seppet, E., Lompre, A. M., Veksler, V., & Ventura-Clapier, R. (1997). Sarcoplasmic reticulum function in determining atrioventricular contractile differences in rat heart *Am J Physiol* 273, H2498-H2507.

Minta, A., Kao, J. P., & Tsien, R. Y. (1989). Fluorescent indicators for cytosolic calcium based on rhodamine and fluorescein chromophores *J Biol Chem* 264, 8171-8178.

Mitcheson, J. S. & Hancox, J. C. (1999). Characteristics of a transient outward current (sensitive to 4-aminopyridine) in Ca2+-tolerant myocytes isolated from the rabbit atrioventricular node. *Pflugers Arch.* 438, 68-78.

Mitcheson, J. S. & Hancox, J. C. (1999). An investigation of the role played by the E-4031-sensitive (rapid delayed rectifier) potassium current in isolated rabbit atrioventricular nodal and ventricular myocytes. *Pflugers Arch.* 438, 843-850.

MOE, G. K., PRESTON, J. B., & BURLINGTON, H. (1956). Physiologic evidence for a dual A-V transmission system. *Circ Res* 4, 357-375.

Monckeberg JG 1910 Beitrage zur normalen und pathologischen Anatomie des Herzens. Verh Dtsch Pathol Ges 14:64-71.

Monteith, G. R. & Roufogalis, B. D. (1995). The plasma membrane calcium pump--a physiological perspective on its regulation. *Cell Calcium* 18, 459-470.

Moorman AFM, Lamers WH. Molecular anatomy of the developing heart. Trends Cardiovasc Med 1994; 4:257-264

Moorman, A. F., De Jong, F., & Lamers, W. H. (1997). Development of the conduction system of the heart. *Pacing Clin.Electrophysiol.* 20, 2087-2092.

Moorman, A. F. & Christoffels, V. M. (2003). Cardiac chamber formation: development, genes, and evolution. *Physiol Rev.* 83, 1223-1267.

Moosmang, S., Stieber, J., Zong, X., Biel, M., Hofmann, F., & Ludwig, A. (2001). Cellular expression and functional characterization of four hyperpolarization-activated pacemaker channels in cardiac and neuronal tissues. *Eur.J.Biochem.* 268, 1646-1652.

Morgan, K., Stevens, E. B., Shah, B., Cox, P. J., Dixon, A. K., Lee, K., Pinnock, R. D., Hughes, J., Richardson, P. J., Mizuguchi, K., & Jackson, A. P. (2000). beta 3: an additional auxiliary subunit of the voltage-sensitive sodium channel that modulates channel gating with distinct kinetics. *Proc.Natl.Acad.Sci.U.S.A* 97, 2308-2313.

Moroni A Kinetic and ionic properties of the human HCN2 pacemaker channel. Pflugers Arch. 439[5],618-626.(2000).

Moroni, A., Gorza, L., Beltrame, M., Gravante, B., Vaccari, T., Bianchi, M. E., Altomare, C., Longhi, R., Heurteaux, C., Vitadello, M., Malgaroli, A., & DiFrancesco, D. (2001). Hyperpolarization-activated cyclic nucleotide-gated channel 1 is a molecular determinant of the cardiac pacemaker current I(f). *J.Biol.Chem.* 276, 29233-29241.

Munch, G., Bolck, B., Sugaru, A., & Schwinger, R. H. (2000). Isoform expression of the sarcoplasmic reticulum Ca2+ release channel (ryanodine channel) in human myocardium. *J Mol.Med.* 78, 352-360.

Munk, A. A., Adjemian, R. A., Zhao, J., Ogbaghebriel, A., & Shrier, A. (1996). Electrophysiological properties of morphologically distinct cells isolated from the rabbit atrioventricular node 1. *J Physiol* 493 (Pt 3), 801-818.

Nadal, M. S., Ozaita, A., Amarillo, Y., Vega-Saenz, d. M., Ma, Y., Mo, W., Goldberg, E. M., Misumi, Y., Ikehara, Y., Neubert, T. A., & Rudy, B. (2003). The CD26-related dipeptidyl aminopeptidase-like protein DPPX is a critical component of neuronal A-type K+ channels. *Neuron* 37, 449-461.

Neuhof, A., Rolls, M. M., Jungnickel, B., Kalies, K. U., & Rapoport, T. A. (1998). Binding of signal recognition particle gives ribosome/nascent chain complexes a competitive advantage in endoplasmic reticulum membrane interaction. *Mol.Biol.Cell* 9, 103-115.

Newbury, S. F., Muhlemann, O., & Stoecklin, G. (2006). Turnover in the Alps: an mRNA perspective. Workshops on mechanisms and regulation of mRNA turnover *EMBO Rep.* 7, 143-148.

Nichols, C. G. & Lopatin, A. N. (1997). Inward rectifier potassium channels. *Annu.Rev.Physiol* 59, 171-191.

Nicoll, D. A., Longoni, S., & Philipson, K. D. (1990). Molecular cloning and functional expression of the cardiac sarcolemmal Na(+)-Ca2+ exchanger *Science* 250, 562-565.

Nicoll, D. A., Quednau, B. D., Qui, Z., Xia, Y. R., Lusis, A. J., & Philipson, K. D. (1996). Cloning of a third mammalian Na+-Ca2+ exchanger, NCX3 *J Biol Chem* 271, 24914-24921.

Nicoll, D. A., Quednau, B. D., Qui, Z., Xia, Y. R., Lusis, A. J., & Philipson, K. D. (1996). Cloning of a third mammalian Na+-Ca2+ exchanger, NCX3. *J Biol.Chem.* 271, 24914-24921.

Niggli, E. (1999). Localized intracellular calcium signaling in muscle: calcium sparks and calcium quarks. *Annu Rev Physiol* 61, 311-335.

Nikolski, V. & Efimov, I. (2001). Fluorescent imaging of a dual-pathway atrioventricular-nodal conduction system. *Circ Res* 88, E23-E30.

Nikolski, V. P., Jones, S. A., Lancaster, M. K., Boyett, M. R., & Efimov, I. R. (2003). Cx43 and dual-pathway electrophysiology of the atrioventricular node and atrioventricular nodal reentry. *Circ Res* 92, 469-475.

Noble, D. & Noble, S. J. (1984). A model of sino-atrial node electrical activity based on a modification of the DiFrancesco-Noble (1984) equations. *Proc.R.Soc.Lond B Biol.Sci.* 222, 295-304.

Noma, A. (1983). ATP-regulated K+ channels in cardiac muscle. *Nature* 305, 147-148.

Nowycky, M. C., Fox, A. P., & Tsien, R. W. (1985). Long-opening mode of gating of neuronal calcium channels and its promotion by the dihydropyridine calcium agonist Bay K 8644. *Proc.Natl.Acad.Sci.U.S.A* 82, 2178-2182.

Ono, K. & Ito, H. (1995). Role of rapidly activating delayed rectifier K+ current in sinoatrial node pacemaker activity. *Am.J Physiol* 269, H453-H462.

Oosthoek, P. W., Viragh, S., Lamers, W. H., & Moorman, A. F. (1993). Immunohistochemical delineation of the conduction system. II: The atrioventricular node and Purkinje fibers. *Circ Res* 73, 482-491.

Papadatos, G. A., Wallerstein, P. M., Head, C. E., Ratcliff, R., Brady, P. A., Benndorf, K., Saumarez, R. C., Trezise, A. E., Huang, C. L., Vandenberg, J. I., Colledge, W. H., & Grace, A. A. (2002). Slowed conduction and ventricular tachycardia after targeted disruption of the cardiac sodium channel gene Scn5a. *Proc.Natl.Acad.Sci.U.S.A* 99, 6210-6215.

Papp, B., Enyedi, A., Paszty, K., Kovacs, T., Sarkadi, B., Gardos, G., Magnier, C., Wuytack, F., & Enouf, J. (1992). Simultaneous presence of two distinct endoplasmic-reticulum-type calcium-pump isoforms in human cells. Characterization by radio-immunoblotting and inhibition by 2,5-di-(t-butyl)-1,4-benzohydroquinone *Biochem J* 288 (Pt 1), 297-302.

Patel, S. P., Campbell, D. L., & Strauss, H. C. (2002). Elucidating KChIP effects on Kv4.3 inactivation and recovery kinetics with a minimal KChIP2 isoform. *J Physiol* 545, 5-11.

Patten, B and Kramer, T (1933). The intiation of contraction in the embryonic chick heart. *Am. J. Anat.* 53: 349-375.

Patten, B.M. Initiation and early changes in the character of the heartbeat in vertebrate embryos. Physiol. Rev. 1949; 29:31-47

Paxton, C., Zhao, H., Chin, Y., Langner, K., & Reecy, J. (2002). Murine Tbx2 contains domains that activate and repress gene transcription. *Gene* 283, 117-124.

Periasamy, M. & Huke, S. (2001). SERCA pump level is a critical determinant of Ca(2+)homeostasis and cardiac contractility. *J Mol.Cell Cardiol.* 33, 1053-1063.

Perry, J. C. & Garson, A., Jr. (1993). Complexities of junctional tachycardias. *J Cardiovasc.Electrophysiol.* 4, 224-238.

Petrecca, K., Amellal, F., Laird, D. W., Cohen, S. A., & Shrier, A. (1997). Sodium channel distribution within the rabbit atrioventricular node as analysed by confocal microscopy. *J Physiol* 501 (Pt 2), 263-274.

Platzer, J., Engel, J., Schrott-Fischer, A., Stephan, K., Bova, S., Chen, H., Zheng, H., & Striessnig, J. (2000). Congenital deafness and sinoatrial node dysfunction in mice lacking class D L-type Ca2+ channels. *Cell* 102, 89-97.

Poitry, S., van Bever, L., Coppex, F., Roatti, A., & Baertschi, A. J. (2003). Differential sensitivity of atrial and ventricular K(ATP) channels to metabolic inhibition. *Cardiovasc.Res* 57, 468-476.

Pongs, O., Leicher, T., Berger, M., Roeper, J., Bahring, R., Wray, D., Giese, K. P., Silva, A. J., & Storm, J. F. (1999). Functional and molecular aspects of voltage-gated K+ channel beta subunits. *Ann.N.Y.Acad.Sci.* 868, 344-355.

Protas, L., Barbuti, A., Qu, J., Rybin, V. O., Palmiter, R. D., Steinberg, S. F., & Robinson, R. B. (2003). Neuropeptide Y is an essential in vivo developmental regulator of cardiac ICa,L. *Circ Res* 93, 972-979.

Qu, J., Kryukova, Y., Potapova, I. A., Doronin, S. V., Larsen, M., Krishnamurthy, G., Cohen, I. S., & Robinson, R. B. (2004). MiRP1 modulates HCN2 channel expression and gating in cardiac myocytes. *J.Biol.Chem.* 279, 43497-43502.

Reeves, J. P. & Hale, C. C. (1984). The stoichiometry of the cardiac sodium-calcium exchange system. *J Biol.Chem.* 259, 7733-7739.

Reuter, H. (1967). The dependence of slow inward current in Purkinje fibres on the extracellular calcium-concentration. *J Physiol* 192, 479-492.

Reuter, H. & Seitz, N. (1968). The dependence of calcium efflux from cardiac muscle on temperature and external ion composition *J Physiol* 195, 451-470.

Reuter, H., Pott, C., Goldhaber, J. I., Henderson, S. A., Philipson, K. D., & Schwinger, R. H. (2005). Na(+)--Ca2+ exchange in the regulation of cardiac excitation-contraction coupling *Cardiovasc Res* 67, 198-207.

Rogart, R. B., Cribbs, L. L., Muglia, L. K., Kephart, D. D., & Kaiser, M. W. (1989). Molecular cloning of a putative tetrodotoxin-resistant rat heart Na+ channel isoform. *Proc.Natl.Acad.Sci.U.S.A* 86, 8170-8174.

Rohr, S., Kucera, J. P., & Kleber, A. G. (1998). Slow conduction in cardiac tissue, I: effects of a reduction of excitability versus a reduction of electrical coupling on microconduction. *Circ Res* 83, 781-794.

Rosati, B., Pan, Z., Lypen, S., Wang, H. S., Cohen, I., Dixon, J. E., & McKinnon, D. (2001). Regulation of KChIP2 potassium channel beta subunit gene expression underlies the gradient of transient outward current in canine and human ventricle. *J Physiol* 533, 119-125.

Ross, D. L., Johnson, D. C., Denniss, A. R., Cooper, M. J., Richards, D. A., & Uther, J. B. (1985). Curative surgery for atrioventricular junctional ("AV nodal") reentrant tachycardia. *J Am.Coll.Cardiol.* 6, 1383-1392.

Ruder, M. A., Mead, R. H., Smith, N. A., Gaudiani, V. A., & Winkle, R. A. (1991). Comparison of pre- and postoperative conduction patterns in patients surgically cured of atrioventricular node reentrant tachycardia. *J Am.Coll.Cardiol.* 17, 397-402.

Sadoshima, J. & Izumo, S. (1997). Tyrosine kinases mediation of c-fos expression by cell swelling in cardiac myocytes. *Heart Vessels* Suppl 12, 194-197.

Sakai, T., Hirota, A., Fujii, S., & Kamino, K. (1983). Flexibility of regional pacemaking priority in early embryonic heart monitored by simultaneous optical recording of action potentials from multiple sites. *Jpn.J Physiol* 33, 337-350.

Sanchez-Quintana, D., Davies, D. W., Ho, S. Y., Oslizlok, P., & Anderson, R. H. (1997). Architecture of the atrial musculature in and around the triangle of Koch: its potential relevance to atrioventricular nodal reentry. *J Cardiovasc.Electrophysiol.* 8, 1396-1407.

Sanguinetti, M. C. & Jurkiewicz, N. K. (1991). Delayed rectifier outward K+ current is composed of two currents in guinea pig atrial cells. *Am.J Physiol* 260, H393-H399.

Santoro, B., Liu, D. T., Yao, H., Bartsch, D., Kandel, E. R., Siegelbaum, S. A., & Tibbs, G. R. (1998). Identification of a gene encoding a hyperpolarization-activated pacemaker channel of brain. *Cell* 93, 717-729.

Santoro, B. & Tibbs, G. R. (1999). The HCN gene family: molecular basis of the hyperpolarization-activated pacemaker channels. *Ann N Y Acad Sci* 868, 741-764.

Sato, N., Tanaka, H., Habuchi, Y., & Giles, W. R. (2000). Electrophysiological effects of ibutilide on the delayed rectifier K(+) current in rabbit sinoatrial and atrioventricular node cells 1. *Eur J Pharmacol* 404, 281-288.

Scherlag, B. J., Antz, M., Otomo, K., Tondo, C., Patterson, E., Lazzara, R., & Jackman, W. M. (1995). Atrial inputs as determinants of atrioventricular nodal conduction: re-evaluation and new concepts. *Cardiologia* 40, 753-761.

Schott, J. J., Alshinawi, C., Kyndt, F., Probst, V., Hoorntje, T. M., Hulsbeek, M., Wilde, A. A., Escande, D., Mannens, M. M., & Le Marec, H. (1999). Cardiac conduction defects associate with mutations in SCN5A. *Nat.Genet.* 23, 20-21.

Seckin, I., Sieck, G. C., & Prakash, Y. S. (2001). Volatile anaesthetic effects on Na+-Ca2+ exchange in rat cardiac myocytes. *J Physiol* 532, 91-104.

Seharaseyon, J., Sasaki, N., Ohler, A., Sato, T., Fraser, H., Johns, D. C., O'Rourke, B., & Marban, E. (2000). Evidence against functional heteromultimerization of the KATP channel subunits Kir6.1 and Kir6.2. *J Biol.Chem.* 275, 17561-17565.

Seifert, R., Scholten, A., Gauss, R., Mincheva, A., Lichter, P., & Kaupp, U. B. (1999). Molecular characterization of a slowly gating human hyperpolarization-activated channel predominantly expressed in thalamus, heart, and testis. *Proc.Natl.Acad.Sci.U.S.A* 96, 9391-9396.

Seisenberger, C., Specht, V., Welling, A., Platzer, J., Pfeifer, A., Kuhbandner, S., Striessnig, J., Klugbauer, N., Feil, R., & Hofmann, F. (2000). Functional embryonic cardiomyocytes after disruption of the L-type alpha1C (Cav1.2) calcium channel gene in the mouse. *J Biol.Chem.* 275, 39193-39199.

Severs, N. J. (1990). The cardiac gap junction and intercalated disc. *Int.J Cardiol.* 26, 137-173.

Sharma, S., Razeghi, P., Shakir, A., Keneson, B. J., Clubb, F., & Taegtmeyer, H. (2003). Regional heterogeneity in gene expression profiles: a transcript analysis in human and rat heart. *Cardiology* 100, 73-79.

Shaw, R. M. & Rudy, Y. (1997). Ionic mechanisms of propagation in cardiac tissue. Roles of the sodium and L-type calcium currents during reduced excitability and decreased gap junction coupling. *Circ Res* 81, 727-741.

Sheahan, R. G., Klein, G. J., Yee, R., Le Feuvre, C. A., & Krahn, A. D. (1996). Atrioventricular node reentry with 'smooth' AV node function curves: a different arrhythmia substrate? *Circulation* **93**, 969-972.

Shimada, T., Noguchi, T., Asami, I., & Campbell, G. R. (1986). Functional morphology of the conduction system and the myocardium in the sheep heart as revealed by scanning and transmission electron microscopic analyses *Arch.Histol Jpn.* 49, 283-295.

Silka, M. J., Kron, J., Halperin, B. D., & McAnulty, J. H. (1994). Mechanisms of AV node reentrant tachycardia in young patients with and without dual AV node physiology. *Pacing Clin.Electrophysiol.* 17, 2129-2133.

Simon, A. M., Goodenough, D. A., & Paul, D. L. (1998). Mice lacking connexin40 have cardiac conduction abnormalities characteristic of atrioventricular block and bundle branch block. *Curr.Biol.* 8, 295-298.

Soldatov, N. M., Zuhlke, R. D., Bouron, A., & Reuter, H. (1997). Molecular structures involved in L-type calcium channel inactivation. Role of the carboxyl-terminal region encoded by exons 40-42 in alpha1C subunit in the kinetics and Ca2+ dependence of inactivation. *J Biol.Chem.* 272, 3560-3566.

Spach, M. S., Lieberman, M., Scott, J. G., Barr, R. C., Johnson, E. A., & Kootsey, J. M. (1971). Excitation sequences of the atrial septum and the AV node in isolated hearts of the dog and rabbit. *Circ Res* 29, 156-172.

Spach, M. S., Miller, W. T., III, Miller-Jones, E., Warren, R. B., & Barr, R. C. (1979). Extracellular potentials related to intracellular action potentials during impulse conduction in anisotropic canine cardiac muscle. *Circ Res* 45, 188-204.

Spach, M. S., Miller, W. T., III, Geselowitz, D. B., Barr, R. C., Kootsey, J. M., & Johnson, E. A. (1981). The discontinuous nature of propagation in normal canine cardiac muscle. Evidence for recurrent discontinuities of intracellular resistance that affect the membrane currents. *Circ Res* 48, 39-54.

Spach, M. S., Dolber, P. C., & Sommer, J. R. (1985). Discontinuous propagation: an hypothesis based on known cardiac structural complexities. *Int.J Cardiol.* 7, 167-174.

Srivastava, D. & Olson, E. N. (2000). A genetic blueprint for cardiac development. *Nature* 407, 221-226.

Standley, S., Roche, K. W., McCallum, J., Sans, N., & Wenthold, R. J. (2000). PDZ domain suppression of an ER retention signal in NMDA receptor NR1 splice variants. *Neuron* 28, 887-898.

Stein, K. M. & Lerman, B. B. (1994). Evidence for functionally distinct dual atrial inputs to the human AV node. *Am.J Physiol* 267, H2333-H2341.

Stewart, P. S. & MacLennan, D. H. (1974). Surface particles of sarcoplasmic reticulum membranes. Structural features of the adenosine triphosphatase. *J Biol.Chem.* 249, 985-993.

Stewart, P. S. & MacLennan, D. H. (1976). Isolation and characterization of tryptic fragments of the adenosine triphosphatase of sarcoplasmic reticulum *J Biol Chem* 251, 712-719.

Takamatsu, T. & Wier, W. G. (1990). Calcium waves in mammalian heart: quantification of origin, magnitude, waveform, and velocity *FASEB J* 4, 1519-1525.

Takimoto, K., Li, D., Nerbonne, J. M., & Levitan, E. S. (1997). Distribution, splicing and glucocorticoid-induced expression of cardiac alpha 1C and alpha 1D voltage-gated Ca2+ channel mRNAs. *J Mol.Cell Cardiol.* 29, 3035-3042.

Takumi, T., Ohkubo, H., & Nakanishi, S. (1988). Cloning of a membrane protein that induces a slow voltage-gated potassium current. *Science* 242, 1042-1045.

Tan, H. L., Bink-Boelkens, M. T., Bezzina, C. R., Viswanathan, P. C., Beaufort-Krol, G. C., van Tintelen, P. J., van den Berg, M. P., Wilde, A. A., & Balser, J. R. (2001). A sodium-channel mutation causes isolated cardiac conduction disease. *Nature* 409, 1043-1047.

Tarone, G. & Lembo, G. (2003). Molecular interplay between mechanical and humoral signalling in cardiac hypertrophy. *Trends Mol.Med.* 9, 376-382.

Tawara S. *Das Reitzleitungssystem des Säugetierherzens: Eine anatomisch-histologische Studie über das Atrioventrikularbündel und die Purkinjeschen Fäden.* Jena, Germany: Gustav Fischer; 1906:135–136.

Tchou, P. J., Cheng, Y. N., Mowrey, K., Efimov, I. R., Van Wagoner, D. R., & Mazgalev, T. N. (1997). Relation of the atrial input sites to the dual atrioventricular nodal pathways: crossing of conduction curves generated with posterior and anterior pacing. *J Cardiovasc.Electrophysiol.* 8, 1133-1144.

Tellez, J. O. Molecular mapping of the rabbit sinoatrial node. (2005) Thesis. University of Leeds.

Toyofuku, T., Kurzydlowski, K., Tada, M., & MacLennan, D. H. (1994). Amino acids Glu2 to Ile18 in the cytoplasmic domain of phospholamban are essential for functional association with the Ca(2+)-ATPase of sarcoplasmic reticulum *J Biol Chem* 269, 3088-3094.

Tseng-Crank, J. C., Tseng, G. N., Schwartz, A., & Tanouye, M. A. (1990). Molecular cloning and functional expression of a potassium channel cDNA isolated from a rat cardiac library. *FEBS Lett.* 268, 63-68.

Ulens, C. & Tytgat, J. (2001). Functional heteromerization of HCN1 and HCN2 pacemaker channels 218. *J.Biol.Chem.* 276, 6069-6072.

van Bever, L., Poitry, S., Faure, C., Norman, R. I., Roatti, A., & Baertschi, A. J. (2004). Pore loop-mutated rat KIR6.1 and KIR6.2 suppress KATP current in rat cardiomyocytes. *Am.J Physiol Heart Circ Physiol* 287, H850-H859.

van Capelle, F. J., Janse, M. J., Varghese, P. J., Freud, G. E., Mater, C., & Durrer, D. (1972). Spread of excitation in the atrioventricular node of isolated rabbit hearts studied by multiple microelectrode recording. *Circ Res* 31, 602-616.

van Kempen, M. J., Fromaget, C., Gros, D., Moorman, A. F., & Lamers, W. H. (1991). Spatial distribution of connexin43, the major cardiac gap junction protein, in the developing and adult rat heart. *Circ Res* 68, 1638-1651.

Vassal-adams, P.R. (1982) The development of the atrioventricular bundle and its branches in the avian heart. *J. Anat.* 134: 169-183.

Verheule, S., van Kempen, M. J., te Welscher, P. H., Kwak, B. R., & Jongsma, H. J. (1997). Characterization of gap junction channels in adult rabbit atrial and ventricular myocardium. *Circ Res* 80, 673-681.

Vinogradova, T. M., Zhou, Y. Y., Maltsev, V., Lyashkov, A., Stern, M., & Lakatta, E. G. (2004). Rhythmic ryanodine receptor Ca2+ releases during diastolic depolarization of sinoatrial pacemaker cells do not require membrane depolarization. *Circ Res* 94, 802-809.

Viragh, S. & Challice, C. E. (1977). The development of the conduction system in the mouse embryo heart. I. The first embryonic A-V conduction pathway. *Dev.Biol.* 56, 382-396.

Viscomi, C., Altomare, C., Bucchi, A., Camatini, E., Baruscotti, M., Moroni, A., & DiFrancesco, D. (2001). C terminus-mediated control of voltage and cAMP gating of hyperpolarization-activated cyclic nucleotide-gated channels *J Biol Chem* 276, 29930-29934.

Viswanathan, P. C., Benson, D. W., & Balser, J. R. (2003). A common SCN5A polymorphism modulates the biophysical effects of an SCN5A mutation. *J Clin.Invest* 111, 341-346.

Vitadello, M., Vettore, S., Lamar, E., Chien, K. R., & Gorza, L. (1996). Neurofilament M mRNA is expressed in conduction system myocytes of the developing and adult rabbit heart. *J Mol.Cell Cardiol.* 28, 1833-1844.

Vozzi, C., Dupont, E., Coppen, S. R., Yeh, H. I., & Severs, N. J. (1999). Chamber-related differences in connexin expression in the human heart. *J Mol.Cell Cardiol.* 31, 991-1003.

Wang, D. W., Viswanathan, P. C., Balser, J. R., George, A. L., Jr., & Benson, D. W. (2002). Clinical, genetic, and biophysical characterization of SCN5A mutations associated with atrioventricular conduction block. *Circulation* 105, 341-346.

Wang, Q., Shen, J., Splawski, I., Atkinson, D., Li, Z., Robinson, J. L., Moss, A. J., Towbin, J. A., & Keating, M. T. (1995). SCN5A mutations associated with an inherited cardiac arrhythmia, long QT syndrome. *Cell* 80, 805-811.

Wang, Z., Fermini, B., & Nattel, S. (1993). Sustained depolarization-induced outward current in human atrial myocytes. Evidence for a novel delayed rectifier K+ current similar to Kv1.5 cloned channel currents. *Circ Res* 73, 1061-1076.

Wang, Z., Yue, L., White, M., Pelletier, G., & Nattel, S. (1998). Differential distribution of inward rectifier potassium channel transcripts in human atrium versus ventricle. *Circulation* 98, 2422-2428.

Watson, J. D. & Crick, F. H. (2003). Molecular structure of nucleic acids. A structure for deoxyribose nucleic acid. 1953. *Rev.Invest Clin.* 55, 108-109.

Wegner, A. & Walsh, T. P. (1981). Interaction of tropomyosin-troponin with actin filaments. *Biochemistry* 20, 5633-5642.

Weidmann, S Heart: Electrophysiology. *Ann. Rev. Physiol.* 36: 155-169, 1974

WEIDMANN, S. (1955). Effects of calcium ions and local anesthetics on electrical properties of Purkinje fibres. *J Physiol* 129, 568-582.

West, A. E., Chen, W. G., Dalva, M. B., Dolmetsch, R. E., Kornhauser, J. M., Shaywitz, A. J., Takasu, M. A., Tao, X., & Greenberg, M. E. (2001). Calcium regulation of neuronal gene expression. *Proc.Natl.Acad.Sci.U.S.A* 98, 11024-11031.

West, A. E., Griffith, E. C., & Greenberg, M. E. (2002). Regulation of transcription factors by neuronal activity. *Nat.Rev.Neurosci.* 3, 921-931.

Wettwer, E., Amos, G., Gath, J., Zerkowski, H. R., Reidemeister, J. C., & Ravens, U. (1993). Transient outward current in human and rat ventricular myocytes. *Cardiovasc.Res* 27, 1662-1669.

Wettwer, E., Amos, G. J., Posival, H., & Ravens, U. (1994). Transient outward current in human ventricular myocytes of subepicardial and subendocardial origin. *Circ Res* 75, 473-482.

Wible, B. A., Yang, Q., Kuryshev, Y. A., Accili, E. A., & Brown, A. M. (1998). Cloning and expression of a novel K+ channel regulatory protein, KChAP. *J Biol.Chem.* 273, 11745-11751.

Wickenden, A. D., Jegla, T. J., Kaprielian, R., & Backx, P. H. (1999). Regional contributions of Kv1.4, Kv4.2, and Kv4.3 to transient outward K+ current in rat ventricle. *Am.J Physiol* 276, H1599-H1607.

Wilde, A. A., Escande, D., Schumacher, C. A., Thuringer, D., Mestre, M., Fiolet, J. W., & Janse, M. J. (1990). Potassium accumulation in the globally ischemic mammalian heart. A role for the ATP-sensitive potassium channel. *Circ Res* 67, 835-843.

Xiao, B., Masumiya, H., Jiang, D., Wang, R., Sei, Y., Zhang, L., Murayama, T., Ogawa, Y., Lai, F. A., Wagenknecht, T., & Chen, S. R. (2002). Isoform-dependent formation of heteromeric Ca2+ release channels (ryanodine receptors). *J Biol.Chem.* 277, 41778-41785.

Xu, W. & Lipscombe, D. (2001). Neuronal Ca(V)1.3alpha(1) L-type channels activate at relatively hyperpolarized membrane potentials and are incompletely inhibited by dihydropyridines. *J Neurosci.* 21, 5944-5951.

Xu, X. P. & Best, P. M. (1991). Decreased transient outward K+ current in ventricular myocytes from acromegalic rats. *Am.J Physiol* 260, H935-H942.

Yamabe, H., Misumi, I., Fukushima, H., Ueno, K., Kimura, Y., & Hokamura, Y. (1999). Electrophysiological delineation of the tachycardia circuit in atrioventricular nodal reentrant tachycardia. *Circulation* 100, 621-627.

Yeola, S. W. & Snyders, D. J. (1997). Electrophysiological and pharmacological correspondence between Kv4.2 current and rat cardiac transient outward current. *Cardiovasc.Res* 33, 540-547.

Yu, H., Wu, J., Potapova, I., Wymore, R. T., Holmes, B., Zuckerman, J., Pan, Z., Wang, H., Shi, W., Robinson, R. B., El Maghrabi, M. R., Benjamin, W., Dixon, J., McKinnon, D., Cohen, I. S., & Wymore, R. (2001). MinK-related peptide 1: A beta subunit for the HCN ion channel subunit family enhances expression and speeds activation 223. *Circ.Res.* 88, E84-E87.

Yue, L., Feng, J., Li, G. R., & Nattel, S. (1996). Transient outward and delayed rectifier currents in canine atrium: properties and role of isolation methods. *Am.J Physiol* 270, H2157-H2168.

Yuill, K. H. & Hancox, J. C. (2002). Characteristics of single cells isolated from the atrioventricular node of the adult guinea-pig heart *Pflugers Arch.* 445, 311-320.

Yutzey, K. E., Rhee, J. T., & Bader, D. (1994). Expression of the atrial-specific myosin heavy chain AMHC1 and the establishment of anteroposterior polarity in the developing chicken heart. *Development* 120, 871-883.

Zarain-Herzberg, A., MacLennan, D. H., & Periasamy, M. (1990). Characterization of rabbit cardiac sarco(endo)plasmic reticulum Ca2(+)-ATPase gene. *J Biol.Chem.* 265, 4670-4677.

Zaritsky, J. J., Redell, J. B., Tempel, B. L., & Schwarz, T. L. (2001). The consequences of disrupting cardiac inwardly rectifying K(+) current (I(K1)) as revealed by the targeted deletion of the murine Kir2.1 and Kir2.2 genes. *J Physiol* 533, 697-710.

Zhang, M., Jiang, M., & Tseng, G. N. (2001). minK-related peptide 1 associates with Kv4.2 and modulates its gating function: potential role as beta subunit of cardiac transient outward channel? *Circ Res* 88, 1012-1019.

Zhang, Z., Xu, Y., Song, H., Rodriguez, J., Tuteja, D., Namkung, Y., Shin, H. S., & Chiamvimonvat, N. (2002). Functional Roles of Ca(v)1.3 (alpha(1D)) calcium channel in sinoatrial nodes: insight gained using gene-targeted null mutant mice. *Circ Res* 90, 981-987.

Zhang, Z., He, Y., Tuteja, D., Xu, D., Timofeyev, V., Zhang, Q., Glatter, K. A., Xu, Y., Shin, H. S., Low, R., & Chiamvimonvat, N. (2005). Functional roles of Cav1.3(alpha1D) calcium channels in atria: insights gained from gene-targeted null mutant mice. *Circulation* 112, 1936-1944.

Zhong, H. & Simons, J. W. (1999). Direct comparison of GAPDH, beta-actin, cyclophilin, and 28S rRNA as internal standards for quantifying RNA levels under hypoxia. *Biochem.Biophys.Res Commun.* 259, 523-526.

Zipes, D. P. & Mendez, C. (1973). Action of manganese ions and tetrodotoxin on atrioventricular nodal transmembrane potentials in isolated rabbit hearts. *Circ Res* 32, 447-454.

Zipes, D. P. & Fischer, J. C. (1974). Effects of agents which inhibit the slow channel on sinus node automaticity and atrioventricular conduction in the dog. *Circ Res* 34, 184-192.

Zobel, C., Cho, H. C., Nguyen, T. T., Pekhletski, R., Diaz, R. J., Wilson, G. J., & Backx, P. H. (2003). Molecular dissection of the inward rectifier potassium current (IK1) in rabbit cardiomyocytes: evidence for heteromeric co-assembly of Kir2.1 and Kir2.2. *J Physiol* 550, 365-372.

Publications

Full papers:

GREENER, I.D., DOBRZYNSKI, H., LI, J., NIKOLSKI, V., YAMAMOTO, M., BILLETER, R., EFIMOV, I. & BOYETT, M.R. (2006). A three-dimensional model of the rabbit atrioventricular node conduction axis. (manuscript being written)

GREENER, I.D., TELLEZ, J, DOBRZYNSKI, H., LI, J., YAMAMOTO, M., BOYETT, M.R. & BILLETER, R (2006). Ion channel expression in the rabbit atrioventricular node conduction axis. (manuscript being written).

J Li, JE Schneider, M Yamamoto, **ID Greener**, H Dobrzynski, K Clarke, MR Boyett. (2006). A Detailed 3D Model of the Rabbit Right Atrium Including the Sinoatrial Node, the Atrioventricular Node, Surrounding Blood Vessels and Valves (In Press).

Tellez, j., Boyett, M.R., Dobrzynski, H., Li, J., **Greener, I.D.**, Graham, G.M., Yamamoto, M., Honjo, h. & Billeter, R. (2004). Ion channel transcripts in the rabbit SA node (submitted to Circ. Res)

DOBRZYNSKI, H., LI, J., TELLEZ, J., **GREENER, I.D.**, NIKOLSKI, V.P., WRIGHT, S.E., PARSON, S.H., JONES, S.A., LANCASTER, M.K., YAMAMOTO, M., HONJO, H., TAKAGISHI, Y., KODAMA, I., EFIMOF, I.R., BILLETER, R. & BOYETT, M.R. (2005). Three-dimensional model of the sinoatrial node including distribution of different cell types and a specialised exit pathway. Circulation 111: 846-854.

EFIMOV, I.R., NIKOLSKI, V.P., ROTHENBERG, F., **GREENER, I.D.**, LI, J., DOBRZYNSKI, H. & BOYETT, M.R. (2004). Structure-function relationship in the AV junction. Anatomical Record 280A, 953-965.

DOBRZYNSKI, H., NIKOLSKI, V.P., SAMBELASHVILI, A.T., **GREENER, I.D.**, YAMAMOTO, M., BOYETT, M.R. & EFIMOV, I.R. (2003). The site of origin and molecular substrate of AV junctional rhythm in the rabbit heart. Circulation Research 93, 1102-1110.

Abstracts:

LI, J., DOBRZYNSKI, H., **GREENER, I.D.**, NIKOLSKI, V.P., YAMAMOTO, M., BILLETER, R., EFIMOV, I.R. BOYETT, M.R., (2004). Development of 3-D anatomically-detailed mathematical models of the sinoatrial and atrioventricular nodes. IEEE proceedings (in press).

BOYETT, M.R., DOBRZYNSKI, H., TELLEZ, J., **GREENER, I.D.**, LI, J. & BILLETER, R. (2004). Sinoatrial node heterogeneity and pacemaking (2004). Journal of Cellular and Molecular Cardiology (in press).

GREENER, I.D., DOBRZYNSKI, H., LI, J., NIKOLSKI, V., YAMAMOTO, M., BILLETER, R., EFIMOV, I. & BOYETT, M.R. (2004). A three-dimensional model of the rabbit atrioventricular node conduction axis. Journal of Physiology (in press).

BOYETT, M.R., DOBRZYNSKI, H., LI, J., TELLEZ, J., **GREENER, I.D.**, BILLETER, R., NIKOLSKI, V.P. & EFIMOV, I.R. (2004). Connexins and SA and AV node function. Journal of Cellular and Molecular Cardiology 36, 718-719.

BOYETT, M.R., DOBRZYNSKI, H., LI, J., TELLEZ, J., **GREENER, I.D.**, LI, J., GRAHAM, G.M., YAMAMOTO, M., HONJO, H. & BILLETER, R. (2004). The sinoatrial node: complex histology and ion channel expression. FASEB Journal 18, A20.

DOBRZYNSKI, H., TELLEZ, J., **GREENER, I.D.**, HONJO, H., YAMAMOTO, M., BILLETER-CLARK, R. & BOYETT, M.R. (2004). Quantitative real-time PCR analysis of expression of Cx43, Cx45, HCN1, HCN4, NF-M and ANP mRNAs in different regions of the rabbit sinoatrial node and its surrounding atrial muscle. Biophysical Journal 86, 15a.